



# Balkan Journal of Electrical & Computer Engineering

An International Peer Reviewed, Referred, Indexed and Open Access Journal

[www.bajece.com](http://www.bajece.com)

Vol :9  
No : 3  
Year : 2021  
ISSN : 2147 - 284X



It is abstracted and indexed in, Index Google Scholarship, the PSCR, Cross ref, DOAJ, Research Bible, Indian Open Access Journals (OAJ), Institutional Repositories (IR), J-Gate (Informatics India), Ulrich's, International Society of Universal Research in Sciences, DRJI, EyeSource, Cosmos Impact Factor, Cite Factor, SIS Scientific Indexing Service, IJIF, iifactor. ULAKBİM-TR Dizin.

**General Publication Director & Editor-in-Chief**  
Musa Yılmaz, Batman University, Turkey.

**Vice Editor**  
Hamidreza Nazarpouya, University of California Riverside, USA

**Scientific Committee**  
Abhishek Shukla (India)  
Abraham Lomi (Indonesia)  
Aleksandar Georgiev (Bulgaria)  
Arunas Lipnickas (Lithuania)  
Audrius Senulis (Lithuania)  
Belle R. Upadhyaya (USA)  
Brijender Kahanwal (India)  
Chandar Kumar Chanda (India)  
Daniela Dzhonova-Atanasova (Bulgaria)  
Deris Stiawan (Indonesia)  
Emel Onal (Turkey)  
Emine Ayaz (Turkey)  
Enver Hatimi (Kosovo)  
Ferhat Sahin (USA)  
Gursel Alici (Australia)  
Hakan Temeltaş (Turkey)  
Ibrahim Akduman (Turkey)  
Jan Izykowski (Poland)  
Javier Bilbao Landatxe (Spain)  
Jelena Dikun (Lithuania)  
Karol Kyslan (Slovakia)  
Kunihiko Nabeshima (Japan)  
Lambros Ekonomou (Greece)  
Lazhar Rahmani (Algerie)  
Marcel Istrate (Romania)  
Marija Eidukeviciute (Lithuania)  
Milena Lazarova (Bulgaria)  
Muhammad Hadi (Australia)  
Muhamed Turkanović (Slovenia)  
Mourad Houabes (Algerie)  
Murari Mohan Saha (Sweden)  
Nick Papanikolaou (Greece)  
Okyay Kaynak (Turkey)  
Osman Nuri Ucan (Turkey)  
Ozgun E. Mustecaplioglu (Turkey)  
Padmanaban Sanjeevikumar (India)  
Ramazan Caglar (Turkey)  
Rumen Popov (Bulgaria)  
Tarek Bouktir (Algeria)  
Sead Berberovic (Croatia)  
Seta Bogosyan (USA)  
Savvas G. Vassiliadis (Greece)  
Suwarno (Indonesia)  
Tulay Adali (USA)  
Yogeshwarsing Calleecharan (Mauritius)  
YangQuan Chen (USA)  
Youcef Soufi (Algeria)

#### Aim & Scope

The journal publishes original papers in the extensive field of Electrical-Electronics and Computer engineering. It accepts contributions which are fundamental for the development of electrical engineering, computer engineering and its applications, including overlaps to physics. Manuscripts on both theoretical and experimental work are welcome. Review articles and letters to the editors are also included.

Application areas include (but are not limited to): Electrical & Electronics Engineering, Computer Engineering, Software Engineering, Biomedical Engineering, Electrical Power Engineering, Control Engineering, Signal and Image Processing, Communications & Networking, Sensors, Actuators, Remote Sensing, Consumer Electronics, Fiber-Optics, Radar and Sonar Systems, Artificial Intelligence and its applications, Expert Systems, Medical Imaging, Biomedical Analysis and its applications, Computer Vision, Pattern Recognition, Robotics, Industrial Automation.



ISSN: 2147- 284X  
Vol: 9  
No : 3  
Year: July 2021

#### CONTENTS

- M. E. Başoğlu;** Comparisons of Different Maximum Power Point Tracking Strategies with Zeta Converter,..... **221-228**
- A. Bas, H. E. Kocer;** Real-Time Hand Motion Recognition: A Robust Low-Cost Approach,.....**229-234**
- B. Buz, B. Gülçiçek, Ş. Bahtiyar;** A Hybrid Machine Learning Model to Detect Reflected XSS Attack,..... **235-241**
- Murat Aslan;** An Approach Based on Tunicate Swarm Algorithm to Solve Partitional Clustering Problem,..... **242-248**
- H. Ali, E. Erçelebi;** Development of an Embedded System for Building System Management Based on PV-Powered,..... **249-254**
- H. Savci, H. Sajjad, S. Khan, F. Kaburcu;** A Compact Multi-Band Antenna on Textile for Wearable Body Area Network Devices,....**255-260**
- S. Doğan;** Design and Optimization of Directive Circular Patch Antenna with Asymmetric Pixels Using Genetic Algorithm,..... **261-267**
- S. I. Omurca, E. Ekinci, E. Yakupoğlu, E. Arslan, B. Çapar;** Automatic Detection of the Topics in Customer Complaints with Artificial Intelligence,.....**268-277**
- G. Ertaş;** Signal Attenuation Model Free Classification of Diffusion MR Signals of the Breast Tissue using Long Short-Term Memory Networks,.....**278-283**
- M. E. Asker, H. Kürüm;**A Novel Chaotic Switched Modulation for EMI Suppression in Electrical Drive System,.....**284-289**
- İ. Özer;** Classification of Urease Activity in Full-Fat Soybean Production by Extrusion Using Machine Learning Algorithms,..... **290-296**
- E. Ozdogan, R. Das;** IoT based a Smart Home Automation System Design: Simulation Case,.....**297-303**
- G. Mendi, C. Budak;** Automatic Cell Nucleus Segmentation Using Superpixels and Clustering Methods in Histopathological Images,.....**304-309**
- E. Dursun;** Solar Energy Potential in Horn of Africa: A Comparative Study Using Matlab/Simulink .....**310-319**

**BALKAN  
JOURNAL OF  
ELECTRICAL & COMPUTER ENGINEERING**  
(An International Peer Reviewed, Indexed and Open Access Journal)

**Contact**  
Batman University  
Department of Electrical-Electronics Engineering  
Bati Raman Campus Batman-Turkey

**Web:** <http://dergipark.gov.tr/bajece>  
<https://www.bajece.com>  
**e-mail:** [bajece@hotmail.com](mailto:bajece@hotmail.com)

# Comparisons of different Maximum Power Point Tracking Strategies with Zeta Converter

Mustafa Engin Başoğlu

**Abstract**—Maximum power point tracking (MPPT) strategy is one of the major parameters affecting efficiency in photovoltaic (PV) systems. In this paper, distributed MPPT approaches are compared with central mode MPPT. Advantages and disadvantages of submodule level MPPT technique and module level MPPT approach are shown with simulation studies. Comparisons are made with incremental conductance (IC) algorithm. In this context, non-isolated zeta converter is used as a power-processing unit. Effect of the MPPT strategy on the collected energy performance is observed by simulation studies performed in MATLAB/Simulink. It is clear by these studies that energy capture is bigger in submodule level MPPT strategy and module level MPPT with respect to central mode which is seen by simulations. However, central mode MPPT offers cost effective solution because of the low hardware requirements.


**Index Terms**— Distributed MPPT, zeta converter, maximum power point tracking, central MPPT, module level MPPT, submodule level MPPT.

## I. INTRODUCTION

SINCE THE beginning of the 2000s, the use of renewable energy sources in electrical energy production has become increasingly widespread. Despite its intermittent and uncertain characteristics, solar energy has the highest potential among renewable energy sources [1].

The most important component of a solar energy system is the PV module. PV modules consist of solar cells with a voltage of about 0.6V and the efficiency of these cells is very low. In addition, due to the intermittent and uncertain nature of solar energy, PV modules can reach the highest efficiency value at a certain time of the day [2-3]. On the other hand, the current-voltage characteristics of PV modules have exponential function characteristics and they must be operated at specified current and voltage values in order to generate maximum power. Thus, high efficiency is obtained from the PV module.

MUSTAFA ENGİN BAŞOĞLU, is with Department of Electrical and Electronics Engineering University of Gümüşhane, Gümüşhane, Turkey.(e-mail: [menginbasoglu@gumushane.edu.tr](mailto:menginbasoglu@gumushane.edu.tr)).

 <https://orcid.org/0000-0002-6228-4112>

Manuscript received April 3, 2021; accepted July 5, 2021.  
DOI: [10.17694/bajece.908875](https://doi.org/10.17694/bajece.908875)

In order for PV modules to operate at their maximum power point, they must not be connected directly to the load. Because it is very likely that there is impedance mismatch between module and load. In order to avoid this mismatch, a power converter is used between the module and the load. DC-DC converters are used for this purpose [4-5]. However, in order to obtain maximum power from a PV module, the converter must be controlled by a MPPT algorithm. In recent years, many algorithms have been proposed for this purpose [6-11].

When the literature is reviewed, it is seen that many MPPT studies with zeta converter have been conducted. In [12], variable step size based MPPT algorithm is used with discontinuous mode (DCM) zeta converter. Perturb and observe (P&O) algorithm, IC algorithm and modified P&O algorithm have been compared each other. In another study [13], the performances of buck-boost converter topologies using P&O algorithm were compared. According to this study, the zeta converter showed a lower oscillating performance in MPPT. In [14], MPPT application with IC algorithm based zeta converter is presented. A comparative study between synchronous zeta and synchronous SEPIC converter [15]. Analysis and design of a non-inverted zeta converter is investigated in [16]. The model of the zeta converter was designed in MATLAB/Simulink environment. In addition, MPPT application with zeta converter was carried out. In [17], performances of P&O algorithm and IC algorithm with zeta converter is analyzed. According to the result obtained in [17] that IC algorithm has superior performance with respect to P&O algorithm. Artificial neural network based optimization algorithm using zeta converter is studied in [18]. According to the findings obtained in this study, the ANN algorithm works better than the P&O algorithm. In another optimization-based study, human psychology algorithm is used for partial shading conditions (PSC) [19]. It is seen that FPGA-based MPPT studies have increased in recent years. Comparisons of two of the popular algorithms are made for different irradiation conditions [20].

In a PV system, the MPPT strategy can be implemented in different ways. While determining this strategy, issues such as system power, location, climate characteristics and cost are taken into account. It is also important whether MPPT is performed at the sub-module level, module level, array level, or centrally. In this study, the comparison of central MPPT with MPPT applications at sub-module and module level has been made. For this purpose, the zeta converter was used. The rest of the study can be summarized as follows. In the first part

of the study, MPPT strategies are illustrated. In the second part, the basic mathematical model of the zeta converter is explained. Then, the simulation studies performed were explained and the results were evaluated. In the last section, the results of the study are shared.

II. MPPT STRATEGIES

MPPT strategy can be defined as how the MPPT process is performed. Generally, MPPT controlled from a single point is defined as centrally controlled MPPT. In this type of control, the system where a large number of solar panels are connected in series/parallel is considered as if there is a single maximum power point and situations that may cause incompatibility such as partial shading are not taken into account. The central mode MPPT circuit with two PV modules is given in Fig. 1. It is seen here that the PV modules are connected in series. In such an implementation, MPPT efficiency may be reduced if one of the modules is fully or partially shaded.

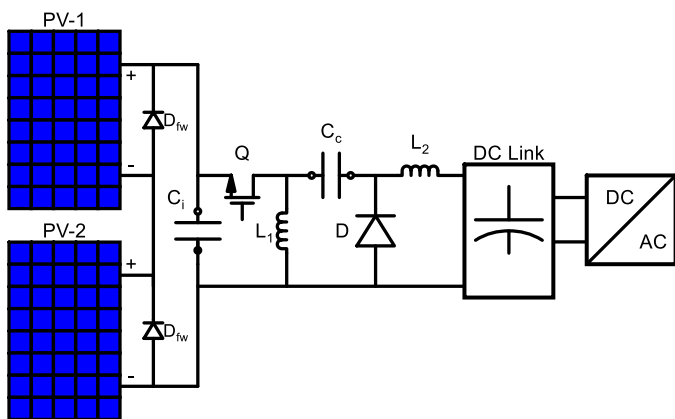


Fig. 1 Central MPPT configuration

In the module-based MPPT strategy, MPPT operation is performed independently in all modules. Thus, situations such as incompatibility between PV modules are less frequent [21]. MPPT efficiency is greater than centrally controlled MPPT. Module level MPPT configuration is presented in Fig. 2.

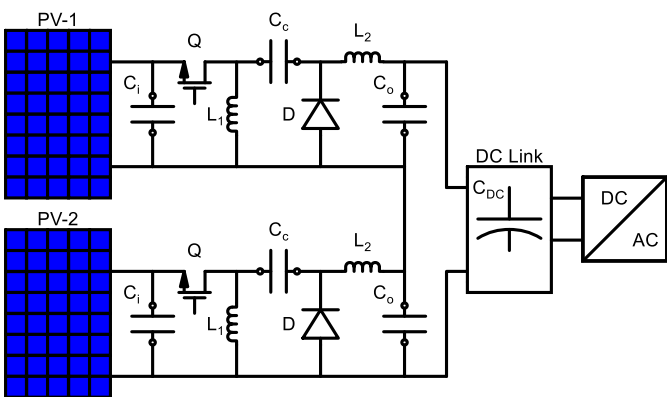


Fig. 2 Module level MPPT configuration

PV modules consist of 3-6 sub-modules. The number of sub-modules depends on the power of the PV module and the manufacturer's choice. Sub-module-based MPPT is a complex

approach with high hardware requirements and less software needs. As shown in Fig. 3, each sub-module is connected to a converter and the converter output is connected in series or parallel to create a DC link for the inverter circuit. Higher efficiency values are achieved in sub-module based MPPT applications compared to the other two strategies. This strategy works especially well in shadowing situations [22].

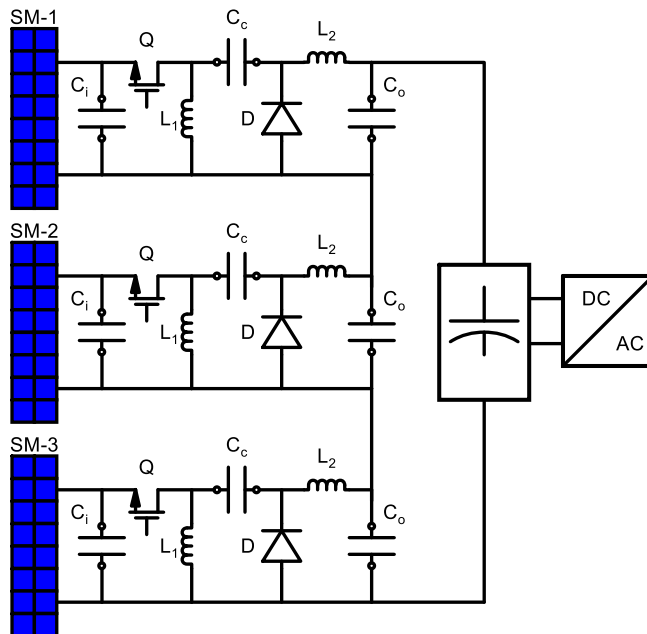


Fig. 3 Submodule level MPPT configuration

III. MPPT SYSTEM COMPONENTS

In order to compare MPPT strategies, it is useful to explain the components of the system first. System components can be listed as PV module, converter and algorithm.

Zeta converter is a circuit with the ability to decrease and increase the voltage. Although the zeta converter is similar to the single ended primary inductance converter (SEPIC) with this feature, the use of semiconductor switch is different from the SEPIC converter. High-side PMOS FET is used in the zeta converter. As seen in Fig. 4, this converter has two inductors, three capacitors, a diode and an active switch. [23].

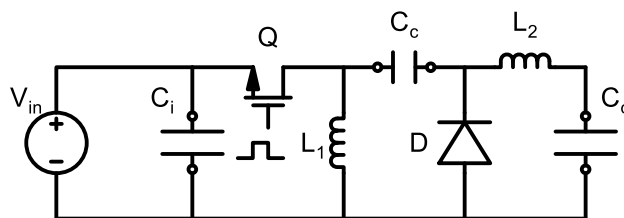


Fig.4. Electrical circuit of non-isolated zeta converter

A. Operation Modes of Zeta Converters

The operating principle of the zeta converter is explained based on the open and closed states of the PMOS FET switch. In order to determine the mathematical relationship between input and output in a zeta converter, it is necessary to determine the current variations on inductances. While the

switch Q is turned on, the  $L_1$  and  $L_2$  are fed from the input voltage and the energies of the inductances increase. In this case, the voltages on the inductances are equal to the source voltage as presented in Fig. 5. Current variations on  $L_1$  and  $L_2$  are respectively;

$$v_{L1} = L_1 \frac{di_{L1}}{dt} \rightarrow \Delta i_{L1} = \frac{V_{in} D}{L_1 f} \quad (1)$$

$$v_{L2} = L_2 \frac{di_{L2}}{dt} \rightarrow \Delta i_{L2} = \frac{V_{in} D}{L_2 f} \quad (2)$$

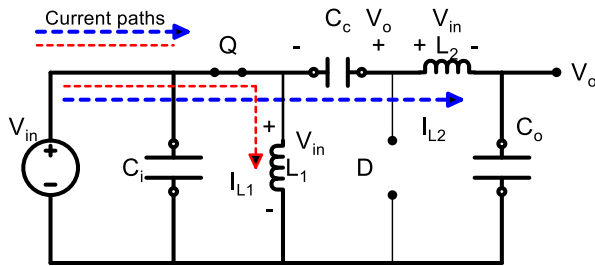


Fig. 5 Equivalent circuit when Q1 is turned on (red line:  $I_{L1}$ , blue line:  $I_{L2}$ )

When Q is turned off, currents of  $L_1$  and  $L_2$  pass through the diode as shown in Fig. 6. Currents of  $L_1$  and  $L_2$  decrease. The voltage across inductances is equal to the output voltage. The amount of reduction of inductance current in this range is expressed in Eq. (3) and Eq. (4), respectively.

$$v_{L1} = L_1 \frac{di_{L1}}{dt} \rightarrow \Delta i_{L1} = \frac{V_o(1-D)}{L_1 f} \quad (3)$$

$$v_{L2} = L_2 \frac{di_{L2}}{dt} \rightarrow \Delta i_{L2} = \frac{V_o(1-D)}{L_2 f} \quad (4)$$

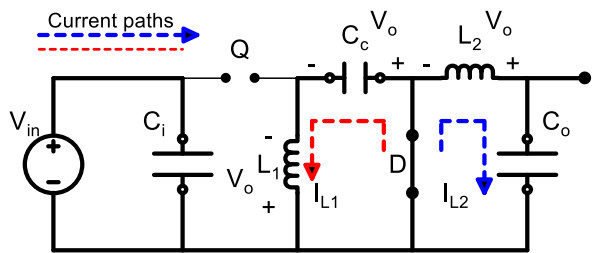


Fig. 6 Equivalent circuit when Q1 is turned off (red line:  $I_{L1}$ , blue line:  $I_{L2}$ )

To prevent saturation; at steady state the current changes across inductances must be equal. According to this; if the current increase of the inductance  $L_1$  and the current decrease of the inductance  $L_1$  are equal to each other, the mathematical relationship between the input voltage and the output voltage is obtained as in Eq. (5).

$$V_o = V_{in} \frac{D}{1-D} \quad (5)$$

### B. Zeta Converter for MPPT Application

Zeta converter is a suitable topology for MPPT application since its input and output voltage polarity is the same, and it has the characteristics of voltage reduction and increase.. In order to perform MPPT with a zeta converter, it is necessary to obtain the relationship between the input and output of the converter. Thanks to this relation, it is determined whether the maximum power point can be determined in the PV module current-voltage curve.

The input power of the converter is equal to the power of the PV system. This power can be expressed as in Eq. (6). PV system voltage can be expressed in Eq. (7).

$$P_{PV} = V_{PV} I_{PV} = I_{PV} R_{PV} \quad (6)$$

$$V_{PV} = I_{PV} R_{PV} \quad (7)$$

In Eq. (6) and Eq. (7),  $P_{PV}$  is the power of the PV system;  $V_{PV}$  and  $I_{PV}$  are the voltage of PV system and current of PV system, respectively.  $R_{PV}$  is the instantaneous equivalent impedance of PV system. Eq. (8) and Eq. (9) can be written for the output power and output voltage of the zeta converter, respectively.

$$P_o = V_o I_o = I_o^2 R_L \quad (8)$$

$$V_o = I_o R_L \quad (9)$$

In Eq. (8) and Eq. (9),  $P_o$  is the power of the zeta output,  $V_o$  and  $I_o$  are the output voltage of the zeta and output current of the zeta converter.  $R_L$  is the load resistance. By using Eq. (5-9), the relationship between  $R_L$  and  $R_{PV}$  can be formulated as in Eq. (10),

$$R_{PV} = R_L \frac{(1-D)^2}{D^2} \quad (10)$$

### C. Incremental Conductance Algorithm

The IC algorithm is a hill climbing-based approach in which current and voltage changes are monitored. Although many of its properties are similar to the P&O algorithm, it is accepted that its dynamic response is better than P&O under suddenly changing irradiation conditions [9]. As can be seen from Fig. 7, the operation principle of the IC algorithm is based on the evaluation of the ratio of the PV system current change to the voltage change in general. Eq. (11) explains the algorithm.

$$\begin{cases} \frac{\Delta P}{\Delta V} = 0 & \left\{ \begin{array}{l} \frac{\Delta I}{\Delta V} = \frac{-I}{V} \rightarrow MPP \\ \frac{\Delta P}{\Delta V} > 0 \Rightarrow \frac{\Delta I}{\Delta V} > \frac{-I}{V} \rightarrow \text{left of MPP} \\ \frac{\Delta P}{\Delta V} < 0 & \left\{ \begin{array}{l} \frac{\Delta I}{\Delta V} < \frac{-I}{V} \rightarrow \text{right of MPP} \end{array} \right. \end{array} \right. \quad (11)$$

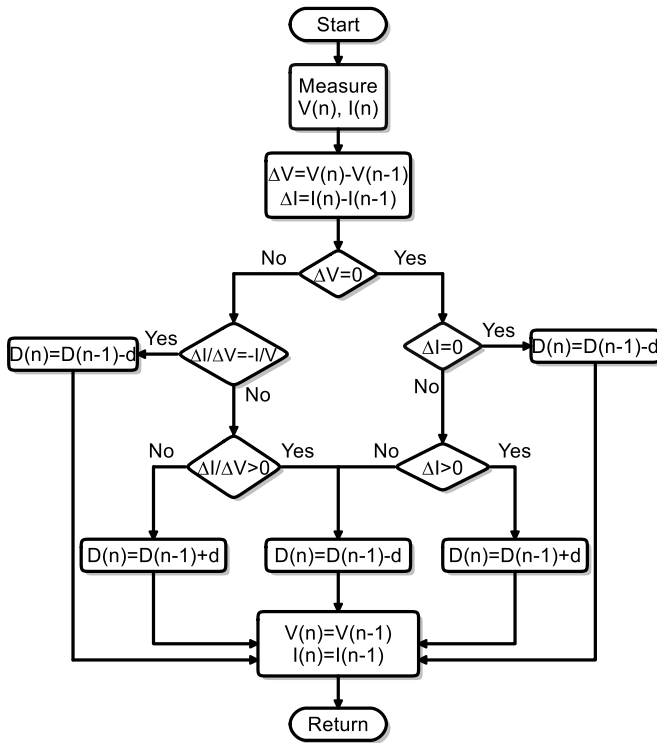


Fig. 7 Flowchart of the IC algorithm

IV. SIMULATION RESULTS

The performance of three different MPPT strategies has been examined under different shading conditions with simulation studies. These strategies can be listed as central mode MPPT, module based MPPT, and submodule based MPPT. In these three approaches, a non-isolated zeta converter designed for a fixed power level and c-Si PV modules are used. Technical information of the module and submodule are listed in Table I. The basic parameters of the zeta converter are also listed in Table II.

TABLE I  
SPECIFICATIONS OF THE PV MODULE [23]

Bosch PV Module c-Si M 48	Value
Short circuit current	8.5A
Open circuit voltage	28.9V
Maximum power voltage	23.4V
Maximum power current	7.9A
Maximum power	180W
Bypass diodes	3
Submodule - Bosch	Value
Maximum power voltage	7.8V
Maximum power current	7.9A
Maximum power	60W
<b>Note:</b> 1000W/m <sup>2</sup> 25 °C AM: 1.5	

TABLE II  
SPECIFICATIONS OF THE ZETA CONVERTER

Features	Value
Input / output capacitor	630µF / 100 µF
Primary/Secondary inductance	1mH/1mH
Switching frequency	20kHz

In central mode MPPT, two PV modules are connected in series. The modules whose technical specifications are given in Table I consist of three serially connected submodules. All submodules are connected to the diode in reverse parallel. The model for the simulation studies is shown in Fig. 8.

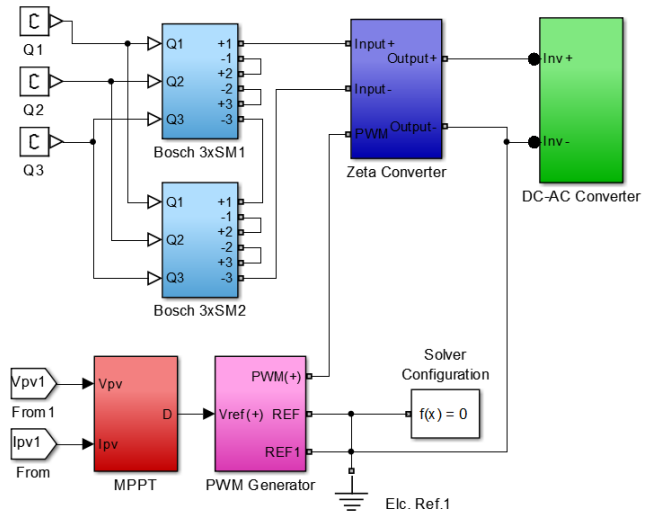


Fig. 8 Central mode MPPT

Simulation studies in three MPPT approaches were carried out for PSCs. In the first simulation study, the irradiation values of the shading situation are 200-500-1000W/m<sup>2</sup>, in this case the global maximum power value of the PV system is around 127.5W. As can be seen from Fig. 9, there are three peaks in the PV system power-voltage (P-V) curve and the initial duty ratio value of the IC algorithm is determined as 80%. Under these conditions, it is possible to work at the global maximum power point (GMPP). Tracking efficiency is calculated as 96.24% within 0.3 seconds.

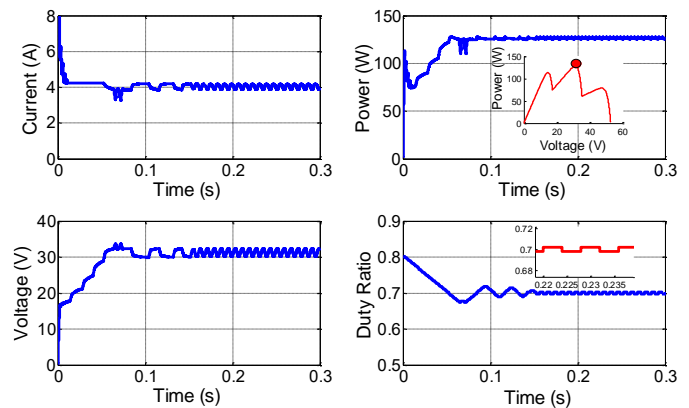


Fig. 9 Result of central mode MPPT for 200-500-1000W/m<sup>2</sup>: Current, voltage, power and duty ratio variations.

In the second simulation study, an irradiation profile case with four different values was investigated. As can be seen in Fig. 10, there are four peaks in the P-V curve. Global maximum power value is around 150W. The initial duty ratio is 80%, and GMPP tracking (GMPPT) has been successfully implemented. However, since the IC algorithm is hill climbing

based, the performance is directly related to the initial duty rate being randomly well determined.

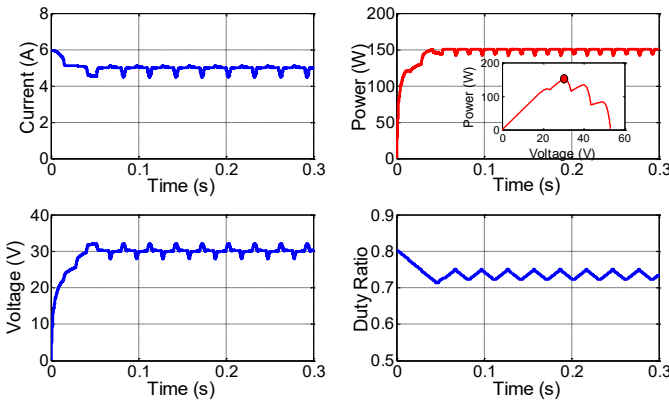


Fig. 10 Result of central mode MPPT for 200-400-600-700W/m<sup>2</sup>: Current, voltage, power and duty ratio variations.

In the last simulation study for central mode MPPT, GMPP could not be achieved. Although the GMPP is located at the far right of the P-V curve as given in Fig. 11, the IC algorithm remains stuck at the middle MPP. For this reason, tracking efficiency is calculated as 76.11%

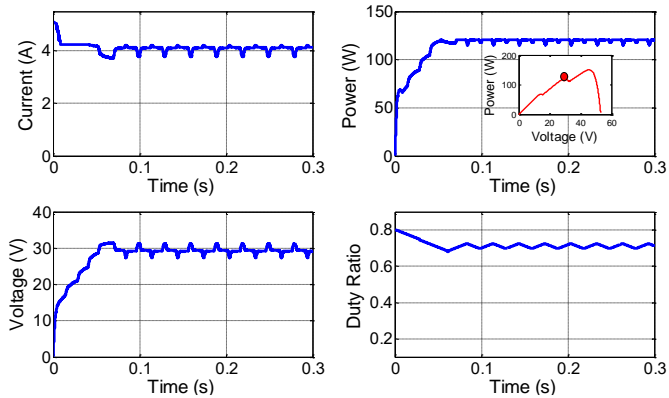


Fig. 11 Result of central mode MPPT for 400-500-600W/m<sup>2</sup>: Current, voltage, power and duty ratio variations.

The same PV system is used in the module-based MPPT approach. The difference of module-based MPPT according to the central mode is that a zeta converter is used for each PV module and the MPPT operation is performed separately for each PV module, which is seen in Fig. 12. In the first simulation study, PV modules are exposed to three different irradiances and subjected to partial shading. Thanks to the bypass diodes in the PV module, the shadowed sub-modules are bypassed. The global maximum power value of the PV module in the P-V curve is 63.75W. Initial value of duty ratio is 80%. In Fig. 13, the result of the first simulation study for the first module-based MPPT approach is given. As can be seen from Fig. 13, GMPP is successfully monitored, within 0.3 seconds; the tracking efficiency is calculated as 97.59%. However, because of the multi-peak P-V curve condition, increased conductivity may not always give successful results. For example; if initial value of duty ratio is 20%, the tracking

efficiency is 86.65%. Because, the IC algorithm fails in the first MPP which is located at the left side of the P-V curve.

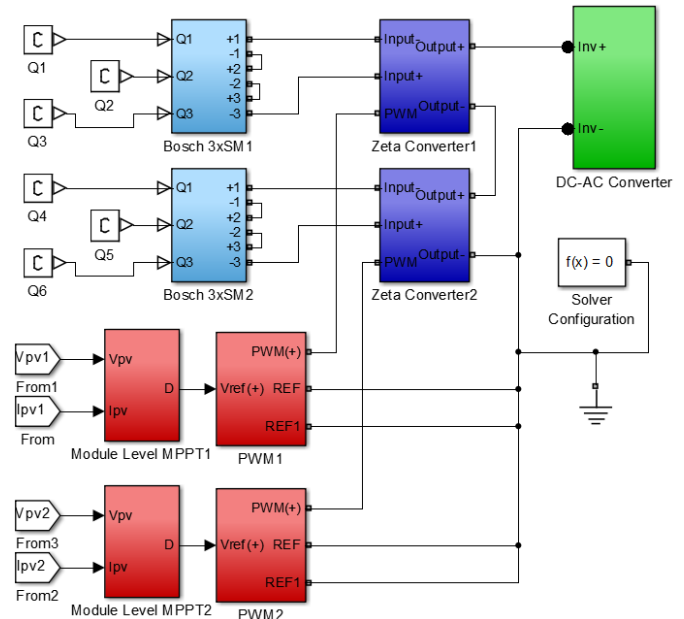


Fig. 12 Module level MPPT model

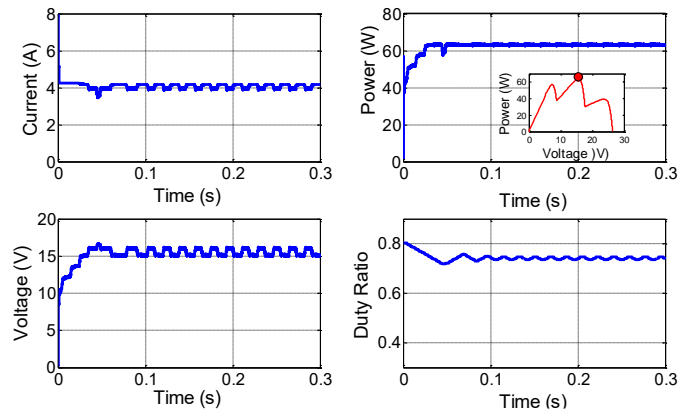


Fig. 13 Result of module level MPPT for 200-500-1000W/m<sup>2</sup>: Current, voltage, power and duty ratio variations.

In the other simulation study, the PV modules receive 200-400-600W/m<sup>2</sup> and 700-700-700W/m<sup>2</sup>, respectively. As it can be understood from here, one of the modules is partly shaded and the other is under uniform radiation. For this reason, the current and voltage changes of PV modules are different from each other. The PV module, which is subject to partial shading, has three peaks in the P-V curve, while the other module has a single MPP. The current, voltage and power changes of the two modules are given in Fig. 14. The modules operate continuously at the MPP with a power of 48.92W and 123.2W, respectively. Tracking efficiency is around 97% for both modules, respectively.

In the last module-based simulation study, the irradiance values are 400-500-600W/m<sup>2</sup>. These irradiance values are applied to both modules. Since they have the same irradiance values, the MPPT of the PV modules is identical. The results

of this simulation scenario are given in Fig. 15. Each module generates 75W of power.

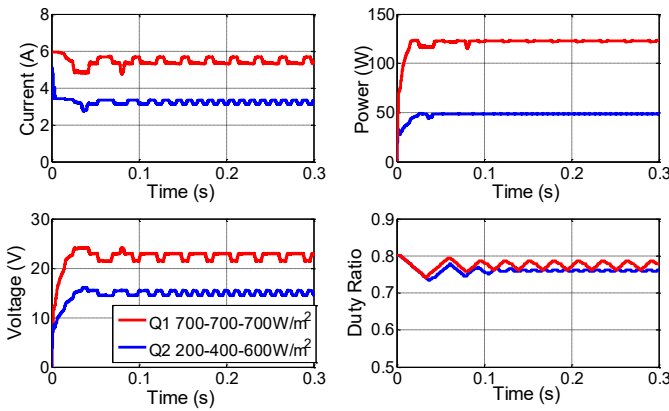


Fig. 14 Result of module level MPPT for 200-400-600-700W/m<sup>2</sup>: Current, voltage, power and duty ratio variations.

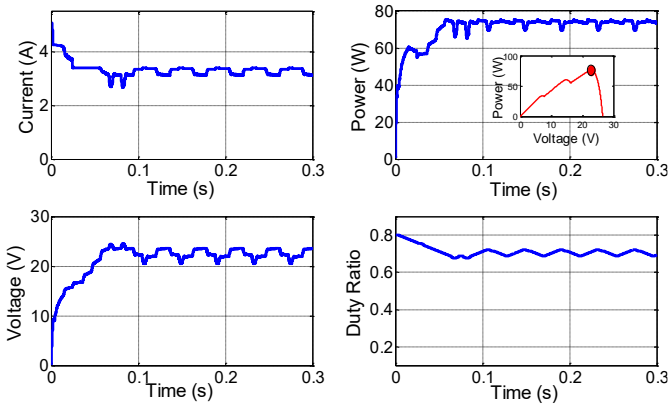


Fig. 15 Result of module level MPPT for 400-500-600W/m<sup>2</sup>: Current, voltage, power and duty ratio variations.

In the submodule based MPPT approach, each submodule is connected to the zeta converter. Since PV two modules are used in this study, there is a PV system consisting of six submodules in total. All submodules are electrically independent from each other and there is no need to use a bypass diode. Because a multi-peak situation does not occur in the P-V curve. MPPT operation is performed separately in all submodules and outputs of the zeta converters are connected in series or parallel. Simulink model for submodule based MPPT approach is given in Fig. 16. Six different MPPT processes are applied to six submodules in this approach. In this way, it is ensured that the biggest possible powers are generated from submodules.

The first shading condition is the same as in the central mode MPPT and module-based MPPT approach. The irradiance values of the first module and the irradiance values of the second module are the same. Therefore, the changes in current, voltage, power and fill rate are the same in the two modules. When the changes given in Fig. 17 are evaluated; submodule exposed to 1000W/m<sup>2</sup> produces around 60W of power. Since the current and voltage values for this submodule are close to each other and the duty ratio converges to 100%, an unstable and oscillating operation has occurred. Although

oscillating operation can be eliminated by changing the load value at the zeta converter output, this issue has been evaluated outside the scope of this study. On the other hand, stable operation has been realized for two submodules exposed to 200W/m<sup>2</sup> and 500W/m<sup>2</sup> irradiation. Tracking efficiency of around 97% has been achieved in these sub-modules. However, in the sub-module where high oscillation occurs due to unstable operation, the tracking efficiency is around 80%.

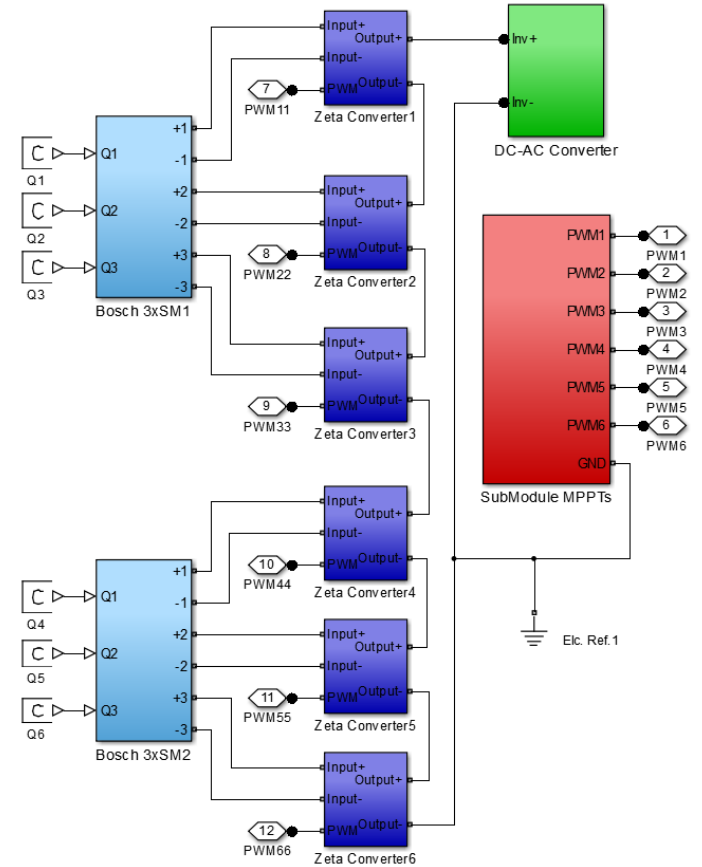


Fig. 16 Submodule level MPPT model

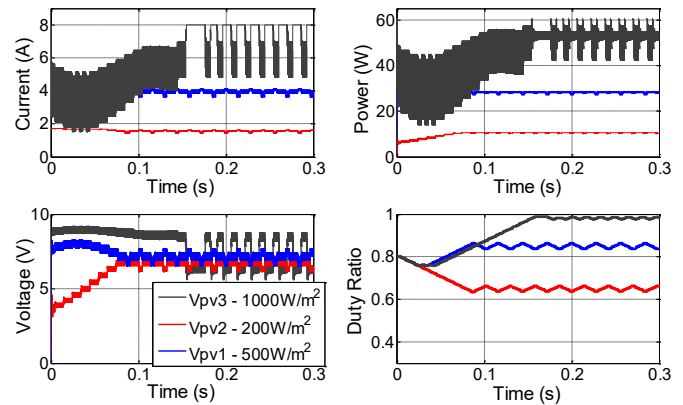


Fig. 17 Result of submodule level MPPT for 200-300-1000W/m<sup>2</sup>: Current, voltage, power and duty ratio variations.

The results of the other two simulation studies related to the submodule based MPPT approach are given in Fig. 18 and Fig. 19. Since the P-V curve cannot be multi-peaked in a



submodule, GMPPT has been successfully realized. As can be seen from Fig. 18, submodules produce different power values according to the irradiation they are exposed to. A similar comment can be made for Fig. 19.

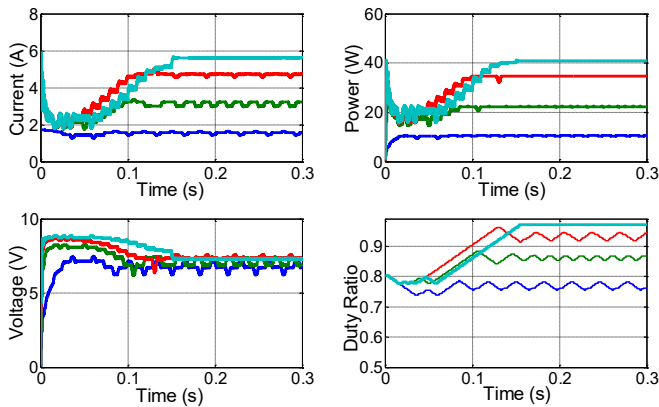


Fig. 18 Result of submodule level MPPT for 200-400-600-700W/m<sup>2</sup>: Current, voltage, power and duty ratio variations.

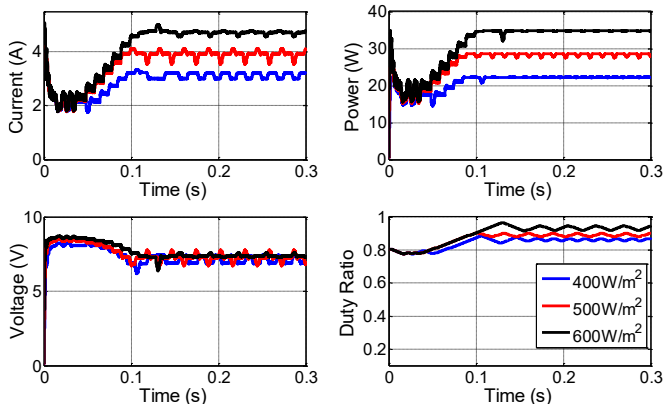


Fig. 19 Result of submodule level MPPT for 400-500-600W/m<sup>2</sup>: Current, voltage, power and duty ratio variations.

## V. DISCUSSION

According to the simulation results, it is understood that the success of the MPPT depends on many parameters. These parameters can be listed as panel structure, algorithm used, approach type, load conditions, radiation, partial shading and some parameters in the algorithm. Table III shows the results for all MPPT approaches. Although these results may differ for different converters and conditions, they have had some outcomes. It is useful to explain one of these inferences with an example. Suppose the irradiance values are 400-500-600W/m<sup>2</sup>. According to these irradiance values, when the initial value of duty ratio is taken as 80%, the efficiency of the central mode MPPT was calculated as 76% and the efficiency of the module-based MPPT approach was calculated as 93.98%. If the initial value of the duty ratio is taken as 35%, the efficiency values vary considerably. In this case, the efficiency is 58.67% for central mode MPPT, 54.9% for module based MPPT, and 80% for sub-module based MPPT application. In the central mode MPPT and module based MPPT approaches, the algorithm stuck at the wrong peak

points in the P-V curve. On the other hand, in the submodule-based approach, it was able to catch the global power point. The reason for the small efficiency is related to the simulation time.

TABLE III  
SIMULATOR RESULTS

MPPT Approach	200-500-1000 W/m <sup>2</sup>	200-400-600-700 W/m <sup>2</sup>	400-500-600 W/m <sup>2</sup>
Central	96.24%	96.58%	76.11%
Module	97.59%	97.18%	93.98%
Submodule	97.5% 94.42% 76%	97.28% 93.87% 89.77% 83.19%	93.83% 92.25% 89.77%

## VI. CONCLUSIONS

Performance evaluation of different MPPT strategies was made in this study. For this purpose, the zeta type buck-boost topology, which is a kind of DC-DC converter used in MPPT applications, has been chosen. The IC algorithm has been chosen as the algorithm in the comparisons. This performance evaluation has been conducted with many simulation studies and some of them are presented. It has been seen that MPPT performance depends on many parameters. However, MPPT precision increases from the central mode MPPT approach to the submodule-based MPPT approach. In this case, although the cost and hardware requirement increases, the need for complex algorithms disappears. On the other hand, hybrid and complex algorithms are required to ensure GMPPT in centralized mode and module-based approaches.

## REFERENCES

- [1] Başoğlu M.E., Kazdaloğlu A., Erfidan T., Bilgin M.Z., Çakır B., Performance analyzes of different photovoltaic module technologies under İzmit, Kocaeli climatic conditions, *Renewable & Sustainable Energy Reviews*, vol. 52, pp. 357-365, 2015.
- [2] Wolf P., Benda V., Identification of PV solar cells and modules parameters by combining statistical and analytical methods, *Solar Energy*, vol. 93, pp. 151-157, 2013.
- [3] Başoğlu M.E., Çakır B., An improved incremental conductance based MPPT approach for PV modules, *Turkish Journal of Electrical Engineering & Computer Sciences*, vol. 23, no. 6, pp. 1687-1697, 2015.
- [4] Başoğlu M.E., Çakır B., Comparisons of MPPT performances of isolated and non-isolated DC-DC converters by using a new approach, *Renewable & Sustainable Energy Reviews*, vol. 60, pp. 1100-1113, 2016.
- [5] Taghvaei M.H., Radzi M.A.M., Moosavain S.M., Hizam H., Marhaban M.H., A current and future study on non-isolated DC-DC converters for photovoltaic applications, *Renewable & Sustainable Energy Reviews*, vol. 17, pp. 216-227, 2013.
- [6] ESRAM T., Chapman P. L., Comparison of photovoltaic array maximum power point tracking techniques, *IEEE Transactions on Energy Conversion*, vol. 22, no. 2, pp. 439-449, 2007.
- [7] Mei Q., Shan M., Liu L., Guerrero J. M., A novel improved variable step size incremental resistance MPPT method for PV systems, *IEEE Transactions on Industrial Electronics*, vol. 58, no. 6, pp. 2427-2434, 2011.
- [8] Liu F., Duan S., Liu F., Liu B., Kang Y., A variable step size INC MPPT method for PV systems, *IEEE Transactions on Industrial Electronics*, vol. 55, no. 7, pp. 2622-2628, 2008.
- [9] Reisi A. R., Moradi M. H., Jamasb S., Classification and comparison of maximum power point tracking techniques for photovoltaic system: A

- review, *Renewable and Sustainable Energy Reviews*, vol. 19, pp. 433-443, 2013.
- [10] Başoğlu M.E., Çakır B., Hybrid global maximum power point tracking approach for photovoltaic power optimizers, *IET Renewable Power Generation*, vol. 12, no. 8, pp. 875-882, 2018.
- [11] Başoğlu M.E., An approximate short circuit strategy for transient MPPT performance of uniformly irradiated photovoltaic modules, *Balkan Journal of Electrical & Computer Engineering*, vol. 7, no.1, pp. 88-93, 2019.
- [12] Satapathy S., Dash K. M. Babu B. C., Variable step size MPPT algorithm for photovoltaic array using zeta converter – A comparative analysis, Allahabad India, 2013, pp. 1-6.
- [13] Soedibyo, Ashari M., Amri B., The comparative study of buck-boost, cuk, Sepic and zeta converters for maximum power point tracking photovoltaic using P&O method, 2<sup>nd</sup> International Conference on Information Technology, Computer and Electrical Engineering, Tampa, Indonesia, 2015, pp. 327-332.
- [14] Boukhelifa A., Kaouane M., Cheriti A., Implementation of incremental conductance MPPT algorithm in a photovoltaic conversion system based on DC-DC Zeta converter, 8<sup>th</sup> International Conference on Modelling, Identification and Control, Algiers, Algeria, 2016, pp. 612-617.
- [15] Rashmi, Manohar J., Rajesh K.S., A comparative study and performance analysis of synchronous SEPIC converter and synchronous zeta converter by using PV system with MPPT technique, 1<sup>st</sup> IEEE International Conference on Power Electronics, Intelligent Control and Energy Systems, Delhi, 2016, pp. 1-6.
- [16] Vineeth Kumar P. K., Manjunath K., Analysis, design and implementation for control of non-inverted zeta converter using incremental conductance MPPT algorithm for SPV applications, International Conference on Inventive Systems and Control, Hiroshima, 2017, pp. 1-5.
- [17] Jayashree U., Nightingale R. H., Divya S., Implementation of basic MPPT techniques for zeta converter, 3<sup>rd</sup> International Conference on Science Technology Engineering & Management, 2017, pp. 601-604.
- [18] Yunitasari D.R., Sunamo E., Ferdiansyah I., Putra P.A.M., Raharja L.P.S., Implementation of ANN for optimization MPPT using zeta converter, 3<sup>rd</sup> International Conference on Information and Communications Technology, Yogyakarta Indonesia, 2020, pp. 153-158.
- [19] Fitriyah, Efendi M.Z., Murdianto F.D., Modeling and simulation of MPPT zeta converter using human psychology optimization algorithm under partial shading condition, International Electronics Symposium (IES), Surabaya, Indonesia, 2020, pp. 14-20.
- [20] Çelikel R., Gündoğdu A., Comparison of PO and INC MPPT methods using FPGA In-the-Loop under different radiation conditions, *Balkan Journal of Electrical & Computer Engineering*, vol. 9, no. 2, pp. 114-122, 2021.
- [21] Başoğlu M.E., Analyzes of flyback DC-DC converter for submodule level maximum power point tracking in off-grid photovoltaic systems, *Balkan Journal of Electrical & Computer Engineering*, vol. 7, no. 3, pp. 269-275, 2019.
- [22] Başoğlu M. E., Forward converter based distributed global maximum power point tracking in partial shading conditions, *SN Applied Sciences*, vol. 2, pp. 248-253, 2020.
- [23] Designing DC/DC converters based on zeta topology, <https://www.ti.com/lit/an/slyt372/slyt372.pdf?ts=1616318393550>, (accessed: 21.03.2021).
- [24] Bosch Solar Services, <http://bosch-solarenergy.de/en/customer-service/product/kundendienst-2.html> (accessed: 25.03.2021)

Kocaeli. From 2020, he is associate professor in Electrical and Electronics Department of Gümüşhane University. His research interests include: photovoltaic systems, renewable energy, maximum power point tracking algorithms, power electronics, switch mode power supplies and control of electrical machines.

## BIOGRAPHY



**MUSTAFA ENGİN BAŞOĞLU** was born in 1988. He received the M.Sc. degree of Electrical Engineering at Kocaeli University, Turkey in 2013. He receives Ph.D. in 2017 with thesis “Development and implementation of a new maximum power point tracking method for photovoltaic systems”. From 2012, he is research assistant in

the department of Electrical Engineering in University

# Real-Time Hand Motion Recognition: A Robust Low-Cost Approach

Anil Bas and Hasan Erdinç Koçer

**Abstract**— This study presents a robust, low-cost hand motion recognition approach designed to run on low-end computer systems. Our method detects and tracks hand region using real-time images obtained from a low-resolution camera (i.e. webcam) and is not depended on any training or calibration and is not required any special camera apparatus or selectors. The proposed system involves several image processing techniques such as background subtraction, face detection, skin colour detection and template matching. The experimental results show promising performance under various conditions. The method has a wide range of applications where more natural ways of interaction required, such as virtual reality applications, assistive technologies and simulation.


**Index Terms**— Background subtraction, Face detection, Hand movement recognition, Motion tracking, Template matching

## I. INTRODUCTION


AS A RESULT of the rapid development of information technology, computers have become an indispensable part of human lives. Although we see both hardware and software advancements on many levels, it has not changed or affected how we use conventional input devices such as mouse and keyboard. Unfortunately, the control ability of the user is very limited with these devices in virtual reality applications like simulation games, robotic surgery and military training which often require more natural ways of interaction.

In recent years, using the human body as an “input device” has become more popular from education [1] to entertainment [2] to health care [3-4]. Moreover, rather than relying on physical control devices, end-users prefer to communicate with computers using interactive input interfaces (e.g. touch screen and voice command) [5]. Within this context, movement recognition is emerging as an important research area in human-computer interaction and virtual reality.

ANIL BAS is with Department of Computer Engineering, Marmara University, Istanbul, Turkey, (e-mail: anil.bas@marmara.edu.tr).

 <https://orcid.org/0000-0002-3833-6023>

HASAN ERDİNÇ KOÇER, is with Department of Electrical and Electronics Engineering, Selcuk University, Konya, Turkey, (e-mail: ekocer@selcuk.edu.tr).

 <https://orcid.org/0000-0002-0799-2140>

Manuscript received December 25, 2020; accepted May 4, 2021.

DOI: [10.17694/bajece.845276](https://doi.org/10.17694/bajece.845276)

The aim of this study is to develop a robust, accurate and computationally efficient hand motion recognition system without using any special camera apparatus and particular selectors such as bracelets, gloves or finger tapes. Furthermore, the study can be used as a base library and renew outdated applications by adding interactivity at no cost.

In this paper, we present a holistic approach to hand movement detection. First, the moving regions are determined on the real-time video frames by using background subtraction. Second, the area of interest is filtered from the unrelated movement parts such as face, hair and shoulders. Third, the hand template is searched in the filtered area. Fourth, the skin colour matching is performed on the best-resulted section from the previous phase. Finally, hand movements are categorised into standby, vertical, horizontal and cross directions using timed hand position data.

The paper is organised as follows: Section 2 provides an overview of the related work on hand detection and motion recognition. Section 3 presents the proposed algorithm by describing used image processing methods. Experimental results of our approach are shown in Section 4. Section 5 discusses the future work for improving the study.

## II. RELATED WORK

Throughout the years, a considerable amount of diverse techniques has been proposed in hand detection and motion recognition fields. In this section, we reviewed this body of literature as broadly as possible by focusing mainly (but not limited to) cost and performance aspects.

In Aran's video-based sign language recognition study [6], hand gestures and shapes were captured with the help of coloured gloves. Yin [7] performed hand gesture recognition with a camera directed to partly coloured gloves and obtained impressive results with regards to the control of map operations. With the help of infrared markers, Yang [8] operated a forklift truck effectively. Ikizler [9] focused on motion understanding from whole-body images. Results were separated into four categories: walking, running, throwing and catching movement. Al-Rajab [10] successfully applied the motion recognition process to a media player controller.

In order to obtain high success rates, additional video equipment (sensor and lighting apparatus) or distinctive pointers (gloves and finger tapes) are commonly used in the literature. Studies based on this approach have achieved very high accuracy rates, around 97% [11-14].

Another approach for motion recognition is to use only one hand with a constant background. Wang and Qin [15] presented

a hand tracking and gesture recognition framework that allows users to control their fingers as a virtual mouse with six-degree-freedom.

Dardas and Georganas [16] and Dardas and Petriu [17] focused on solving the real-time hand gesture recognition problem by classifying hand poses with pattern learning models such as Support Vector Machine (SVM) and Principal Component Analysis (PCA).

Hsieh et al. [18] explored the recognition of four-way hand movement and achieved 93.13% classification rate on 750 images. Trigueiros et al. [19] compared four different training algorithms to measure the detection accuracy of static hand gestures. Testing K-NN, Naive Bayes, ANN and SVM algorithms on two datasets, they obtained success rates of 95.45%, 25.87%, 96.99%, 91.66% and 88.52%, 66.50%, 85.18%, 80.02% respectively.

As part of their study, Sangineto and Cupelli [20] presented a model-based approach that applies curve and graph matching techniques to finger models. They achieved 90% hand detection rate on 1645 images. Similar to our approach, Toni and Darko [21] reached a 78% success rate using skin colour classification and background subtraction.

Recent studies in a similar vein include Jacobs et al. [22] and Molchanov et al. [23]. Both incorporate an additional focus on deep learning which is used as a classifier for dynamic hand gesture recognition.

#### A. Contributions

Hand segmentation and hand motion recognition have been studied for many years in both computer vision and human computer interaction societies. Numerous works have been presented in the past two decades. These also include existing commercial solutions like Microsoft Kinect [24] and Leap Motion [25].

Our primary aim in this paper is not to compete directly with these methods. Moreover, the quantitative comparison with state-of-the-art methods would not be reasonable given that our approach rigidly focuses on low-cost and real-time functioning. For this reason, we only provide an evaluation that examines the performance of our work.

The main contribution of study is as follows: (1) Our approach is designed to run on low-end computer systems under the assumption of no learning or training process and using limited sources. (2) The algorithm identifies the hand region on real-time images obtained from a low-resolution camera (i.e. webcam), without using any special camera apparatus and selectors. (3) Proposed work could be used as a base library and renew outdated applications at no cost. (4) To our knowledge, such software is not publicly available (free) for educational or academic purposes. We would like to fill this gap by releasing the source code of our algorithm.

### III. METHODS

Our approach to motion detection is primarily based on examining the correlation between current and previous frames. The major problem for similar systems is that the process should be accurate and efficient enough to perform task operations accordingly. Therefore, delays and failures are two critical concerns for the correct functioning, especially during

complex procedures such as template matching or frame segmentation. We begin by highlighting the novelty of the research and giving a brief description of the methods used in the study.

#### A. Background Subtraction

The background subtraction is a cleaning process by separating the moving parts from the constant ones in an image. We apply this process right after the conversion from RGB to grayscale. The grayscale representation simplifies the algorithm and reduces computational requirements as grayscale transformations are often used for extracting descriptors instead of operating directly on colour images. The weighted sum of the R (red), G (green) and B (blue) components is used in the conversion of values in RGB colour space to grayscale form [26]. We follow the equation:

$$P_{grey} = 0.2989 \times P_{red} + 0.5870 \times P_{green} + 0.1140 \times P_{blue} \quad (1)$$

where  $P_{grey}$  is a grey level value of pixel,  $P_{red}$ ,  $P_{green}$  and  $P_{blue}$  represent RGB pixel values, respectively.

After the grayscale transformation, we start the background subtraction process. The motion detection is carried out by a practical comparison of two vectors which each contains pixel values of two sequential images. Because the comparison process is conducted at the pixel level, each pixel value is subtracted from the one that is at the same coordinate in the previous frame. The variance is calculated by:

$$J_t(x) = \begin{cases} 1, & \text{if } I_t(x) - I_{t-1}(x) > T \\ 0, & \text{otherwise.} \end{cases} \quad (2)$$

where  $J_t(x)$  is the pixel value of  $x$  position at time  $t$  and  $I_{t-1}(x)$  is the previous pixel value of  $x$  position (at time  $t - 1$ ) and  $T$  is the threshold value [27].

#### B. Face Detection

Avoiding unnecessary regions is a feasible and common technique in image processing to reduce the processing time and simplify refinement operations. Therefore, we excluded the face area from the control area. We used the face detection algorithm of Viola and Jones, which is based on Haar Cascade classifiers [28]. Figure 1 shows sample Haar-like features applied on a face image. Note that any type of face detection method can be used at this stage. The use of the technique has been exemplified in these studies [29],[30].



Fig. 1. The working principle of Haar-like features. Rapid face detection can be achieved by calculating features (the difference of the sum of pixels of white and blue rectangles)

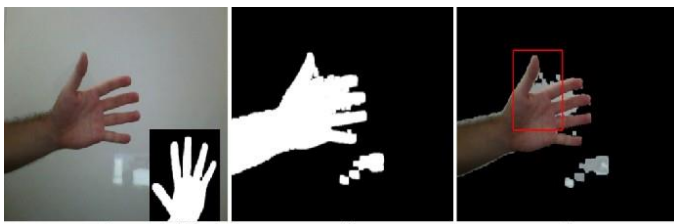


Fig. 2. The template matching progress. Main frame (a), hand pattern (b), motion area (c), template detection (d)

As a fundamental part of our detection mechanism, the majority of the motionless regions are blacked out in the background subtraction process. The remaining movement areas mainly appear around the face region. Another advantage of this is that it allows us to avoid involuntary body movements (e.g. head, face and shoulders). An example blockage case is shown in Figure 5. This increases the speed of the recognition process and provides a better initialisation.

### C. Template Matching

Template matching is a similarity measurement process between the referenced template and each potential sub window of an image. The position of the sub window with the highest similarity indicates the location of the template in an image [31]. The matching progress and the scanned pattern are shown in Figure 2.

We used the normalised correlation coefficient method as a template matching operation. The process and the coefficient calculation are shown in Figure 3 and in Equation 3:

$$p[u, v] = \frac{\sum_{u=-n}^n \sum_{v=-n}^n (f_1[X_1 + u, Y_1 + v] - \bar{f}_1) \cdot (f_2[X_2 + u, Y_2 + v] - \bar{f}_2)}{\sqrt{\sum_{u=-n}^n \sum_{v=-n}^n (f_1[X_1 + u, Y_1 + v] - \bar{f}_1)^2 \cdot \sum_{u=-n}^n \sum_{v=-n}^n (f_2[X_2 + u, Y_2 + v] - \bar{f}_2)^2}} \quad (3)$$

where  $X_1, Y_1, X_2, Y_2$  are the image coordinates of the search windows,  $u$  and  $v$  are the coordinates of relation windows and  $f_1, f_2$  are the gray values of windows (left and right images). We assume the correlation coefficient is between  $[-1, 1]$  range. If the calculated  $p = -1$  then there is no relationship between two windows. If  $p = 1$  then there is an exact match.

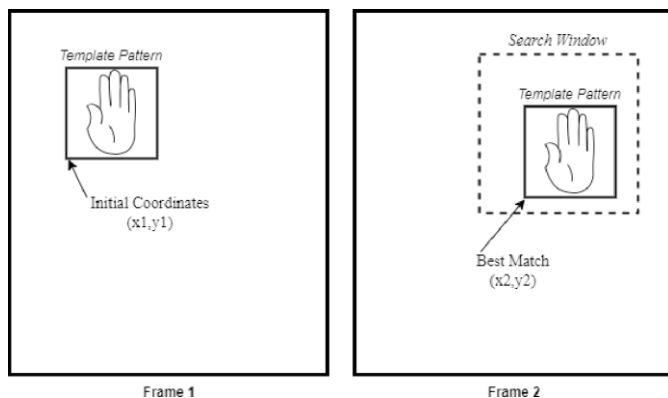


Fig. 3. Normalised cross correlation computation. The template is compared with possible candidates in the search window within the frame to detect the highest similarity

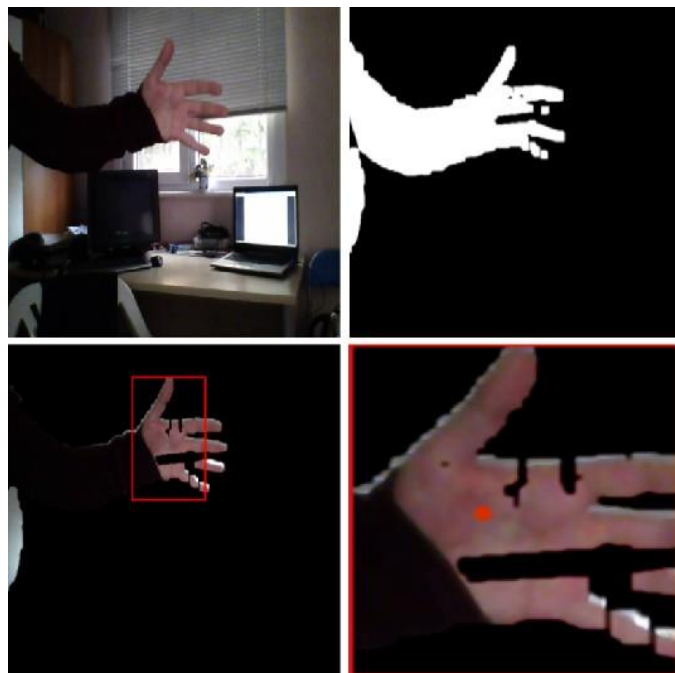


Fig. 4. Skin colour detection on a cluttered background

### D. Skin Colour Detection

The main aim of detecting the skin colour is to decide on the movement categorisation and to make sure that the interest area contains a realistic hand, instead of hand-shaped objects in the scene. In this stage, the detected area of interest (obtained from the template matching process) is merged with the raw input image to compute skin colour. Pixels with similar colours in that area create blocks. The largest block is determined by the number of connected pixels and the centre of the largest part is marked as the motion point. The algorithm makes the prediction based on the position of the marks. Figure 4 shows the marking and the handshape area on a complex scene.

This step is necessary to compute the movement direction between frames. However, it is not directly aiding hand detection and used for the motion recognition task only.

## IV. RESULTS

The proposed system was tested with several conditions on different backgrounds. The experimental study contains eight categories of hand movements (up, down, left, right, up-left, up-right, down-left and down-right) and the click action (stop at a certain time, at a certain point). Two main status (hand only or entire body) and arm conditions (bare or clothed) were examined considering the effectiveness of the performance. The experiments repeated on four various backgrounds (white, red, green and complex). Figure 5 shows a mixture of settings examined in our analysis. Ten individual trials were made for each movement, condition and background. In total, 1440 movements were collected for the measurement.

The study was conducted on a computer that has a 3rd generation Intel i7 processor, 8 GB RAM, a Nvidia GT650M graphics card and a 1.3 MP webcam. We used EmguCV library which is a C# wrapper for the well-known OpenCV video-processing library; both of which are open-source and freely licensed [32]. EmguCV is preferred because of the accessibility

and abundance of source code, its easy-to-use multi-platform structure and, most importantly, memory management (automatic garbage collection). In our experiments, our method approximately runs at 20 fps rate, which is suitable for real-time applications.

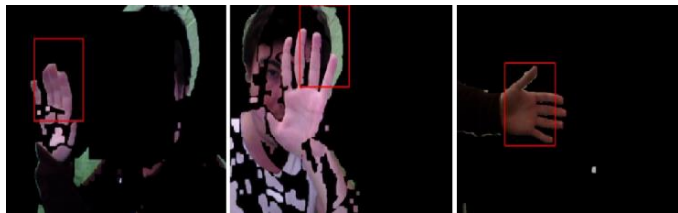


Fig. 5. Various experimental settings: entire body-clothed arm (left), entire body-bare arm (middle) and hand only-clothed arm (right)

Table 1 presents the movement recognition rates of the proposed method. Total of 360 experiments collected on 4 different static backgrounds and with 2 conditions. We identify four significant factors that emerged from this table.

First, a comparison between hand only and entire body results shows that using hand only in the field-of-view gives better results in the recognition process. Second, similarly, the complexity of the scene directly affects the successful detection rate. Third, we observed higher values on clothed arm than bare arm results. This outcome is reasonable because of the skin colour similarity between hand and arm.

The insufficient hit ratio of the click movement stands out as a fourth factor. There are two likely causes for this result: One is that the consistency between continuous frames could not be appropriately achieved since there is no learning/training

TABLE I  
MOVEMENT RECOGNITION RATES (%)

Condition #1	Condition #2	Movement	White Bg	Red Bg	Green Bg	Complex Bg	
Hand only	Bare arm	up	80	100	90	80	
		down	90	80	80	60	
		left	100	90	100	90	
		right	80	80	90	80	
		up-left	90	90	90	60	
		up-right	80	90	80	70	
		down-left	90	80	90	80	
		down-right	80	80	80	70	
		click	70	70	60	60	
	Partial Success Rate			84.84	84.84	84.84	72.22
	Clothed arm	up	100	100	90	80	
		down	90	90	90	80	
		left	100	100	100	90	
		right	90	100	90	70	
		up-left	90	90	90	80	
		up-right	90	90	100	80	
		down-left	90	90	100	70	
		down-right	100	100	90	90	
click		90	90	80	70		
Partial Success Rate			93.33	94.44	92.22	78.89	
Entire body	Bare arm	up	90	80	80	80	
		down	70	90	70	70	
		left	100	80	70	70	
		right	80	80	90	80	
		up-left	90	70	80	70	
		up-right	70	60	70	60	
		down-left	100	70	60	70	
		down-right	80	70	80	60	
		click	50	60	50	50	
	Partial Success Rate			81.11	73.33	72.22	67.78
	Clothed arm	up	90	100	100	90	
		down	90	90	100	80	
		left	90	70	90	60	
		right	100	90	80	70	
		up-left	80	90	80	60	
		up-right	100	100	90	80	
		down-left	80	90	70	70	
		down-right	90	90	90	80	
click		60	70	60	50		
Partial Success Rate			86.67	87.78	84.44	71.11	
<b>Total Success Rate</b>			<b>86.39</b>	<b>85</b>	<b>83.33</b>	<b>72.5</b>	

option in our low-cost approach. The other cause is related to involuntary (reflex) hand and finger movement that fails the template matching correlation in a very short period of time. This is because the click data collection is mainly relied on freezing the hand in the same region.

Finally, the movement values achieved a better success rate when the hand is positioned above the mid-frame. The reason behind this is that, while the subject moves its hand to a lower level, the handshape slightly loses its parallel structure to the camera. Therefore, the algorithm could not cope with this challenging hand posture which is difficult to perceive with a single device and thus counted as a wrong move.

Figure 6 provides an example comparison between the success rates of bare arm and clothed arm conditions. It is clearly observed that our algorithm is performing better on a clothed arm (textile blocking the region of interest) compared to bare arm. This can be partially explained by the false detection of the arm region in some cases.

The proposed work has achieved an average of 81.81% success rate on 1440 real-time video sequences, which is highly promising considering possible complications including illumination, cluttered scene, camera distance, camera quality absence of any indicators or apparatus. Moreover, the evaluation has shown better performance than some of the studies [19],[21] mentioned in the literature review section. We would like to note again that the approach is not depended on any training or calibration, or particular selectors such as finger tapes, bracelets or gloves.

## V. DISCUSSION AND CONCLUSION

With the increasing use of computer-simulated technology in daily life, sensors and cameras have been moving gradually towards substituting for buttons and touch screens. Smart TVs and game consoles have already started to apply such advancements and it is expected to spread to other electronic devices in the near future.

While powerful new devices equipped with high resolution cameras and sensors are being developed rapidly, low-level machines are not completely ignored. Mainstream products (e.g. remote controller, headset and wristband) are able to fill this gap during the transition stage. However, they add further complexity to the current system as well as the required

computational resources that are needed for compiling the code of the gear. Even though those hardware tools produce better results than software enhancements, it creates a financial burden for the user and is inadequate in terms of user preference and application compatibility.

The two main contributions of this paper are as follows. (1) It is possible to treat our application as a base library and build projects with high level performance. (2) Existing projects can extend to an interactive version by implementing the study. For this reason, we release the source code of the publication to the community for further research on the subject and development of new techniques.

Although the study provides solid results, some features could still be improved. First, optimising the face detection algorithm could directly affect the accuracy of the whole system. Incorrect area detection may occur given confusion caused by misleading objects such as a hat or glasses. Second, the clicking movement, which has the lowest success rate, could be refined by tracking the movement over frames without increasing the complexity. Third, multiple hand detection could not be applied due to real-time computational costs. This could be achieved by applying computationally lightweight skin detection, similar to Conaire et al. [33].

## REFERENCES

- [1] Z. Merchant, E.T. Goetz, L. Cifuentes, W. Keeney-Kennicutt, T.J. Davis, "Effectiveness of virtual reality-based instruction on students' learning outcomes in K-12 and higher education: A meta-analysis", *Computers & Education*, Vol. 70, 2014, pp. 29–40.
- [2] D. Chambers, "Wii play as a family': the rise in family-centred video gaming", *Leisure Studies*, Vol. 31, 2012, pp. 69–82.
- [3] H.H. Mousavi, M. Khademi, "A review on technical and clinical impact of microsoft kinect on physical therapy and rehabilitation", *Journal of Medical Engineering*, 2014.
- [4] N.E. Seymour, A.G. Gallagher, S.A. Roman, M.K. O'brien, V.K. Bansal, D.K. Andersen, R.M. Satava, "Virtual reality training improves operating room performance: results of a randomized, double-blinded study", *Annals of Surgery*, Vol. 236, No. 4, 2002, pp. 458–464.
- [5] P.W. Lee, H.Y. Wang, Y.C. Tung, J.W. Lin, A. Valstar, "TranSection: hand-based interaction for playing a game within a virtual reality game", *33rd ACM Conference on Human Factors in Computing Systems*, Seoul, South Korea, 18 – 23 April 2015.
- [6] O. Aran, *Vision based sign language recognition: modeling and recognizing isolated signs with manual and non-manual components*, PhD Thesis, Bogazici University, Istanbul, Turkey, 2008.

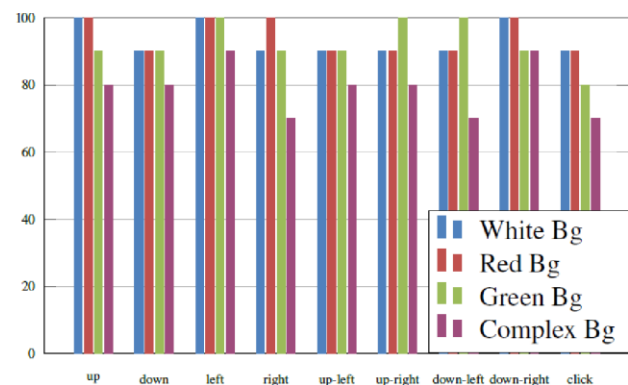
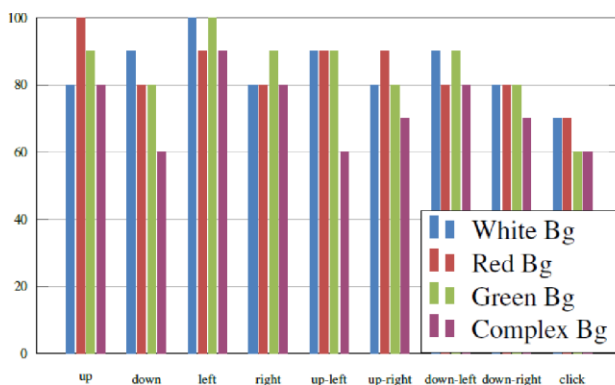


Fig. 6. Example comparison of hand only motion recognition for bare arm and clothed arm conditions

- [7] Y. Yin, Toward an intelligent multimodal interface for natural interaction. MSc Thesis, Massachusetts Institute of Technology, Cambridge, MA, United States, 2010.
- [8] X. Yang, A hand input-based approach to intuitive human-computer interactions in virtual reality. MPhil Thesis, The University of Hong Kong, Pokfulam, Hong Kong, 2010.
- [9] N. Ikizler, Understanding human motion: recognition and retrieval of human activities, PhD Thesis, Bilkent University; Ankara, Turkey, 2008.
- [10] M. Al-Rajab, Hand gesture recognition for multimedia applications, PhD Thesis, University of Leeds, Leeds, UK, 2008.
- [11] C.P. Chen, Y.T. Chen, P.H. Lee, Y.P. Tsai, S. Lei, "Real-time hand tracking on depth images", Visual Communications and Image Processing, 2011, pp. 1–4.
- [12] C. Keskin, L. Akarun, "STARS: Sign tracking and recognition system using input–output HMMs", Pattern Recognition Letters, Vol. 30, No. 12, 2009, pp. 1086–1095.
- [13] L. Lamberti, F. Camastra, "Handy: a real-time three color glove-based gesture recognizer with learning vector quantization", Expert Systems with Applications, Vol. 39, No. 12, 2012, pp. 10489–10494.
- [14] Y.H. Lee, S.K. Wu, Y.P. Liu, "Performance of remote target pointing hand movements in a 3D environment", Human Movement Science, Vol. 32, No. 3, 2013, pp. 511–526.
- [15] X. Wang, K. Qin, "A Six-degree-of-freedom Virtual Mouse based on Hand Gestures", International Conference on Electrical and Control Engineering, Wuhan, China, 25–27 June 2010.
- [16] N.H. Dardas, N.D. Georganas, "Real-time hand gesture detection and recognition using bag-of-features and support vector machine techniques", IEEE Transactions on Instrumentation and Measurement, Vol. 60, No. 11, 2011, pp. 3592–3607.
- [17] N.H. Dardas, E.M. Petriu, "Hand gesture detection and recognition using principal component analysis", IEEE International Conference on Computational Intelligence for Measurement Systems and Applications, Ottawa, Canada, 19–21 September 2011.
- [18] C.C. Hsieh, D.H. Liou, D. Lee, "A real time hand gesture recognition system using motion history image", 2nd International Conference on Signal Processing Systems, Dalian, China, 5–7 July 2010.
- [19] P. Trigueiros, F. Ribeiro, L.P. Reis, "A comparison of machine learning algorithms applied to hand gesture recognition", 7th Iberian Conference on Information Systems and Technologies, Madrid, Spain, 20–23 June 2012.
- [20] E. Sangineto, M. Cupelli, "Real-time viewpoint-invariant hand localization with cluttered backgrounds", Image and Vision Computing, Vol. 30, 2012, pp. 26–37.
- [21] B. Toni, J. Darko, "A robust hand detection and tracking algorithm with application to natural user interface", 35th International Convention MIPRO, Opatija, Croatia, 21–25 May 2012.
- [22] K. Jacobs, M. Ghasiazgar, I. Venter, R. Dodds, "Hand Gesture Recognition of Hand Shapes in Varied Orientations using Deep Learning", Annual Conference of the South African Institute of Computer Scientists and Information Technologists, Johannesburg, South Africa, 26–28 September 2016.
- [23] P. Molchanov, S. Gupta, K. Kim, J. Kautz, "Hand gesture recognition with 3D convolutional neural networks", IEEE Conference on Computer Vision and Pattern Recognition Workshops, Boston, MA, United States, 7–12 June 2015.
- [24] Microsoft Kinect, "Kinect for Windows", <https://developer.microsoft.com/windows/kinect> (24.12.2020).
- [25] Ultraleap, "Leap Motion Controller", <http://www.ultraleap.com/product/leap-motion-controller> (24.12.2020).
- [26] C. Kanan, G.W. Cottrell, "Color-to-grayscale: does the method matter in image recognition?", PLoS one, Vol. 7, 2012, pp. e29740:1–7.
- [27] K. Toyama, J. Krumm, B. Brumitt, B. Meyers, "Wallflower: Principles and practice of background maintenance", International Conference on Computer Vision, Kerkyra, Greece, 20–27 September 1999.
- [28] P. Viola, M. Jones, "Rapid object detection using a boosted cascade of simple features", IEEE Conference on Computer Vision and Pattern Recognition, Kauai, HI, United States, 8–14 December 2001.
- [29] S.A. Dabhade, M.S. Bewoor, "Real time face detection and recognition using haar-based cascade classifier and principal component analysis", International Journal of Computer Science and Management Research, 2012, pp. 59–64.
- [30] R. Padilla, C. Costa Filho, M. Costa, "Evaluation of haar cascade classifiers designed for face detection", International Journal of Computer, Electrical, Automation, Control and Information Engineering, Vol. 6, No. 4, 2012, pp. 466–469.
- [31] S. Mattoccia, F. Tombari, L. Di Stefano, "Efficient template matching for multi-channel images", Pattern Recognition Letters, Vol. 32, No. 5, 2011, pp. 694–700.
- [32] Emgu CV, "Emgu CV: OpenCV in .NET", <http://www.emgu.com> (24.12.2020).
- [33] C.O. Conaire, N.E. O'Connor, A.F. Smeaton, "Detector adaptation by maximising agreement between independent data sources", IEEE Conference on Computer Vision and Pattern Recognition, Minneapolis, MN, United States, 17–22 June 2007.

## BIOGRAPHIES



**ANIL BAS** is an assistant professor at the Department of Computer Engineering, Faculty of Technology, Marmara University, Turkey. He received his BSc degree in Electronics and Computer Education from Kocaeli University in 2011, MSc degree in Computer Engineering from Selcuk University in 2013 and PhD degree in Computer Science from the University of York, UK in 2018. His research interests include computer vision, computer graphics, image processing and human computer interaction.



**HASAN ERDİÑÇ KOÇER** is an associate professor at the Department of Electrical and Electronics Engineering, Faculty of Technology, Selcuk University, Turkey. He received his BSc degree in Electronics and Computer Education from Marmara University in 1998, MSc degree in Electronics and Computer Systems Education and PhD degree in Electrical and Electronic Engineering from Selcuk University in 2001 and 2007, respectively. His research interests are related to image processing, computer vision, biometric identification and pattern recognition.



# A Hybrid Machine Learning Model to Detect Reflected XSS Attack

Beraat Buz, Berke Gülçiçek, and Şerif Bahtiyar\*


**Abstract**—Since web technologies are getting more advanced with longer codes, the number of vulnerabilities has increased considerably. Cross-site scripting (XSS) attacks are one of the most common attacks that use vulnerabilities in web applications. There are three types of cross-site scripting attacks namely, reflected, stored, and DOM-based attacks. Reflected XSS attacks are the most common type that is usually implemented by injecting a malicious code into the URL and then sending the URL to the targeted system by using phishing methods, which is a significant threat for recent web applications. Our motivation is the lack of a high-performance detection method of reflected XSS attacks with high accuracy. In this paper, we propose a hybrid machine learning model to detect vulnerabilities related to reflected XSS attacks for a given URL of a website. Our model uses a scanner to discover vulnerabilities in a web site and convolutional neural networks to predict the most common vulnerabilities that may be used for reflected XSS attacks, which makes the proposed model hybrid. We analyzed the model experimentally. Analyses results show that the proposed model is able to detect vulnerable attack surfaces with 99 % accuracy.

**Index Terms**—Deep Learning, Detection, Reflected XSS, N-gram, Vulnerability, XSS Scanner.


## I. INTRODUCTION

RECENTLY, THE number of web applications have increased dramatically with the rapid proliferation of the Internet. More and more applications, even complex ones, are converted into web applications. A lot of new ideas are also implemented using web technologies. People with different levels of expertise are working to develop web applications


**BERAAT BUZ**, is with Department of Computer Engineering of Istanbul Technical University, Istanbul, Turkey, (e-mail: [buz16@itu.edu.tr](mailto:buz16@itu.edu.tr)).

 <https://orcid.org/0000-0002-9455-1537>

**BERKE GÜLÇİÇEK**, is with Department of Computer Engineering of Istanbul Technical University, Istanbul, Turkey, (e-mail: [gulcicek16@itu.edu.tr](mailto:gulcicek16@itu.edu.tr)).

 <https://orcid.org/0000-0002-2282-5404>

**ŞERİF BAHTİYAR**, is with Department of Computer Engineering of Istanbul Technical University, Istanbul, Turkey, (e-mail: [bahtiyars@itu.edu.tr](mailto:bahtiyars@itu.edu.tr)).

 <https://orcid.org/0000-0003-0314-2621>

\*Corresponding Author

Manuscript received April 25, 2021; accepted July 27, 2021.

DOI: [10.17694/bajece.927417](https://doi.org/10.17694/bajece.927417)

that case has created many additional vulnerabilities. This circumstance takes attentions of adversaries therefore web application security has become more significant than ever. Analyses also show that 32% of the web applications have extremely poor security levels, and 23% of web applications have poor security levels [1]. Even websites that seem secure may have vulnerabilities. For instance, an XSS security flaw was discovered in the UK Parliament website (Gupta, 2014) [2].

One of the most common types of web application attacks is cross-site scripting attacks. According to OWASP, crosssite scripting attacks are the 7th most common type of web application security risk [3]. In cross-site scripting attacks, an adversary may inject malicious code into some parts of the web application. The vulnerable parts of the website are also parts that involve user input. The malicious code is usually a JavaScript script that steals information of other users. The vulnerable parts of web applications allow attackers to exploit the website by using session hijacking, misinformation, defacing web site, inserting hostile content, phishing attacks, taking over user's browser, pop-up-flooding, steal personal information and access to business data [4].

Cross-site scripting attacks can be categorized into three types. Reflected cross-site scripting attacks, stored cross-site scripting attacks, and DOM-based cross-site scripting attacks as shown in Figure 1. In this paper, our focus is on reflected cross-site scripting attacks, which are also called nonpersistent XSS attacks. These attacks are the most common XSS attack type. It can be implemented by injecting malicious code into the URL of the website, or in a form element of the website where user input is taken. Either way, when the victim opens the website, a malicious script is run.

The initial step of a reflected cross-site scripting attack is to find vulnerabilities in the targeted system. The vulnerabilities usually reside in the parts where user input is taken. It can be the URL of the website, or an HTML form. The attacker injects the malicious code in these areas. For example, in the case of the URL, the attacker sends URL containing malicious code using phishing methods. When the victim opens the URL, the victim's browser will start executing the malicious code.

Stored cross-site scripting attacks, which are also called persistent XSS attacks, are implemented by adding a malicious code snippet into the database of a website. When a user enters that page, the malicious code is executed in the user's browser. On the other hand, DOM-based XSS attacks use

vulnerabilities found in web browsers.

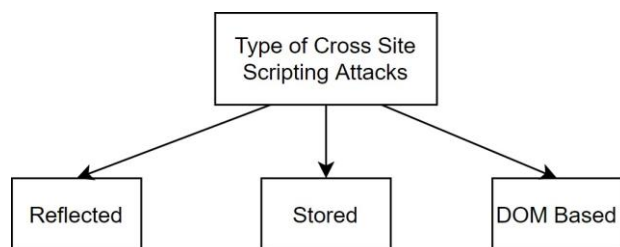


Fig. 1. Types of XSS Attacks

In this paper, we propose a hybrid model, two-step solution, implemented as a tool. In the first step, vulnerable parts of a web application or a web site is analyzed to discover potential vulnerabilities that allow reflected-XSS attacks. Specifically, the tool crawls the website for potentially vulnerable areas. In the next step, potential reflected-XSS attacks are detected. Particularly, the payloads that managed to successfully attack are run through the deep learning model that is trained with payloads beforehand. The deep learning method tries to guess the dangerous payloads. In the payload file, there are thousands of payloads.

To the best of our knowledge, the proposed model is a unique two-step hybrid solution that detect potential reflected XSS attacks with 99% of accuracy. The proposed model is adaptive to newly found web vulnerabilities that provides better accuracy than existing solutions. Experimental analyses verify that our model provides high accuracy with adaptive nature.

The rest of the paper is organized as follows. Section II is about XSS attacks and machine learning algorithms. In the next section the proposed hybrid model to detect reflected-XSS attacks is presented. We analyze the proposed model in Section IV. The last section is devoted to conclusion.

## II. CROSS-SITE SCRIPTING ATTACKS AND MACHINE LEARNING

There are many researches about XSS attacks and their prevention methods. For instance, Sarmah, Bhattacharyya, and Kalita explain the type of XSS attacks, which have occurred for two decades [5]. In the research, both client side and server-side XSS attacks detection approaches are analyzed, including static analysis, dynamic analysis, and hybrid analysis mechanisms. On the other hand, Liu et al. explains what makes XSS attacks dangerous by explaining of XSS attacks [6] with static and dynamic analysis methods to detect the vulnerabilities in the system.

Cookies and cookie theft, as well as analysis of tools are significant about XSS attacks detection researches [7]. Types of XSS attacks and in which conditions they arise, how are cookies used, what type of cookies are used, how they can be stolen, which detection tools are common, and how the detection tools work are explained in [7]. However, there is always a detection accuracy of XSS attacks with these tools.

Galan et al. discuss a scanner used to detect vulnerabilities about stored XSS in a website [8]. In the architecture, the Webpage parser agent is the first to be launched. Script injector agent is the next agent, and it takes the attack point repository created by the previous agent as input. Finally, a verification agent, which may not be run until the injector agent, has created a list to launch attacks. Li and Wei create a model for a more efficient automatic XSS detection tool by using SVM algorithm, which is used to determine whether parameters submitted by users are malicious or not in case of XSS attacks [9]. Also, they use DQN algorithm for reinforcement learning for bypassing the rule-based WAF system.

From another point of view, Syaifuddin et al. explain how to prevent XSS attacks with a honeypot [10]. In this approach, when the program detects anomalies on the URL request packet, the honeypot records its log and the URL request. Then, according to the log file, they implement a snort rule.

A dynamic detection technique for XSS attacks is explained with dynamic detection algorithm that contains five steps, namely crawler, feature construct, attacks simulation, results in detection, and report generation [11]. Authors summarize common detection methods that include dynamic analysis based on black-box testing, static analysis based on white box testing, and fuzzing test. They compare three typical XSS attack detection tools which are XSS-ME, Wapiti and Punk.

Habibi and Surantha briefly explain XSS attack detection methods, which are created by using Support Vector Machine (SVM), K-Nearest Neighbour (KNN), and Naive Bayes (NB) techniques with N-gram method which is a method for detecting similarities between two sentences [12]. Dong et al. explore possible XSS vulnerabilities in HTML5 [13]. They introduce a XSS attack detection tool that produces a large number of test emails by configuring each checkpoint of a test email with an attack vector derived from their repository and then connects to the SMTP server in the detection process. The tool automatically sends test emails to target mailboxes after they have been checked and approved by SMTP. When these test emails are successfully opened in target mailboxes, they may quickly evaluate if the attack vectors on each checkpoint have been filtered.

Li et al. represent their XSS attack detection approach based on the attention mechanism of Long Short-Term Memory (LSTM) recurrent neural network [14]. The proposed XSS attack detection model is based on LSTM. In addition, recall and precision are weighted harmonic means, and the F1 metric is a weighted harmonic mean of these two metrics [15].

These researches provide some solutions to detect XSS attacks. However, they barely satisfy increasing number of vulnerabilities about XSS attacks with high accuracy that depends on precision and recall. In the light of all this information, we propose a hybrid detection model that is more accurate according to two parameters, namely precision and recall. Vulnerabilities about reflected XSS have been a huge threat for societies that use web applications and web sites.

### III. A HYBRID MODEL TO DETECT REFLECTED-XSS ATTACKS

We have proposed a hybrid model that has two important features. The first one is a scanner of potential vulnerabilities that allow reflected XSS attacks and the other one is a detection mechanism for XSS attacks. We also implemented the model as a tool called XSS-Guard.

XSS-Guard takes an URL of a website in the first step about reflected XSS. This URL may be on a web server or on a local server. There are two options to scan the website, with a crawler or without a crawler. In the crawler mode, the tool searches all usable links that are not used before. Then, these links are scanned to find vulnerabilities related to reflected XSS attacks.

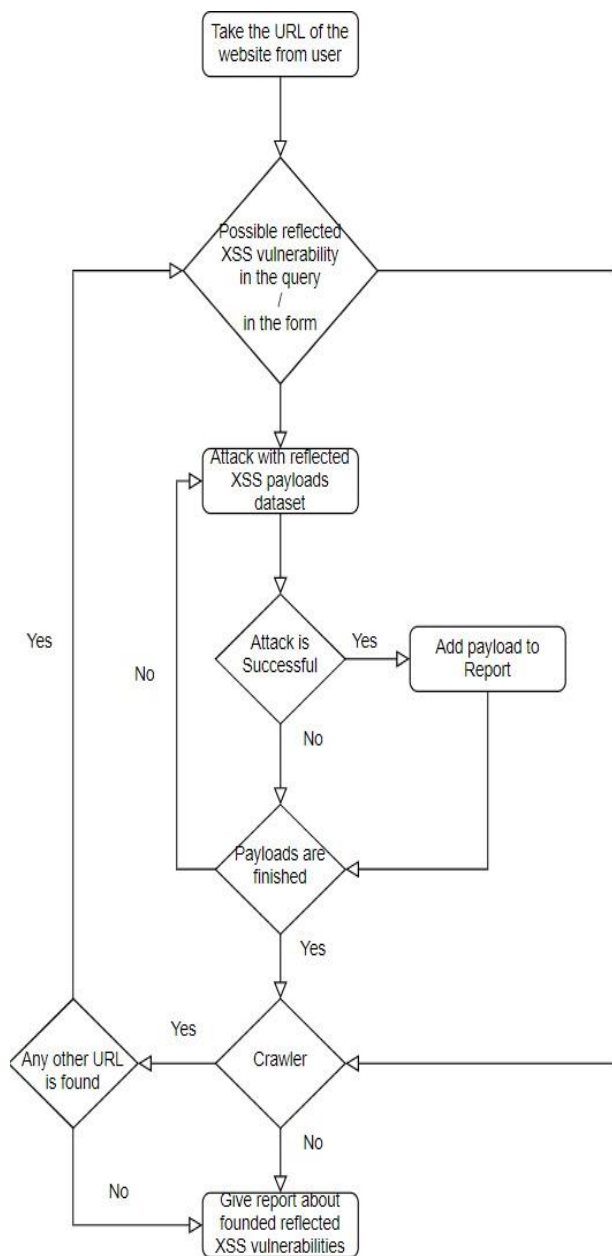


Fig. 2. The algorithm of the scanner

When the website is ready, and there are suitable places for reflected XSS attacks, the tool starts to attack with static reflected XSS payloads. Our payload dataset contains 8000 lines of script codes. These scripts are found from various sources. If a script run on targeted system, this means that there is at least one vulnerability that allows reflected XSS attacks. Vulnerabilities about this script are added to the vulnerability list of the scanner. Figure 2 shows the algorithm of this process.

In the detection mechanism, we have used a convolutional neural network (CNN) that is usually used for image classification, medical image analysis, and natural language processing. CNN provides an effective approach to prevent reflected XSS attacks. We have used a built-in Keras to determine if the script is reflected XSS attack data or benign data.

The proposed model starts by reading the dataset from a csv file where payloads and labels are stored. Then, each payload is converted to an ASCII value array and the array is resized. Next, we convert the data in the form that it is suitable to be processed by CNN. Moreover, we split the dataset as train payloads, train labels, test payloads, and test labels.

We use sequential approach in our model. At the beginning, we have three convolution layers (2D) and three max pooling layers. To flatten data in matrix form, we use a flatten layer. Next, the model is finished with four dense layers. We compile the proposed model with Adam optimizer. We tested many optimizers and we found out that Adam optimizer provides better results in our approach.

In our model, the batch size is 128 and the number of epochs is 10. After we fit the model, we move on to the test-set phase. We accept values greater than 0.5 as attack data, and values less than 0.5 as benign data. Finally, we calculate the accuracy, the precision and the recall values.

Our dataset contains approximately 13000 data with different payloads that are used in the scanner. This dataset has two columns. The first column is script data and the second column is label data in which "0" means XSS attack data, and "1" means benign script data.

- `<inputtype = imagesrc = 1onerror = alert(1) >`
- `<htmlontouchstart = alert(1) >`
- `<xonmouseover = alert(1) >`
- `%3Cxonxxx = alert(1)`

In the list above, you can see a few example payloads from the dataset. Each XSS attack payload is a JavaScript that tries to pop an alert. In this way, we check the success of the attack if the payload successfully popped an alert in the website. This makes easy to automate the testing process.

The script may be inside of different HTML tags, such as img, html, body, form, and etc. It may also be in different HTML events, such as onmouseover, ondrag, and etc. Attackers can use such tricks to get the browser to execute the code, therefore we take into account these tricks. The script may also be encoded to escape simple sanitation techniques.

After the training with CNN, N-gram model is used to detect XSS attacks as shown in Figure 3. N-gram algorithm is

used to find the repetition rate in a consecutive sequence. The variable expressed with  $n$  represents the value by which the repetition is controlled. The gram corresponds to the weight of this repeated value in the array. N-gram model requires a payload dataset therefore we have used all XSS attacks scripts and get the high-frequency words. Specifically, we use 9-grams and 10-grams which means that words have only 9 or 10 characters. Since these words may contain benign words like the "javascript" word, we have passed these high-frequency words through the model. Finally, restricted words are obtained.

After completing the scanning step, the model moves to the detection step. Initially, the created scripts are tested with CNN model. Then, the restricted words are used to determine benign actions or XSS attacks. Finally, XSS-Guard creates a report about the results.

#### IV. ANALYSIS OF PROPOSED MODEL

We create a reflected XSS attack detection tool, called XSS-Guard, on Ubuntu 20.04 LTS Operating system by using python3. The foremost requirements are Keras, Selenium, PyQt5, and OpenCV.

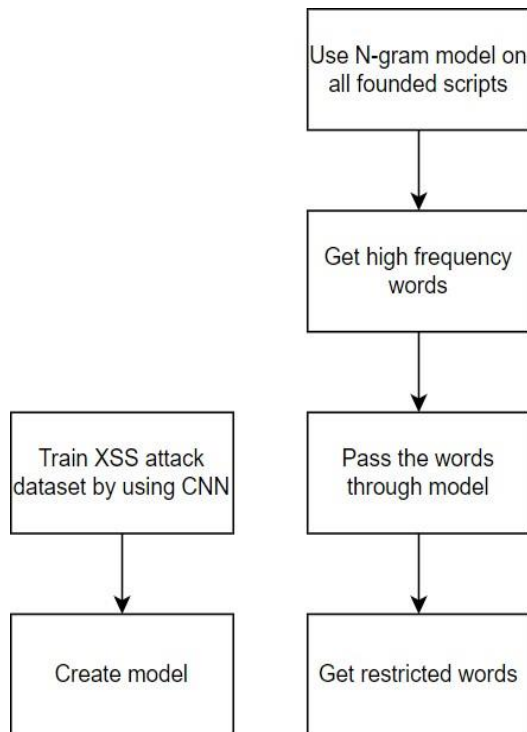


Fig. 3. The algorithm of the detection mechanism

We tested the proposed model with the tool on Web for Pentester from pentesterlab.com. We used a docker version from Github. This website is basically a website designed to be vulnerable against attacks with the purpose to test and practice applications. We used XSS-Guard with one of examples on the website. Our tool is used to attack the URL with around 500 payloads and managed to find 26 of these

payloads successfully, which means the website is vulnerable to reflected-XSS attacks as shown in Figure 4.

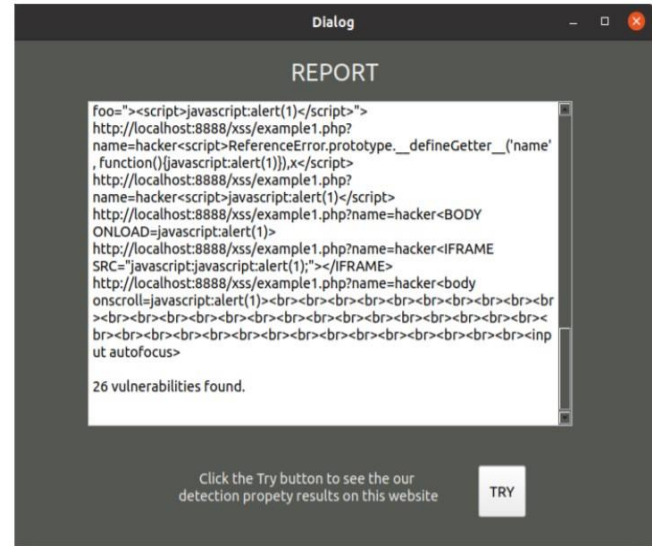


Fig. 4. Some results of XSS-Guard

We have used the following four metrics to specify the detection step of the proposed model with CNN.

- True Positive (TP): The number of attack instances identified as attacks.
- True Negative (TN): The number of instances of non-attacks known as non-attacks.
- False Negative (FN): The number of cases of attack defined as non-attacks.
- False Positive (FP): The number of cases of non-attacks classified as attacks.

We created a confusion matrix with TP, TN, FP, FN. We analyze the detection performance metrics that use the confusion matrix with the classification model. Performance metrics calculated using the confusion matrix are:

Accuracy: The estimated correct classifications are divided by the total number of classifications as follows.

$$Accuracy = \frac{TP + TN}{TP + TN + FN + FP} \quad (1)$$

Precision: Determine how accurate is when a positive estimate is obtained from the classification. This is divided by the number of correctly predicted positive instances by the total number of positive predictions, as true or false as follows.

$$Precision = \frac{TP}{TP + FP} \quad (2)$$

Recall: It is also known as Sensitivity or True Positive Rate (TPR). Recall is the number of positive predictions divided by the number of positive classified values in the test data calculated as follows.

$$Recall = \frac{TP}{TP + FN} \tag{3}$$

These three metrics are used to observe the success of the neural network that is used for the detection mechanism and how the n-gram model boosts it.

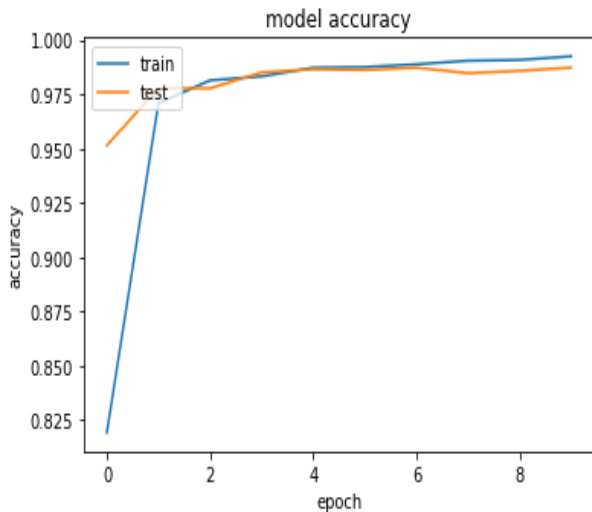


Fig. 5. The accuracy model

We used Adam optimizer to compile the model. Although RMSprop optimizer and Stochastic Gradient Descent optimizer also achieve high accuracy, Adam optimizer provides best performance in our cases. In the experiments, we have 10 epoch sizes and 128 batch sizes to fit the model. In the following figures, visualizations of model accuracy and model loss are shown. These models are created by using CNN without N-gram model.

The accuracy of the proposed model with experimental evaluation is shown in Figure 5. Experimental results show that after the first epoch, the value of accuracy on the training dataset increase considerably. Additionally, the accuracy for both datasets rise till the end of epochs.

We show the experimental results of the loss model in Figure 6. It can be observed that the behavior of loss is the same as the behavior of accuracy. Differently from the accuracy, the loss decreases with the similar behavior. The performance of the loss model for both train and validation datasets are parallel. The performance results for the three metrics are given on Table I related to the validation dataset. These results show that XSS-Guad detects XSS attacks with high performance.

TABLE I  
PERFORMANCE RESULTS WITHOUT N-GRAM

Performance Measures	Values
Accuracy	0.9890430971512053
Precision	0.9852546916890008
Recall	0.9945872801082544

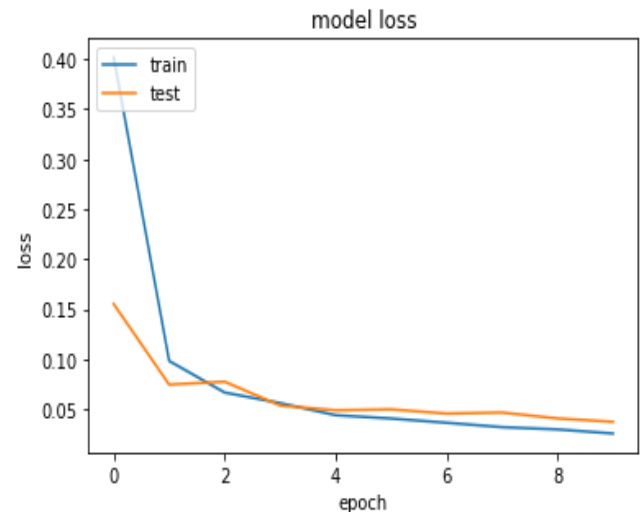


Fig. 6. The loss model

In addition to CNN, we used N-gram model to restrict some words since scripts may be hidden inside many non-sense characters. The performance results with N-gram model is shown in Table II. The performance results show that using Ngram helps to increase the performance of accuracy. Actually, if these payloads are found as benign in our model, we can control these restricted words to label them as XSS attacks. Some of these restricted words we found by using N-gram and passing through the model are as follows:

- ypress = ""
- nstart = ""
- solute;""
- useout = ""
- ofocus ><

TABLE II  
PERFORMANCE RESULTS WITH N-GRAM

Performance Measures	Values
Accuracy	0.9901387874360847
Precision	0.9872397582269979
Recall	0.9945872801082544

In order to validate the performance of the hybrid model, we have used K Fold Cross Validation. We chose K to be 5. Table III contains the accuracy results of 5 fold cross validation in our dataset with or without N-gram algorithm. These results also show that N-gram provides better accuracy results for the proposed model.

TABLE III  
CROSS VALIDATION RESULTS

# Group	Without N-gram	With N-gram
1	Accuracy : 0.982191780821	Accuracy : 0.988645838609
2	Accuracy : 0.987671232876	Accuracy : 0.990244198456
3	Accuracy : 0.986301369863	Accuracy : 0.989195991534
4	Accuracy : 0.989497716894	Accuracy : 0.991157563924
5	Accuracy : 0.977168949771	Accuracy : 0.980293547470

After creating the model and the restricted words, we tested the detection mechanism to prevent XSS attacks on the founded XSS attack scripts by using XSS-Guard, the tool we developed. We detected 25 XSS attacks scripts as XSS attacks and one XSS attack script as benign. The results are shown in Figure 7.

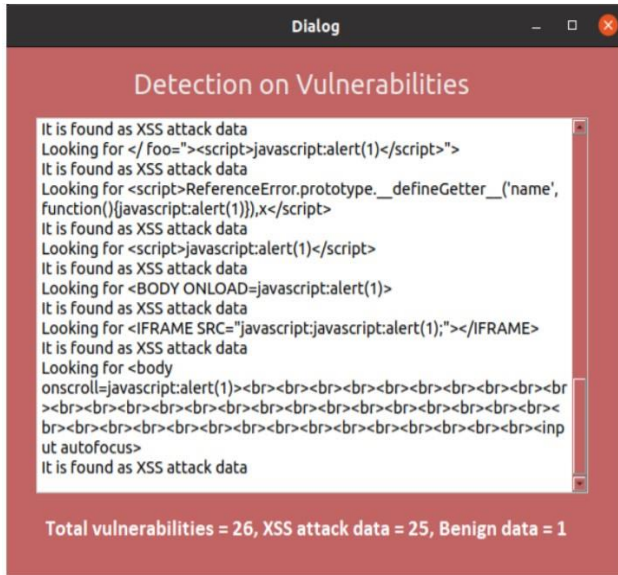


Fig. 7. An example results for reflected XSS attack detection

Overall analyses results show that classifications by using N-gram provides better accuracy for detecting reflected XSS attacks. Additionally, the proposed hybrid model, which implemented on XSS-Guard helps to determine vulnerable websites against reflected-XSS attacks with high accuracy. Thus, the proposed hybrid model is expected to counter reflected XSS attacks more accurately.

## V. CONCLUSION

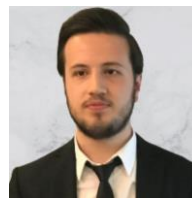
In this paper, we consider one of the most common and significant web vulnerabilities that are used for cross-site scripting attacks. Specifically, we take into account reflected-XSS attacks and related vulnerabilities. We proposed a hybrid model that provides more than 99% accuracy by using web scanning and deep learning methods. The model extracts vulnerabilities in a website and detects potential reflected XSS attacks with deep learning methods. We created a tool, called XSS-Guard, to test our model. The proposed model will help to detect reflected XSS attacks in a more accurate way.

## REFERENCES

- [1] "Web Applications vulnerabilities and threats: statistics for 2019." [Online]. Available: <https://www.ptsecurity.com/ww-en/analytcs/web-vulnerabilities-2020/>
- [2] S. Gupta and B. B. Gupta, "Cross-Site Scripting (XSS) attacks and defense mechanisms: classification and state-of-the-art," *International Journal of System Assurance Engineering and Management*, vol. 8, no. S1, pp. 512–530, Jan. 2017. [Online]. Available: <http://link.springer.com/10.1007/s13198-015-0376-0>

- [3] "OWASP Top Ten Web Application Security Risks | OWASP." [Online]. Available: <https://owasp.org/www-project-top-ten/>
- [4] V. Nithya, S. L. Pandian, and C. Malarvizhi, "A Survey on Detection and Prevention of Cross-Site Scripting Attack," *International Journal of Security and Its Applications*, vol. 9, no. 3, pp. 139–152, Mar. 2015.
- [5] U. Sarmah, D. Bhattacharyya, and J. Kalita, "A survey of detection methods for XSS attacks," *Journal of Network and Computer Applications*, vol. 118, pp. 113–143, Sep. 2018. [Online]. Available: <https://linkinghub.elsevier.com/retrieve/pii/S1084804518302042>
- [6] M. Liu, B. Zhang, W. Chen, and X. Zhang, "A Survey of Exploitation and Detection Methods of XSS Vulnerabilities," *IEEE Access*, vol. 7, pp. 182004–182016, 2019. [Online]. Available: <https://ieeexplore.ieee.org/document/8935148/>
- [7] G. E. Rodríguez, J. G. Torres, P. Flores, and D. E. Benavides, "Crosssite scripting (XSS) attacks and mitigation: A survey," *Computer Networks*, vol. 166, p. 106960, Jan. 2020. [Online]. Available: <https://linkinghub.elsevier.com/retrieve/pii/S1389128619311247>
- [8] E. Galan, A. Alcaide, A. Orfila, and J. Blasco, "A multi-agent scanner' to detect stored-xss vulnerabilities," in *2010 International Conference for Internet Technology and Secured Transactions*, 2010, pp. 1–6.
- [9] L. Li and L. Wei, "Automatic XSS Detection and Automatic Anti-Anti-Virus Payload Generation," in *2019 International Conference on Cyber-Enabled Distributed Computing and Knowledge Discovery (CyberC)*. Guilin, China: IEEE, Oct. 2019, pp. 71–76. [Online]. Available: <https://ieeexplore.ieee.org/document/8945988/>
- [10] S. Syaifuddin, D. Risqiwati, and H. A. Sidharta, "Automation Snort Rule for XSS Detection with HoneyPot," in *2018 5th International Conference on Electrical Engineering, Computer Science and Informatics (EECSI)*. Malang, Indonesia: IEEE, Oct. 2018, pp. 584–588. [Online]. Available: <https://ieeexplore.ieee.org/document/8752961/>
- [11] X.-Y. Hou, X.-L. Zhao, M.-J. Wu, R. Ma, and Y.-P. Chen, "A Dynamic Detection Technique for XSS Vulnerabilities," in *2018 4th Annual International Conference on Network and Information Systems for Computers (ICNISC)*. Wuhan, China: IEEE, Apr. 2018, pp. 34–43. [Online]. Available: <https://ieeexplore.ieee.org/document/8842866/>
- [12] G. Habibi and N. Surantha, "XSS Attack Detection with Machine Learning and n-Gram Methods," in *2020 International Conference on Information Management and Technology (ICIMTech)*. Bandung, Indonesia: IEEE, Aug. 2020, pp. 516–520. [Online]. Available: <https://ieeexplore.ieee.org/document/9210946/>
- [13] G. Dong, Y. Zhang, X. Wang, P. Wang, and L. Liu, "Detecting cross site scripting vulnerabilities introduced by HTML5," in *2014 11th International Joint Conference on Computer Science and Software Engineering (JCSE)*. Chon Buri: IEEE, May 2014, pp. 319–323. [Online]. Available: <https://ieeexplore.ieee.org/document/6841888/>
- [14] L. Lei, M. Chen, C. He, and D. Li, "XSS Detection Technology Based on LSTM-Attention," in *2020 5th International Conference on Control, Robotics and Cybernetics (CRC)*. Wuhan, China: IEEE, Oct. 2020, pp. 175–180. [Online]. Available: <https://ieeexplore.ieee.org/document/9253484/>
- [15] D. M. W. Powers, "What the F-measure doesn't measure: Features, Flaws, Fallacies and Fixes," *arXiv:1503.06410 [cs, stat]*, Sep. 2019, arXiv: 1503.06410. [Online]. Available: <http://arxiv.org/abs/1503.06410>

## BIOGRAPHIES



**BERAAT BUZ** was born in Istanbul, Turkey in 1998. He is a student at Istanbul Technical University, Department of Computer Engineering. He is working on artificial intelligence and computer security.



**BERKE GÜLÇİÇEK** was born in Samsun, Turkey in 1998. He is a student at Istanbul Technical University, Department of Computer Engineering. His research

interests include computer security and machine learning.



**ŞERİF BAHTİYAR** is an associate professor in the Department of Computer Engineering at Istanbul Technical University and he is the vice dean in the Faculty of Computer and Informatics at Istanbul Technical University. He received his BS in Control and Computer Engineering and MS in Computer

Engineering degrees both from Istanbul Technical University respectively, and his PhD degree in Computer Engineering from Boğaziçi University. Dr. Bahtiyar was with MasterCard, TUBerlin in Germany, and National Research Institute of Electronics and Cryptology.

Dr. Bahtiyar is the founder and the director of Cyber Security and Privacy Research Laboratory, SPF LAB, at Istanbul Technical University. His current research interests include cyber security and privacy, mobile systems, trust modeling, and financial systems.

# An Approach Based on Tunicate Swarm Algorithm to Solve Partitional Clustering Problem

Murat Aslan

**Abstract**—The tunicate swarm algorithm (TSA) is a newly proposed population-based swarm optimizer for solving global optimization problems. TSA uses best solution in the population in order improve the intensification and diversification of the tunicates. Thus, the possibility of finding a better position for search agents has increased. The aim of the clustering algorithms is to distributed the data instances into some groups according to similar and dissimilar features of instances. Therefore, with a proper clustering algorithm the dataset will be separated to some groups and it's expected that the similarities of groups will be minimum. In this work, firstly, an approach based on TSA has proposed for solving partitional clustering problem. Then, the TSA is implemented on ten different clustering problems taken from UCI Machine Learning Repository, and the clustering performance of the TSA is compared with the performances of the three well known clustering algorithms such as fuzzy c-means, k-means and k-medoids. The experimental results and comparisons show that the TSA based approach is highly competitive and robust optimizer for solving the partitional clustering problems.

**Index Terms**—Clustering, fuzzy c-means, k-means, k-medoid, tunicate swarm algorithm.

## I. INTRODUCTION

THE PURPOSE of unsupervised learning technique is to find out potential views from data without any class information and data clustering which is an important unsupervised learning technique is a considerable part of data mining [1, 2]. The intention of the clustering algorithms is to split instances into some groups according to their similar and dissimilar features. If one of the clustering technique is implemented on any dataset, the dataset separated to some groups and it is expected that the similarities of these groups will be in a minimum level [3, 4]. The main goal of the using the previous data samples is to obtain a conclusion, estimate a future statement and in diagnosis process [2]. Data clustering methods are used for various research areas such as marketing [5], text mining [6], financial analysis [7], web analysis [8], image segmentation [9], education [10], bioinformatics [11],

medical diagnosis [12], wireless sensor networks [13], data science [14], business [15] and so on.


Many techniques proposed in literature such as hierarchical approaches [16], graph based methods [17, 18], partitional (non-hierarchical) techniques [19-28], density based methods [29] and optimization-based clustering approaches [30-32] for solving data clustering problems [2, 33]. Some of optimization-based local search algorithms are Tabu Search (TS) algorithm [34] and Simulated Annealing (SA) algorithm [35]. In recently, optimization-based metaheuristic algorithms are used for many different optimization problems, because of problem free, has a simple structure and easy adaptable to any optimization problems [36]. Some of these metaheuristic algorithms for solving data clustering problems are such as Genetic Algorithm (GA) [37, 38], Teacher Learning Based Optimization (TLBO) [39], Ant Colony Optimization (ACO) [40], Artificial Bee Colony (ABC) [3, 41], Gravitational Search Algorithm (GSA) [42], Particle Swarm Optimization (PSO) [43], Grey Wolf Optimizer (GWO) [4] and Cuckoo Search (CS) [44, 45] algorithms.

In this study, the tunicate swarm algorithm (TSA) which is one of the swarm behavior based optimization algorithm proposed by Kaur et al. [47] to solve global optimization problems is implemented on ten different partitional clustering problems which are taken from UCI Machine Learning Repository [46]. The remainder section of this paper is detailed as follows: the clustering problem is extended in Section II. In Section III, the partitional clustering techniques such as Fuzzy C-Means, K-Medoids and K-Means are explained. In Section IV, each steps of the Tunicate Swarm Algorithm (TSA) are detailed. In Section V, the experimental outputs are given. The conclusions of experiments are given in Section VI.

## II. THE CLUSTERING PROBLEM

In the phase of clustering process, the data instances are divided into some sub groups according to their similar and dissimilar attributes. Eventually, the main goal of the data clustering is to obtain some homogeneous sets [3, 4, 45]. Partitional clustering methods are distributed the N data instances to k clusters (sets) in accordance with the similarity of the data instances. When data instances are distributed to clusters, some distance metrics [3, 45] such as Manhattan distance [48], Euclidean distance [49] and Minkowski distance [50] are used to find the best centroids. Therefore, the dataset is distributed homogeneously and the efficiency of the clustering is increased. In my study, the sum of squared

Murat ASLAN, is with Department of Computer Engineering, Faculty of Engineering, Şırnak University, Şırnak Turkey, (e-mail: [murataslan@sirnak.edu.tr](mailto:murataslan@sirnak.edu.tr)).

 <https://orcid.org/0000-0002-7459-3035>

Manuscript received March 29, 2021; accepted July 16, 2021.  
DOI: [10.17694/bajece.904882](https://doi.org/10.17694/bajece.904882)



Euclidean (SSE) distance which is calculated by present instance and the cluster center of the present instance is used as the objective function of the algorithms. The mathematical formulation of objective function SSE is given in Equation (1) [4, 21].

$$SSE = \sum_{i=1}^k \sum_{x \in C_i} d(x, C_i) \quad (1)$$

In Equation (1),  $C_i$  indicates the set of  $k$  centers,  $x$  is the data instance which assigned to the  $C_i$  cluster and  $d(x, C_i)$  shows the SSE distance between center  $C_i$  and  $x$  instance.

### III. PARTITIONAL CLUSTERING TECHNIQUES

In this study, one of the newest optimization-based metaheuristic algorithm which is called TSA is implemented on a dataset taken from UCI Machine Learning Repository for solving partitional clustering problems, and also some classical partitional clustering methods such as Fuzzy C-Means, K-Medoids and K-Means approaches are also implemented on the same dataset. The steps and framework of these approximate methods are detailed in under this section.

#### A. K-Means Algorithm

K-Means method is one of the important and simple, and besides an effective partitional clustering algorithms. When K-Means algorithm is executed, it is tried to find the best possible centroid (total centroids is  $k$ ) for each data instances in  $N$ . In K-Means approach the data instances are distributed into the centroids according to their maximum similarities and each instance can belong to just one cluster. The fitness value of K-Means is calculated with Equation (1). The value of the each center ( $C_j$ ) is calculated with Equation (2) [4].

$$C_i = \frac{1}{N_i} \sum_{j=1}^N w_{ji} x_j \quad (2)$$

**Step 1:** Create the centers of  $k$  cluster randomly in upper and lower boundaries.  
**Step 2:** Find the nearest cluster center for each data instances.  
**Step 3:** After the each instance is distributed to the nearest cluster, update the center of the each cluster.  
**Step 4:** Until the center of clusters are being stable or reach the maximum number of iteration, return the Step 2.

Fig. 1. The pseudo code of K-Means method [23]

Where  $N_i$  indicates the number of instances related to  $i$ th cluster.  $w_{ji}$  indicates a binary value in a set of [0,1] and if  $w_{ji}$  is assigned with '1', it is mean that  $x_j$  is associated with  $i$ th cluster, otherwise  $x_j$  is not a member of  $i$ th cluster. The steps of k-Means algorithm detailed by Velmurugan [23] and they

are shown in Fig 1. The centers of clusters are generated with a random initializing in K-Means algorithm. Hence, the performance of K-Means clustering method increases or decreases according to the position of starting centers.

#### B. K-Medoids Algorithm

The framework of K-Medoids method is similar to K-means algorithm. However, the selection strategy for cluster centers are different to each other. When a cluster center is determined in K-Means algorithm, any location in upper and lower bound can be a center of cluster. In K-Medoids method the best medoids are selected as cluster centers and a medoid should be an instance from all dataset [4, 51]. In this study, the Partitioning Around Medoids (PAM) [24] is selected as K-Medoids algorithm. The steps of K-Medoids algorithm are given in Fig. 2.

**Step 1:** Create the centers of K-Medoids randomly from dataset.  
**Step 2:** Find the nearest cluster center for each data instances.  
**Step 3:** For any medoid ( $m$ ) instance and non-medoid ( $o$ ) instance which depended with  $m$ ; swap  $m$  and  $o$ , and now  $o$  is a potential medoid. After then, the fitness values are calculated according to the Equation (1) for new potential medoid set and update position of  $k$  medoids.  
**Step 4:** Until the center of clusters are being stable or reach the maximum number of iteration, return the Step 2.

Fig. 2. The pseudo code of K-Medoids method [21, 43]

#### C. Fuzzy C-Means Algorithm

The framework of Fuzzy C-Means method is similar to K-Means algorithm. Fuzzy C-Means approach is developed by Dunn [27] and an extended version of this algorithm is developed by Bezdek [28]. In traditional clustering algorithm like K-Means and K-Medoids methods each data instance only can distribute to the one cluster. However, in fuzzy algorithm, each instance can belong to the one or more than one data clusters according to the membership degree of each cluster. For each instance, the sum of the membership degree for all clusters is equal to 1. The objective of the Fuzzy C-Means algorithm is given in Equation (3) [4, 25, 26].

$$J_m = \sum_{i=1}^N \sum_{j=1}^k u_{ij}^m \|x_i - C_j\|^2 \quad (3)$$

In here,  $N$  indicates the total data instances,  $k$  shows the total number of clusters,  $x_i$  shows the  $i$ th data instance,  $m$  shows a value upper than 1,  $u_{ij}$  shows the membership degree of the  $i$ th instance in  $j$ th cluster and  $C_j$  shows the center of the  $j$ th cluster. When an iteration is carried out  $u_{ij}$  and  $C_j$  values are updated by the Equation (4) and (5).

$$u_{ij} = \frac{1}{\sum_{n=1}^k \left( \frac{\|x_i - C_j\|^2}{\|x_i - C_n\|^2} \right)^{2/m-1}} \quad (4)$$

$$C_j = \frac{\sum_{i=1}^N u_{ij}^m \cdot x_i}{\sum_{i=1}^N u_{ij}^m} \quad (5)$$

The value of each membership degree is generated randomly in a range of [0,1] and the constraints are given below:

$$0 \leq u_{ij} \leq 1 \quad \text{and} \quad \sum_{i=1}^k u_{ij} = 1 \quad \text{for each } j = \{1, 2, \dots, k\}$$

The steps of Fuzzy C-Means algorithm are detailed in Fig. 3.

- Step 1:** Create membership degree matrix (u) randomly.
- Step 2:** Calculate the Equation (4) and determine the center of clusters according to the matrix u.
- Step 3:** Recalculate the matrix u with Equation (4).
- Step 4:** If the stopping criteria is not met, repeat the Step 2 and Step 3.

Fig. 3. The steps of Fuzzy C-Means algorithm [23]

#### IV. TUNICATE SWARM ALGORITHM (TSA)

The tunicate swarm optimization method is a population-based swarm approach proposed to solve global optimization problems. Tunicates are shining bio-luminescent and generates a faded blue-green light that can be realized from more than many meters away [52]. Each tunicate has a few millimeters length. There is a collective gelatinous tunic in each tunicate, and thanks to this feature all tunicate are connected to each other. Besides, each tunicate separately gets the water from the present sea and creating the jet propulsion by its open end through atrial siphons. Tunicate change the its current position with a propulsion like fluid jet. This propulsion makes to migrate the tunicates vertically in deep ocean. The most spectacular features of tunicate are their jet propulsion and swarm behaviors [47].

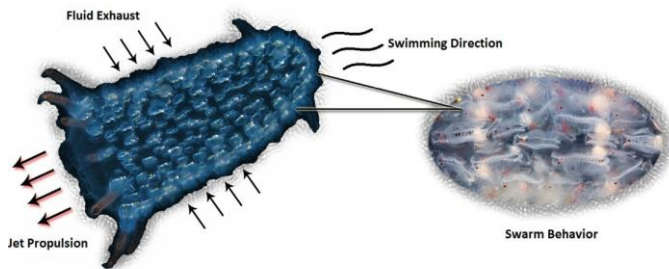


Fig. 4. swarm behavior of tunicate [47]

TSA uses the position of the best tunicate of the population for the purpose of improve the intensification and diversification of the tunicate. Thus, the possibility of finding a better position for search agents has increased. The swarm behavior of TSA is given in Fig. 4. Although tunicate has no idea what is the quality of food source, tunicate has the ability to locate the food source in the sea. tunicate uses Jet propulsion and swarm behavior structures while reaching the food source. Tunicate has three behaviors during Jet propulsion behavior. These behaviors are; Avoiding conflicts between the population of tunicate during the discovering process is that any tunicate constantly try to mobilize itself towards the individual with the best fitness value and try to keep itself close to the best individual. In order to prevent conflicts between tunicates, the vector  $\vec{A}$  is used to create the new position of the current tunicate and it is calculated according to the equations given below:

$$\vec{A} = \frac{\vec{G}}{\vec{M}} \quad (6)$$

$$\vec{G} = c_2 + c_3 - \vec{F} \quad (7)$$

$$\vec{F} = 2 \cdot c_1 \quad (8)$$

Where,  $\vec{G}$  refers to gravity force and  $\vec{F}$  indicates to the direction of water in the depths of the ocean.  $c_1$ ,  $c_2$  and  $c_3$  represent a random reel value generated in the range of [0,1]. The vector  $\vec{M}$  is expressed the social forces between the tunicates (search agents) in the search space and calculated according to Equation (9).

$$\vec{M} = [P_{\min} + c_1 \cdot P_{\max} - P_{\min}] \quad (9)$$

Where,  $P_{\min}$  and  $P_{\max}$  values shows the initial and secondary velocities for social interaction, and these values are accepted as 1 and 4, respectively [47]. After conflicts between adjacent tunicates are prevented, search agents begin to move towards adjacent tunicate which has the best fitness value. The movement of present tunicate to the best tunicate is calculated by Equation (10):

$$\vec{P}_D = |\vec{F}_S - r_{\text{rand}} \cdot \vec{P}_p(x)| \quad (10)$$

Where,  $\vec{P}_D$  refers to the distance between the food source and the search agent, x refers to current iteration,  $\vec{F}_S$  is the position of the tunicate with the best fitness value,  $\vec{P}_p(x)$  is the location of the present individual, and  $r_{\text{rand}}$  indicates a random reel value generated in the range of [0,1]. The new position of  $\vec{P}_p(x')$  is calculated according to Equation (11).

$$\vec{P}_p(x') = \begin{cases} \vec{FS} + \vec{A} \cdot \vec{PD} , & \text{if } r_{\text{rand}} \geq 0.5 \\ \vec{FS} - \vec{A} \cdot \vec{PD} , & \text{if } r_{\text{rand}} < 0.5 \end{cases} \quad (11)$$

$\vec{P}_p(x')$  shows the new position created for  $\vec{P}_p(x)$  according to the position of the best food source  $\vec{FS}$ . The mathematical model of the swarm behavior for tunicates is explained by Equation (12); the first two best optimum solutions are memorized and the positions of the other search agents are updated according to the location of these recorded best solutions.

$$\vec{P}_p(x+1) = \frac{\vec{P}_p(x) + \vec{P}_p(x+1)}{2+c_1} \quad (12)$$

After position update process, the latest position of tunicate will be in a random location, within a cylindrical or cone-shaped.  $\vec{A}$ ,  $\vec{G}$ , and  $\vec{F}$  promote the location of tunicates to move randomly in a specific search space and prevent the conflicts in tunicates population. The capability exploration and exploitation of TSA is provided by vectors  $\vec{A}$ ,  $\vec{G}$ , and  $\vec{F}$ . After these explanations, the steps of TSA are given in Fig. 5.

- Step 1:** Create the initial tunicate population ( $\vec{P}_p$ ).
- Step 2:** Determine the control units of TSA and stopping criteria.
- Step 3:** Compute the fitness values of the initial population.
- Step 4:** Select the position of the tunicate with the best fitness value.
- Step 5:** Create the new position for each tunicate by using the Equation (12).
- Step 6:** Update the position of the tunicates which are out of the search space.
- Step 7:** Compute the fitness values for the new positions of tunicates.
- Step 8:** Until stopping criteria is satisfied, repeat steps between 5 to 8.
- Step 9:** After stopping criteria is satisfied, save the best tunicate position.

Fig. 5. The steps of tunicate swarm algorithm [47]

The flowchart of TSA to solve partitional clustering problem is shown in Fig. 6. It is understood from Fig. 6, firstly, the TSA is initialized with control parameters. Then, the other steps of TSA are executed for solving clustering problem. And finally, the position of the tunicate which has the best fitness value is registered.

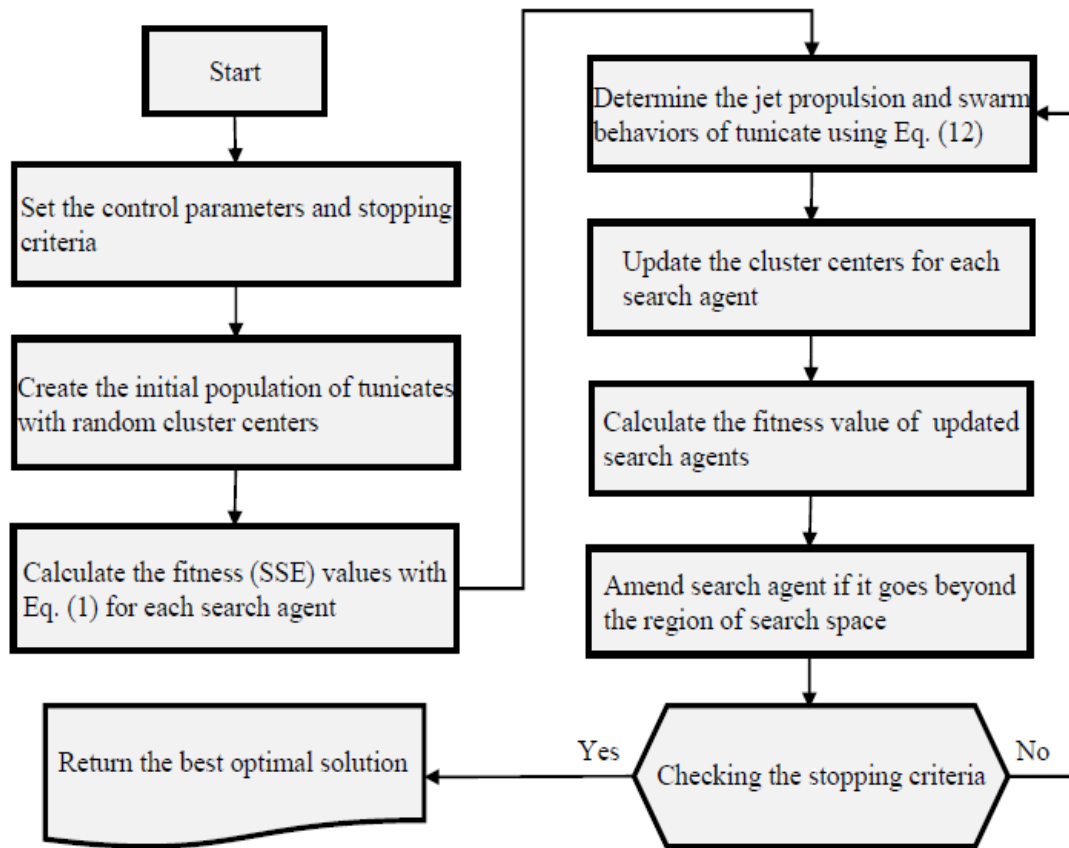


Fig. 6. The flowchart of TSA for solving data clustering problem

## V. EXPERIMENTAL RESULTS

In this study, TSA is applied on data clustering problem. For experiments, a dataset within 10 instances were taken from UCI Machine Learning Repository [46]. And besides, Fuzzy C-Means (F. C-Means), K-Medoids and K-Means partitioning clustering algorithms are implemented on the this dataset. All experiments were carried out on a Windows 10 Pro OS laptop using Intel(R) Core(TM) i7-6700HQ 2.60 GHz CPU, 24 GB of RAM and F.C-Means, K-Medoids, TSA and K-Means algorithms are coded in MATLAB platform. All algorithms are run 30 independent times and the experimental outcomes are reported as best, mean, worst and standard deviation (Std. Dev.) of 30 runs. For all methods the stopping criteria is selected as maximum iteration and it is set to 1000. The population size is set 100 for TSA and the other control parameters of TSA are selected according to the Kaur et al. [47] study.

TABLE I  
THE ATTRIBUTES OF THE DATASET [46]

Data	N. of Clusters	N. of Dimensions	N. of Instances	
D1	Balance	3	4	625
D2	Cancer	2	30	569
D3	Cancer-Int	2	9	699
D4	Credit	2	14	690
D5	Dermatology	6	34	366
D6	E. Coli	5	7	327
D7	Glass	6	9	214
D8	Iris	3	4	150
D9	Thyroid	3	5	215
D10	Wine	3	13	178

TABLE II  
COMPARISON RESULTS OF TSA WITH K-MEANS, K- MEDOIDS AND F. C-MEANS ALGORITHMS

Data	Criteria	TSA	K-Means	K-Medoids	F. C-Means	
D1	Balance	Best	1424.97	1423.85	1661.82	1722.24
		Worst	1426.39	1433.64	1813.56	1722.24
		Mean	<b>1425.58</b>	1425.95	1721.79	1722.24
		Std. Dev.	3.85E-01	2.15E+00	3.94E+01	1.16E-12
		Time	75.406	1.204	0.696	1.275
D2	Cancer	Best	1.34E+154	1.34E+154	1.79E+308	7.63E+156
		Worst	1.34E+154	1.34E+154	1.79E+308	7.63E+156
		Mean	<b>1.34E+154</b>	<b>1.34E+154</b>	1.79E+308	7.63E+156
		Std. Dev.	0.00E+00	0.00E+00	0.00E+00	0.00E+00
		Time	110.937	1.565	0.865	2.339
D3	Cancer-Int	Best	2968.81	2986.96	3311.56	3286.11
		Worst	2973.64	2988.43	4717.47	3286.11
		Mean	<b>2971.34</b>	2987.94	3733.51	3286.11
		Std. Dev.	1.24E+00	7.03E-01	3.99E+02	1.08E-12
		Time	86.058	1.412	0.497	1.408
D4	Credit	Best	556749.66	748491.65	558644.51	759180.47
		Worst	556834.46	808744.44	688213.99	759180.47
		Mean	<b>556769.82</b>	789553.64	591941.43	759180.47
		Std. Dev.	2.17E+01	2.69E+04	3.49E+04	6.84E-11
		Time	95.497	1.536	0.633	1.748
D5	Dermatology	Best	2247.38	2022.26	2732.90	5196.38
		Worst	2376.46	2197.77	3131.02	5196.38
		Mean	2309.36	<b>2090.85</b>	2930.87	5196.38
		Std. Dev.	3.13E+01	5.87E+01	1.04E+02	1.38E-11
		Time	180.005	1.525	4.710	8.680
D6	E. Coli	Best	69.72	66.02	133.02	108.44
		Worst	92.14	70.42	249.46	108.44
		Mean	75.60	<b>67.52</b>	160.47	108.44
		Std. Dev.	4.83E+00	1.20E+00	2.13E+01	5.48E-10
		Time	57.812	0.721	1.234	1.574
D7	Glass	Best	303.02	213.42	307.46	400.98
		Worst	372.19	262.57	479.53	404.41
		Mean	341.11	<b>235.98</b>	358.90	402.35
		Std. Dev.	1.41E+01	1.48E+01	5.19E+01	1.6042
		Time	54.44	0.515	1.375	1.621
D8	Iris	Best	97.88	97.33	184.54	106.36
		Worst	128.13	122.28	240.30	106.36
		Mean	101.46	<b>99.00</b>	210.46	106.36
		Std. Dev.	7.29E+00	6.33E+00	1.62E+01	7.07E-14
		Time	22.340	0.291	0.361	0.310
D9	Thyroid	Best	1886.96	2000.12	2085.73	2812.50
		Worst	2066.64	2024.62	2457.95	2812.50
		Mean	<b>1916.41</b>	2011.52	2224.35	2812.50
		Std. Dev.	2.97E+01	8.21E+00	9.43E+01	5.94E-11
		Time	31.546	0.427	0.423	0.492
D10	Wine	Best	16323.45	16555.68	17048.52	17128.46
		Worst	16380.04	18436.95	31007.19	17128.46
		Mean	<b>16338.28</b>	18044.71	20981.74	17128.46
		Std. Dev.	1.10E+01	7.60E+02	2.88E+03	6.19E-12
		Time	40.718	0.416	0.494	0.674

The objective function is selected as Equation (1) for all methods. The attributes of the dataset taken from UCI Machine Learning Repository are given in Table I, and in Table I,  $N$ . of Clusters indicates the total number of clusters,  $N$ . of Dimensions shows the size of problem and  $N$ . of Instances shows the size of samples. The obtained experimental outcomes of F.C-Means, K-Medoids, TSA and K-Means algorithms are given in Table II. As seen from Table II, TSA obtains the best mean results for 6 problems (the total number of data instances is 10) such as Balance, Cancer, Cancer-Int, Credit, Thyroid and Wine samples, and TSA finds the second best results for Dermatology, E. Coli, Glass and Iris samples. K-Means algorithm is found the best mean results for 5 problems such as Cancer, Dermatology, E. Coli, Glass and Iris samples. In the light of these obtained experiments, it is shown that the performance of the TSA is higher than F.C-Means, K-Medoids and K-Means algorithms. K-Means algorithm reaches the second best results and the experimental results of F. C-Means algorithm are the worst results among the compared algorithms. In addition, the running time of F.C-Means, K-Medoids, TSA and K-Means algorithms are also given in Table II. It is understood that TSA uses up more time than the other compared algorithms in terms of running time of the methods. The reason of TSA consumes more time is TSA one of the population based metaheuristic algorithm. Metaheuristic algorithms are problem free and they can easily adaptable any problem in generally. But approximate algorithms such as K-Means, K-Medoids and F. C-Means algorithms are proposed for solving clustering problems and they cannot adaptable any other problem in generally. So, it is expected the running time of the approximate methods less than metaheuristic algorithms.

TABLE III  
COMPARISON RESULTS OF TSA WITH K-MEANS,  
K-MEDOIDS AND F. C-MEANS ALGORITHM

Data	Criteria	TSA	K-Means	K-Medoids	F.C-Means
D1	Mean	1425.58	1425.95	1721.79	1722.24
	Rank	<b>1</b>	2	3	4
D2	Mean	1.34E+154	1.34E+154	1.79E+308	7.63E+156
	Rank	<b>1</b>	<b>1</b>	4	3
D3	Mean	2971.34	2987.94	3733.51	3286.11
	Rank	<b>1</b>	2	4	3
D4	Mean	556769.82	789553.64	591941.43	759180.47
	Rank	<b>1</b>	4	2	3
D5	Mean	2309.36	2090.85	2930.87	5196.38
	Rank	2	<b>1</b>	3	4
D6	Mean	75.60	67.52	160.47	108.44
	Rank	2	<b>1</b>	4	3
D7	Mean	341.11	235.98	358.90	402.35
	Rank	2	<b>1</b>	3	4
D8	Mean	101.46	99.00	210.46	106.36
	Rank	2	<b>1</b>	3	4
D9	Mean	1916.41	2011.52	2224.35	2812.50
	Rank	<b>1</b>	2	3	4
D10	Mean	16338.28	18044.71	20981.74	17128.46
	Rank	<b>1</b>	2	4	3

For a comprehensive analysis of experimental results of compared algorithms, the mean results of 30 run and the rank values of F.C-Means, K-Medoids, TSA and K-Means are shown in Table III. A comparison of rank rate of TSA, K-Means, K-Medoids and F. C-Means algorithms is given in Fig. 7. When the sum of rank rates dedicated in Fig. 7 are considered, the total rank rate of the TSA is 14, and TSA has shown a more powerful yield compared with F.C-Means, K-Medoids and K-Means. And according to the rank results, K-Means algorithm has shown the second best performance and the rank rate of K-Means is 17, the third best solver algorithm is the K-Medoids and the rank rate of K-Medoids is 33, and the performance of F. C Means algorithm is less than the other compared algorithms with 35 rank value.

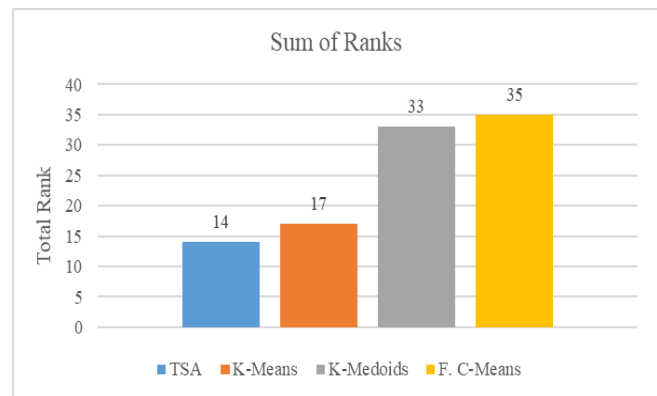


Fig. 7. The total ranks of compared algorithms

## VI. CONCLUSIONS

In this study, an approach based on TSA which is newly proposed a population-based swarm optimizer for solving global optimization problems has implemented for solving partitional clustering problem. The experimental outcomes of TSA is compared with three state-of-art classical clustering algorithms: F. C-Means, K-Medoids and K-Means algorithms. In accordance with the analysis and comparisons, the TSA based clustering approach finds a better or comparable performances than K-Means, K-Medoids and F. C-Means algorithms on the UCI Machine Learning Repository dataset in terms of solution quality and robustness.

## REFERENCES

- [1] A.K. Jain, Data clustering: 50 years beyond k-means, in: Joint European Conference on Machine Learning and Knowledge Discovery in Databases, Springer, 2008, pp. 3-4.
- [2] A. Kaur, Y. Kumar, A new metaheuristic algorithm based on water wave optimization for data clustering, Evolutionary Intelligence, (2021) 1-25.
- [3] D. Karaboga, C. Ozturk, A novel clustering approach: Artificial Bee Colony (ABC) algorithm, Applied soft computing, 11 (2011) 652-657.
- [4] M. Karakoyun, O. İnan, İ. Akto, Grey Wolf Optimizer (GWO) Algorithm to Solve the Partitional Clustering Problem, International Journal of Intelligent Systems and Applications in Engineering, 7 (2019) 201-206.
- [5] V. Holý, O. Sokol, M. Černý, Clustering retail products based on customer behaviour, Applied Soft Computing, 60 (2017) 752-762.
- [6] L.M. Abualigah, A.T. Khader, M.A. Al-Betar, O.A. Alomari, Text feature selection with a robust weight scheme and dynamic dimension reduction to text document clustering, Expert Systems with Applications, 84 (2017) 24-36.

- [7] Y. Marinakis, M. Marinaki, M. Doumpos, C. Zopounidis, Ant colony and particle swarm optimization for financial classification problems, *Expert Systems with Applications*, 36 (2009) 10604-10611.
- [8] S. Gong, W. Hu, H. Li, Y. Qu, Property Clustering in Linked Data: An Empirical Study and Its Application to Entity Browsing, *International Journal on Semantic Web and Information Systems (IJSWIS)*, 14 (2018) 31-70.
- [9] A. Mekhmoukh, K. Mokrani, Improved Fuzzy C-Means based Particle Swarm Optimization (PSO) initialization and outlier rejection with level set methods for MR brain image segmentation, *Computer methods and programs in biomedicine*, 122 (2015) 266-281.
- [10] Á.A.M. Navarro, P.M. Ger, Comparison of clustering algorithms for learning analytics with educational datasets, *IJIMAI*, 5 (2018) 9-16.
- [11] I. Triguero, S. del Río, V. López, J. Bacardit, J.M. Benítez, F. Herrera, ROSEFW-RF: the winner algorithm for the ECBDL'14 big data competition: an extremely imbalanced big data bioinformatics problem, *Knowledge-Based Systems*, 87 (2015) 69-79.
- [12] L. Wang, X. Zhou, Y. Xing, M. Yang, C. Zhang, Clustering ECG heartbeat using improved semi-supervised affinity propagation, *IET Software*, 11 (2017) 207-213.
- [13] J. Zhu, C.-H. Lung, V. Srivastava, A hybrid clustering technique using quantitative and qualitative data for wireless sensor networks, *Ad Hoc Networks*, 25 (2015) 38-53.
- [14] R. Hyde, P. Angelov, A.R. MacKenzie, Fully online clustering of evolving data streams into arbitrarily shaped clusters, *Information Sciences*, 382 (2017) 96-114.
- [15] C.-H. Chou, S.-C. Hsieh, C.-J. Qiu, Hybrid genetic algorithm and fuzzy clustering for bankruptcy prediction, *Applied Soft Computing*, 56 (2017) 298-316.
- [16] J. Han, M. Kamber, J. Pei, *Data mining concepts and techniques third edition*, The Morgan Kaufmann Series in Data Management Systems, 5 (2011) 83-124.
- [17] S. Schaeffer, Graph clustering. *Comput. Sci. Rev.* 1 (1), 27-64, in, 2007.
- [18] B. Hufnagl, H. Lohninger, A graph-based clustering method with special focus on hyperspectral imaging, *Analytica chimica acta*, 1097 (2020) 37-48.
- [19] M.E. Celebi, H.A. Kingravi, P.A. Vela, A comparative study of efficient initialization methods for the k-means clustering algorithm, *Expert systems with applications*, 40 (2013) 200-210.
- [20] J.A. Hartigan, M.A. Wong, AK-means clustering algorithm, *Journal of the Royal Statistical Society: Series C (Applied Statistics)*, 28 (1979) 100-108.
- [21] P. Arora, S. Varshney, Analysis of k-means and k-medoids algorithm for big data, *Procedia Computer Science*, 78 (2016) 507-512.
- [22] M. Capó, A. Pérez, J.A. Lozano, An efficient approximation to the K-means clustering for massive data, *Knowledge-Based Systems*, 117 (2017) 56-69.
- [23] T. Velmurugan, Performance based analysis between k-Means and Fuzzy C-Means clustering algorithms for connection oriented telecommunication data, *Applied Soft Computing*, 19 (2014) 134-146.
- [24] L. Kaufman, P.J. Rousseeuw, Partitioning around medoids (program pam), *Finding groups in data: an introduction to cluster analysis*, 344 (1990) 68-125.
- [25] J. Jędrzejowicz, P. Jędrzejowicz, Distance-based online classifiers, *Expert Systems with Applications*, 60 (2016) 249-257.
- [26] X. Qiu, Y. Qiu, G. Feng, P. Li, A sparse fuzzy c-means algorithm based on sparse clustering framework, *Neurocomputing*, 157 (2015) 290-295.
- [27] J.C. Dunn, A fuzzy relative of the ISODATA process and its use in detecting compact well-separated clusters, (1973).
- [28] J.C. Bezdek, Objective function clustering, in: *Pattern recognition with fuzzy objective function algorithms*, Springer, 1981, pp. 43-93.
- [29] A. Moreira, M.Y. Santos, S. Carneiro, Density-based clustering algorithms-DBSCAN and SNN, University of Minho-Portugal, (2005) 1-18.
- [30] S.J. Nanda, G. Panda, A survey on nature inspired metaheuristic algorithms for partitioning clustering, *Swarm and Evolutionary computation*, 16 (2014) 1-18.
- [31] A. Nayyar, N.G. Nguyen, Introduction to swarm intelligence, *Advances in swarm intelligence for optimizing problems in computer science*, (2018) 53-78.
- [32] A. Nayyar, S. Garg, D. Gupta, A. Khanna, Evolutionary computation: theory and algorithms, *Advances in swarm intelligence for optimizing problems in computer science*, (2018) 1-26.
- [33] S. Saraswathi, M.I. Sheela, A comparative study of various clustering algorithms in data mining, *International Journal of Computer Science and Mobile Computing*, 11 (2014) 422-428.
- [34] C.S. Sung, H.W. Jin, A tabu-search-based heuristic for clustering, *Pattern Recognition*, 33 (2000) 849-858.
- [35] S.Z. Selim, M. Alsultan, A simulated annealing algorithm for the clustering problem, *Pattern recognition*, 24 (1991) 1003-1008.
- [36] M. Aslan, M. Gunduz, M.S. Kiran, JayaX: Jaya algorithm with xor operator for binary optimization, *Applied Soft Computing*, 82 (2019) 105576.
- [37] M.A. Rahman, M.Z. Islam, A hybrid clustering technique combining a novel genetic algorithm with K-Means, *Knowledge-Based Systems*, 71 (2014) 345-365.
- [38] Y. Marinakis, M. Marinaki, M. Doumpos, N. Matsatsinis, C. Zopounidis, A hybrid stochastic genetic-GRASP algorithm for clustering analysis, *Operational Research*, 8 (2008) 33-46.
- [39] Y. Kumar, P.K. Singh, A chaotic teaching learning based optimization algorithm for clustering problems, *Applied Intelligence*, 49 (2019) 1036-1062.
- [40] P. Shelokar, V.K. Jayaraman, B.D. Kulkarni, An ant colony approach for clustering, *Analytica Chimica Acta*, 509 (2004) 187-195.
- [41] G. Sahoo, A two-step artificial bee colony algorithm for clustering, *Neural Computing and Applications*, 28 (2017) 537-551.
- [42] X. Han, L. Quan, X. Xiong, M. Almeter, J. Xiang, Y. Lan, A novel data clustering algorithm based on modified gravitational search algorithm, *Engineering Applications of Artificial Intelligence*, 61 (2017) 1-7.
- [43] A. Khatami, S. Mirghasemi, A. Khosravi, C.P. Lim, S. Nahavandi, A new PSO-based approach to fire flame detection using K-Medoids clustering, *Expert Systems with Applications*, 68 (2017) 69-80.
- [44] A. Bouyer, A. Hatamlou, An efficient hybrid clustering method based on improved cuckoo optimization and modified particle swarm optimization algorithms, *Applied Soft Computing*, 67 (2018) 172-182.
- [45] S.I. Boushaki, N. Kamel, O. Bendjehaba, A new quantum chaotic cuckoo search algorithm for data clustering, *Expert Systems with Applications*, 96 (2018) 358-372.
- [46] UCI Machine Learning Repository, <https://archive.ics.uci.edu/ml/datasets.html>, in, 2021.
- [47] S. Kaur, L.K. Awasthi, A. Sangal, G. Dhiman, Tunicate swarm algorithm: a new bio-inspired based metaheuristic paradigm for global optimization, *Engineering Applications of Artificial Intelligence*, 90 (2020) 103541.
- [48] S.N. Neyman, B. Sitohang, S. Sutisna, Reversible fragile watermarking based on difference expansion using manhattan distances for 2d vector map, *Procedia Technology*, 11 (2013) 614-620.
- [49] D.P. Mesquita, J.P. Gomes, A.H.S. Junior, J.S. Nobre, Euclidean distance estimation in incomplete datasets, *Neurocomputing*, 248 (2017) 11-18.
- [50] M. Luo, B. Liu, Robustness of interval-valued fuzzy inference triple I algorithms based on normalized Minkowski distance, *Journal of Logical and Algebraic Methods in Programming*, 86 (2017) 298-307.
- [51] H.-S. Park, C.-H. Jun, A simple and fast algorithm for K-medoids clustering, *Expert systems with applications*, 36 (2009) 3336-3341.
- [52] J. Berrill, *The Tunicata*, The Royal Society: London, (1950).

## BIOGRAPHIES



**Murat Aslan** received B.Sc. and M.Sc. degrees in Computer Engineering from Selçuk University in 2011 and 2017 respectively and received Ph.D. degrees in Department of Computer Engineering, Faculty of Engineering and Natural Sciences, Konya Technical University in 2020. Recently, he is an Assistant Professor in the Department of the Computer Engineering at Şırnak University and his current interests include applications of Graph Theory, Discrete and Binary Optimization Problems, Swarm Intelligence or Evolutionary Computation Algorithms.

# Development of an Embedded System for Building System Management Based on PV-Powered

Hussein Ali\* and Ergun Erçelebi


**Abstract**—As complexity and the type of electrical applications perpetually expands, monitor and control will require new systems which are based on some features in such feature of self-powered and distantly management. Building management systems (BMSs) are developed as efficient solutions to monitor and control users electrical and mechanical applications. A BMS employs cheap sensors and a real-time module to create prior knowledge about the climate inside the building. As a result, these features give some attractive advantages in taking a precise decision and managing vital operations of electrical applications. In this paper, a Raspberry Pi as minicomputer for collecting information from server room or data centre for detection the existence of human, temperature and humidity sensor and gas sensors to control ventilation systems, Arduino platform is responsible for receiving sensors signal and control actions according to the statues in the server room. While the Xbee protocol has been used to transmit data from the sensing node (Raspberry PI3) to mentors and control nodes (Arduino mega2560). The prototype design has been verified experimentally.

**Index Terms**—Building management systems, Power Saving, Smart Power System, Raspberry PI 3, XBee modules.

## I. INTRODUCTION

**P**OWER CONSUMPTION and security systems for buildings is one of the topics has great interest at this time, all the time the institutions, researchers and governments looking for keeping every topic related power consumption, security systems for buildings, firefighting systems, cooling systems under development by conception of smart management systems. In the last decades, the application of embedded systems encouraged Stakeholders to develop embedded systems for managing and monitoring the energy units all the time. These systems are developed based on a modern wireless connection and minicomputers.

**HUSSEIN ALI**, is with Department of Electrical Engineering University of Gaziantep, Gaziantep, Turkey, (e-mail: [hussain.a.abd1986@gmail.com](mailto:hussain.a.abd1986@gmail.com)).

 <https://orcid.org/0000-0003-2543-1205>

**ERGUN ERÇELEBI**, is with Department of Electrical Engineering University of Gaziantep, Gaziantep, Turkey, (e-mail: [ercelebi@gantep.edu.tr](mailto:ercelebi@gantep.edu.tr)).

 <https://orcid.org/0000-0002-4289-7026>

Manuscript received May 6, 2021; accepted July 26, 2021.

DOI: [10.17694/bajece.933353](https://doi.org/10.17694/bajece.933353)

Most embedded systems required energy storage to stabilize the operation of the system and prevent any damage to the OS of embedded systems. However, power consumption represents a critical concern for embedded devices. There are always need to increase battery life, which contributes to reduce the system's environmental impact. Previously, the improving battery life was exclusively responsibility by the hardware design, but those days are gone. Software in embedded systems has recently taken responsibility for controlling power consumption. In the same way, power consumption represents a major problem in embedded systems, while self-powered systems have become extensively used. As the device size has become smaller and thinner, this limitation prevents the system from incorporating a large capacity battery for long-term use [1].

In order to manage power consumption, the manufacturing people can perform on either hardware or software. On the other hand, their techniques are widely used such as; clock-gating clock off for the region does not need to work anymore, using multiple threshold voltage levels for different blocks with different operating speeds, power-gating turn off the block that is no longer working, and dynamic frequency/voltage scaling (DFVS), and frequency/voltage grading in order to appropriate workloads [2–5]. On the software, solutions are often focused on optimizing compiler. These assistances to build small and highly efficient execution code.

Regardless the software and interface facilities, a data centre must provide many important features like: consistent, stable power, even in the event of a utility outage, as well as cooling, physical site security, lighting, firefighting, access control and other systems [6]. at this time, many of these systems are wildly used in a typical building, but uses it in a data centre requires added capabilities or special measures owing to the critical purposes. for instance, fire suppression should ideally enable extinguishing fires without destroying servers and other equipment.

Data centres remain critical unite in automation systems, which encompass energy-hungry infrastructures that run large-scale Internet-based services. Energy consumption models are pivotal in designing and optimizing energy-efficient operations to curb excessive energy consumption in data centres [7].

A detailed BMS was designed and implemented as the

primary part of system to collect data and monitor alarms in the event of malfunctions or significant failures. Another important point related server's room and data centre protection that each data centre servers includes data base and software like example digital transfer projects, these databases need to working without any reasons for failure at any time. For these reasons building management system for server's room and data centre founded in order to solving some of failure reasons.

However, the protection of fire due to overheating in electronic components and controlling to air ventilation remotely has still obscure [3,4,7]..

In this paper, a Raspberry Pi has been used as min computer unite to collect sensors signal from server room or data centre such that signals for detection the existence of human, temperature and humidity sensor and gas sensors to control ventilation systems, Arduino Mega2560 responsible for receiving a decision from Raspberry Pi and take control actions according to the server room statues. While Xbee protocol has been used to transmit data from the sensing node to the mentoring node.

## II. COMPONENTS OF DEVELOPED BMS

The core parts of the proposed design of BMS are Raspberry Pi 4B and Arduino mega2560 [8,9] .The Raspberry Pi 4B works as a mini-computer that is responsible to collect sensors measurement from two types of sensors SHT3x for temperature/humidity and MQ2 for gas/smoke sensing. In addition to that, Raspberry Pi includes a program responsible for takes actions according to the sensors reading and send this action to Arduino mega2560 through Xbee module. Arduino mega2560 is responsible to take fast actions under the critical situation of fire or smoke occurred in the closed room. In addition to the developed system has the capability to control the temperature and humidity of the room and also take action to turn on or turn off the cooling system based on the status. These actions are taken according to the control signal coming from the mini-computer. The block diagram of the developed system is illustrated in Fig1.

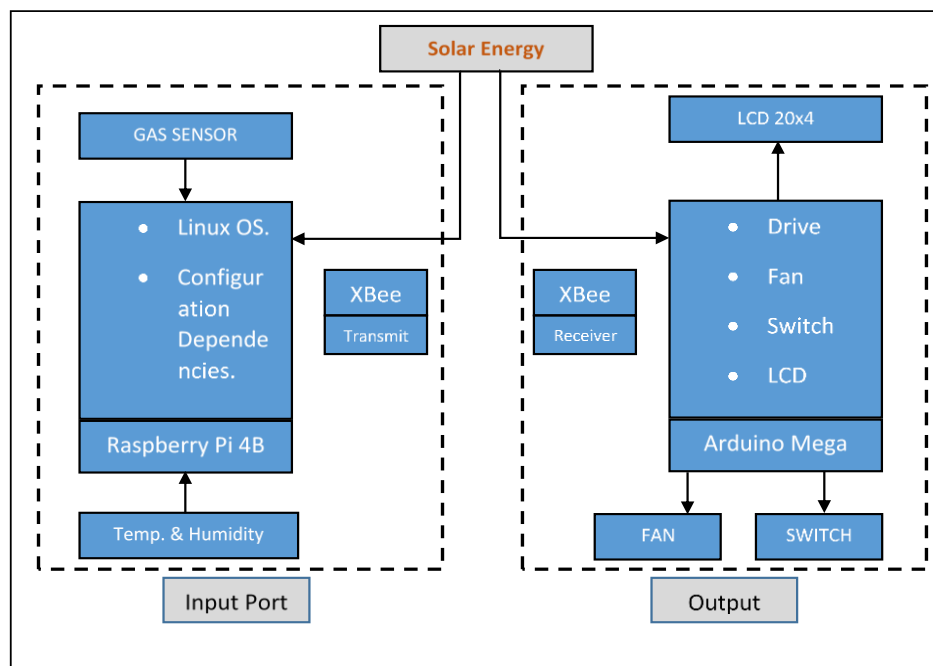


Fig1 Conceptual design of the proposed system.

According to the conceptual block diagram of BMS, Raspberry Pi putting in a data centre room. The two types of sensors connect with Raspberry Pi via digital pins, the benefits of these sensors are checking the environment inside the room like temperature, humidity, and during fire alarm statues the control action is directly open the door. Moreover, fire status appears on LCD.

### A. Algorithms for data collate and take control of actions

Fig 2 describes the algorithm of Raspberry Pi Python code. This algorithm is used for data collection from different sensors inside the server room or data center and send by using XBee protocol to the receiver site. The receiver site consists of Arduino mega2560 with XBee shield, the input/output pins of

Arduino mega2560 are utilised to qualified control signal according to action that been taken. Also, LCD is used to display the situation of control action. The algorithm of control action is shown in Fig 3. This algorithm is written in C++ program code in order to proper the architecture of Arduino.



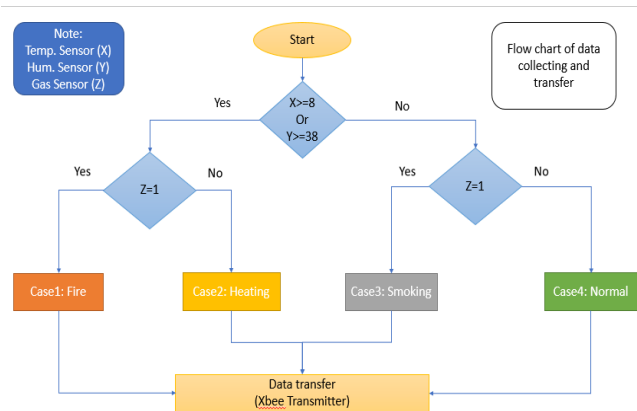


Fig 2. flow chart of data collection and transfer via Xbee to receiver site.

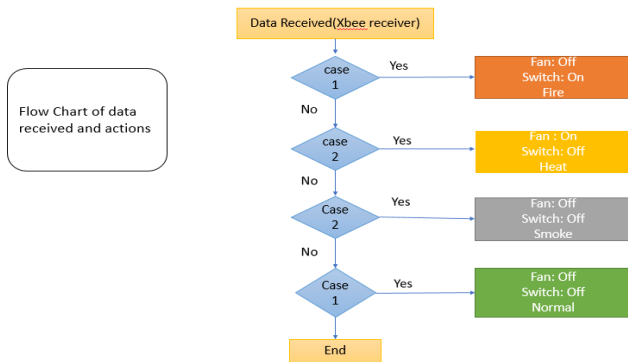


Fig3. flow chart of received data and take actions at Arduino MEGA 2560.

III. SIMULATION RESULTS AND DESIGN DESCRIPTION

The developed system has been implemented using LabVIEW simulation program based on the block diagram in Fig 1. On the other hand, the prototype hardware consists of Raspberry Pi for collecting data of sensors reading from inside the building all the time[10]. The Xbee s2 module is connected with Raspberry Pi in order to ensure a fast transfer of measured data to the monitoring side. On the monitoring and control side, Arduino connected with the Xbee shield in order to ensure receiving sensors signals from Raspberry Pi and begin to take action for cooling, fire alarm, access control. The Arduino MEGA 2560 pins are used as output for sending decision signals to access control devices. The switch or really consists of electric-magnetic used as electromechanical door locking, which is under fire status the Arduino sending open door action to electromechanical lock that would be satisfaction more safety stranded inside the building.

In addition to that the setting for the cooling system to turn on at temperature 8 °C and humidity 38 presents. Furthermore, the setting values of temperature and humidity for the cooling system is easily adjustable. Under fire case if there heating and smoke the fire case will be starting and safety action will be starting also, the Smoke case can appear on HMI (LCD) in case there is such a level of smoke inside. Finally, the solar panel has been used as main source for system power, MPPT and batteries also in order to keep PC economy. The simulation blocks of the developed BMS under the simulation program appears in Fig 4. While, the interface blocks of the BMS have appeared in Fig 5.

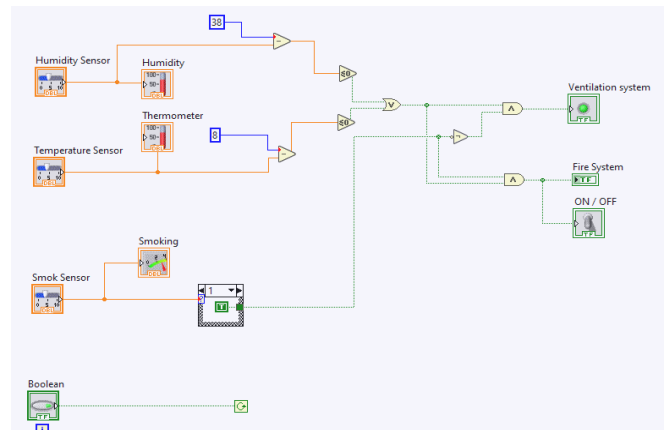


Fig4.Simulation blocks for developed BMS system under simulation program.

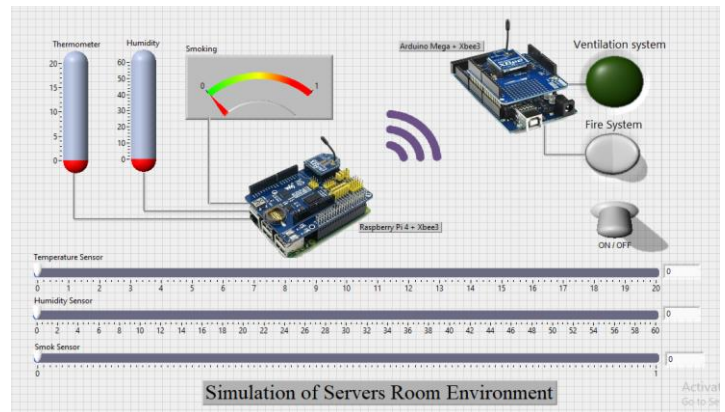


Fig 5 interface blocks for developed BMS system under simulation program.

The prototype hardware implementation for the BMS is shown in Fig 6. finally, the system is powered by a PV -source with a battery the connection of the BMS energy source appears in Fig 7.

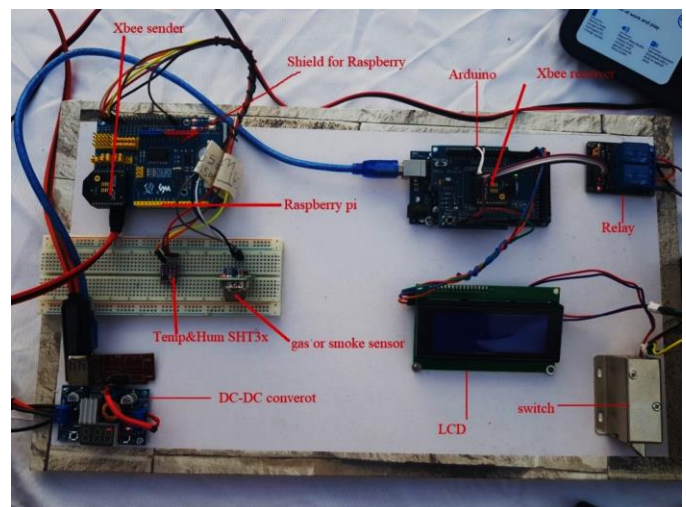


Fig 6 Hardware implementation of the developed BMS.

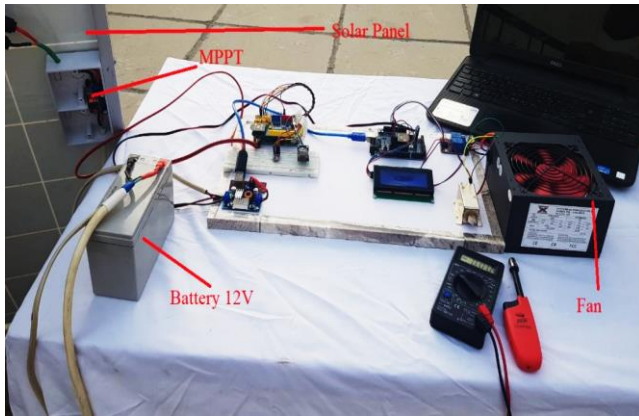


Fig 7. Hardware implementation of solar and MPPT.

IV. DISCUSSION

The critical aspect of the developed design was how we could clarify the main environmental issue inside the server room or data centre room. Therefore, the LabVIEW simulation software was utilised to evaluate the performance of developed BMS. In performance evaluate four different cases have been studied; heating sensor SHT3x, humidity sensor SHT3x, smoke and gas leakage detector sensor MQ2 (fire), and smoke and gas leakage detector sensor MQ2 (smoke). The status of these events appears on the monitoring LCD and the results are listed in Table I.

- *Case 1: Heating sensor SHT3x:*When the temperature degree inside closed building change to 8°C or greater than 8°C, the temperature sensor inside the server room will send the signal statues to the Raspberry pi in order to collect information for all sensors inside the room, after that the Raspberry pi will send the signals by using XBEE protocol to Arduino outside to the room near to the door of the server room, Arduino will take

control action according to the above-mentioned ( see in Fig 3). This activates will be available on the LCD monitor device installed outside. The result of simulation interface of this case appears in Fig 8a.

- *Case 2 Humidity sensor SHT3x:* When the humidity presents inside closed building change to equal 38 or greater than 38, the humidity sensor inside the server room will send the signal statues to the Raspberry pi in order to collect information for all sensors inside the room, after that the Raspberry pi will send the signals by using XBEE protocol for Arduino outside to the room near to the door of the server room. Fig 8b describes the simulation interface of case 2.

- *Case 3: Smoke and gas leakage detector sensor MQ2 (fire):* When the heating and smoke statues level change inside a closed building, the temperature sensor and smoke sensor inside the server room will send the signal statues to the Raspberry pi in order to collect information for all sensors inside the room, after that the Raspberry pi will send the signals by using XBEE protocol for Arduino outside to the room near to the door of the server room. In this event, all activities stop run and the magnetic lock of the door is directly open. Fig 8c describes case 3.

- *Case 4 Smoke and gas leakage detector sensor MQ2 (smoke):*In this case, the smoke sensor will be sensitive for the low level from smoke, if there is and little smoke inside the server room without heating that means there are no fire statues, so the smoke sensor will send the signal to the Raspberry pi in order to collect data for all sensors inside the room, after that the Raspberry pi will send the signals by using XBEE protocol for Arduino outside to the room near to the door of the server room, Arduino will take action according to the statues. Fig 8 d describes case 4.

TABLE I  
BMS SYSTEM OPERATION STATUS ON LCD.

Statues	LCD- status	Action
Heating and Humidity	Temperature: 28°C Humidity: 50%RH Status: Hot Cooling	Cooling system is turn on
Smoke /gas leakage	Temperature: 25°C Humidity: 56%RH Status: Smoking Normal	smoke inside normal/ fire alarm
Smoke/ gas leakage (Fire)	Temperature: 27°C Humidity: 53%RH Status: Fire Site Under Maint	Fire inside the door unluck and turn off all activities

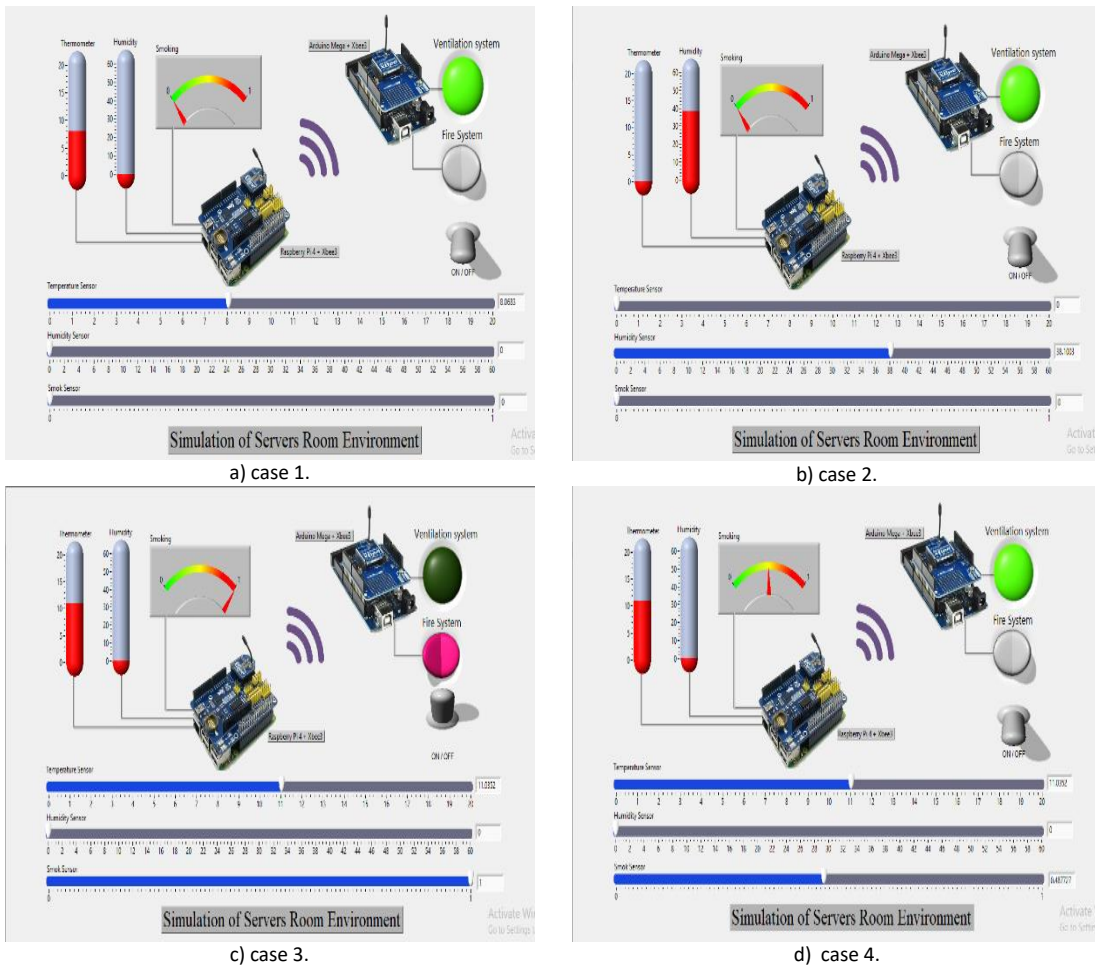


Fig 8 evaluate the BMS performance against different events.

TABLE II  
COMPARISON WITH SAME SYSTEM IN LITERATURE

References	Control characteristics	Design details
[6]	Raspberry Pi	Re-distributed heat on building by using temperature sensors. The proposed system depends on some classical control strategy and the flexibility of the open-source Building energy Management System.
[11]	1.Arduino Mega 2560 2. Raspberry Pi	Development a remotely controllable home energy management and control system with support control through mobile.
[12]	1. Arduino Uno 2. Raspberry Pi	Developed energy management system in order to energy conservation at household.
Proposed BMS	1.Arduino Mega 2560 2. Raspberry Pi	Classical control is used and in dangerous conditions, the decision is taken automatically depend on prior settings while the action appears to the user.

A primary design objective of the BMS system for the server room is the minimum total cost. The total cost increases with increasing the number of features because increase the required number of sensors such as camera or motion detection sensor. The number of major components and the prices of these components for BMS of server room are tabulated in Table III.

The systems developed [6,11,12] using a traditional power source which includes a battery for supplying the components of the system. In contrast to that, the proposed BMS has a feature that is self-powered by PV and with a backup energy source by battery.

TABLE III. THE NUMBER OF MAJOR COMPONENTS FOR BMS WITH COST OF EACH COMPONENT.

Component	Number of items	Local price
Raspberry Pi	1	25\$
Arduino Mega 2560	1	7\$
Xbee S2 Module	2	12\$
Solar panel 10W, 12 V+MPPT	1	15\$
Battery	1	4\$
Heating sensor SHT3x	1	0.5\$
Gas Sensor (MQ2) module	1	0.25\$
LCD 16x4	1	3\$
Approximately total price	8	66.75\$

## V. CONCLUSION

In this paper, the design and implementation of a flexible solution for a building management system for the server room or data centre is presented, which essentially provides safety as well as comfortable work at a data centre. In addition to that, it is featured by simply install, cheap technologies for design, also the control and watch of devices insides a building can be easier without visiting the place of a device. Moreover, it provides a status of temperatures, fire if that occurred inside and smoke leak by using wireless technology to transmits events inside building to the monitoring station. Accordingly, the building management system that has been presented in this paper works properly for electric power management, mainly in the server room or data centre.

## ACKNOWLEDGMENT

The author likes to recognise the observable support from PhD. Ahmed K. Ali in the Al Mustansiriyah University, Baghdad-Iraq for his precious discussions and comments.

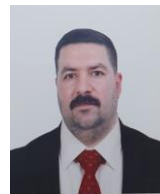
## REFERENCES

- [1] Do QN, Le TC. Low Power Embedded System Design Using Code Compression 2015:0–4.
- [2] Emmett F, Biegel M. Power Reduction Through RTL Clock Gating. Power 2000.
- [3] Lee J, Nam BG, Yoo HJ. Dynamic Voltage and Frequency Scaling (DVFS) scheme for multi-domains power management. 2007 IEEE Asian Solid-State Circuits Conf A-SSCC 2007:360–3. doi:10.1109/ASSCC.2007.4425705.
- [4] System M, Li W, Member GS, Logenthiran T, Member S. Implemented IoT-Based Self-Learning Home Management System (SHMS) for Singapore 2018;5:2212–9.
- [5] Paolo Ricci P, Donatelli M, Falabella A, Mazza A, Onofri M. Evolution of the Building Management System in the INFN CNAF Tier-1 data center facility. J Phys Conf Ser 2017;898. doi:10.1088/1742-6596/898/8/082005.
- [6] Jones SR, Beardmore J, Gillott M, Boukhanouf R, Walker G. A control methodology for Building Energy Management Systems (BEMS) in heat networks with distributed generation. Energy Procedia 2018;153:295–302. doi:10.1016/j.egypro.2018.10.011.
- [7] Benson T, Anand A, Akella A, Zhang M. Understanding data center traffic characteristics. Comput Commun Rev 2010;40:92–9. doi:10.1145/1672308.1672325.
- [8] Pi UR, B RPM-. Internet of Things Based Home

Security. 2018 Fourth Int Conf Comput Commun Control Autom n.d.:1–6.

- [9] Audio C, Storage CE, Power C, Basics L, Debian I, External U, et al. Raspberry Pi ® User Guide. n.d.
- [10] Blaifi S, Moulahoum S, Colak I, Merrouche W. Monitoring and enhanced dynamic modeling of battery by genetic algorithm using LabVIEW applied in photovoltaic system. Electr Eng 2018;100:1021–38. doi:10.1007/s00202-017-0567-6.
- [11] Barnes V, Collins TK, Mills GA. Design and implementation of home energy and power management and control system. Midwest Symp Circuits Syst 2017;2017-Augus:241–4. doi:10.1109/MWSCAS.2017.8052905.
- [12] Dhobale KM, Gorgile SP, Gunjal PJ, Hirve KA, U. A. PM. IOT based Smart Water Supply management System. Ijarcce 2017;6:297–9. doi:10.17148/ijarcce.2017.6157.

## BIOGRAPHIES



**HUSSEIN ALI**, Iraq, Baghdad in 2009, he received the B.S in computers and information technology from university of Anbar –College of computers.

From 2019 to 2021 he was preparing to M.S in Gaziantep university – electrical and electronic engineering college, he starting research in building management system and prepare article includes model for BMS system for data centre or control centre, Practical and Laboratory experiments for his thesis and acritical focused on the same subject for BMS system.



**ERGUN ERCELEBI**, received the B.S. degree in electrical and electronics engineering from M.E.T.U., Gaziantep, Turkey in 1990 and M.S. and PhD. degrees in electrical and electronics engineering from the University of Gaziantep in 1992 and 1999, respectively.

Between 2000–2005, he was Assistant Professor of Electrical and Electronics Engineering at the University of Gaziantep. He was the head of computer engineering between 2003 and 2004. He is presently a full Professor.

# Analysis of a Compact Multi-Band Textile Antenna for WBAN and WLAN Applications

Hüseyin Şerif Savcı, Hassan. Sajjad, Fatih Kaburcuk, and Sana Khan


**Abstract**—A dual-band wearable antenna is designed on a textile material. The design operates at ISM bands available for Wireless Body Area Network (WBAN) and Wireless Local Area Network (WLAN) with an input match better than -15 dB. The antenna is designed by using Computational Electromagnetic Software (CEMS) based on Finite-Difference Time-Domain (FDTD) method. A three-layer phantom model including skin, fat and muscle has been considered to compute the specific absorption rate (SAR). The maximum value of SAR averaged over 1g and 10g of tissue is less than 1.6 W/Kg and 2 W/Kg, respectively, when the maximum incident power of the antenna is 63 mW. These values are in compliance with the international electromagnetic safety standards.

**Index Terms**— Antennas on textile, multi-band antennas, Specific Absorption Rate (SAR), wearable antennas, wireless Body Area Network (WBAN), 802.15.6, 802.11n.


## I. INTRODUCTION

THE ADVANCEMENT of wireless networks and Complementary Metal Oxide Semiconductor (CMOS) low power integrated circuit technology introduced the usage of wireless sensor nodes in many applications ranging from comfort enhancing consumer products to therapeutic medical devices.


**HÜSEYİN ŞERİF SAVCI** is with Department of Electrical and Electronic Engineering of Istanbul Medipol University, Istanbul, Turkey, (e-mail: hsavci@medipol.edu.tr).

 <https://orcid.org/0000-0002-5881-1557>


**HASSAN SAJJAD** is with Department of Electrical and Electronic Engineering of Istanbul Medipol University, Istanbul, Turkey, (e-mail: hsajjad@st.medipol.edu.tr).

 <https://orcid.org/0000-0002-2306-6008>

**FATİH KABURCUK** is with Department of Electrical and Electronic Engineering of Sivas Cumhuriyet University, Sivas, Turkey, (e-mail: fkaburcuk@cumhuriyet.edu.tr).

 <https://orcid.org/0000-0002-7527-3850>

**SANA KHAN** is with Department of Electrical and Electronic Engineering of Istanbul Medipol University, Istanbul, Turkey, (e-mail: skhan@st.medipol.edu.tr).

 <https://orcid.org/0000-0001-5349-5930>

Manuscript received December 29, 2020; accepted May 25, 2021.

DOI: [10.17694/bajece.849699](https://doi.org/10.17694/bajece.849699)

In the last two decades, several standards have been developed for such use. Wireless Personal Area Network (WPAN), Medical Implant Communication Service (MICS) and WBAN are examples of these standards. Some outdoor applications also utilize 802.11n bands.

The allocation of 402-405MHz band for MICS for the use of devices in diagnostic and therapeutic purposes enabled numerous application opportunities [1]. Many implantable, in-vitro and body worn medical devices from cardiac defibrillators to wireless capsule endoscopic devices which utilizes this band are being developed [2]. The communication shift from inductive coupling to wireless telemetry put more emphasis on the antennas used in such systems. Many different varieties of antennas have been developed for such applications. The remote-control units utilized helical or dipole antennas whereas planar antennas such as meandered inverted-F type is preferred for body implants [3], [4].

Although the MICS frequencies were close to optimum in terms of balancing the size of antennas and losses due to human tissue and flesh, the applications suffered from the low data rates. The allocation of only 300 kHz bandwidth allowed the maximum achievable data rate up to around 450 kbit/s for the MICS applications [4]. This greatly reduce use cases as many modern wireless links involve the fusion of many sensor nodes requiring much higher data rates and smaller device sizes. In 2012, Federal Communications Commission (FCC) allocated 40 MHz of spectrum at 2360-2400 MHz band to Medical Body Area Network (MBAN) as a secondary basis user of the band for short range indoor low power wireless links. The short range is defined as wireless communications in the vicinity of, or inside, a human body. IEEE 802.15.6 communication standard is established for these MBAN devices which can operate with data rates up to 10 Mbps. The standard also considers effects on portable antennas due to human presence. It covers radiation pattern shaping to minimize SAR into the body [5].

With the standardization of WBAN, many wearable medical and consumer products have been released to market. Although the sensors and electronics differ depending on the applications, these devices all utilize some sort of antennas for wireless communications. Many different topologies, materials and forms are investigated to be used as antennas. In addition to wireless medical applications [6], the wearables found applications in many areas such as mobile communications [7] and military [8]. Printing the antenna on textile materials, which is mostly jeans, has become a preferred method for most of the wearable electronics. These antennas must be flexible, low cost, lightweight, and easy to implement on clothes. The antennas are usually placed in proximity of human body which is the

antenna's reactive near-field region namely Rayleigh region. The performance of the antennas is significantly affected by the presence of the human tissues due to their lossy behavior.

In addition to the degradation of antenna performance, prior studies [9] show that electromagnetic radiations from the antennas may produce a detrimental effect on the human body. As defined in the 802.15.6 standard, the power rating of WBAN device antenna is limited to keep the SAR below a certain level. However, as more wearable applications with complex features are introduced to our daily life, some features require WLAN connection in addition to WBAN operations. Therefore, it is important to consider the rate of electromagnetic energy absorbed by the human tissues at both bands and keep the SAR below the internationally accepted levels.

In this paper, a dual-band wearable microstrip antenna on textile which is operating in both WBAN and WLAN bands is designed, fabricated, and measured. Although a separate piece of jeans fabric material and copper woven conductive fabric are used to build the prototype, it can be printed/painted by using conductive paints on a t-shirt made of jeans fabric, as shown in Fig. 1. The antenna design is carried out by using Computational Electromagnetic Software (CEMS) [10] based on the finite-difference time-domain (FDTD) method [11]. The antenna operates in the WBAN and WLAN ISM bands (2.45 GHz and 5.7 GHz). A three-layer phantom consisting of skin, fat, and muscle is used to imitate the human model. The effects of phantom on the radiation patterns and input reflection coefficient of the antenna are investigated. The SAR distributions over 1g ( $SAR_{1g}$ ) and 10g ( $SAR_{10g}$ ) of tissues on the model are computed at 2.45 GHz and 5.7 GHz using ANSYS HFSS [12] with an incident power of 63mW. Numerical results show that the performance of the antenna is affected by the presence of the phantom and maximum  $SAR_{1g}$  and  $SAR_{10g}$  values for the tissues are less than the internationally accepted standards of 1.6 W/kg set by FCC in the United States [13] and 2 W/kg set by CENELEC in the EU [14], respectively.

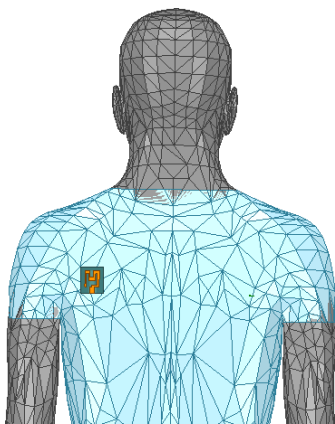


Fig.1. Antenna printed on the back of dress shirt worn by a human.

## II. ANTENNA DESIGN AND PERFORMANCE

The top and bottom views of the proposed antenna along with its dimensions in mm are shown in Fig. 2. The wearable microstrip antenna is backed by a partial ground on the bottom of the substrate with a slot. The design is compact with an area of 40mm x 35mm. The antenna is designed on a 2 mm thick jeans substrate of dielectric constant 1.54 with negligible loss. It operates in the industrial, scientific, and medical (ISM) band at 2.45 GHz and 5.7 GHz. The input reflection coefficient ( $S_{11}$ ) of the antenna is below -15 dB as seen from Fig. 3. Here, the dashed curve shows the simulated performance with phantom where there is 15mm separation between antenna and phantom. The radiation pattern and gain plots of the antenna are shown in Fig. 4.A-C which are similar to that of a monopole antenna, except that it is transformed due to the partial ground plane and the slot.

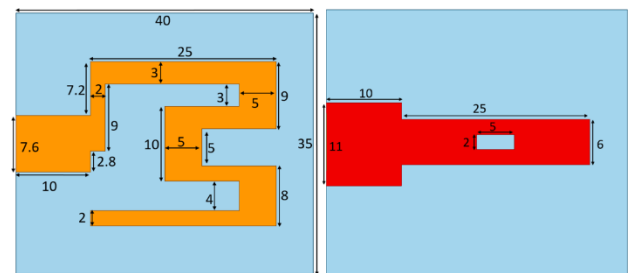


Fig.2. Proposed wearable microstrip antenna, all dimensions in mm. (left) Top view of the antenna, (right) bottom view with a slotted partial ground.

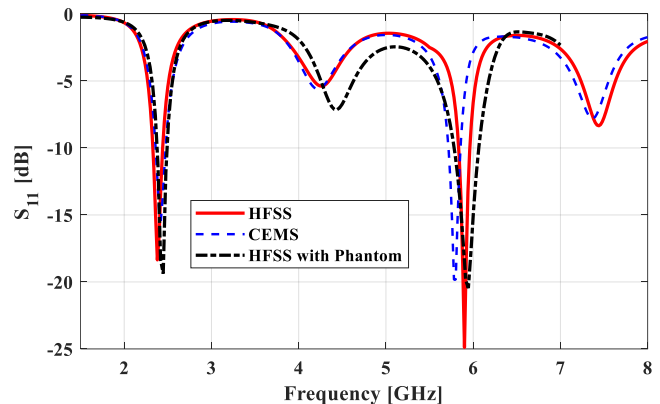


Fig.3. Simulated  $S_{11}$  of the antenna.

## III. PROPOSED ANTENNA WITH PHANTOM

After the satisfactory performance of the antenna, it was placed in the proximity of a phantom, as shown in Fig. 4. The phantom shown in Fig. 5 consists of a three-layered tissue, namely, skin, fat, and muscle. The electrical properties of the tissues, at the two resonant frequencies, are provided in Table 1. In the table,  $\epsilon_r$  and  $\sigma$  represent the relative permittivity and the electrical conductivity of the tissues, respectively.

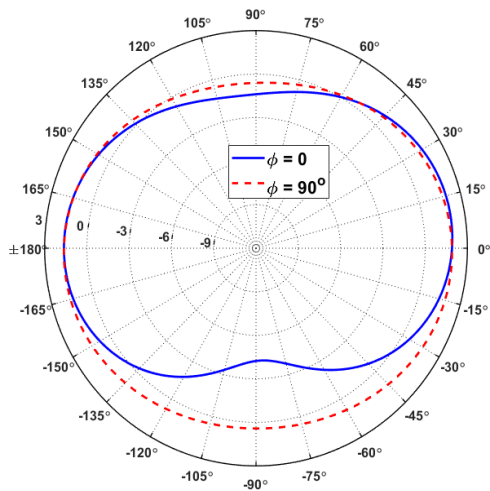


Fig.4.A. Radiation pattern of the antenna.

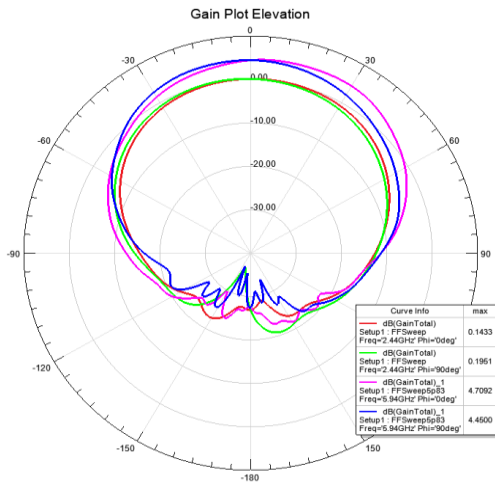


Fig.4.B. Gain plot vs. elevation angles.

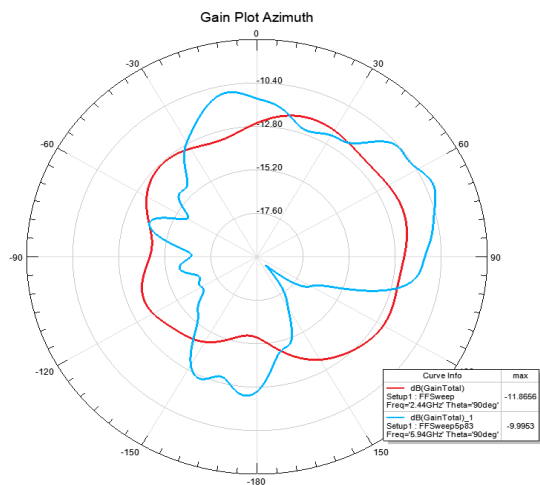


Fig.4.C. Gain plot vs. azimuth angles.

TABLE I  
ELECTRICAL PROPERTIES OF TISSUES AT  
THE TWO RESONANT FREQUENCIES [14].

Tissue	Thickness (mm)	2.45 GHz		5.7 GHz	
		$\epsilon_r$	$\sigma$ (S/m)	$\epsilon_r$	$\sigma$ (S/m)
Skin	5	38	1.46	35.2	3.63
Fat	7	5.3	0.11	9.88	0.81
Muscle	30	52.7	1.77	48.6	4.84

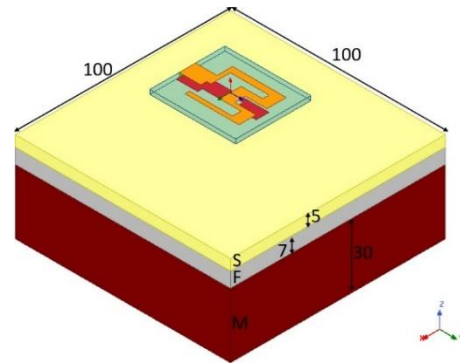


Fig.5. Proposed antenna placed on a three-layered phantom consisting of skin (S), fat (F) and muscle (M) tissue. Dimensions are in mm.

The mass densities of skin, fat, and muscle are assigned as  $1020 \text{ kg/m}^3$ ,  $909.4 \text{ kg/m}^3$ , and  $1060 \text{ kg/m}^3$ , respectively. The volume of the phantom was  $(100 \times 100 \times 42) \text{ mm}^3$ . The antenna was placed 15 mm above the phantom in order to compute the  $\text{SAR}_{1g}$  and  $\text{SAR}_{10g}$  distribution over the phantom. The input reflection coefficient of the antenna was not drastically affected by the phantom. It was noticed that the resonance at 7 GHz was further enhanced. The manufactured prototype is shown in Fig. 6.A. Figure 6.B shows the simulated  $S_{11}$  of antenna with and without phantom. The measured  $S_{11}$  of the antenna being placed at three different locations, chest, back, and shoulder are shown in Fig. 6.C. The  $\text{SAR}_{1g}$  and  $\text{SAR}_{10g}$  distributions are calculated for two different frequencies. Since the tissues are dispersive, their electromagnetic properties change with frequency [15]. Therefore, we must use the electrical properties of the tissues at the specific frequency as given in Table 1.

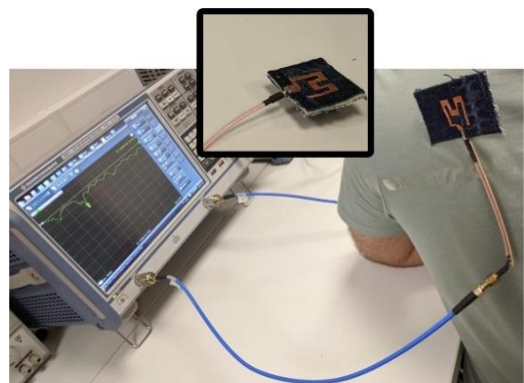


Fig.6. A. Measurement of the proposed antenna.

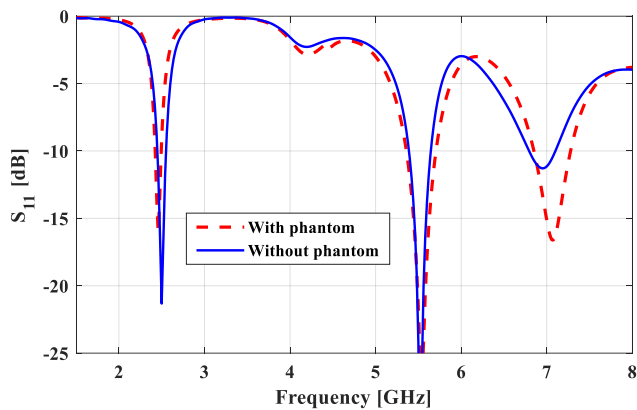


Fig.6. B. Simulated  $S_{11}$  of the antenna with and without the phantom.

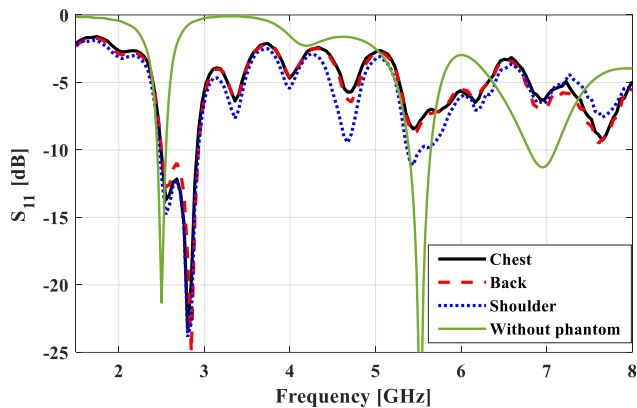


Fig.6. C. Measured  $S_{11}$  of the antenna placed on different body parts.

The obtained  $SAR_{1g}$  and  $SAR_{10g}$  distributions on the phantom due to the proposed antenna are shown at each frequency of interest in Fig. 7 and 8, respectively. The simulation was performed using ANSYS HFSS with an incident power of the antenna set to 63 mW. It can be realized that the maximum  $SAR_{1g}$  and  $SAR_{10g}$  values are less than 1.6 W/kg and 2 W/Kg, respectively.

Figure 9 shows the radiation pattern of the proposed antenna when it is placed above the phantom. The phantom behaves as a reflector which results in the pattern being directive, unlike the one shown in Fig. 3.

The gain has increased from 2 dB to 6.5 dB. The directivity allows more efficient communication with less power. Similar pattern is observed at 5.7 GHz. Comparison of the results for the proposed antenna with previously published results are presented in Table 2. An ideal antenna for a WBAN device should have maximum gain with minimum dimensions and it should have minimal SAR.

Based on these performance criteria, a Figure of Merit (FOM) which is given in Eq. (1) is defined to compare our antenna with prior work. The performance numbers are shown in Table 2.

$$FOM = \frac{Gain (linear)}{1000(SAR_{1g} \times DIM)} \quad (1)$$

Here,  $Gain$  is the linear gain of the antenna and  $DIM$  is the area of the antenna normalized with respect to  $\lambda_0^2$  at 2.45 GHz. The larger the FOM value is, the more suitable the antenna would be for the intended applications. As shown in the last column of Table II, the proposed antenna in this work has the best performance for such wearable WBAN applications when compared with prior work. Only simulation results are compared.

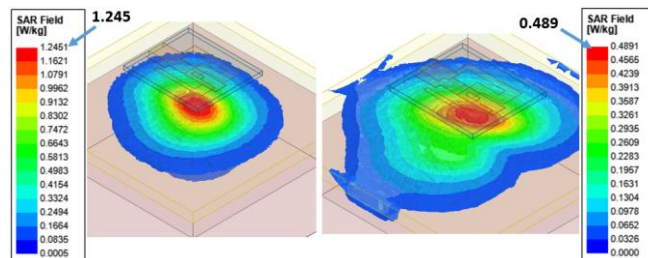


Fig.7.  $SAR_{1g}$  distribution in the phantom at (left) 2.45 and (right) 5.7 GHz.

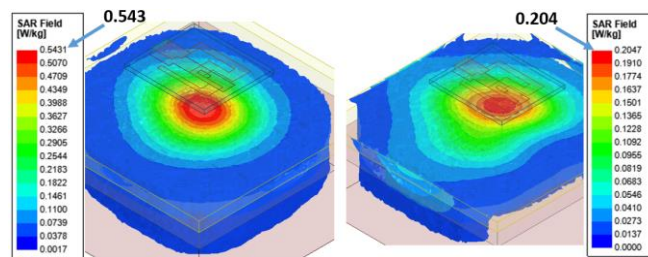


Fig.8.  $SAR_{10g}$  distributions in the phantom at (left) 2.45 and (right) 5.7 GHz.

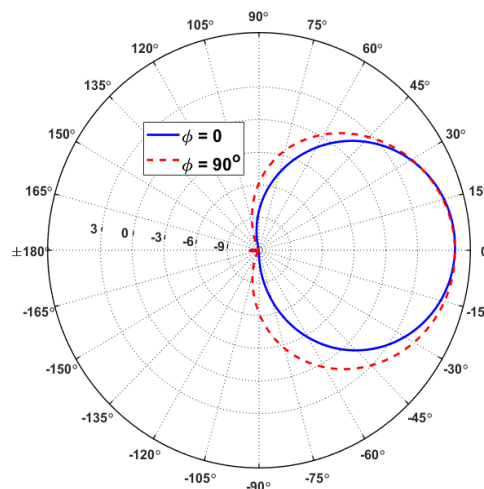


Fig.9. Radiation pattern of the antenna in the presence of the phantom.



TABLE II  
COMPARISON OF THE PROPOSED WORK WITH PRIOR  
ART AT 2.45 GHZ.

Ref.	Dimensions/ $\lambda_0^2$	Gain (dBi)	SAR <sub>1g</sub> (W/Kg)	SAR <sub>10g</sub> (W/Kg)	FOM
[16]	0.43×0.43	6.8	8.7	NA	378
[17]	0.37×0.30	5.0	32.5	133	2.8
[18]	0.50×0.46	6.8	53.6	11.2	53
[19]	0.50×0.30	6.2	16.8	NA	63
This Work	0.32×0.29	6.5	1.25	0.54	2917

#### IV. CONCLUSION

An M-shaped dual band wearable antenna on a textile material has been designed at 2.45 GHz and 5.7 GHz for wireless medical body area network and ISM applications. The performance of the wearable antenna is evaluated in the presence of human phantom which is a three-layered model reflecting the electrical properties of a human body. The antenna is built on a textile material and measured by attaching on different locations of a dressed t-shirt on a human torso. Besides verifying electrical performance of the proposed antenna, the specific absorption rate due to the proximity of the antenna is also investigated. The computed maximum SAR<sub>1g</sub> and SAR<sub>10g</sub> values at 2.45 GHz and 5.7 GHz are less than 1.6 W/Kg and 2 W/kg, respectively, for the antenna input power of 63 mW. A figure of merit is defined considering the antenna gain, compactness, and SAR values. It can be seen from the numerical results that the proposed antenna has the best FOM and superior performance than prior art and is a suitable candidate for wearable devices operating in the WBAN and WLAN dual-bands.

#### REFERENCES

- [1] H. S. Savci, A. Sula, Z. Wang, N. S. Dogan and E. Arvas, "MICS transceivers: regulatory standards and applications," Proceedings. IEEE SoutheastCon, 2005., Ft. Lauderdale, FL, USA, pp. 179-182, 2005.
- [2] A. Basir, M. Zada, Y. Cho and H. Yoo, "A Dual-Circular-Polarized Endoscopic Antenna with Wideband Characteristics and Wireless Biotelemetric Link Characterization," in IEEE Transactions on Antennas and Propagation, vol. 68, no. 10, pp. 6953-6963, Oct. 2020.
- [3] Hassan Sajjad, W. Sethi, L. Jan, and S. Khan, "Compact dual-band implantable antenna for E-health monitoring," 2017 International Symposium on Wireless Systems and Networks (ISWSN), Lahore, Pakistan, 2017, pp. 1-4, 2017.
- [4] J. Lee, D. Seo and H. Lee, "Design of implantable antenna on the dielectric/ferrite substrate for wireless biotelemetry," 2015 International Symposium on Antennas and Propagation (ISAP), Hobart, TAS, pp. 1-3, 2015.
- [5] IEEE Standard for Local and metropolitan area networks- Part 15.6: Wireless Body Area Networks, IEEE Standard 802.15.6-2012, pp.1-271,29 Feb. 2012.
- [6] A. Sabban, "New Wideband Printed Antennas for Medical Applications," in IEEE Transactions on Antennas and Propagation, vol. 61, no. 1, pp. 84-91, Jan. 2013.
- [7] H. Rogier et al., "Novel wearable antenna systems for high data rate mobile communication in healthcare," 2014 4th International

- Conference on Wireless Mobile Communication and Healthcare-Transforming Healthcare Through Innovations in Mobile and Wireless Technologies (MOBIHEALTH), Athens, pp. 188-191, 2014.
- [8] H. Lee, J. Tak and J. Choi, "Wearable Antenna Integrated into Military Berets for Indoor/Outdoor Positioning System," in IEEE Antennas and Wireless Propagation Letters, vol. 16, pp. 1919-1922, 2017.
- [9] Lennart Hardell, Cindy Sage, "Biological effects from electromagnetic field exposure and public exposure standards," *Biomedicine & pharmacotherapy*, vol. 62, no. 2, pp. 104-109, 2008.
- [10] V. Demir and A. Z. Elsherbeni, "Computational Electromagnetics Software package," veysdemir@gmail.com, Version 3, August. 2019.
- [11] A. Z. Elsherbeni and V. Demir, "The Finite-Difference Time-Domain Method for Electromagnetics with MATLAB Simulations," second edition, ACES Series on Computational Electromagnetics and Engineering, SciTech Publishing, an Imprint of IET, Edison, NJ, 2016.
- [12] Ansys Corporation, "HFSS," 2014, Suite v15, Pittsburg (PA), USA.
- [13] Federal Communications Commission, "Evaluating compliance with FCC guidelines for human exposure to radio frequency electromagnetic fields," Rep., Washington, DC, Tech. Rep. OET Bull. 65, 1997.
- [14] IEEE C95.1. IEEE standard for safety levels with respect to human exposure to radio frequency electromagnetic fields, 3 kHz to 300 GHz, IEEE Standard C95.1-2005, 2006.
- [15] F. Kaburcuk and A. Z. Elsherbeni, "Temperature rise and SAR distribution at wide range of frequencies in a human head due to an antenna radiation," *ACES Journal*, vol. 33, no. 4, pp. 367-372, April 20.
- [16] D. Vital, S. Bhardwaj and J. L. Volakis, "Textile Based Large Area RF-Power Harvesting System for Wearable Applications," in IEEE Transactions on Antennas and Propagation, vol. 68, no. 3, pp. 2323-2331, March 2020.
- [17] A. Y. I. Ashyap, Z. Z. Abidin, S. H. Dahlan, H. A. Majid, M. R. Kamarudin and R. A. Abd-Alhameed, "Robust low-profile electromagnetic band-gap-based on textile wearable antennas for medical application," 2017 International Workshop on Antenna Technology: Small Antennas, Innovative Structures, and Applications (iWAT), Athens, pp. 158-161, 2017.
- [18] M. Abdullah and A. Khan, "Multiband wearable textile antenna for I.S.M body center communication systems," 2015 XXth IEEE International Seminar/Workshop on Direct and Inverse Problems of Electromagnetic and Acoustic Wave Theory (DIPED), pp. 90-96, 2015.
- [19] Z. H. Jiang, D. E. Brocker, P. E. Sieber and D. H. Werner, "A Compact, Low-Profile Metasurface-Enabled Antenna for Wearable Medical Body-Area Network Devices," in IEEE Transactions on Antennas and Propagation, vol. 62, no. 8, pp. 4021-4030, Aug. 2014.

#### BIOGRAPHIES



HÜSEYİN ŞERİF SAVCI was born in 1979, in Erzurum, Turkey. He received his B.Sc. in Electronics & Communication Engineering from Yıldız Technical University in 2001 and his M.Sc. and Ph.D. degrees in Electrical Engineering from Syracuse University, Syracuse, NY, USA, in 2005 and 2008, respectively. From 2008 to 2013, he was with Skyworks Solutions Inc., Cedar Rapids, IA, USA as senior RFIC design engineer. Between 2013 and 2020, he was with Hittite Microwave Corporation, Chelmsford Massachusetts and Analog Devices Inc., Istanbul Turkey as a principal design engineer where he designed many RFIC and MMIC products on SOI, GaN, and GaAs technologies for various market segments such as test and measurement, cellular infrastructure and ADEF. In 2020, he joined the Department of Electrical and Electronics Engineering at Istanbul Medipol University, Istanbul, Turkey as an Assistant Professor. His research interests include RF and Microwave Integrated Circuits, devices, systems and antennas.



**HASSAN SAJJAD** received his B.S. degree in Telecommunication Engineering from FAST-NUCES Peshawar, Pakistan in 2009 and M.S. degree in Electrical Engineering from Linnaeus University, Vaxjo, Sweden in 2012. He worked as a researcher in King Saud University, Saudi Arabia from 2012 to 2014. Currently, he is pursuing his Ph.D. in Electrical Engineering at Istanbul Medipol University, Istanbul, Turkey. His research interests include numerical electromagnetics, plane wave scattering problems, RF/Microwave devices, and antennas.



**FATİH KABURCUK** received both the Master of Science and Doctor of Philosophy degrees from Syracuse University, Syracuse, NY, USA, in 2011 and 2014, respectively, all in electrical engineering. During his graduate studies, he worked as a Research Assistant with Syracuse University and PPC-Belden Inc. in Liverpool, NY, USA. He worked as a Visiting Research Scholar at the Department of Electrical Engineering, Colorado School of Mines, Golden, CO, USA in 2014. He joined the Erzurum Technical University in 2015 and served as an Assistant Professor until 2019. Currently, Dr. Kaburcu has been serving as an Associate Professor with the Department of Electrical and Electronic Engineering, Sivas Cumhuriyet University, Turkey. His research interest includes numerical methods in electromagnetics, biological effect of electromagnetic radiation, antennas, and RF/microwave circuits.

**SANA KHAN** received the B.S. degree in engineering sciences from the Ghulam Ishaq Khan Institute (GIKI) of Engineering Sciences and Technology, Topi, Pakistan, in 2013, and the M.S. degree from Istanbul Medipol University, Istanbul, Turkey, in August 2017, where she is currently pursuing the Ph.D. degree in electrical engineering. Her research interests include computational electromagnetics, antennas, RF/MW devices, software defined radios, and optical communication.

# Design and Optimization of Directive Circular Patch Antenna with Asymmetric Pixels Using Genetic Algorithm

Sinan Doğusan

**Abstract**— In this study, a low-profile, high directive circular microstrip antenna was designed for 5.8 GHz ISM band applications. In the design, the GA / MoM approach based on the Method of Moments (MoM) integrated with the Genetic Algorithm (GA) optimization method was used. The simulations of the best first and second antennas obtained as a result of the optimization process were made using the ANSYS HFSS software program. According to the simulation results, it was determined that the input reflection coefficient of both antennas was below -10 dB in the ISM band where the antenna was operating and had maximum directivity. It was observed that the radiation characteristics of both antennas obtained with the GA / MoM approach were steady-state in the operating band. It was concluded that asymmetric pixelation used in this method can be used in the design of antennas with different geometries.

**Index Terms**—Genetic Algorithm, Method of Moments, Microstrip Patch Antenna, Optimization

## I. INTRODUCTION

RECENTLY, WITH the increase in performance levels demanded in wireless communication technology, the need for low-profile and high-performance antenna design throughout the operating band is increasing. This need has led to the emergence of new developed solution methods different from traditional design methods [1,2]. Because traditional design methods used in antenna design problems are insufficient in solving complex problems.


In line with this rapid development, numerical solution methods are used in solving complex electromagnetic problems to obtain more accurate results in a shorter time [3-5]. In addition to these methods, optimization algorithms also play an important role in solving antenna design problems. As the complexity of the antenna design problems to be solved increased, optimization algorithms (Stochastic, Deterministic, Heuristic, Mathematical) that can discover many powerful, innovative and large solution sets that can be used by integrating numerical methods have been developed to overcome these problems in a short time [6-8]. One of the most

preferred of these optimization algorithms is the Genetic Algorithm (GA) that models biological processes inspired by Darwin's theory of evolution. GA is an heuristic stochastic global optimization algorithm based on the principle of survival of the best [9]. Since GA has the property of converging to the best result, it is highly preferred in antenna design problems [10-17].

GA searches for the most suitable substructure with the radiation characteristic targeted for the design by optimizing any physical properties of an antenna to be designed. One of the most important of these is the problem of finding the best current distribution on the surface for a specified purpose. By using GA in these problems, removing some pixels from the radiating pixelized surface of the antenna during the optimization process, the best surface current distribution with the targeted radiation characteristics is obtained. In previous studies, symmetric pixel selection for such problems has been perfectly adapted to quadratic surfaces and it was observed that the radiation parameters of the antennas had as a result of optimization were quite good [18,19]. However, if surfaces with circular or non-quadratic geometry are wanted to be separated into symmetrical pixels for optimization, gaps will occur at the end regions of the surface. As a result, analysis will have to be applied in a more limited area. Due to its inclusion in a limited surface area optimization process, obtaining the antenna with the targeted radiation parameters will be difficult. To overcome this problem, the empty surface area can be filled by creating smaller symmetrical pixels. Hereby, an antenna with aimed radiation parameters can be achieved by increasing the surface area to be included in the optimization thanks to the increasing number of pixels. However, an increase in the number of pixels will also cause an increase in the size of the moment matrix. Therefore, the increase in the time spent for optimization and in memory used should be considered.

For this reason, in order to get the antenna with the targeted radiation parameters, a new pixel architecture has emerged that will create a lower-dimensional moment matrix by dividing the surface to be optimized into a minimum number of pixels and enable analysis on all geometric surfaces. So as to meet this need, the method of asymmetric pixelation was suggested for the design of antennas that have circular or non-quadratic geometries in this study. The method of shaping the radiating

SİNAN DOĞUSAN is with Department of Electrical-Electronics Engineering Inonu University, Malatya, Turkey, (e-mail: [sinandogusan@gmail.com](mailto:sinandogusan@gmail.com)).

 <https://orcid.org/0000-0002-2207-8904>

Manuscript received February 20, 2021; accepted June 13, 2021.  
DOI: [10.17694/bajece.883468](https://doi.org/10.17694/bajece.883468)

surface of the antenna to be included in the optimization into asymmetric pixels enables full surface analysis without any restrictions on the surface areas. Thanks to this method proposed, it is possible to design the antenna with the radiation parameters targeted by the designer in a shorter time using the minimum number of pixels.

In this article, a circular patch antenna with high directivity and low input reflection coefficient characteristics was designed. For this purpose, a 5.8 GHz ISM (Industrial, Scientific, and Medical) frequency band 50  $\Omega$  coaxial probe and an antenna model fed from the center [20] were discussed. To obtain the antenna with these characteristics, the GA / MoM optimization method based on the use of Genetic Algorithm (GA) integrated with Method of Moments (MoM) was used [1]. In order to apply this technique, the lengths of the main circular radiating surface were first determined. Then this radiating conductive surface was then divided into asymmetric pixels to be optimized and optimization was made for each pixel. The results achieved were shown in graphics and a table.

## II. MATERIAL AND METHODS

### A. Antenna Geometry

The proposed antenna geometry is shown in Figure 1. The antenna that designed to work in the 5.8 GHz ISM band consists of 406 asymmetrical copper parts with a radiating surface of 0.02 mm in height. The radius of the antenna was determined 5.1 cm, which is equivalent to a wavelength, and the dielectric material height was determined 1.575 mm. The length of a single pixel of the antenna surface was determined as  $\lambda/10$ . The proposed antenna was fed from the center with a 50 ohm SMA connector.

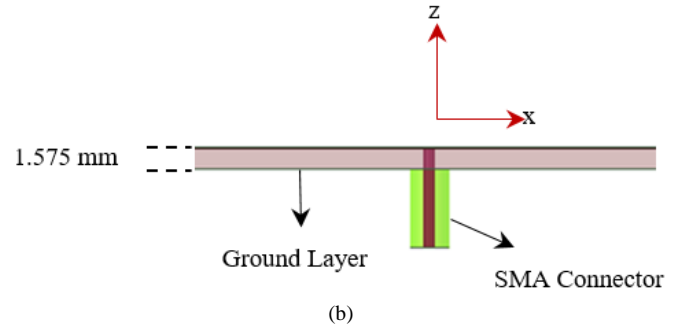
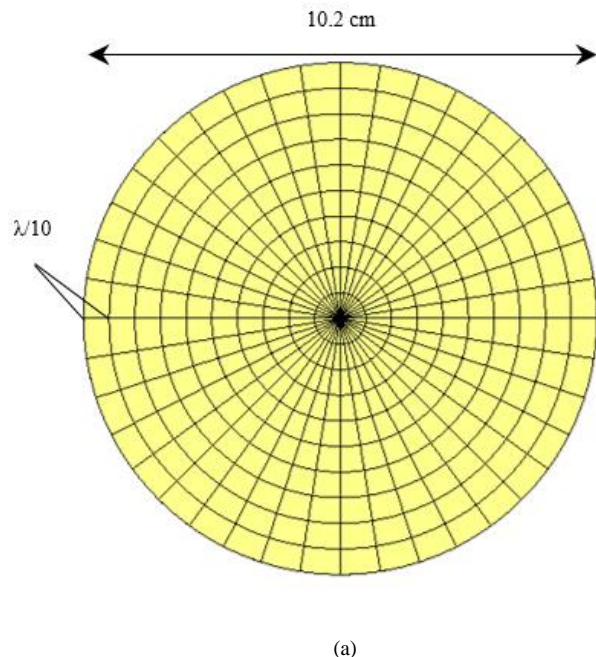


Fig.1. Antenna geometry: (a) top view of antenna that tailored asymmetric pixels (b) side view of antenna.

### B. Genetic Algorithm

In the first step of the GA process, the initial population is created and the fitness value of each individual in the population is calculated. Then, individuals selected from the population according to the fitness value are crossed and the two parents create a new individual from the individual's genetic codes. The search space is expanded by making random changes in the individual's genes with the mutation in the next step. The rate at which genes are selected for the mutation process is determined by the mutation rate. In the last stage of evolution, the fitness value of the newly created individual is calculated. The fitness of the individual is calculated with the fitness function created according to the determined goal. If the algorithm's maximum iteration count or certain fitness values deemed sufficient for the algorithm are reached, the process ends. Otherwise, the algorithm is restarted depending on the properties of the problem [9].

There are a total of 406 pixels in the structure on the main radiating surface of the antenna (Figure 1a). In the GA we applied, 100 iterations were run for 320 individuals in each generation. The mutation rate in the algorithm was determined as 0.5%. The elitism operator, which ensures that the best chromosomes were not lost during the crossing and mutation stages, was also included in the application. The elitism rate was determined as 1%. The GA has searched automatically for the most suitable structure as it progressed. In this study, we aimed to design both have low input reflection coefficient and high directive antenna.

For this purpose;

$$fitness = max \left( \left[ \frac{1}{(VSWR - 1)^{m_1}} \right] (D_{max})^{m_2} \right) \quad (1)$$

$$m_1 = \begin{cases} 0.02, & VSWR \leq 2 \\ 0.4, & VSWR > 2 \end{cases} \quad (2)$$

$$m_2 = 0.4$$

the above fitness function was created where  $D_{max}$  represents the maximum directivity and  $VSWR$  represents voltage standing wave ratio. The weight values  $m_1$  and  $m_2$  are very important for the fitness function. These weight values ensured that the VSWR and maximum directivity variables used in the

fitness function were close to each other. As a result, the Genetic Algorithm searched for an antenna with both directivity and low input reflection coefficient properties at the same time.

Maximum directivity:

$$D_{max} = \frac{4\pi U_{max}}{P_{rad}} \quad (3)$$

expressed in the form. Here,  $U_{max}$  represents the max. radiant intensity and  $P_{rad}$  represents the total radiated power [5]. VSWR's formula [5] is as follows:

$$VSWR = \frac{1 + |\Gamma|}{1 - |\Gamma|} \quad (4)$$

### C. Method of Moments

So as to calculate the scattered fields from the antenna surface, the surface current densities induced at the antenna surface must be known. The surface current density  $\vec{j}(\vec{r})$  is obtained by solving the electric field integral equation (EFIE) created by applying Perfect Electric Conductor (PEC) boundary conditions to conductive surface. The most frequently used basis functions in EFIE's solution with the method of moments are Rao-Wilton-Glisson (RWG) basis functions [22]. Because RWG functions can easily model randomly generated geometric structures with triangles. Due to this feature, full surface analysis of structures with different geometric shapes can be performed by using RWG basis functions. Expressing the surface current density with RWG basis functions using the Galerkin Method [23] is defined as follows:

$$\vec{j}(\vec{r}) \cong \sum_{n=1}^N I_n \vec{f}_n(\vec{r}) \quad (5)$$

Since the current distributing on the antenna surface is vectorial, the RWG function  $\vec{f}_n$  is also a vector function. In Galerkin Method, test and basis functions are chosen equally. In this way, since the reciprocity theorem will be provided, high accuracy results are be obtained. One of the most suitable methods that can be used to solve EFIE is Moments Method (MoM) [24]. The method of moments is based on transforming the problem into a matrix equation and solving the resulting matrix equation. The generalized problem;

$$L\{f(x)\} = g(x) \quad (6)$$

where  $L$  is a linear operator,  $g(x)$  is a known feed function and  $f(x)$  is the unknown function representing the current distribution. Using the Method of Moments and Galerkin Test Method, this equation;

$$[V_m] = [Z_{mn}][I_n] \quad (7)$$

turns into the matrix equation where  $[Z_{mn}]$  is the impedance matrix,  $[I_n]$  is the unknown coefficients vector and  $[V_m]$  is the voltage vector to become.

The most computational step in the simulation of an antenna is the step that involves filling the moment matrix. On the other hand, even a small change in antenna geometry requires full or partial recalculation of the moment matrix. Refilled to the moment matrix each time greatly limits the optimization algorithms to work efficiently in solving the problem. In order to overcome this problem, Direct Matrix Manipulation (DMM) technique, which enables GA optimization to work more efficiently was applied [1]. The DMM method prevents the Z-matrix from being refilled after each evaluation of the fitness function. Thanks to this method, the optimization time is shortened considerably.

## III. RESULTS AND DISCUSSIONS

In the design, firstly, the antenna geometry was created using the software program. In this step, the main geometry of the antenna was drawn and the parts to be included in the optimization were defined. Then, the Z-matrix is calculated. The Z-matrix was calculated taking into account all the metal parts involved in the optimization process on the radiating surface of the antenna. Each metal part was represented by a bit (1 or 0) on the chromosome. While "1" means the presence of metal, setting a bit to "0" means that the electric current on that part was zero. This means that the rows and columns of the Z matrix containing the extracted part were be filled with zeros [1].

Optimization of the antenna was carried out in the MATLAB [25] program and took approximately 50 hours. As a result of optimization process, the best first antenna (BA-1) (Figure 2a), the second best antenna (BA-2) (Figure 2b), the third best antenna (BA-3) (Figure 2c) and (BA-4) (Figure 2d) MATLAB structures of the fourth best antenna were achieved as in Figure 2. The "yellow" color represents the metal regions and the "green" color represents the empty space. Although their shapes were not very different from each other, there were clear differences in the radiation parameters of these antennas.

In this study, the simulations of only the first two antennas with the best fitness value were done using the ANSYS HFSS software program. In addition to these two antennas, an antenna with the same geometric structure but not optimized was simulated and the terminal results (input reflection coefficient, VSWR, group delay) were compared with each other.



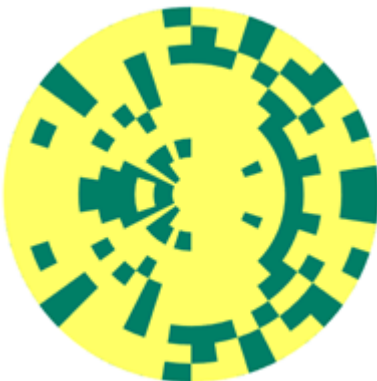
(a)



(b)



(c)



(d)

Fig.2. MATLAB Optimization results (a) the best first antenna (BA-1) (b) the best second antenna (BA-2) (c) the best third antenna (BA-3) (d) the best fourth antenna (BA-4).

#### A. Surface Current Distribution

The surface current distributions at 5.8 GHz at the center frequency of the ISM band where the best first antenna (BA-1) and the best second antenna (BA-2) achieved in consequence of the optimization work are shown in Figure 3. In the optimization process, it was aimed to find the best current distribution on the surface according to the specified purpose. As can be seen in Figure 3, while the current on BA-1 was nearly homogeneously distributed on the surface (Figure 3a), on the BA-2 the current was more concentrated in a certain area (Figure 3b).

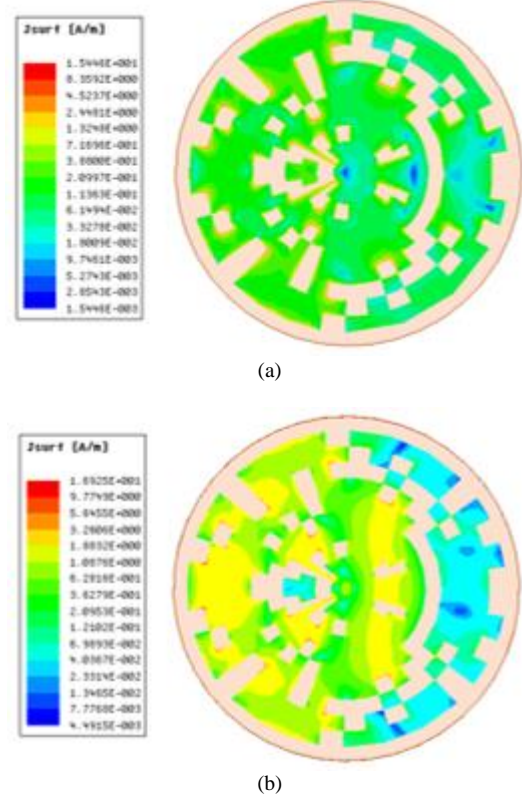


Fig.3. Surface current distribution of antennas: (a) BA-1 (b) BA-2

#### B. The Input Reflection Coefficient, Voltage Standing Wave Ratio, and Group Delay

In Figure 4, the input reflection coefficient of the antenna with the same surface geometry but not optimized (Non-Opt) was compared in addition to the BA-1 and BA-2 antennas. As can be seen, while the Non-Opt antenna did not resonate in the working band, the BA-1's values of  $|S_{11}|$  was -14.68 dB at 5.8 GHz and a 120 MHz bandwidth. The BA-2's values of  $|S_{11}|$  was -13.29 dB at 5.8 GHz and a 130 MHz. bandwidth. It was determined that the minimum  $|S_{11}|$  value was between 5.75 GHz and 5.8 GHz for both antennas. To get lower input reflection coefficient values of BA-1 and BA-2 antennas at 5.8

GHz, the height of the radiating surface, pixel dimensions, and the position of the feeding point can be changed.

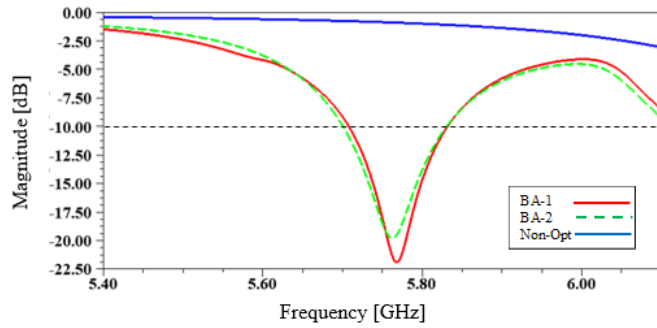


Fig.4. The input reflection coefficient magnitude

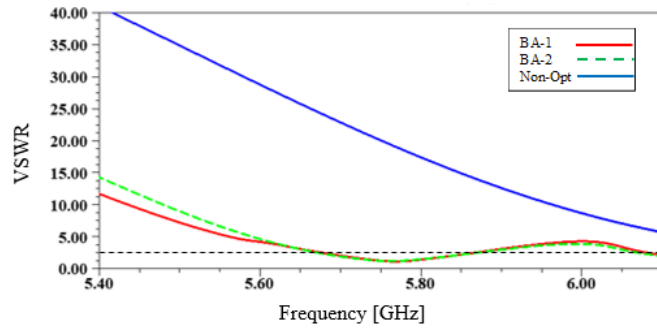


Fig.5. VSWR

The voltage standing wave ratio (VSWR) simulation results for BA-1, BA-2, and Non-Opt antennas are given in Figure 5. In the operation band, the VSWR values of BA-1 and BA-2 antennas were quite well below the targeted value of 2. The VSWR value of the Non-Opt antenna was much higher than 2.

The group delay of proposed antennas designs is given Figure 6. The group delay values of BA-1 and BA-2 antennas in the working band were below 1 ns, which is considered necessary for good communication.

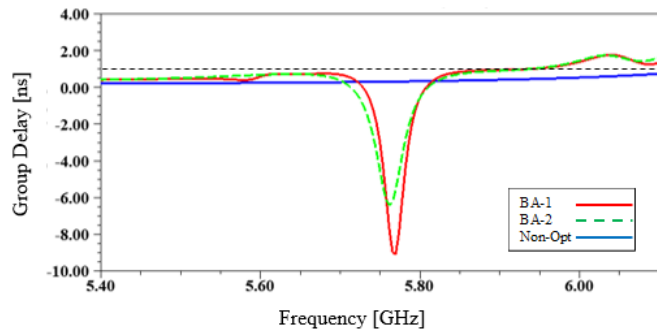


Fig.6. Group Delay

**C. Radiation Efficiency, Directivity, Gain, Aperture Efficiency**

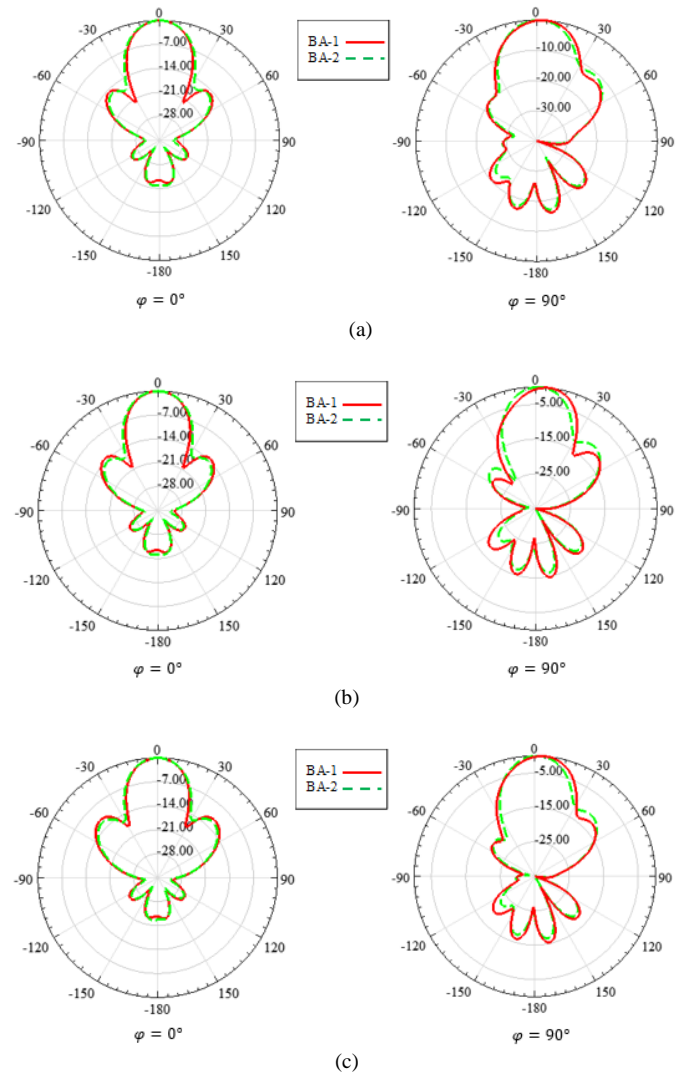
Resistive losses caused by electric materials and non-perfect metal occur in each antenna. Because of these losses, there is a difference between the input power of the antenna and the power radiated from this antenna. The radiation efficiency of an

antenna is defined as the ratio of the antenna's output power to its input power [27].

$$\eta_{re} = \frac{P_{out}}{P_{in}} \tag{8}$$

The radiation efficiency values of the proposed antennas are given in Table I. Accordingly, the radiation efficiency was over 97% for BA-1 antenna and was over 95% for BA-2 antenna.

The main fundamental of a directive antenna is the ability to focus power in one given direction and not radiate it in other directions [27]. The normalized directivity patterns for four different frequencies (5.725, 5.75, 5.8, 5.825 GHz) in the 5.8 GHz ISM band in the E-plane and H-plane of the antennas designed for this purpose are given in Figure 7. As shown in Figure 7, BA-1 and BA-2 antennas had directive characteristics in the E-plane and H-plane for these frequencies in the working band. Although there were some differences in the directivity patterns of these two antennas, it was generally seen that the radiation characteristics of the two antennas were close to each other.



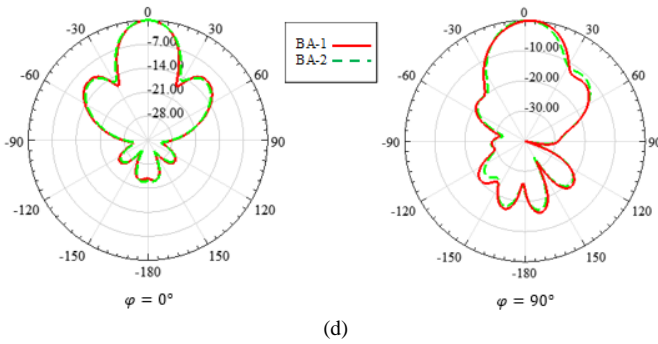


Fig.7. Normalized directivity patterns in E-plane and H-plane of optimized antennas BA-1 and BA-2 (a) 5.725 GHz (b) 5.75 GHz (c) 5.8 GHz (d) 5.825 GHz

The maximum directivity of the proposed BA-1 antenna in the working band was 15.20 dB at 5.725 GHz and the maximum directivity for the BA-2 antenna was 15.17 dB at 5.75 GHz. The maximum directivity values for all frequencies are given in Table I.

The directivity of the antenna is only a function of the shape of the antenna's propagation pattern and is not affected by resistive losses in the antenna. Due to a radiation efficiency less

than unity an antenna cannot radiate all of its input power, the antenna gain is defined as the product of maximum directivity and radiation efficiency [27]:

$$G_{max} = \eta_{re} D_{max} \quad (9)$$

The maximum gain of the proposed antennas BA-1 and BA-2 was obtained above 14.5 dB and close to 15 dB in the ISM band. The maximum gain values for all frequencies are given in Table I.

In practice, there are many reasons why the directivity of an antenna may not be at its maximum possible value. Non-ideal amplitude and phase characteristics of the aperture field can be given as examples of reasons that reduce the directivity of aperture blockage [27]. The aperture efficiency indicates how much a surface of an antenna effectively radiates, and an aperture efficiency is defined as the ratio of the actual directionality of an antenna to its maximum directivity that cannot be greater than 1.

$$\eta_{ap} = \frac{D}{D_{max}} \quad (10)$$

TABLE I  
SIMULATION RESULTS

No	$f$ [GHz]	$S_{11}$ [dB]	VSWR	SLL [dB]	$G_{max}$ [dBi]	$D_{max}$ [dBi]	Rad Eff. [%]	$\epsilon_{ap}$ [%]	HPBW [°]	Gd [ns]	BW [MHz]
BA-1	5.725	-12.38	1.63	-14.68	15.10	15.20	97.62	81.96	26.54	0.16	120
	5.75	-18.01	1.29	-13.36	14.95	15.05	97.64	79.18	26.03	-3.08	
	5.8	-14.68	1.45	-11.30	14.73	14.83	97.74	75.40	25.37	-0.57	
	5.825	-10.73	1.82	-10.55	14.67	14.77	97.75	74.34	25.11	0.57	
BA-2	5.725	-13.50	1.54	-15.57	14.95	15.15	95.43	79.28	27.95	-0.65	130
	5.75	-18.48	1.27	-14.46	14.97	15.17	95.52	79.63	27.43	-4.55	
	5.8	-13.79	1.51	-12.17	14.89	15.09	95.52	78.16	26.40	-0.57	
	5.825	-10.53	1.85	-11.07	14.78	14.98	95.41	76.14	25.89	0.41	

High aperture efficiency was achieved for both proposed antennas. The maximum aperture efficiencies of the proposed BA-1 and BA-2 antennas were obtained at 5.725 GHz with 81.96% and 79.63% at 5.75 GHz, respectively. The aperture efficiency values for all frequencies are given in Table I.

#### IV. CONCLUSION

In this article, two optimal antennas were designed using GA / MoM approach in the 5.8 GHz ISM band. The simulation results of the best first and best second antennas were compared with each other. The gains of both antennas were higher than 14.7 dB at 5.8 GHz center frequency. The input reflection coefficient and side lobe level (SLL) values were below -10 dB for both antennas.

In this study, it was shown that antenna designs with different geometries and aimed properties can be made with the

asymmetric pixelation approach that was introduced for the first time. It was emphasized that by choosing a pixel length very short, the antenna surface can be examined in more detail. However, in this case, it should be noted that the dimensions of the Z matrix will increase and this will result in an increase in optimization time.

#### REFERENCES

- [1] J. M. Johnson and Y. Rahmat-Samii, "Genetic algorithms and method of moments (GA/MOM) for the design of integrated antennas," in IEEE Transactions on Antennas and Propagation, vol. 47, no. 10, pp. 1606-1614, Oct. 1999, doi: 10.1109/8.805906.
- [2] N. Jin and Y. Rahmat-Samii, "Parallel particle swarm optimization and finite-difference time-domain (PSO/FDTD) algorithm for multiband and wide-band patch antenna designs," in IEEE Transactions on Antennas and Propagation, vol. 53, no. 11, pp. 3459-3468, Nov. 2005, doi: 10.1109/TAP.2005.858842.



- [3] K. Kunz and R. Luebbers, The Finite Difference Time Domain Method for Electromagnetics. CRC Press, 1993. J.G. Van Bladel, *Electromagnetic Fields*, John Wiley & Sons, 2007, p.1176.
- [4] J. L. Volakis, A. Chatterjee, and L. C. Kempel, Finite Element Method for Electromagnetics. IEEE Press, 1998.
- [5] C. A. Balanis, Advanced Engineering Electromagnetics. John Wiley and Sons, 1989.
- [6] N. Jin and Y. Rahmat-Samii, "Advances in Particle Swarm Optimization for Antenna Designs: Real-Number, Binary, Single-Objective and Multiobjective Implementations," in IEEE Transactions on Antennas and Propagation, vol. 55, no. 3, pp. 556-567, March 2007, doi: 10.1109/TAP.2007.891552.
- [7] O. Quevedo-Teruel and E. Rajo-Iglesias, "Ant Colony Optimization in Thinned Array Synthesis With Minimum Sidelobe Level," in IEEE Antennas and Wireless Propagation Letters, vol. 5, pp. 349-352, 2006, doi: 10.1109/LAWP.2006.880693.
- [8] W. Wang, S. Gong, X. Wang, Y. Guan and W. Jiang, "Differential Evolution Algorithm and Method of Moments for the Design of Low-RCS Antenna," in IEEE Antennas and Wireless Propagation Letters, vol. 9, pp. 295-298, 2010, doi: 10.1109/LAWP.2010.2047837.
- [9] Haupt, R. L. & Werner, D. H. Genetic Algorithms in Electromagnetics (Wiley, Boca Raton, 2007).
- [10] Bilotti, F., Castellana, F. and Vegni, L. (2002), Multi-frequency patch antenna design via the method of moment and genetic algorithm. *Microw. Opt. Technol. Lett.*, 35: 184-186. <https://doi.org/10.1002/mop.10551>
- [11] J. Leonardo Araque Quijano and G. Vecchi, "Optimization of an Innovative Type of Compact Frequency-Reconfigurable Antenna," in IEEE Transactions on Antennas and Propagation, vol. 57, no. 1, pp. 9-18, Jan. 2009, doi: 10.1109/TAP.2008.2009649.
- [12] Rengarajan, S.R. (2013), Genetic algorithm optimization of a planar slot array using full wave method-of-moments analysis. *Int J RF and Microwave Comp Aid Eng.* 23: 430-436. <https://doi.org/10.1002/mmce.20730>
- [13] S. Song and R. D. Murch, "An Efficient Approach for Optimizing Frequency Reconfigurable Pixel Antennas Using Genetic Algorithms," in IEEE Transactions on Antennas and Propagation, vol. 62, no. 2, pp. 609-620, Feb. 2014, doi: 10.1109/TAP.2013.2293509.
- [14] Khuntia, B., Pattnaik, S.S., Panda, D.C., Neog, D.K., Devi, S. and Dutta, M. (2005), Genetic algorithm with artificial neural networks as its fitness function to design rectangular microstrip antenna on thick substrate. *Microw. Opt. Technol. Lett.*, 44: 144-146. <https://doi.org/10.1002/mop.20570>
- [15] A. H. Hussein, H. H. Abdullah, A. M. Salem, S. Khamis and M. Nasr, "Optimum Design of Linear Antenna Arrays Using a Hybrid MoM/GA Algorithm," in IEEE Antennas and Wireless Propagation Letters, vol. 10, pp. 1232-1235, 2011, doi: 10.1109/LAWP.2011.2174189.
- [16] S. Chakravarty, R. Mitra and N. R. Williams, "Application of a microgenetic algorithm (MGA) to the design of broadband microwave absorbers using multiple frequency selective surface screens buried in dielectrics," in IEEE Transactions on Antennas and Propagation, vol. 50, no. 3, pp. 284-296, March 2002, doi: 10.1109/8.999618.
- [17] L. Alatan, M. I. Aksun, K. Leblebicioglu and M. T. Birand, "Use of computationally efficient method of moments in the optimization of printed antennas," in IEEE Transactions on Antennas and Propagation, vol. 47, no. 4, pp. 725-732, April 1999, doi: 10.1109/8.768813.
- [18] Zucchi, M., Giordanengo, G., Righero, M. et al. First demonstration of machine-designed ultra-flat, low-cost directive antenna. *Sci Rep* 10, 10506 (2020). <https://doi.org/10.1038/s41598-020-67354-2>
- [19] B. Karaosmanoğlu, S. Güler, H. İbili and Ö. Ergül, "Inkjet-printed pixel antennas with hexagonal cells," 2017 11th European Conference on Antennas and Propagation (EUCAP), Paris, 2017, pp. 2013-2016, doi: 10.23919/EuCAP.2017.7928488.
- [20] "IEEE Standard for Definitions of Terms for Antennas," in IEEE Std 145-2013 (Revision of IEEE Std 145-1993), vol., no., pp.1-50, 6 March 2014, doi: 10.1109/IEEESTD.2014.6758443.
- [21] S. Rao, D. Wilton and A. Glisson, "Electromagnetic scattering by surfaces of arbitrary shape," in IEEE Transactions on Antennas and Propagation, vol. 30, no. 3, pp. 409-418, May 1982, doi: 10.1109/TAP.1982.1142818.
- [22] D. Schaubert, D. Wilton and A. Glisson, "A tetrahedral modeling method for electromagnetic scattering by arbitrarily shaped inhomogeneous dielectric bodies," in IEEE Transactions on Antennas and Propagation, vol. 32, no. 1, pp. 77-85, January 1984, doi: 10.1109/TAP.1984.1143193.
- [23] A. F. Peterson, D. R. Wilton and R. E. Jorgenson, "Variational nature of Galerkin and non-Galerkin moment method solutions," in IEEE Transactions on Antennas and Propagation, vol. 44, no. 4, pp. 500-503, April 1996, doi: 10.1109/8.489301.
- [24] Gibson, W. C. The Method of Moments in Electromagnetics (Chapman & Hall/CRC, Boca Raton, 2008).
- [25] <https://www.mathworks.com/products/matlab.html>
- [26] <https://www.ansys.com/products/electronics/ansys-hfss>
- [27] Pozar, D.M. (2011) Microwave Engineering. 4th Edition. Wiley, New York.

## BIOGRAPHY



**SİNAN DOĞUSAN** He was born in Malatya, Turkey, 1989. He received the BSc. Degree in Department of Electrical and Electronics Engineering from Yeditepe University in 2016. Currently, he is continuing his MSc. study at Inonu University. While studying at Inonu University, he worked a term as a Visiting Researcher at Antenna and Compatibility Laboratory (LACE) in Politecnico di Torino. His research interests are Electromagnetic Fields and Applications, Antennas, Microwave and RF Engineering.


# Automatic Detection of the Topics in Customer Complaints with Artificial Intelligence

Sevinç İlhan Omurca, Ekin Ekinci, Enes Yakupoğlu, Emirhan Arslan and Berkay Çapar


**Abstract**— Today, people first make their complaints and compliments on the internet about a product which they use or a company they are a customer of. Therefore, when they are going to buy a new product, they first analyze the complaints made by other users of the product. These complaints play an important role in helping people make decisions of purchasing or not purchasing products. It is impossible to analyze online complaints manually due to the huge data size. However, companies are still losing a lot of time by analyzing and reading thousands of complaints one by one. In this article, online text based customer complaints are analyzed with Latent Dirichlet Allocation (LDA), GenSim LDA, Mallet LDA and Gibbs Sampling for Dirichlet Multinomial Mixture model (GSDMM) and the performances of them are compared. It is observed that GSDMM gives much more successful results than LDA. The obtained topics of the complaints are presented to users with a mobile application developed in React Native. With the developed application not only the customers will be able to see the topics of complaint from the application interface but also the companies will be able to view the distribution and statistics of the topics of complaints.

**Index Terms**—Topic modelling, latent dirichlet allocation, gibbs sampling, gibbs sampling for dirichlet multinomial mixture, natural language processing.

SEVİNÇ İLHAN OMURCA, is with Department of Computer Engineering Kocaeli University, Kocaeli, Turkey, (e-mail: [silhan@kocaeli.edu.tr](mailto:silhan@kocaeli.edu.tr)).

 <https://orcid.org/0000-0003-1214-9235>


EKİN EKİNCİ, is with Department of Computer Engineering Sakarya University of Applied Sciences, Sakarya, Turkey, (e-mail: [ekinekinci@subu.edu.tr](mailto:ekinekinci@subu.edu.tr)).

 <https://orcid.org/0000-0003-0658-592X>


ESES YAKUPOĞLU, is with Department of Computer Engineering Kocaeli University, Kocaeli, Turkey, (e-mail: [enesyakupoglu61@gmail.com](mailto:enesyakupoglu61@gmail.com)).

 <https://orcid.org/0000-0003-1702-2647>

EMİRHAN ARSLAN, is with Department of Computer Engineering Kocaeli University, Kocaeli, Turkey, (e-mail: [emirhan.arslan@outlook.com.tr](mailto:emirhan.arslan@outlook.com.tr)).

 <https://orcid.org/0000-0002-5978-9590>

BERKAY ÇAPAR, is with Department of Computer Engineering Kocaeli University, Kocaeli, Turkey, (e-mail: [berkaycapar@gmail.com](mailto:berkaycapar@gmail.com)).

 <https://orcid.org/0000-0002-3178-0690>

Manuscript received November 27, 2020; accepted July 3, 2021.

DOI: [10.17694/bajece.832274](https://doi.org/10.17694/bajece.832274)

## I. INTRODUCTION

OVER RECENT years, online complaint or compliment narratives play a very important role in people's purchasing decisions. Thus, there has been a great rise on the amount of online customer complaints and compliments. However, complaints attract more attention. The frequently preferred online customer review receiving platforms provide a good resource to collect numerous text based complaints on numerous companies or brands. These collected text based data consider main aspects of the products which customers review about. Thus, there is a huge and valuable resource for detecting the main topics that companies and customers are interested in. Determining the main topics provides a good way to summarize and organize these unstructured text data for companies or customers. The misevaluation or misclassification of complaints delays the start of the resolution process, and, what is worse, causes customer dissatisfaction and soon complaint escalation [1]. Hence, it is very important to detect the main topics of the text based complaints among the huge document collections by automating it. Only this way can carry out relationships between customers and companies correctly.

Latent Dirichlet Allocation (LDA) is a successful, generative probabilistic model that has performed well in analysis of customer complaints as in many text mining tasks. It enables unstructured customer complaints to be clustered into a mixture of topics which underlies the main content of the complaints. One of the strengths of the LDA is that it does not require any prior annotations about the customer narratives and it extracts topics by using original unlabeled documents. LDA has been applied in many fields about text mining, there also have been numerous studies on the analysis of text based customer complaints in the literature. Therefore, LDA addresses the challenge about reading and analyzing complaint narratives by human annotators.

LDA has been applied in many fields about text mining, there also have been numerous studies on the analysis of text based customer complaints in the literature. Kalyoncu *et al.* [2] generated a LDA based solution to manage and visualize the complaints for each Mobile Network Operators (MNOs) in Turkey. Liang *et al.* [3] used the LDA as a topic model to identify product aspects that customers frequently mentioned, then identified the related problems of the product. Bastani *et al.* [4] proposed a method based on LDA to extract latent topics in the CFPB complaint narratives, and explores their associated trends over time. Mai *et al.* [5] built a LDA model

to extract the key points of Guangdong Province consumer complaint text accurately and quickly. Atıcı *et al.* [6] used LDA to determine the key features of complaints and dissatisfactions about products, services or companies by using big data taken from Turkey’s largest customer complaint website.

In this article, the topic of customer complaints is determined by the topic models. In other words, it is determined which category of service the complaints belong to. For this aim, the Natural Language Processing (NLP) and Deep Learning techniques are used together. Unlike LDA, which is the most frequently used topic modelling method, Gibbs Sampling algorithm for a Dirichlet Multinomial mixing model (GSDMM) is used in this article because it gives more successful results in short texts. With more accurate results, user reviews will be categorized correctly, information pollution will be prevented, and both customers and companies will be able to analyze user comments accurately. Furthermore, thanks to realized study, it would be possible to notice the changes and trends of the main topics of complaint narratives over the time. Supposing that, if it is realized that the trend of some topics is decreasing over time then it indicates that the company must take into account these aspects of its brand or products. The companies can be able to improve if and only if they are aware of the trends of complaints of their customers.

## II. TOPIC MODELLING ALGORITHMS

Topic model algorithms convert document collections to low dimensional space for the purpose of modelling hidden thematic structure within. In this study, three different topic models are used. These are LDA with GenSim, LDA with Mallet, GSDMM. The reason for using LDA in this study is because it is a frequently used and generally very successful topic model however may fail on short texts [7]. The GSDMM method was developed to improve topic modelling in short texts [8]. Since working with short texts, the GSDMM method is used.

### A. Latent Dirichlet Allocation

LDA is a generative graphical model used to model discrete data such as textual data to reveal the topics that comprise the document. Its use includes topic modelling. LDA does not need any prior knowledge due to a fully unsupervised model. LDA is based on the “bag-of-words” assumption that while word orders in documents are regarded, word co-occurrence in the same document is taken into account. The basic idea behind LDA is this: topics have probability distribution over a fixed vocabulary and documents are composed of random mixture of latent topics. While the input of the model is documents, its outputs are the topics, probabilities of words under these topics, topic for each word, and the topic mixture for each document [9].

LDA is a generative model and this is its most important feature. In the generative process firstly words are sampled from fixed vocabulary for each topic. For every document topic proportions are sampled. The Dirichlet distribution is

used in these two steps. Each topic in the topic distribution is sampled randomly for every word in all documents. At the end, for a related topic a word is sampled. In the sampling steps multinomial distributions are used.

Graphical representation of LDA takes advantage of plate notation. Plate notation is a graphical model of representing repeated variables. A plate or rectangle is used to group variables together into repeating nodes, rather than plotting each repeating variable separately. Plate notation for LDA is given in Fig. 1. Only documents can be observed; the topics, topic distribution for each document and words in the topics are hidden. Therefore, while the observed variables in the graphical model are represented by shaded, those that cannot be observed are represented by non-shaded.

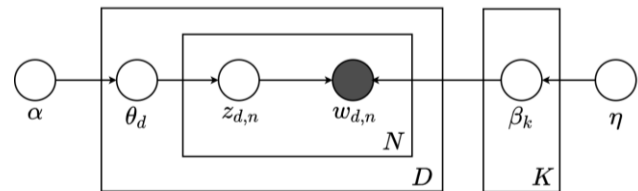


Fig.1. Graphical representation of Bayes [10]

In the graphical model given with Fig. 1  $D$  is the total number of documents in the collection and  $K$  is the total number of topics.  $\alpha$  and  $\eta$  are Dirichlet parameters.  $\theta$  shows the probability of the topics which are found in the document, and  $\beta$  indicates the word distributions in the topics. While  $z_{d,n}$  represents the topic of the word in the  $n$ th position in the  $d$ -th document,  $w_{d,n}$  represents the word in the  $n$ -th position in the  $d$ -th document. According to the graphical model, the joint distribution of all hidden and observed random variables  $p(\beta_{1:K}, \theta_{1:D}, z_{1:D}, w_{1:D})$  is given in Eq. 1.

$$p(\beta_{1:K}, \theta_{1:D}, z_{1:D}, w_{1:D}) = \left( \prod_{k=1}^K p(\beta_k / \eta) \right) \left( \prod_{d=1}^D p(\theta_d / \alpha) \right) \left( \prod_{n=1}^N p(z_{d,n} / \theta_d) p(w_{d,n} / z_{d,n} \beta_k) \right) \quad (1)$$

As mentioned earlier, it is intended to obtain model parameters with LDA. For this purpose, the distribution of  $p(\beta, \theta, z / w)$  is estimated approximately in the form of  $q(\beta, \theta, z)$  using variational inference. Then, model parameters are trained to minimize the Kullback–Leibler Divergence (KL) deviation between  $q$  and  $p$ . This process is called  $KL(q // p)$  Minimization in the literature.  $q$  modelling is extremely difficult for a high dimensional distribution. To further reduce complexity, bold independence assumptions similar to the graphical model is made and the common possibility is divided into independent subcomponents. A more detailed explanation for each subcomponent is in Eq. 2.

$$q(\theta_{1:D}, z_{1:D,1:N}, \beta_{1:K}) = \prod_{k=1}^K q(\tilde{\beta}_k / \tilde{\lambda}_k) \prod_{d=1}^D q(\tilde{\theta}_d / \tilde{\gamma}_d) \prod_{n=1}^N q(z_{d,n} / \tilde{\phi}_{d,n}) \quad (2)$$

Here, instead of a common probability model for multiple variables, each variable is modelled independently, each variable  $v_i$  is modelled as  $q_i(v_i / \rho_i)$  with a given distribution family nominal distribution. This is called Mean field variational inference, where the common distribution is traceable, easy to analyze, separating individual variables into their distributions. Assumptions of independence may be wrong; but observation should be continued as flawed rather than wrong. Subsequent experimental results often produce quality results. To optimize dependent variables, each group is divided into groups with independent variables from each other.

In this way, the parameters of topic assignment modelling and topic ratios are determined in LDA. The most difficult steps here are to assign topics and then update the variational parameters of topic rates. So, it is required to model  $P$  with  $q$  by minimizing KL Divergence. Because it cannot be directly optimized, operations are continued with Evidence lower bound (ELBO). The ELBO definition is made in Eq. 3.

$$\begin{aligned} ELBO &= -\sum_x q(x) \log \frac{q(x)}{\tilde{p}(z, x)} \\ &= -\sum_x q(x) \log \frac{q(x)}{p(z, x)} + \log Z \\ &= -KL(q \parallel p) + \log Z \\ \log Z &= ELBO + KL(q \parallel p) \geq ELBO \end{aligned} \quad (3)$$

The relationship between KL-Divergence and ELBO is evaluated in Eq. 3. KL-Divergence is always positive,  $\log Z$  is therefore always larger or equal to ELBO. ELBO in here is the lower bound of  $\log Z$  for any  $q$ . From this it can be said that when  $q$  is equal to  $p$ ,  $\log Z$  and ELBO are equal to each other. ELBO is wanted to maximize in LDA as in Eq. 4. Here the expectation value is calculated with  $q$ .

$$\begin{aligned} L &= \sum_{k=1}^K E[\log p(\vec{\beta}_k / \vec{\eta})] + \\ &\sum_{d=1}^D E[\log p(\vec{\theta}_d / \vec{\alpha})] + \sum_{d=1}^D \sum_{n=1}^N E[\log p(z_{d,n} / \vec{\theta}_d)] + \\ &\dots + \sum_{d=1}^D \sum_{n=1}^N E[\log p(w_{d,n} / z_{d,n} \vec{\beta}_{1:K})] + H(q) \end{aligned} \quad (4)$$

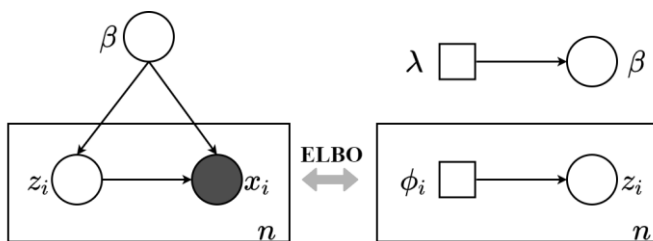


Fig.2. LDA simplified model and ELBO relationship [10]

In Fig. 2, the simplified version of the graphic model of LDA is shown with ELBO. Here  $x_i$  is an observation linked to  $\beta$  and  $z_i$ . The equation 1 is simplified and becomes as in Eq. 5.

$$p(\beta, z_{1:n}, x_{1:n}) = p(\beta) \prod_{i=1}^n p(z_i / \beta) p(x_i / z_i, \beta) \quad (5)$$

The right side of the equation (R.H.S) has an exponential distribution, and  $q$  will be as in the equation  $q(\beta, z) = q(\beta / \lambda) \prod_{i=1}^n q(z_i / \phi_i)$  with Mean field variational inference.  $\beta$  and  $z_i$  Eq. 6 it has been removed as said.

$$\begin{aligned} p(\beta / z, x) &= h(\beta) \exp\{n_g(z, x)^T \beta - \alpha(n_g(z, x))\} \\ p(z_i / \beta, x_i) &= h(z_i) \exp\{n_l(\beta, x_i)^T z_i - \alpha(n_l(\beta, x_i))\} \\ q(\beta / \lambda) &= h(\beta) \exp\{\lambda^T \beta - a(\lambda)\} \\ q(z_i / \phi_i) &= h(z_i) \exp\{\phi_i^T z_i - a(\phi_i)\} \end{aligned} \quad (6)$$

Getting the right side of the equation with  $q$  and  $p$  by optimizing ELBO according to  $\lambda$  and  $\phi_i$  is intended here. The derivative of  $L$  according to  $\lambda$  is taken and set to 0. The optimal  $\lambda^*$  subtraction and optimal  $\phi_i^*$  are obtained with Eq. 7 and 8 respectively.

$$\nabla_{\lambda} L = a'(\lambda) (E_{\phi} [n_g(Z, x)] - \lambda) \quad (7)$$

$$\begin{aligned} \lambda^* &= E_{\phi} [n_g(Z, x)] \\ \phi_i^* &= E_{\lambda} [n_l(\beta, x_i)] \end{aligned} \quad (8)$$

### B. Gibbs Sampling Dirichlet Multinomial Mixture

GSDMM is a collapsed Gibbs Sampling algorithm for a Dirichlet Multinomial mixing model developed specifically to cope with the challenges of topic extraction from short texts. The functioning of GSDMM is as follows; (I) initially, documents are randomly assigned to clusters, and the information  $\vec{z}$  (cluster label),  $m_z$  (number of document in cluster  $z$ ),  $n_z$  (number of words cluster  $z$ ), and  $n_z^w$  (occurrence count of word  $w$  in cluster  $z$ ) are recorded, (II) documents are searched in I iteration, (III) in each iteration, a cluster is assigned to each document  $d$  based on conditional distribution, respectively:  $p(z_d = z / \vec{z}_{-d}, \vec{d})$ ; where  $-d$

means that the label of cluster document  $d$  is removed from  $\vec{z}$ , (IV) in every iteration  $\vec{z}$ ,  $n_z$ , and  $n_z^w$  are updated accordingly, (V) as a result, only some few initial  $K$  clusters will not be empty.

- GSDMM can automatically get the cluster count.
- GSDMM can balance the integrity and homogeneity of the results.
- GSDMM is good for convergence.
- GSDMM can overcome sparsity or high dimensionality of short texts.
- LDA and PLSA etc. as with traditional topic models, GSDMM can obtain representative words of each cluster.
- Yin and Wang proposed the Movie Group process (MGP) for instantiation that could help to understand how GSDMM works and the meaning of its parameters [11].

1) *Movie group process*

A film discussion course can be imagined in which the Professor is planning to split students into a number of groups. The professor wants students to write down the movies they are watching. The list won't be very long and students will probably write down the last movies they've watched recently or the ones they've loved so much. Now each student can be modeled as a list of movies. The professor must find a way to split students into a number of groups. The professor's expectation is that while the students in the same group watch common movies so they will have more to discuss, those in different groups also have different movies to discuss.

If only a few clusters have documents and others are empty, if it is explained through the professor, his students and movies, the story described above becomes the following. The professor invites his students to a restaurant where there are  $K$  tables. At first he assigns the students to  $K$  tables randomly. Then he asks the students to select a table one by one. However, the student should consider the following two rules while selecting the table.

- The student must choose a table which has more students.
- The student must choose the table where the students who have similar interests (watch the common movies more).

These steps repeat until some grow and some disappear. The expectation is that there will be students at some tables and students who are at these tables will share a similar interest.

2) *Gibbs sampling*

Gibbs Sampling is a special case of the Metropolis and Metropolis-Hastings algorithm used to make interpretations about complex stochastic models. Gibbs Sampling produces sample values for the density distribution for the corresponding result values of all the parameters in the model by sampling from all the distribution values in sequence. Due to its simple logical basis and ease of application, this method is quite widely preferred in NLP, artificial intelligence, and deep learning tasks.

$\theta = (\theta_1, \dots, \theta_k)$  parameter vector,  $p(y|\theta)$  possibility and suppose  $\Pi(\theta)$  a predecessor distribution. Expression  $\Pi(\theta_i|\theta_j, i \neq j, y)$  can be written as  $\Pi(\theta_i|\theta_j, i \neq j, y) \propto p(y|\theta)\Pi(\theta)$ . The Gibbs sampling algorithm is as follows:

- i.  $t = 0$  is taken and an arbitrary  $\theta(0) = \{\theta_1(0), \dots, \theta_k(0)\}$  initial value is selected.
- ii. Each component of  $\theta$  is obtained in the format as below:
- iii.  $\Pi(\theta_1|\theta_2(t), \dots, \theta_k(t), y)$  as  $\theta_1(t+1)$ ,
- iv.  $\Pi(\theta_2|\theta_1(t+1), \theta_3(t), \dots, \theta_k(t), y)$  as  $\theta_2(t+1)$ ,
- v. ....
- vi.  $\Pi(\theta_k|\theta_1(t+1), \dots, \theta_{k-1}(t+1), y)$  as  $\theta_k(t+1)$ .
- vii. Take  $t = t + 1$  and go to step 2 if  $t < T$  ( $T$  is the desired sample width). Otherwise, the process is finished.

3) *Dirichlet multinomial mixture*

Unlike normal text clustering, short text clustering poses sparsity problems [12]. Most of the words occur only once in short texts, as a result TF-IDF measure does not fare well in this type of texts. Also, if VSM is used for representation, sparse and high-dimensional feature space results in a waste of both computational time and memory [13] In response to all these short text clustering challenges, the DMM model should be used [14]. DMM is a probabilistic generative model like LDA and is based on two assumptions behind the generative process. The first one is that a mixture model is used in the generative process for documents. The other is there is a one-to-one match between documents and clusters, hence, it is claimed that each document comes from only one topic. When generating document  $d$ , initially DMM chooses cluster  $k$  that is the mixture of cluster based mixture component  $p(z=k)$ . The document  $d$  is then generated with mixture component drawn from  $p(d/z=k)$ . The Fig. 3 represents the plate notation of DMM as below.

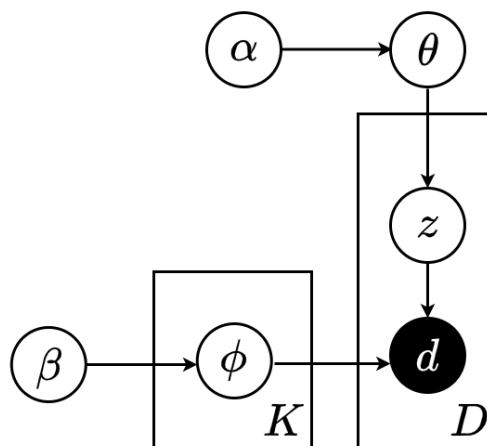


Fig.3. DMM's graphical model [11]

In the Fig. 3 above  $\alpha$  is a parameter that affects the shape of the probability distribution and is derived from the probability that a document is grouped in a cluster.  $\beta$  is another shape parameter for distribution.  $\beta$  represents the similarity of words between two documents.  $\phi$  is the omnidirectional distribution of words,  $p(w/z=k) = \phi$ , where  $w$ , words and  $z$  are the cluster label.  $\theta$  is a multi-term distribution considering alpha, so  $p(d/z=k) = \theta$ ; where  $d$  is the document.

$$p(d) = \sum_{k=1}^K p(d/z=k) p(z=k) \tag{9}$$

In Eq. 9,  $K$  represents the number of clusters, the calculation of  $p(d/z=k)$  is the principal problem, where DMM makes the Naive Bayes assumption. Based on this assumption, if the cluster  $k$  which the document belongs to is known, words in this document are generated independently and probability of each word is accepted as independent within the document. Then, the probability of the document  $d$  generated by cluster  $k$  can be obtained as in Eq. 10.

$$p(d/z=k) = \prod_{w \in d} p(w/z=k) \tag{10}$$

### III. RESULTS AND DISCUSSIONS

#### A. Model Design Process

The first stage of the study is data mining using KNIME from sikayetvar.com website. Customer's complaints data taken with KNIME and saved in csv format. Then, the dataset is cleaned for pre-processing with java and python programming. The purpose of pre-processing is to clear the data as much as possible and reduce it to words that will work only when modelling the topic. Three different topic modelling methods are applied to the cleaned data and the results of the models are compared. The study is continued by using GSDMM because it gives more successful results than other methods. After topic modelling with GSDMM, assigning the topic title to the documents is done with java programming on the NetBeans IDE platform. After assigning the topic title to the documents, the complaints of each document are saved. The complaint-topic information is saved and converted to JSON format and is presented to users in the mobile application developed in the React Native environment. The architecture of the model design process is given in Fig. 4.

#### B. Dataset

The dataset, which is used in this study, consists of the complaints of customers for the products or services they

receive from the companies. The complaint data written on the sikayetvar.com website is used to create experimental dataset and the KNIME software is preferred to get these complaints. KNIME is an open source and cross platform data analysis platform. It was developed by a company named Konstanz Information Miner in Java and was founded on Eclipse basis [6]. With KNIME it is convenient to process large data limited to the available hard disk space, and Weka, Tableau, the statistics package R project, LIBSVM etc. supports other machine learning and data analysis projects. KNIME contains many nodes for machine learning and data mining needs. These nodes can be associated to process, interpret, visualize and report data. The associated nodes are run in the specified order and produce output. The turns of the nodes can be followed on the console. KNIME offers community extensions for needs. These extensions offer many nodes from various application areas. These extensions can be installed from the application interface. extensions from outside the community as ZIP archives can be also added and used. In realized KNIME project, Palladian extension is added to the application to process the data on sikayetvar.com. Palladian KNIME is an open source Java library that is not included in community extensions. With the web mining node, it offers, data on HTML, RSS feeds and JavaScript supported websites can be parsed and important content can be obtained.

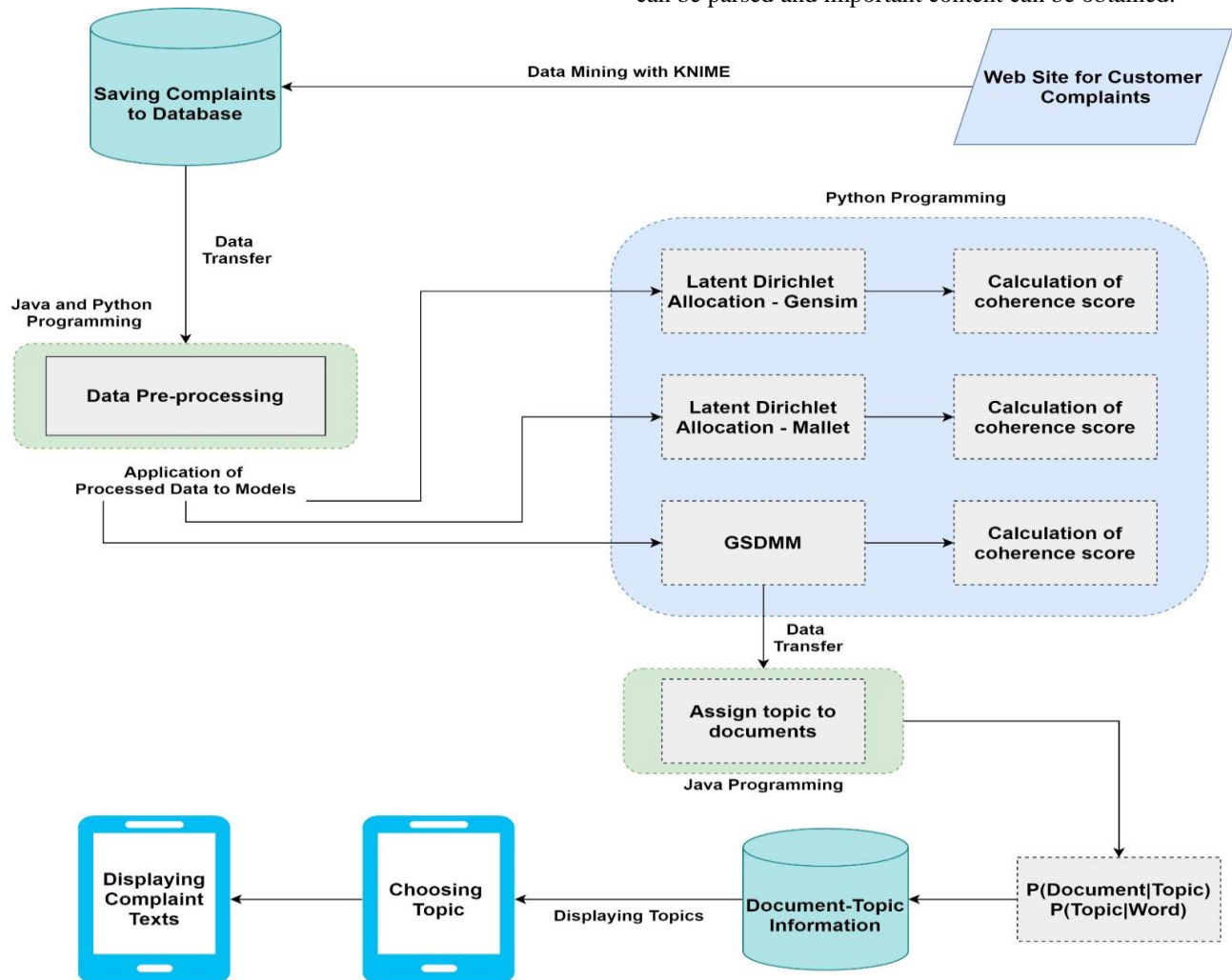


Fig.4. Model design process

### C. Comparison of Topic Modelling Algorithms

In this study three topic modelling methods are used and compared in terms of the performance. These 3 methods are: LDA with GenSim, LDA with Mallet and GSDMM. The reason for choosing these models is that LDA is the most popular topic modelling method and GSDMM is successful in short texts. LDA is one of the most used topic modelling methods and the success rate is generally high. GSDMM is developed to improve topic modelling in short texts.

#### 1) Topic modelling with Mallet LDA

Mallet is a Java based library used for performing topic modelling. With Mallet Latent Dirichlet Allocation, Pachinko Allocation and Hierarchical Latent Dirichlet Allocation topic models can be realized. Mallet version 2.0.8 is used in this study. There are two steps to be followed for Mallet topic modelling; topic import from dataset and topic training [15].

- Data import: In this step, the dataset used for topic extraction is imported and pre-processing is applied to remove noise and improve quality. After this step, ".mallet" binary file is created by using a pre-processed dataset.
- Topic training: In this step, topic training is realized by using pre-processed data that comes from the data import step. In this step, parameters to smooth document-topic distributions can be decided and adjusted.

After these steps, three files which include topic words, matrix of the most appropriate document-topic pairs, and Gibbs sampling results after each iteration is obtained. With Gibbs sampling it can be learnt that which word belongs to which topic, the source of each word, and the alpha and beta values. While applying Mallet LDA to the dataset, random\_seed is set to 100, num\_topics is set to 100, workers is set to 3,  $\alpha$  is set to 0.5 and  $\beta$  is set to 0.01.

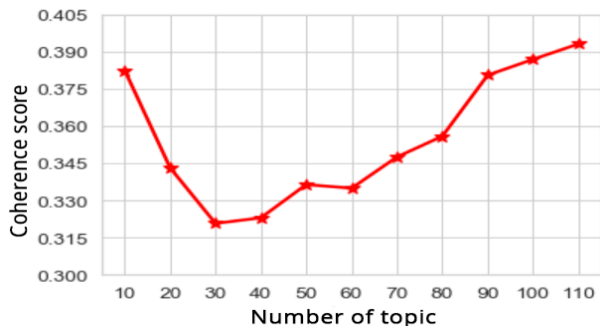


Fig.5. Coherence score graph by topic number with Mallet LDA

Fig. 5 shows the change of coherence score with topic number in Mallet LDA. Here, while calculating the coherence score, the CoherenceModel (c\_v) function available in Mallet and GenSim are used. As seen in the graph, it gives the lowest coherence score at  $K = 30$ , while it gives the highest coherence score at  $K = 110$ .

#### 2) Topic modelling with GenSim LDA

GenSim is a python python for unsupervised topic modelling implementations such as LDA, LSA, Hierarchical Dirichlet Process (HDP). Its biggest advantage is that it is memory

independent. That means there is no need to load all training data to RAM at any given time. While extracting topics with GenSim, at first preprocessing is applied to the dataset to reduce negative effects of noise and then training is carried out. In this study, the parameters m\_state is set to 100, chunksize is set to 10000, passes is set to 20, num\_topics I set to 100,  $\alpha$  is set to 0.5 and  $\beta$  is set to 0.01.

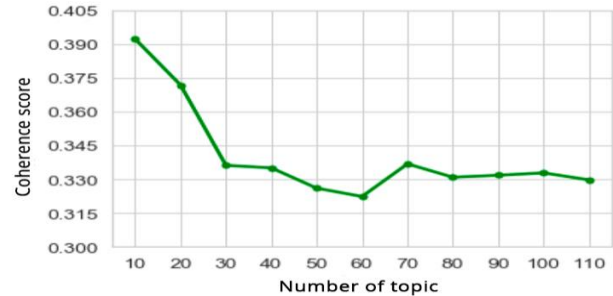


Fig.6. Coherence score graph by topic number with GenSim LDA

Fig. 6 shows the change of coherence score according to the number of topics in GenSim LDA. Here, while calculating the coherence score, the CoherenceModel (c\_v) function available in Mallet and GenSim is used. It gives the lowest coherence score at  $K = 60$ , while it gives the highest coherence score at  $K = 10$ .

#### 3) Topic modelling with GSDMM

In this model, the assumption that each document is related to one topic at most and the words in these documents depend on the related topic. As mentioned earlier, GSDMM can produce successful results in short texts.

When applying GSDMM in the dataset,  $K$  is set to 100,  $\alpha$  is set to 0.5 and  $\beta$  is set to 0.01. Due to the algorithm that GSDMM uses MGP, some clusters are empty.

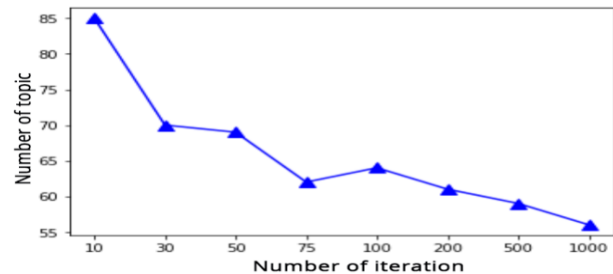


Fig.7. Change in the number of topics with increasing iteration in GSDMM

Fig. 7 shows the number of topics given by GSDMM in different iterations for  $K = 100$ . It gives the closest value to 100 in 10 iterations and the farthest value to 100 in 1000 iterations. It gives 69 topics in 50 iterations, it means that 31 clusters are empty.

According to Fig. 7, it can be said that some of the initial clusters may be empty after a few iterations so at the end number of clusters will be between 1 and  $K$  [16].

In this study, 3 different topic modelling methods are used with same parameters and same dataset and results compared. In all 3 models,  $K$  (topic number) = 100,  $\alpha = 50 / K = 0.5$ ,  $\beta = 0.01$  are taken. All models are run with 50, 100, 200, 500 and 1000 iteration values. The coherence score formula in Eq. 11 is used to compare the results of the topic modelling.

$$C(k;V^{(k)}) = \sum_{n=2}^N \sum_{l=1}^{n-1} \log \frac{D(V_n^{(k)}, V_l^{(k)}) + 1}{D(V_l^{(k)})} \quad (11)$$

In Eq. 11, the value of  $N$  indicates how many words represent each topic. In this study,  $N = 10$  is taken and the most popular 10 words of each topic are used.  $V_n$  and  $V_l$  indicates the number of documents in the number of documents together. The denominator section  $D(V_l)$  gives the number of how many documents the word  $V_l$  contains.

In Fig. 8 and Table II, the coherence scores obtained with different iteration numbers are shown. LDA of the Mallet library, gives the best result in 50 iterations. The LDA of the

GenSim library gives the best coherence score in 500 and 1000 iterations. In addition, it is observed that the results do not change in 500 and 1000 iteration values in GenSim LDA. GSDMM gives the best coherence score with 50 iterations. When the 3 methods are compared, it is seen that the most successful method in each iteration number is the GSDMM method. The biggest reason for this is that the documents contain short texts. Due to the low number of words in short texts, GSDMM gives more successful results than other methods. The next stages of the study is continued with the GSDMM method as it gives the most successful method.

TABLE II  
COMPARISON OF SUCCESS OF THE MODELS

Method	Iteration Count				
	50	100	200	500	1000
LDA Gensim	-90.0322	-89.0056	-87.1602	-86.5808	-86.5808
LDA Mallet	-121.2727	-130.1922	-131.4759	-129.2213	-128.8657
GSDMM	-77.6599	-85.4374	-82.5348	-80.6974	-79.6104

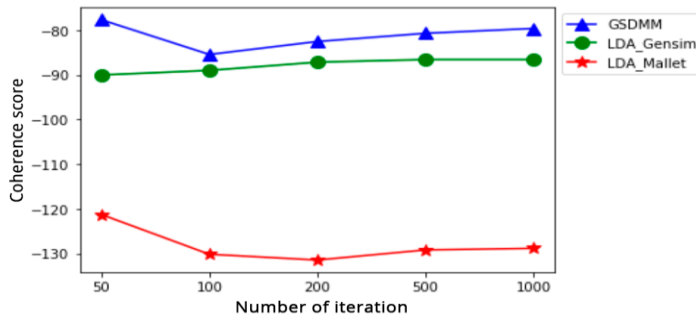


Fig.8. Comparing the success of the model

4) Clustering and topic assignment

GSDMM is used for clustering and topic assignment because it gives the most successful coherence score in experimental results. Topic number ( $K$ ) = 100,  $\alpha = 0.5$ ,  $\beta = 0.01$  and iteration number = 50 values are taken. Due to the algorithm that GSDMM uses, some of the clusters are empty. For this reason, 69 clusters have been obtained, not 100. So 31 clusters are empty clusters. The 69 clusters obtained are reduced to 20 clusters manually, according to their semantic similarities. Thus, 20 semantically most logical, similar and successful topics are obtained. The 10 most popular keywords are used in each topic. The 20 clusters are named manually by us, according to the meanings and similarities of the keywords.

TABLE III  
TOPICS AND KEYWORDS

<b>Campaign</b>	<b>Account Operations</b>	<b>Damaged Product</b>	<b>Shoes</b>	<b>Delivery</b>
tl(turkish lira)	password	product	product	cargo
coupon	member	cargo	shoe	delivery
discount	active	broken	brand	product
product	email	return	original	branch
return	login	damage	quality	order
shopping	account	order	fake	deploy
campaign	address	delivery	return	house
customer	support	company	shopping	company
code	issue	tv	sticker	address
card	mail	box	sport	shopping
<b>Accessory</b>	<b>Electronic Household Stuffs</b>	<b>Pets</b>	<b>Housewares</b>	<b>Home Textile</b>
product	machine	cat	product	product
order	product	food	broken	cover
silver	hair	dealer	karaca	english
necklace	brand	insect	return	quilt
color	coffee	brand	cargo	home
set	order	alive	piece	order
earring	dryer	fair	order	linens
chain	arzum	registry	delivery	image
wristband	return	product	plate	brand
pink	house	goody	set	picture



Table 3 shows the 10 topic titles and 10 keywords for each topic. Keywords that are not related to the topic, that is, clustered incorrectly, are indicated with red.

In order to assign the topic to the complaint documents, a java code on the NetBeans IDE platform is written. For the text of the complaint, it is counted how many times the keywords of each topic are mentioned. A score is kept for

each topic and a complaint is assigned to the topic with the highest score. In addition, a threshold value is determined for the score, complaints that do not exceed this threshold value are assigned to another topic called "Others". In other words, if a complaint is not sufficiently similar to the topics obtained, it is assigned to the topic title containing other complaints called "Others".

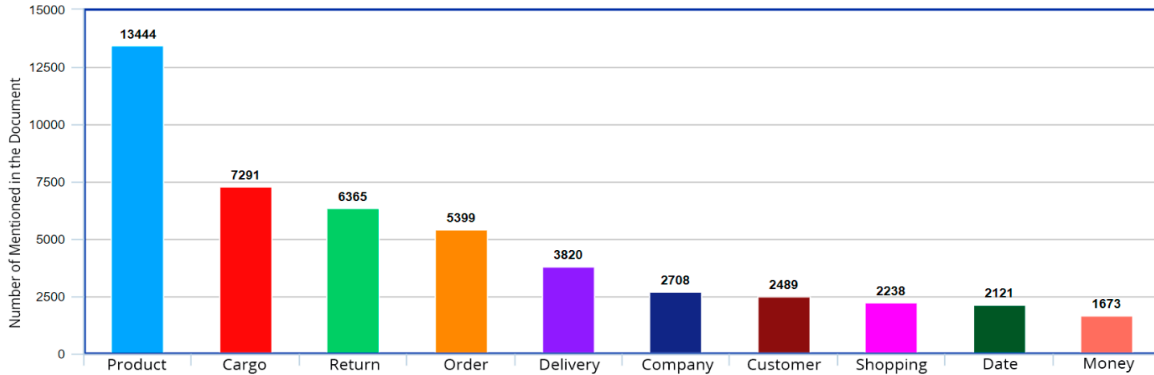


Fig.9. The most popular keywords from the complaints of Trendyol Company

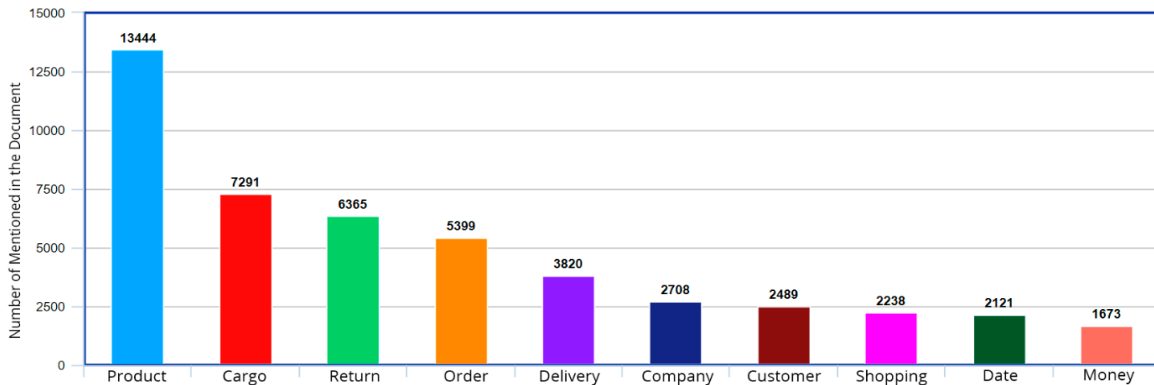


Fig.9. The most popular keywords from the complaints of Trendyol Company

Fig. 9 shows the most popular keywords from 6963 complaints of Trendyol company. Fig. 10 shows the distribution of the topic titles from the 6963 complaints of Trendyol company. In addition, 2477 complaints that do not exceed the threshold value are included in the "Others" topic.

**D. Mobile Application**

After the topic modelling and assignment of complaints, all complaints and statistics are displayed on a mobile application. The mobile application is developed for android with React Native. The person who logs into the application must choose the company first. Since only Trendyol complaints are used in this study, there is Trendyol company as the only choice in the section of companies. After the company selection, the user can choose 3 different options.

These are: complaints, topic distribution statistics and keyword distribution statistics.

The user who chooses the keyword distribution option shows the top 10 keywords in 6963 complaints of Trendyol company as pie chart and column chart. In the 6963 complaints of the Trendyol company, the user who chose the topic distribution option shows the 10 most popular topic titles as pie chart and column chart. The user, who chooses the complaints option, has 22 different options, including 20 topics, all complaints and other complaints. The user can view all the complaints if he wishes, or, if he wishes, the complaints belonging to a specific topic. From the "Others" option, the topic can view and read the complaints that could not be assigned.

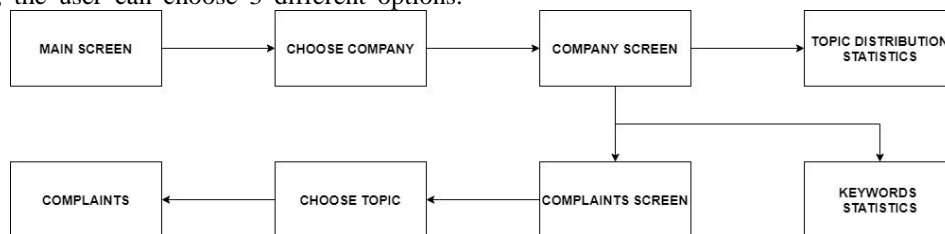


Fig.10. Process of the mobile application

## IV. CONCLUSION

As a result of this study, it is realized that how important user complaints are for both customers and companies. Afterwards, the importance of the categorized process, which can be considered as a summary of the complaints, is understood and researches are made on how this structure could be handled.

For the topic modelling, 6963 complaint data and data set are created from the website of sikayetvar.com. In order to facilitate the machine learning process and achieve more consistent results, the data set is pre-processed. Then 2 different methods for topic modelling is used: LDA and GSDMM. In this study, LDA is applied using two different libraries, GenSim and Mallet. Thus, three different models are tested in the complaint data and the results are compared. Since document data consists of short texts, it is determined that the GSDMM method gives more successful results. Therefore, GSDMM method is used in the continuation of the study.

Topic modelling is applied to the document with GSDMM and clusters are obtained. Then, in order to assign the topic of the complaint data, the ratio of how often the keyword is mentioned in the complaint and document is examined. Scores are kept for each topic and each complaint is assigned to the topic that got the highest score. An average threshold value is determined and complaints that do not exceed the threshold value are assigned to a topic called "Other". The complaints, which are assigned to the topic, are presented to the users with the mobile application developed with React Native. Each topic and all complaints of the title can be displayed on a different screen. At the same time, the most frequently mentioned keywords and the most popular topics in all complaints are presented to the users as pie and column charts. The successes of the thesis study can be listed as follows:

- Customers and companies will be able to conduct complaints analysis more consistently, by categorizing their complaints according to their titles,
- Thanks to the process of categorizing complaints by artificial intelligence, companies will use less time and manpower when they analyze complaints,
- Three different methods from topic modelling methods are compared together. As a result, GSDMM method is more successful than LDA. The main reason for this is that the complaint texts are composed of short texts,
- The most popular topic modelling method LDA's failure in short texts is seen in this study,
- More consistent and successful results can be achieved with DMM based models in short texts,
- Gensim and Mallet applications, which are 2 different LDA Libraries, are compared and as a result, GenSim is more successful than Mallet.

In order for this study to give more successful results, improve suggestions can be listed as follows:

- The dataset can be expanded,
- It can be worked with dataset containing longer texts,
- Pre-processing steps can be more frequent. Thus, more successful results can be obtained by working with minimum stop-words and maximum keywords,

- Multiple topic modelling methods can be used together,
- Other DMM-based methods such as GPU-DMM can be used,
- Different topic modelling methods such as ATM, BTM, TTM, ASTM, TATM, SATM can be tried and compared together. The success of the methods can vary depending on your dataset and the results you want.

More consistent results can be obtained by changing the parameters of the methods used, such as alpha, beta, and the number of topics according to your dataset and the desired outputs.

## ACKNOWLEDGMENT

Thanks to TÜBİTAK for their support to the project numbered 1919B011902805 within the scope of TÜBİTAK-2209-A University Students Research Projects Support Program 2019/2.

## REFERENCES

- [1] S. Prasad, "Use of Natural Language Processing to Improve Complaint Classification in Customer Complaint Management System", *Journal of Critical Reviews*, Vol.7, No.14, 2020, pp.2642-2652.
- [2] F. Kalyoncu, E. Zeydan, İ. O. Yiğit, A. Yıldırım, "A Customer Complaint Analysis Tool for Mobile Network Operators." 2018 IEEE/ACM Int. Conf. on Advances in Social Networks Analysis and Mining, Barcelona, Spain, 2018.
- [3] R. Liang, W. Guo, D. Yang, "Mining product problems from online feedback of Chinese users", *Kybernetes*, Vol.46, No.3, 2017, pp.572-586.
- [4] K. Bastani, N. Hamed, S. Jeffrey, "Latent Dirichlet allocation (LDA) for topic modelling of the CFPB consumer complaints", *Expert System with Applications*, Vol.127, 2019, pp.256-271.
- [5] W. Mai, M. Wei, J. Zhang, F. Yuan, "Research on Chinese text and application based on the Latent Dirichlet Allocation." 3rd International Conference on Advanced Electronic Materials, Computers and Software Engineering, Shenzhen, China, 2020.
- [6] B. Atıcı, S. İlhan Omurca, E. Ekinici, "Product aspect detection in customer complaints by using latent dirichlet allocation." 2017 International Conference on Computer Science and Engineering, Antalya, Turkey, 2017.
- [7] X. He, H. Xu, X. Sun, J. Deng, X. Bai, J. Li, "Optimize collapsed Gibbs sampling for biterm topic model by alias method." 2017 International Joint Conference on Neural Networks, Anchorage, Alaska, 2017.
- [8] R. Albalawi, T. H. Yeap, M. Benyoucef, "Using Topic Modelling Methods for Short-Text Data: A Comparative Analysis," *Frontiers of Artificial Intelligence*, Vol.3, No.42, 2020, pp.1-14.
- [9] E. Ekinici, S. İlhan Omurca, "An Aspect-Sentiment Pair Extraction Approach Based on Latent Dirichlet Allocation for Turkish," *International Journal of Intelligent Systems and Applications in Engineering*, Vol.6, No.3, 2018, pp.209-213.
- [10] D. M. Blei, "Probabilistic topic models," *Communications of ACM*, Vol.55, No.4, 2012, pp.77-84.
- [11] J. Yin, J. Wang, "A Dirichlet Multinomial Mixture Model-based Approach for Short Text Clustering." 20th ACM SIGKDD International Joint Conference on Knowledge discovery and data mining, New York, USA, 2014.
- [12] C. C. Aggarwal, C. Zhai, *Mining text data*, Springer, 2012, pp.77-128.
- [13] G. Salton, C. S. Yang, C. T. Yu, "A theory of term importance in automatic text analysis", *Journal of the American Society for Information Science*, Vol.26, No.1, 1975, pp.33-44.
- [14] K. Nigam, A. K. McCallum, S. Thrun, T. M. Mitchell, "Text classification from labeled and unlabeled documents using EM", *Machine Learning*, Vol.39, No.2/3, 2000, pp.103-134.
- [15] I. Akef, X. Xu, J. S. Munoz Arango "Mallet vs GenSim: Topic modeling for 20 news groups report", 2016.

- [16] P. Stiff, *Analysis of Remarks Using Clustering and Keyword Extraction*, Master Thesis, 2018, p. 7.

### BIOGRAPHIES



**SEVİNÇ İLHAN OMURCA** is an Associate Professor at the Kocaeli University Computer Engineering Department in Turkey. She has Ph.D. at the Kocaeli University Electronics and Communication Engineering. Her main research interest includes text mining, sentiment analysis, natural language processing, machine learning and data mining earned.



**EKİN EKİNCİ** is an Assistant Professor of Computer Engineering Department at Sakarya University of Applied Sciences in Turkey. She has received her BS. in Computer Engineering from Çanakkale Onsekiz Mart University in 2009 and MS. in Computer Engineering from Gebze Technical University in 2013 and Ph.D. degree in Computer

Engineering from Kocaeli University in 2019. Her main research interest includes text mining, sentiment analysis, natural language processing and machine learning.



**ENES YAKUPOĞLU** received the B.S. degree in computer engineering from the Kocaeli University in 2020. From 2018 to September 2020, he worked as an Intern Engineer at Argelabs Information Technologies company. He has been working as a Computer Engineer at the same company since

September 2020. His research interests include artificial intelligence, natural language processing, machine learning, deep learning, digital marketing, mobile and web application developing.



**EMİRHAN ARSLAN** is a student at the Kocaeli University Computer Engineering Department. From July 2018 to August 2018, he was an intern at Kocaeli University, Image Processing Laboratory. His research interests are natural language processing, text mining, big data, data visualizations and internet of things.



**BERKAY ÇAPAR** is a student at the Kocaeli University Computer Engineering Department. From July 2018 to August 2018, he was an intern at Kocaeli University, Image Processing Laboratory. His research interests are natural language processing, artificial intelligence, big data, web and mobile programming applications.

# Signal Attenuation Model Free Classification of Diffusion MR Signals of the Breast Tissue using Long Short-Term Memory Networks

Gökhan Ertas

**Abstract**— Detection and diagnosis of breast cancer from diffusion signals by diffusion-weighted imaging involves in estimation of quantitative metrics by signal attenuation models fitted to the signals. The process suffers from the implementation difficulty of the fitting algorithms and their sensitivity to noise. This study aims development of neural networks to facilitate the classification of the breast tissues from the signals. 37500 diffusion MR signals are synthetically generated for noise-free and noisy conditions by signal-to-noise ratio (SNR) for malignant, benign, and healthy breast tissues. Forty neural networks employing traditional long short-term memory (LSTM) or bidirectional long short-term memory (BiLSTM) blocks up to twenty are trained and tested for the signals using bootstrapping incorporated accuracy analysis. Specificity, sensitivity, and accuracy metrics are computed for the higher performance networks. For noise-free and noisy signals with  $SNR \geq 80$ , networks may achieve excellent sensitivities, specificities, and accuracies (100% at all), but LSTM networks require fewer number of memory blocks. For noisy signals having  $SNRs \leq 40$ , the networks may deliver high to very high sensitivities (74.8-98.3%), specificities (87.4-99.2%), and accuracies (83.2-98.9%) better for malignant and healthy tissues than benign tissue but BiLSTM ones perform slightly better. LSTM networks eliminate the need for any signal decay model while outputting remarkably good performances in the classification of diffusion signals. BiLSTM networks perform slightly better for very noisy conditions. Prospective studies are needed to justify the potential benefits in a clinical setup.

**Index Terms**—Breast, classification, diffusion signal, long short-term memory network.

## I. INTRODUCTION


**D**IFFUSION WEIGHTED IMAGING (DWI) makes use of magnetic resonance (MR) principles to deliver diffusion signals from a living tissue captured for a set of increasing diffusion weighting that indirectly reflects the degree of tissue cellularity and the integrity of cell membranes and also the microcirculation of blood in the capillary network by demonstrating the microscopic Brownian motion of water

molecules within the tissue [1]. Due to their high cell density and limited extracellular space, malignant lesions exhibit slowly attenuated diffusion signals for increased diffusion weighting. On the contrary, diffusion signals with fast attenuation due to less restricted diffusion of water molecules are of concern for benign tissues. Besides, healthy tissues may exhibit diffusion signals with similar degrees of attenuation by benign lesions [2]. For human breast tissue, the diffusion-weighted imaging protocol that utilizes diffusion weightings from 0 to 800 s/mm<sup>2</sup> and the evaluation strategy that practices the apparent diffusion coefficient metric by a mono-exponential signal attenuation model have been promoted as an essential part of multiparametric breast magnetic resonance imaging by the European Society of Breast Radiology (EUSOBI) [3, 4].

The mono-exponential model enables quantitative characterization of the breast tissues from the diffusion signals to distinguish lesions in the detection and diagnosis of cancer. Moreover, it is quite easy to fit the model to diffusion signals to estimate the apparent diffusion coefficient metric. However, the model has a limited capability in expressing the attenuation in the diffusion signal especially for the malignant tissue and therefore advanced models have been under development [5]. The intravoxel incoherent motion (IVIM) model enumerates the attenuation in the diffusion signal using a weighted summation of two exponential functions and is reported to accomplish better sensitivity when compared to the mono-exponential model in distinguishing malignant from benign breast lesions [6, 7]. The IVIM model makes use of three metrics: pure diffusion coefficient, pseudo-diffusion coefficient, and volume fraction for which estimates are obtained by fitting the model to the diffusion signal by using an advanced fitting algorithm. Implementation difficulties of the available algorithms and their sensitivity to noise may lead to metric estimates out of physiologically acceptable ranges making adoption of the model challenging for clinical practice [8-10]. Besides, the diffusion signals may be processed directly without using a fitting algorithm or a signal attenuation model by artificial neural networks.

A diffusion MR signal demonstrates an attenuated amplitude with reference to a monotonically increasing diffusion weighting determined by  $b$ -value and can be deliberated as “ $b$ -series” data very similar to time-series data for which the neural networks housing long short-term memory (LSTM) blocks offer better competence in recognizing long-term dependencies and influencing the dependencies into computations as long as they need to be taken into account for classification tasks [11].

**GOKHAN ERTAS**, is with Department of Biomedical Engineering, Yeditepe University, Istanbul, Turkey, (e-mail: [gokhan.ertas@yeditepe.edu.tr](mailto:gokhan.ertas@yeditepe.edu.tr)).

 <https://orcid.org/0000-0002-3331-9152>

Manuscript received February 7, 2021; accepted May 11, 2021.  
DOI: [10.17694/bajece.876291](https://doi.org/10.17694/bajece.876291)

This study aims the development of LSTM neural network models to facilitate the classification of human breast tissue from diffusion MR signals for the detection and diagnosis of breast cancer.

## II. MATERIALS AND METHODS

### A. Generation of Diffusion Signals for the Breast

The study dataset consists of breast diffusion MR signals generated synthetically by performing the steps illustrated in Fig. 1. The tissue-specific descriptive statistics for the three model parameters of the IVIM model namely the pure diffusion coefficient ( $D$ ), the pseudo-diffusion coefficient ( $D^*$ ), and the microvascular volume fraction ( $f$ ) are entered into excessive analyses incorporating Monte Carlo simulation runs to generate numerous random  $D$ ,  $D^*$ , and  $f$  triples for the tissue satisfying the statistics fed. The triples generated are next used to obtain noise-free signals for the tissue by numerically solving the equation  $s_b/s_o = (1 - f) \exp(-bD) + f \exp[-b(D^* + D)]$  for a set of  $b$ -values [12]. Finally, noise is added to the noise-free signals at the level defined by the signal-to-noise ratio (SNR) to obtain the noisy forms of the signals. In the current work, the descriptive statistics for three breast tissue types are delivered from a recent study stating that on median (lower, upper quartiles),  $D = 0.85$  (0.77, 0.98)  $\times 10^{-3}$  mm<sup>2</sup>/s,  $D^* = 94.71$  (70.33, 113.23)  $\times 10^{-3}$  mm<sup>2</sup>/s, and  $f = 10.34$  (7.68, 11.88) % for the malignant lesion, and  $D = 1.35$  (1.26, 1.44)  $\times 10^{-3}$  mm<sup>2</sup>/s,  $D^* = 107.49$  (83.20, 131.19)  $\times 10^{-3}$  mm<sup>2</sup>/s, and  $f = 6.83$  (4.72, 10.33) % for the benign lesion whereas  $D = 1.96$  (1.81, 2.15)  $\times 10^{-3}$  mm<sup>2</sup>/s,  $D^* = 124.28$  (113.30, 147.86)  $\times 10^{-3}$  mm<sup>2</sup>/s, and  $f = 5.27$  (3.60, 5.87) % for the healthy tissue [13]. For each tissue type, Monte Carlo simulation runs are performed with 2500 repetitions and numerical solutions are computed for ten  $b$ -values of 0, 30, 70, 100, 150, 200, 300, 400, 500, 800 s/mm<sup>2</sup>. Random Gaussian noise is deliberated at knowledgeable SNRs of 80, 40, 20, and 10 where SNR is defined as the ratio of the noise-free signal amplitude at  $b = 0$  s/mm<sup>2</sup> to the standard deviation of the noise [9].

### B. Design of LSTM Networks for Breast Tissue Classification

Long short-term memory (LSTM) networks are a special type of recurrent neural network that offers better competence in recognizing long-term dependencies and influencing the dependencies into computations to analyzing time-series data for regression and classification tasks. The networks can be implemented using “traditional” LSTM memory blocks that are self-connected subnetworks containing multiple internal cells each having dedicated inputs, outputs, and memory sharable with the other cells in the block [14]. An LSTM memory block can be modified to learn bidirectional long-term dependencies between time steps of time series data and this new block is called bidirectional LSTM (biLSTM) [15].

In the current study, two network models, one housing a traditional LSTM layer and the other consisting of a biLSTM layer are established to classify breast tissues from  $b$ -series data from the diffusion MR signals generated. The models have the same layer structure as presented in Fig. 2. The first layer is the sequence input layer that accepts the “ $b$ -series data” of the diffusion signal of breast tissue to the network. The second

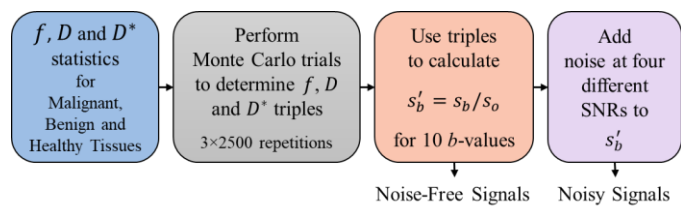


Fig. 1: The framework of synthetic diffusion MR signal generation.

layer is the LSTM layer for the first model and the biLSTM layer for the second model that learns long-term dependencies between  $b$ -values and diffusion MR signal attenuation. The third layer is the fully connected layer that multiplies the output of the LSTM/biLSTM layer by a weight matrix and then adds a bias vector to provide three outputs dedicated to the malignant, benign and healthy breast tissue types. The next layer is the Softmax layer that applies the Softmax function to the outputs of the fully connected layer. The outputs of this layer are evaluated and classification is made concerning the output that provides the largest value. However, during network training, a classification layer is appended to the network to compute loss for the multi-class classification on the outputs of the Softmax layer. During the implementation of the models, neural networks with varying numbers of memory blocks up to twenty are considered for each model.

### C. Training and Testing of Neural Networks

The neural networks implemented are trained using the same training parameters: 300 epochs, a batch size of 125, an initial learning rate of  $5 \times 10^{-4}$ , a gradient threshold of 1, and an adaptive moment estimation optimizer with the cross-entropy loss [16]. Bootstrapping incorporated accuracy analyses are performed to train and then to test the networks [17]. For this purpose, the diffusion MR signals generated are assigned as the original dataset, and twenty bootstrapped datasets, each consisting of random resamples from the original dataset with the same number of signals for each tissue type in the original dataset, are formed.

A network is first trained using the original dataset and on the outputs of the network, an “apparent” accuracy,  $Acc^{app}$  is computed. The network is next trained with the bootstrapped datasets and the outputs of the network for the datasets are processed to compute “bootstrap-sample” accuracies,  $Acc^{bs}$ . Besides, after completion of a training, the network is tested using the original dataset and the outputs are explored to compute “original-sample” accuracies,  $Acc^{os}$ . The differences between  $Acc^{bs}$  and  $Acc^{os}$  pairs are computed and then averaged to calculate an overall optimism value. By subtracting the overall optimism from  $Acc^{app}$ , the “corrected” accuracy,  $Acc^c$  is determined for each network. The network having an  $Acc^{os}$  closest to  $Acc^c$  is deemed the best network.

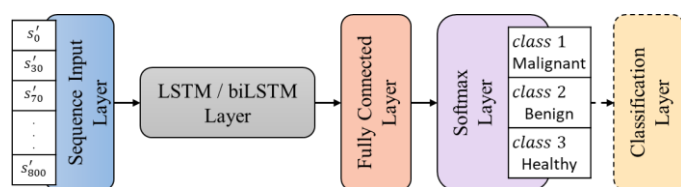


Fig. 2: The LSTM/biLSTM network model to classify breast tissues from the diffusion MR signals of the tissues.

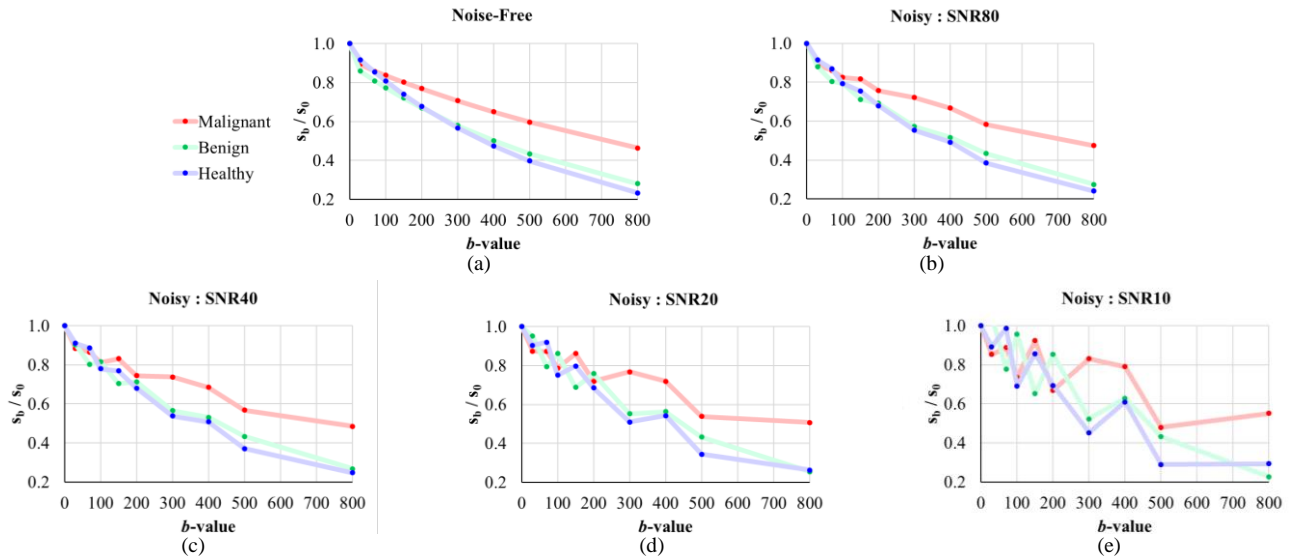


Fig.3: Diffusion MR signals generated using IVIM parameters for the malignant ( $D = 0.84 \times 10^{-3} \text{ mm}^2/\text{s}$ ,  $D^* = 84.42 \times 10^{-3} \text{ mm}^2/\text{s}$ , and  $f = 8.99\%$ ), benign ( $D = 1.45 \times 10^{-3} \text{ mm}^2/\text{s}$ ,  $D^* = 133.08 \times 10^{-3} \text{ mm}^2/\text{s}$ , and  $f = 10.55\%$ ), and healthy tissue ( $D = 1.77 \times 10^{-3} \text{ mm}^2/\text{s}$ ,  $D^* = 110.17 \times 10^{-3} \text{ mm}^2/\text{s}$  and  $f = 3.41\%$ ) considering  $b$ -values of 0, 30, 70, 100, 150, 200, 300, 400, 500, 800 s/mm<sup>2</sup>. (a) Noise-free signals, and (b-e) noisy versions of the signals produced for the noise levels expressed by the SNRs of 80, 40, 20, and 10.

#### D. Assessment of the Neural Network Performance

The performance of the best neural network is assessed using the sensitivity ( $Se$ ), specificity ( $Sp$ ), and accuracy ( $Acc$ ) metrics estimated from the outputs of the network for the original dataset using

$$Se_i = \frac{TP_i}{TP_i + FN_i} \quad (1a)$$

$$Sp_i = \frac{TN_i}{TN_i + FP_i} \quad (1b)$$

$$Acc_i = \frac{TP_i + TN_i}{TP_i + FN_i + TN_i + FP_i} \quad (1c)$$

Here:  $TP$  – is true-positive,  
 $FP$  – is false-positive,  
 $TN$  – is true-negative,  
 $FN$  – is false-negative classifications by the neural network for the  $i$ -th tissue class.

Overall values for the metrics are calculated by summing the performance for a class and dividing the result by three. The metrics are considered very high, high, moderate, low, and very low if their values were 95%-100%, 85%-94.9%, 75%-84.9%, 65%-74.9%, and 0%-64.9%, respectively. The neural networks are numerically implemented and analyzed using our in-house computer software tools developed using MATLAB (v8.2; Natick, MA) on a desktop PC (Intel i7-1065G7 3.90GHz processor, 16GB memory, and 64-bit operating system).

### III. RESULTS

A total of 37500 diffusion MR signals (7500 noise-free and 30000 noisy) are synthetically generated for malignant, benign, and healthy tissues of the human breast. Fig.3 illustrates sample signals for each breast tissue type for noise-free and noisy conditions expressed using the SNR. Signal attenuation is characterized very well using the IVIM model for the noise-free

signals but the model has difficulty describing the attenuation for the noisy signals. Meanwhile, available fitting algorithms probably output misleading estimates for the  $D$ ,  $D^*$  and  $f$  metrics especially for lower SNRs resulting in incorrect classifications.

A total of forty neural networks are developed to perform tissue classification from diffusion MR signals. Twenty networks are relying on an LSTM model, while the remaining networks are based on a BiLSTM model. The networks are implemented with the same layer structure but with different numbers of memory blocks up to twenty in the LSTM/biLSTM layer. By bootstrapping incorporated accuracy analysis, twenty-one training and testing tasks are performed for each network and a total of 840 training and testing tasks are handled at all. Plots for the “corrected” accuracies for the networks for the noise-free and the noisy conditions are seen in Fig. 4. The LSTM and BiLSTM network models reveal very similar moderate to very high accuracies that improve when SNR increases. The accuracy also improves when a larger number of memory blocks is utilized in the models for a specific SNR. The accuracy reaches its maximum value of 100% for the noise-free signals and the noisy signals with an SNR of 80 for both models. Lower accuracies are of concern for the models for the noisy signals with  $SNR \leq 40$ . When SNR is reduced to 40, the LSTM and BiLSTM models provide high to very high accuracies (range: 88.1-98.2% and 88.6-98.9%, mean: 97.1% and 97.2%). For SNR of 20, high accuracies are delivered by the models (range: 86.1-92.4% and 86.2-92.6%, mean: 91.7% and 91.5%). When SNR is further reduced to 10, the models offer moderate to high accuracies (range: 79.3-83.4% and 80.5-83.2%, mean: 82.9% and 82.8%). Higher accuracies are achieved for the models when they are implemented using three or more memory blocks in their LSTM/biLSTM layer. Change in the number of memory blocks results in fewer accuracy variations for the LSTM model while that may cause large fluctuations in the accuracy for the biLSTM model.

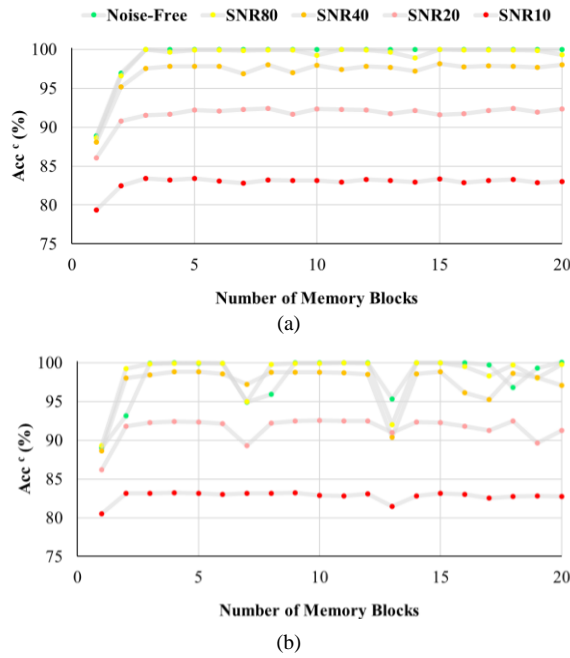


Fig.4: “Corrected” accuracy for the number of memory blocks for the (a) LSTM and (b) biLSTM network models.

The attributes and the classification performances of the best networks by the network model and the noise level are listed in Table I. Corresponding bar graphs for the accuracy and the number of memory blocks of the networks are seen Fig. 5. Use of the LSTM model leads to networks with three memory blocks, while the biLSTM model induces networks with nine and fourteen memory blocks to classify the noise-free and the noisy signals with SNR of 80 of the malignant, benign and healthy breast tissues. The overall performances of the networks are excellent at all ( $Se= 100.0\%$ ,  $Sp= 100.0\%$ , and  $Acc= 100.0\%$ ). For SNR of 40, the models both convey networks with fifteen memory blocks that perform very good, however, a reasonably better overall performance is offered by the BiLSTM model based network ( $Se= 98.3\%$ ,  $Sp= 99.2\%$ , and  $Acc= 98.9\%$ ) compared to the LSTM model based network ( $Se= 97.2\%$ ,  $Sp= 98.6\%$ , and  $Acc= 98.2\%$ ). For SNR of 20, the biLSTM model induces a network with ten memory blocks ( $Se= 88.9\%$ ,  $Sp= 94.5\%$ , and  $Acc= 92.7\%$ ) that performs

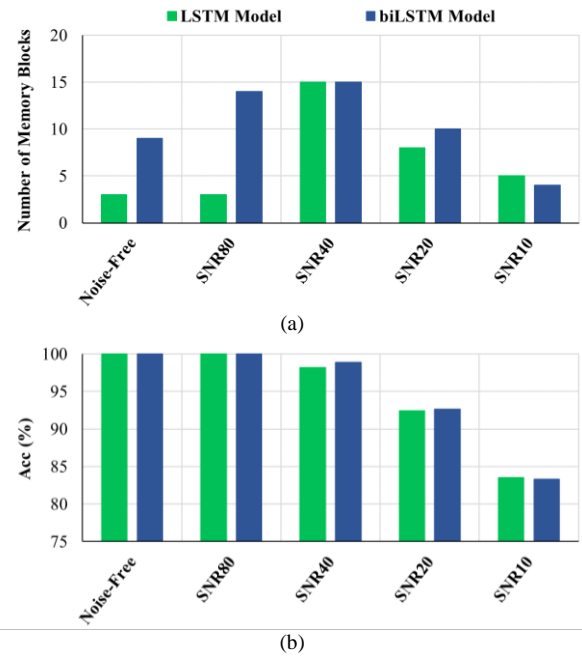


Fig.5: Best networks by the LSTM and BiLSTM network models. (a) Number of memory blocks and (b) overall classification accuracy.

slightly better than the network with eight memory blocks by the LSTM model ( $Se= 88.6.2\%$ ,  $Sp= 94.3\%$ , and  $Acc= 92.4\%$ ). For SNR of 10, the biLSTM model introduces a network with four memory blocks that performs good ( $Se= 74.8\%$ ,  $Sp= 87.4\%$ , and  $Acc= 83.2\%$ ), however, a slightly better performance is achieved by the LSTM model by a network with five memory blocks ( $Se= 75.1\%$ ,  $Sp= 87.6\%$ , and  $Acc= 83.4\%$ ).

Regardless of the model that it relies on, a network may achieve excellent sensitivities, specificities, and accuracies in the classification of the malignant, benign and healthy breast tissues for SNRs  $\geq 80$  and noise-free cases. On the other hand, for SNRs  $\leq 40$ , an LSTM network delivers very high to high sensitivities, specificities, and accuracies better for malignant and healthy tissues than benign tissue; however, a biLSTM network performs slightly better than the LSTM one.

TABLE I  
THE ATTRIBUTES AND PERFORMANCES OF THE BEST NEURAL NETWORKS

		Noise-Free		Noisy : SNR80		Noisy : SNR40		Noisy : SNR20		Noisy : SNR10	
		LSTM	biLSTM	LSTM	biLSTM	LSTM	biLSTM	LSTM	biLSTM	LSTM	biLSTM
<b>Number of Memory Blocks</b>		<b>3</b>	<b>9</b>	<b>3</b>	<b>14</b>	<b>15</b>	<b>15</b>	<b>8</b>	<b>10</b>	<b>5</b>	<b>4</b>
<b>Acc (%)</b>	<b>Overall</b>	<b>100</b>	<b>100</b>	<b>100</b>	<b>100</b>	<b>98.2</b>	<b>98.9</b>	<b>92.4</b>	<b>92.7</b>	<b>83.4</b>	<b>83.2</b>
	Malignant	100	100	100	100	98.5	99.1	93.9	94.1	86.8	86.7
	Benign	100	100	100	100	97.3	98.3	88.6	89.0	75.3	75.0
	Healthy	100	100	100	100	98.8	99.1	94.7	94.9	88.1	87.9
<b>Se (%)</b>	<b>Overall</b>	<b>100</b>	<b>100</b>	<b>100</b>	<b>100</b>	<b>97.2</b>	<b>98.3</b>	<b>88.6</b>	<b>88.9</b>	<b>75.1</b>	<b>74.8</b>
	Malignant	100	100	100	100	97.2	98.5	91.5	90.3	78.4	75.8
	Benign	100	100	100	100	96.3	97.9	83.4	84.6	63.5	63.9
	Healthy	100	100	100	100	98.2	98.4	90.9	91.9	83.4	84.6
<b>Sp (%)</b>	<b>Overall</b>	<b>100</b>	<b>100</b>	<b>100</b>	<b>100</b>	<b>98.6</b>	<b>99.2</b>	<b>94.3</b>	<b>94.5</b>	<b>87.6</b>	<b>87.4</b>
	Malignant	100	100	100	100	99.1	99.5	95.2	96.0	91.1	92.1
	Benign	100	100	100	100	97.7	98.5	91.2	91.1	81.2	80.5
	Healthy	100	100	100	100	99.0	99.5	96.5	96.3	90.4	89.5

## IV. DISCUSSIONS

Long short-term memory (LSTM) networks offer competence in recognizing long-term dependencies and influencing the dependencies into computations in classifying time-series data and their use has been gaining increased interest in medicine predominantly for detection of medical events from electronic health records, classification of diseases from physiological signals and segmentation of lesions from medical images [18-22]. Besides, an LSTM network has been proposed to distinguish malignant and benign breast tissues using the features extracted by a fine-tuned VGGNet from dynamic contrast-enhanced MR signals pondered as “contrast-enhanced time-series data” [23]. The current study inspires LSTM networks for classifying human breast tissues from diffusion MR signals that can be deliberated as “*b*-series data”. Many LSTM networks relying on the traditional LSTM model and the bidirectional LSTM (biLSTM) model are developed to classify the malignant, benign, and healthy tissues from noise-free and noisy signals expressed with signal-to-noise ratio (SNR). Results show that regardless of the model it relies on, an LSTM network may achieve excellent sensitivities, specificities, and accuracies in classifying the tissues from noise-free signals and also from noisy signals with SNRs  $\geq 80$ . These performances are supplied by fewer number of memory blocks when the network is implemented using the traditional LSTM model. For noisy signals having SNRs  $\leq 40$ , a network may deliver high to very high sensitivities, specificities, and accuracies better for the malignant and healthy tissues than the benign tissue regardless of the model it relies on. However, a biLSTM model based network would perform slightly better than a traditional LSTM model based one by supplying an effectively increased amount of data to the network.

There are some limitations of the current study. The diffusion MR signals for the malignant, benign and healthy breast tissues are generated by processing the descriptive statistics of the IVIM model parameters reported from a single-center study [13] and therefore may not be generalized well. Noisy versions of the signals are produced considering Gaussian noise and acknowledgeable range and definition for SNR that might imitate the noise in practice in a limited way. The networks developed house either LSTMs or biLSTMs populated in a single layer and the adoption of additional layers may improve the performances of the networks. Moreover, the networks are trained using a “cross-entropy” loss and better trainings can be accomplished using more sophisticated measures such as “AUC loss” [24] that may further improve the classification performances. The networks are trained using bootstrap incorporated accuracy analysis and the use of alternative methods such as k-fold cross validation may lead to different performances by the networks [25].

In conclusion, LSTM networks eliminate the need for any signal decay model while outputting remarkably good performances in the classification of diffusion MR signals of the human breast tissue. BiLSTM networks perform slightly better for very noisy conditions. Prospective studies are needed to justify the potential benefits in a clinical setup.

## REFERENCES

- [1] G.S. Chilla, C.H. Tan, C. Xu, C.L. Poh. “Diffusion weighted magnetic resonance imaging and its recent trend-a survey.” *Quantitative imaging in medicine and surgery*, vol. 5, no. 3, 2015, pp. 407-422.
- [2] L. Tang, and X.J. Zhou. “Diffusion MRI of cancer: From low to high b-values.” *J. Magn. Reson. Imaging*, vol. 49, 2019, pp. 23-40.
- [3] R. Woodhams, S. Ramadan, P. Stanwell, S. Sakamoto, H. Hata, M. Ozaki, S. Kan, Y. Inoue. “Diffusion-weighted imaging of the breast: Principles and clinical applications.” *RadioGraphics*, vol. 31, 2011, pp. 1059-1084.
- [4] P. Baltzer, R.M. Mann, M. Iima, E.E. Sigmund, P. Clauser, F.J. Gilbert, L. Martincich, S.C. Partridge, A. Patterson, K. Pinker, F. Thibault et al. “Diffusion-weighted imaging of the breast-a consensus and mission statement from the EUSOBI International Breast Diffusion-Weighted Imaging working group.” *Eur Radiol.*, vol. 30, no. 3, 2020, pp. 1436-1450.
- [5] D. Le Bihan, and M. Iima. “Diffusion magnetic resonance imaging: What water tells us about biological tissues.” *PLoS Biol.*, vol. 13, 2015, e1002203.
- [6] M. Zhao, K. Fu, L. Zhang, W. Guo, Q. Wu, X. Bai, Z. Li, Q. Guo, J. Tian. “Intravoxel incoherent motion magnetic resonance imaging for breast cancer: A comparison with benign lesions and evaluation of heterogeneity in different tumor regions with prognostic factors and molecular classification”. *Oncology Letters*, vol. 16, 2018, pp. 5100-5112.
- [7] Y. Kim, K. Ko, D. Kim, C. Min, S.G. Kim, J. Joo, and B. Park. “Intravoxel incoherent motion diffusion-weighted MR imaging of breast cancer: association with histopathological features and subtypes.” *Br. J. Radiol.*, vol. 89, no. 1063, 2016, pp. 20160140.
- [8] N.R. Doudou, Y. Liu, S. Kampo, K. Zhang, Y. Dai, S. Wang. “Optimization of intravoxel incoherent motion (IVIM): variability of parameters measurements using a reduced distribution of b values for breast tumors analysis.” *MAGMA*, vol. 33, 2020, pp. 273-281.
- [9] G.Y. Cho, L. Moy, J.L. Zhang, S. Baete, R. Lattanzi, M. Moccaldi, J.S. Babb, S. Kim, D.K. Sodickson, E.E. Sigmund. “Comparison of fitting methods and b-value sampling strategies for intravoxel incoherent motion in breast cancer.” *Magn. Reson. Med.*, vol. 74, no. 4, 2015, pp. 1077-1085.
- [10] G. Ertas. “Fitting intravoxel incoherent motion model to diffusion MR signals of the human breast tissue using particle swarm optimization.” *An International Journal of Optimization and Control: Theories & Applications (IJOCTA)*, vol. 9, no.2, 2019, pp. 105-112.
- [11] G. Van Houdt, C. Mosquera, and G. Nápoles. “A review on the long short-term memory model.” *Artif. Intell. Rev.*, vol. 53, 2020, pp. 5929-5955.
- [12] D. Le Bihan, E. Breton, D. Lallemand, P. Grenier, E. Cabanis, and M. Laval-Jeantet. “MR imaging of intravoxel incoherent motions: application to diffusion and perfusion in neurologic disorders.” *Radiology*, vol. 161, no. 2, 1986, pp. 401-417.
- [13] C. Liu, C. Liang, Z. Liu, S. Zhang, B. Huang. “Intravoxel incoherent motion (IVIM) in evaluation of breast lesions: Comparison with conventional DWI.” *European Journal of Radiology*, vol. 82, no. 12, 2013, pp. e782-e789,
- [14] S. Hochreiter and S. Jürgen. “Long short-term memory.” *Neural computation*, vol. 9, no. 8, 1997, pp. 1735-1780.
- [15] M. Schuster and P.K. Kuldip. “Bidirectional Recurrent Neural Networks.” *IEEE Trans. Signal Processing*, vol. 45, no. 11, 1997, pp. 2673-2681.
- [16] D. P. Kingma, and J. Ba. “Adam: A method for stochastic optimization.” *arXiv preprint arXiv:1412.6980*, 2014.
- [17] F.E. Harrell, K.L. Lee, D.B. Mark. “Multivariable prognostic models: issues in developing models, evaluating assumptions and adequacy, and measuring and reducing errors.” *Stat Med.*, vol. 15, no. 4, 1996, pp. 361-387.
- [18] J. Chu, W. Dong, K. He, H. Duan, Z. Huang. “Using neural attention networks to detect adverse medical events from electronic health records.” *Journal of Biomedical Informatics*, vol. 87, 2018, pp. 118-130.
- [19] B. Rim, N.J. Sung, S. Min, M. Hong. “Deep learning in physiological signal data: A survey.” *Sensors (Basel)*, vol. 20, no. 4, 2020, pp. 969.
- [20] P. Nagabushanam, S. Thomas George, S. Radha. “EEG signal classification using LSTM and improved neural network algorithms.” *Soft Computing*, vol. 24, 2020, pp. 9981-10003.
- [21] S. Saadatnejad, M. Oveisi, M. Hashemi. “LSTM-Based ECG classification for continuous monitoring on personal wearable devices. *IEEE J. Biomed. Health Inform.*, vol. 24, no. 2, 2020, pp. 515-523.
- [22] M.H. Hesamian, W. Jia, X. He, P. Kennedy. “Deep learning techniques for medical image segmentation: Achievements and challenges.” *J. Digit. Imaging.*, vol. 32, no. 4, 2019, pp. 582-596.



- [23] N. Antropova, B. Huynh, H. Li, M.L. Giger. "Breast lesion classification based on dynamic contrast-enhanced magnetic resonance images sequences with long short-term memory networks." *J. Med. Imaging (Bellingham)*, vol. 6, 2018, 011002.
- [24] S. Gultekin, A. Saha, A. Ratnaparkhi, J. Paisley. "MBA: Mini-Batch AUC Optimization." *IEEE Transactions on Neural Networks and Learning Systems*, vol. 31, no. 12, 2020, pp. 5561-5574.
- [25] J.H Kim. "Estimating classification error rate: Repeated cross-validation, repeated hold-out and bootstrap." *Computational Statistics & Data Analysis*, vol. 53, no. 11, 2009, pp. 3735-3745.

#### BIOGRAPHIES



**GOKHAN ERTAS** Istanbul, in 1976, received his B.S. degree from Erciyes University in Electronics Engineering in 1998 and his M.S. and Ph.D. degrees from Bogazici University in Biomedical Engineering in 2001 and 2007, respectively. He led efforts in developing computational methods to comparing breast MR images at the

Institute of Cancer Research and the Royal Marsden Hospital, UK. He is currently the vice-chairman of the Biomedical Engineering Department at Yeditepe University. His interests include machine learning methods for better characterization of breast tissues to improve the detection and diagnosis of breast cancer using MR imaging.

# A Novel Chaotic Switched Modulation for EMI Suppression in Electrical Drive System

Mehmet Emin Asker and Hasan Kurum


**Abstract**—In electric drive systems common mod voltage (CMV) is known as voltage between power line and ground. CMV causes negative effects on both electric engine and its driver whereas switching operation occurs in power devices. In addition switching frequency and its multiples in CMV cause electromagnetic and acoustic noises. In this paper a novel Fixed-Frequency chaotic switched sinusoidal pulse width modulation (FFCS-SPWM) is proposed. The crucial point in proposed FFCS-SPWM method is to obtain a new carrier wave by summation of carrier wave and its inverse form. In FFCS-SPWM method extra switching losses were reduced due to constant switching frequency. This method also applied to permanent magnet synchronous motor (PMSM) vector control system. The reduction of electromagnetic interference (EMI), acoustic noises and  $dv/dt$  stress effects that occur in CMV is simulated by proposed method. Moreover SPWM combined with chaotic-frequency chaotic switched (CFCS) is proposed to reduce the differential mode voltage (DMV) which occurs due to voltage between lines. Finally in this method switching frequency change chaotically and also in this paper it is shown that, CFCS-SPWM provides to reduce EMI, acoustic noises which are caused by CMV and DMV.

**Index Terms**— Common Mod Voltage, Chaotic switching, Elektromagnetic interference (EMI), Acoustic noise


## I. INTRODUCTION

CMV AND DMV have some bad effects on PWM voltage based inverter. DMV can damage engine windings or reduce engine life under condition of immediately change occurs in high frequency inverter voltage. On the other hand change occurs in CMV, causes leakage current between engine shaft and ground due to immediately change in CMV that provide electrostatic coupling between stator and rotor. These leakage currents that have high amplitude damages grounding system and causes EMI in transmission line. In addition coupling effect and leakage current that is in engine bearing cause physical disruption in motor bearing. The immediately

**MEHMET EMİN ASKER**, is with vocational school of technical sciences of Dicle University, Diyarbakir, Turkey (e-mail: measker@dicle.edu.tr).

 <https://orcid.org/0000-0003-4585-4168>

**HASAN KÜRÜM**, is with Department of Electrical-Electronics Engineering of Firat University, Elazig, Turkey, (e-mail: hkurum@firat.edu.tr)

 <https://orcid.org/0000-0002-5498-6819>

Manuscript received January 9, 2021; accepted May 25, 2021.

DOI: [10.17694/bajece.857247](https://doi.org/10.17694/bajece.857247)

change occurs due to switching frequency of inverter. Therefore voltage causes harmonics that create EMI and acoustic noises in switching frequency and its multiples [1-9]. The harmonics that are in the interval of (9-150) KHz known as EMI, whereas (6-20) KHz called as audible acoustic noise. Especially the harmonics between 6-12 KHz create noises that disturb ears. The solution for mentioned problem is not increasing switching frequency because it causes losses [8-14].

Switching of power devices causes to change in voltage and current in a short time that creates EMI. The establishments related with electromagnetic compatibility (EMC) specify some limitation about EMI. An electrical equipment or devices must have certificate of conformity which provided by these establishments [15-17].

To avoid the bad effects of CMV and DMV several methods were improved such as increasing switching frequency, suitable filter design. Filter design can be solution for harmonics, however it has drawback in terms of cost, volume and weight [15].

To reduce the harmonics amplitude of CMV and DMV spreading of amplitude in an interval which known as modulation techniques [15-25] are used to avoid the negative effects of CMV, DMV and acoustic noises [16-17]. These modulation techniques known as random and chaotic modulation.

Moreover in lower switching frequency case especially engine/motor with a low leakage inductance has high current harmonic components that causes vibration, noise and losses [21].

There are various paper reduction of EMI and acoustic noise with modulation method in AC drive systems [9-14]. Random modulation methods are improved to suppress EMI [18-24,29]. Due to spreading harmonic in these methods. They provide reduction in acoustic noises and mechanical vibration.

Random PWM can be realized as method such as random frequency switching, random pulse position technique and random switching [18]. On the other hand SPWM and space vector (SV) modulation can be employed to realize random modulation. There some paper about reduction of EMI and acoustic noise by using random PWM techniques [23-24,30].

Another problem appears in electrical driver is noises occurs during motor operation. These acoustic noises are caused by magnetic, mechanical, aerodynamics or electronic effects [10].

The noises based on electronic effects appears due to switching frequency in power converters. In Inverter based AC driver switching frequency causes to undesirable problems such as switching losses vibration, momentum ripple and EMI. Acoustic noises especially below 20 KHz are disturbing for

ears. Random or chaotic PWM modulation is usually applied to induction motor. However for PMSM driver researches are limited. On the other hand the papers focused on chaotic modulation that, is applied to PMSM driver, are rare [10-14,23,31].

PSMS becomes to compete with induction motor in terms of volume, efficiency and lifetime coast. Recently they become popular in air and sea transport [32]. Especially in surface mounted PMSM motor has a lower phase inductance than induction motors. Therefore, PMSM affects EMI more than induction motor [30].

Inspire the chaotic modulation methods improved from random modulation methods. Chaotic signal can be obtained and applied easier than random signal because random signals are obtained from different circuits by help of algorithm [24]. There are some methods about chaotic modulation in literature. These are known as chaotic pulse position PWM, hybrid chaotic SPWM and SV-PWM [15-17,29]. The chaotic methods are applied to induction motor driver and obtained reduction in EMI, acoustic noises and mechanical vibration by Zheng [16-17].

In this paper for PMSM vector controlled driver a novel constant frequency chaotic switched FFCS-SPWM method and chaotic frequency chaotic switched CFCS-SPWM methods is proposed. In this method it is shown that with the advantage of constant switching frequency EMI and acoustic noises due to CMV are reduced.

Although this method is successful to reduce CMV negative effects, it is not successful to reduce DMV based noise. Therefore CFCS- SPWM method is improved to show reduction of noises that are based on DMV. The effects of method is shown by using power density comparison of CMV and DMV.

In this study, conventional SPWM, chaotic switching frequency PWM (CSPWM), random switching frequency SPWM (RSPWM), FFCS-SPWM, CFCS- SPWM, fixed-frequency random Switched (FFRS) SPWM and random-frequency random switched (RFRS) SPWM were compared. In literature, generally random bits are obtained by shift registers in random switching methods. This proposal method only one D type flip-flop is used to obtain random bits. The feature of the method is reduced the complexity of the method and unnecessary elements requirement. Furthermore first time in this paper the bits that are obtained by D type flip flop is used for inverter modulation.

## II. EFFECTS OF CMV AND DMV ON DRIVER SYSTEMS

CMV is the potential difference between the midpoint of DC inverter's bus and star point of load. This value is dependent to inverter output voltage. The output voltage of inverter is formed by pulse which its average value is sinusoidal wave. The frequencies that except basic frequency is known as harmonic and these frequencies causes undesirable effects on motor. Especially due to sudden sharp rising and falling in voltage high frequency harmonics occurs in switching operation. This harmonic also causes to damage seriously both on motor and driver circuit. In lower switching frequency motors whose leakage inductances are small and its harmonics in current are high cause vibration, noise and loses. Therefore switching frequency increases in range of switching loses are allowed. In KW power applications switching

frequency is selected interval between 3-25 KHz[21].

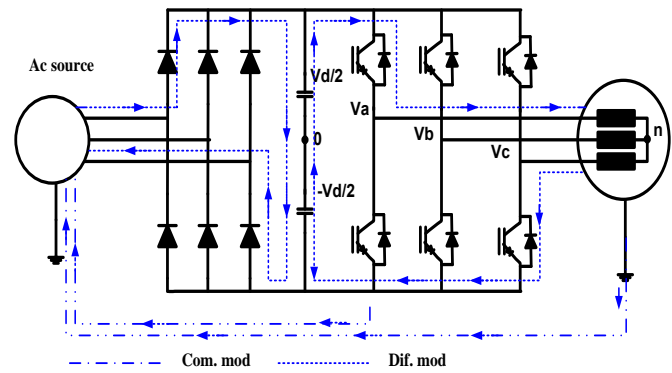


Fig. 1. Effects of CMV and DMV on AC drivers system

Using figure 1 CMV and DMV can be computed from equation (1-2)

$$V_{CM} = V_{n0} = (V_{a0} + V_{b0} + V_{c0}) / 3 \quad (1)$$

$$V_{DM} = V_{i0} - V_{j0}, (i, j = a, b, c) \quad (2)$$

## III. PROPOSED CHAOTIC MODULATION METHODS

### A. Chaotic Switching Frequency

In most of chaotic modulation methods it is need a chaotic switching frequency or a carrier triangle wave whose period is changed chaotically in specific interval. To make frequency chaotic in equation (4) chaotic map variable is used [15-16, 24].

In literature and also in this paper to make a frequency chaotic logic map is used. In these maps depends of parameters system behaves periodic or in some case it behaves as chaotic. The logic map that is given in equation (3) behaves as chaotic in case A changes in interval of (3, 57-4).

In this paper A is taken as 3,9

$$X_{n+1} = AX_n(1 - X_n) \quad (3)$$

$$f = f_0 + X_n \Delta f \sin(2\pi f_m t) \quad (4)$$

$f$  is real switching frequency  $f_0$  is fixed switching frequency  $\Delta f$  the amount of change in frequency,  $f_m$  frequency of modulation.  $X_n$  is chaotic map variable

### B. Chaotic Bit

Chaotic bits can be obtained from a chaotic map or an oscillator. Chaotic maps can be in one or two dimension. The variable of one dimension maps is a sign that varies in the interval of [0-1]. It varies interval of [(-1)-1] in two dimension maps. The chaotic bits in sampling period can be obtain in case where chaotic map variables match with a reference value or two obtained signal as a chaotic map performs in two different star point.

### C. Carrier Wave with Chaotic Period

The switching frequency is same as frequency of carrier triangle wave. Therefore the frequency of carrier triangle wave

can be changed chaotically as switching frequency changes chaotically. The carrier triangle wave can be obtained in different ways. For example in each 0.25 period of wave an equation constructs and then they can be combined to obtain triangle wave equation or identify method can be employed. Equation (6,18) can be employed to obtain triangle wave. In this paper carrier wave is obtained from equation (4). Equation (5) and (6) is also used to obtain carrier wave [16].

$$V_t = \frac{2}{\pi} \arcsin(\sin(X)) \tag{5}$$

$$X = \int_{-\infty}^t \left[ 2\pi f_0 + 2\pi \Delta f X_n \sin \left( \int_{-\infty}^t 2\pi f m dt \right) \right] dt \tag{6}$$

**D. FFCS-SPWM Method**

The aim of to improve a novel constant switching frequency method it is easy to used in application. In FFCS-SPWM a carrier wave that has a constant switching frequency and its negative (reverse/inverse) form and with help of 2x1 multiplexer it is matched with reference wave. Selected control signal is obtained from random bit generator. The output wave is carrier wave as random bit generator output is 1 otherwise it is reverse form of carrier wave. Thus a new carrier wave is obtained by help of random switching frequency. By comparing this new carrier wave with the reference wave, the inverter control signal (PWM) is obtained.

In this method, chaotic bits obtained with the help of logistic maps are obtained. Then these chaotic bits are transformed into random bits at the carrier wave frequency with the help of D-type flip flops. This method is illustrated in fig 2.

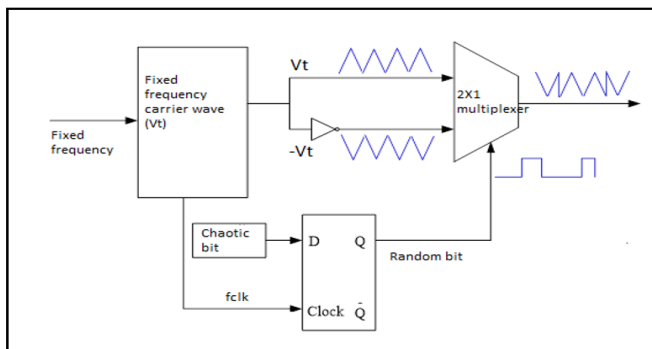


Fig. 2. The principal scheme of FFCS- SPWM method

**E. CFCS-SPWM Method**

In this method a new method is formed from carrier wave frequency which is made chaotic. In this method switching frequency change chaotically. It means carrier wave period change chaotically. In DSP applications, it is difficult to apply CFCS-SPWM because its frequency changes chaotically [24]. However, it can be applied as open and closed loop to DSP and FPGA applications where the switching frequency is variable. The principal CFCS-SPWM method scheme is given in fig. 3

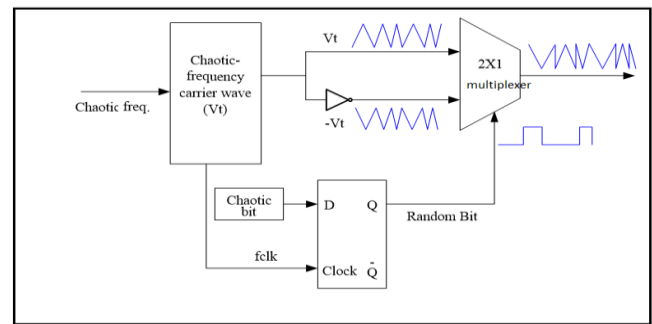


Fig. 3. The principal scheme of CFCS-SPWM method

**IV. SIMULATION RESULTS**

The simulations were done by matlab-simulink. In this research simulation were done for c conventional SPWM, CSPWM (logistic map), FFCS-SPWM (logistic map), FFRS-SPWM (random signal,) CFCS-SPWM (logistic map) and RFRS-SPWM (random signal). For power spectrum matlab periodogram was used.

In simulation it is compared the effect of proposal method for CMV and DMV in view of reduction of EMI and acoustic noises. For EMI the power spectral density of VCM and VDM was investigate.

The result obtained from PSD is in the acceptable range (9-150) KHz. It is allowed in country by VDE[16-17].

Acoustic noise can be analysed in the frequency that is below 20 KHz. However interval of (6-12) KHz in power spectrum that disturbs ears can informed clearly for acoustic noise [16-17]. In addition the negative effects of harmonics that occurs in CMV are analysed in interval of (0-25) KHz which the negative effect of harmonic is reduced. In simulation used motor has 5N.m loaded and 63 Rad/s reference velocity and for each method CMV and DMV power spectral density is obtained.

All discussion is made for EMI between intervals of 9-150 kHz over max PSD value. The amplitude of harmonic is indicated the amplitude of EMI.

In figure 4 the CMV power spectrum is obtained and the result shows that it is 19 dB/Hz for SPWM, 0 dB/Hz for CSPWM, 0 dB/Hz for FFCS-SPWM, 2 dB/Hz for FFRS-SPWM, -5 dB/Hz for CFCS-SPWM, -1 dB/Hz for RFRS-SPWM. Moreover form VDM result that are given in fig.5. It is 18 dB/Hz for SPWM, 9 dB/Hz for CSPWM, 17 dB/Hz for FFCS-SPWM, 17 dB/Hz FFRS-SPWM, 5 dB/Hz for CFCS-SPWM, 8 dB/Hz for RFRS-SPWM. These values of the methods are given in Table II.

The CMV analyses show that the performance of FFCS-SPWM is better than the performance of conventional fixed frequency SPWM and FFRS-SPWM. However for all methods CFCS-SPWM shows the best performance. The result shows proposal methods are successful in reduction EMI.

Furthermore for acoustic noise the interval of (0-12) KHz was analyzed in figure 4. For that interval of (0-12) KHz CMV is 39 dB/Hz for SPWM, 19 dB/Hz for CSPWM, 13 dB/Hz for FFCS-SPWM, 12 dB/Hz for FFRA-SPWM, 10 dB/Hz for CFCS-SPWM, 12 dB/Hz for RFRS-SPWM. The result of VDM in figure 5. It is 18 dB/Hz for SPWM, 10 dB/Hz for CSPWM, 17 dB/Hz for FFCS-SPWM, 17 dB/Hz

for FFRS-SPWM, 5 dB/Hz for CFCS-SPWM, 7 dB/Hz for RFRS-SPWM. These values of the methods are given in Table II.

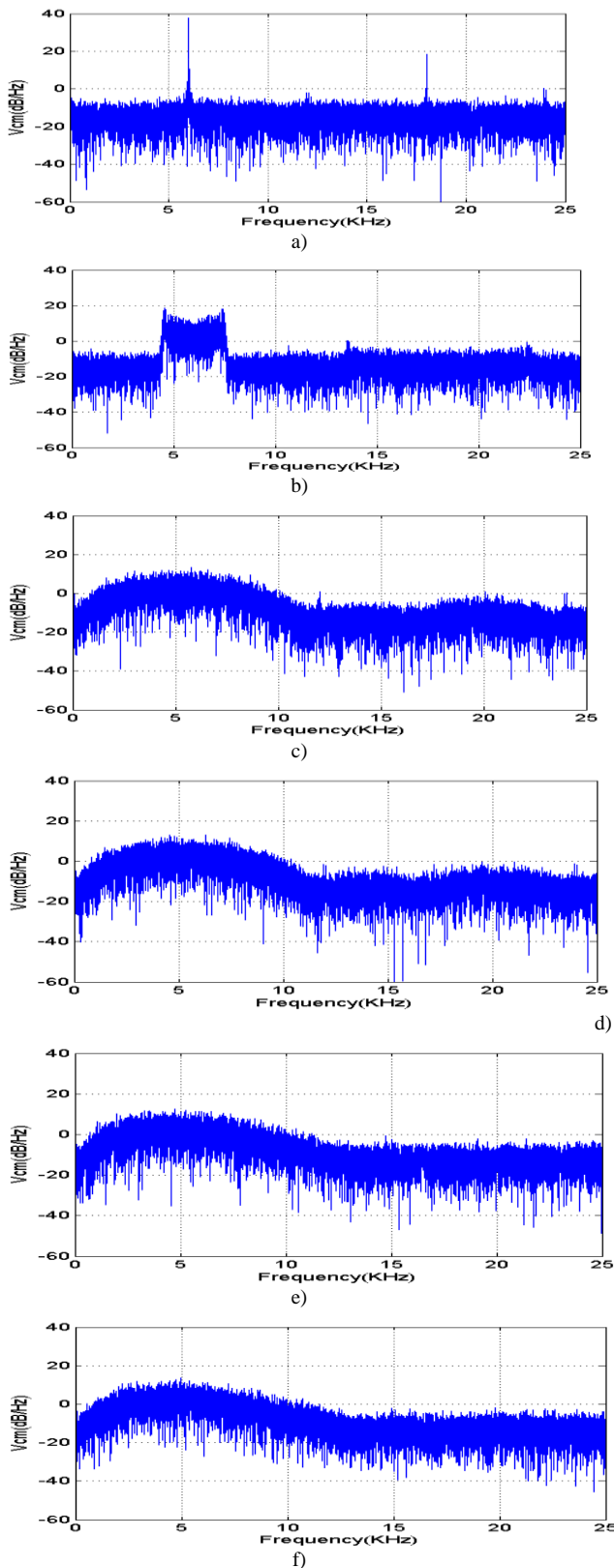


Fig. 4. Power Spectral Density for  $V_{cm}$  (CMV) a) SPWM b) CSPWM (logistic map) c) FFCS-SPWM (logistic map) d) FFRS-SPWM (random signal) e) CFCS-SPWM (logistic map) f) RFRS-SPWM (random signal)

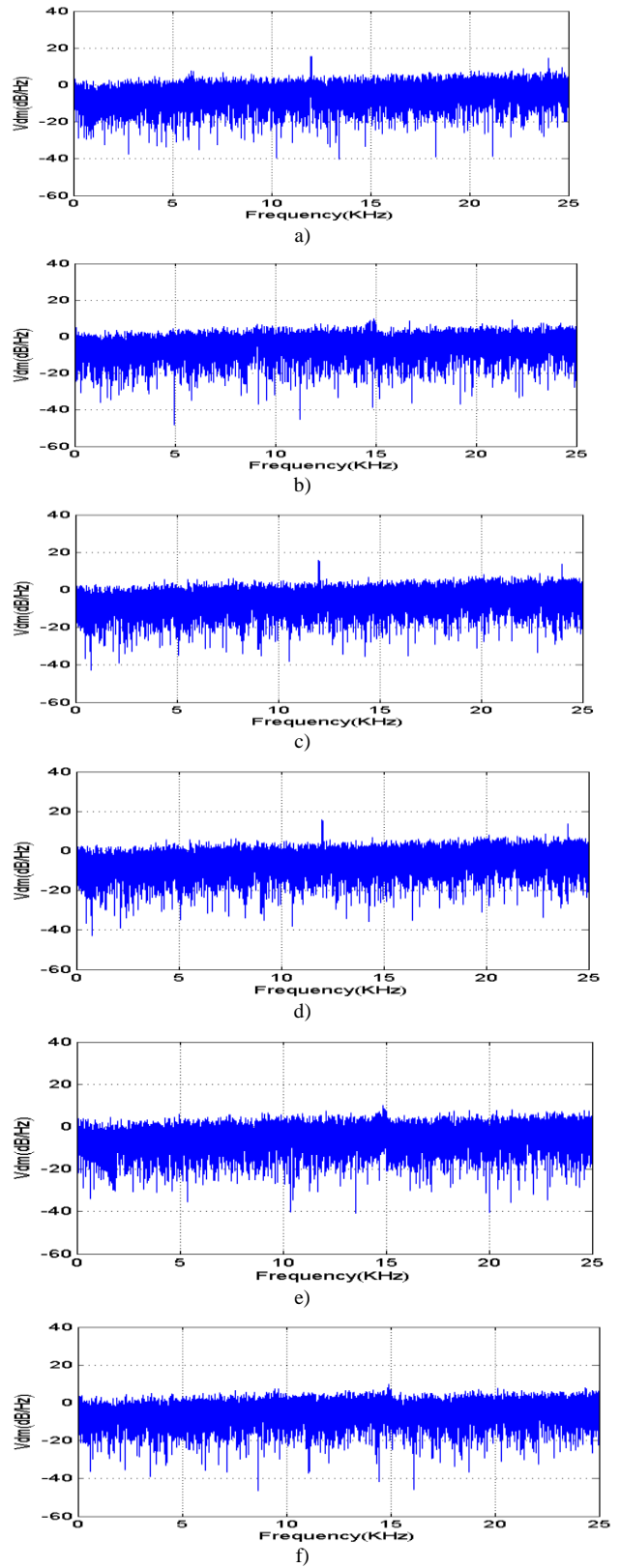


Fig. 5. Power Spectral Density for  $V_{dm}$  (DMV) a) SPWM b) CSPWM (logistic map) c) FFCS-SPWM (logistic map) d) FFRS-SPWM (random signal) e) CFCS-SPWM (logistic map) f) RFRS-SPWM (random signal)

The result show the proposal methods are successful in reduction acoustic noise and the best result is obtained in CFCS-SPWM method.

Finally the proposal methods are succesful enough for CMV which is know resans of harmonics that spreads to reduce their amplitude by the proposal methods.

TABLE I.  
MOTOR PARAMETERS

$R_s$	0.41 $\Omega$	J	0.0222 $\text{Kg}\cdot\text{m}^2$
$L_d$	6.8 mH	B	0 Nms/rad
$L_q$	6.8 mH	$U_N$	220 V
P	2	$K_T$	0.653 Nm/A

TABLE II  
EMI AND ACOUSTIC NOISE OF METHODS

METHODS		Common Mod Voltage ( $V_{cm}$ )		Differential Mode Voltage ( $V_{dm}$ )	
		(PSD)		(PSD)	
		EMI (dB/Hz)	Acoustic noise (dB/Hz)	EMI (dB/Hz)	Acoustic noise (dB/Hz)
Fixed Frequency	SPWM	19	39	18	18
	CSPWM	0	19	9	10
	FFCS-SPWM	0	13	17	17
	FFRS-SPWM	2	12	17	17
Chaotic Frequency	CFCS-SPWM	-5	10	5	5
	RFRS-SPWM	-1	12	8	7

## V. CONCLUSIONS

In this paper method are proposed to reduce EMI and acoustic noises that are based switching frequency. In addition the reduction of effect of harmonics that are CMV based were analysed. The comparison that is based fixed switching frequency methods over CMV results show that the proposed FFCS-SPWM method has closer result to FFRS SPWM, but it has better result than FFRS-SPWM. The CFCS-SPWM method is the best proposal method due to result of simulations.

The result of chaotic and random method are closer. On the other hand the result of chaotic methods are better than the result of random methods. However the chaotic signal can be obtained more easier than random signal. These properties of chaotic method make them superior. In the chaotic method does not need filter due to reduce the effects of harmonics.

## REFERENCES

[1] D. Jiang, F. Wang, and J. Xue, "PWM impact on CM noise and AC CM choke for variable-speed motor drives," *IEEE Trans. Ind. Appl.*, vol. 49, no. 2, pp. 963–972, Mar./Apr. 2013.

[2] C.-C. Hou, C.-C. Shih, P.-T. Cheng, and A. M. Hava, "Common-mode voltage reduction pulse width modulation techniques for three-phase grid connected

converters," *IEEE Trans. Power Electron.* vol. 28, no. 4, pp. 1971–1979, Apr. 2013.

- [3] J. Huang and H. Shi, "Reducing the common-mode voltage through carrier peak position modulation in an SPWM three-phase inverter," *IEEE Trans. Power Electron.*, vol. 29, no. 9, pp. 4490–4495, Sep. 2014.
- [4] J. W. Kimball and M. Zawodniok, "Reducing common-mode voltage in three-phase sine-triangle PWM with interleaved carriers," *IEEE Trans Power Electron.*, vol. 26, no. 8, pp. 2229–2236, Aug. 2011.
- [5] S. Kwak, and S.Mun, "Model Predictive Control Methods to Reduce Common-Mode Voltage for Three-Phase Voltage Source Inverters" *IEEE Trans Power Electron.*, vol. 30, no. 9, pp. 5019–5034, Sep. 2015.
- [6] M. C. Di Piazza, G. Tine, and G. Vital, "An improved active common mode voltage compensation device for induction motor drives," *IEEE Trans. Ind. Electron.*, vol. 55, no. 4, pp. 1823–1834, Apr. 2008.
- [7] J. Huang and H. Shi, "A Hybrid Filter for the Suppression of Common-Mode Voltage and Differential-Mode Harmonics in Three-Phase Inverters With CPPM," *IEEE Trans. Ind. Electron.*, vol. 62, no. 7, pp. 3991–4000, Jul. 2015.
- [8] L. Xing and J. Sun, "Conducted common-mode EMI reduction by impedance balancing," *IEEE Trans. Power Electron.*, vol. 27, no. 3, pp. 1084–1089, Mar. 2012.
- [9] D. Han, S. Li, Y. Wu, W. Choi and B. Sarlioglu, "Comparative analysis on conducted CM EMI emission of motor drives: WBG versus Si devices", *IEEE Trans. Ind. Electron.*, vol. 64, no. 10, pp. 8353-8363, Oct. 2017.
- [10] K. Borisov, T. E. Calvert, J. A. Kleppe, E. Martin, and A. M. Trzynadlowski, "Experimental investigation of a naval propulsion drive model with the PWM-based attenuation of the acoustic and electromagnetic noise," *IEEE Trans. Ind. Electron.*, vol. 53, no. 2, pp. 450–457, Apr. 2006.
- [11] Y. G. Jung, S. H. Na, Y. C. Lim, and S. H. Yang, "Reduction of audible switching noise in induction motor drives using random position space vector PWM," *IEE Proc.—Electr. Power Appl.*, vol. 149, no. 3, pp. 195–200, May 2002.
- [12] T. G. Habetler and D. M. Divian, "Acoustic noise reduction in sinusoidal PWM drives using a randomly modulated carrier," *IEEE Trans. Power Electron.*, vol. 6, no. 3, pp. 356–363, Jul. 1991.
- [13] J. A. Ferreira, P. Dorland, and F. G. de Beer, "An active inline notch filter for reducing acoustic noise in drives," *IEEE Trans. Ind. Appl.*, vol. 43, no. 3, pp. 798–804, May/June. 2007.
- [14] H. B. Ertan and N. Balkan, "Comparison of PWM and PFM induction drives regarding audible noise and vibration for household applications," *IEEE Trans. Ind. Appl.*, vol. 40, no. 6, pp. 1621–1628, Nov./Dec. 2004.
- [15] H. Li, Y.Liu, J.Lü, T. Zheng, and X. Yu, "Suppressing EMI in Power Converters via Chaotic SPWM Control Based on Spectrum Analysis Approach" *IEEE Trans. Ind. Electron.*, VOL. 61, NO. 11, pp.6128-6136,2014.
- [16] Z. Wang, K. T. Chau, and C. H. Liu, "Improvement of electromagnetic compatibility of motor drives using chaotic PWM," *IEEE Trans. Magn.*, vol. 43, pp. 2612–2614, 2007.

- [17] Z. Zhang, K. T. Chau, Z. Wang, and W. Li, "Improvement of electromagnetic compatibility of motor drives using hybrid chaotic pulse width modulation," *IEEE Trans. Magn.*, vol. 47, no. 10, pp. 4018- 4021, 2011.
- [18] R. L. Kirlin, S. Kwok, S. Legowski, and A. M. Trzynadlowski, "Power spectra of a PWM inverter with randomized pulse position" , *IEEE Trans. Power Electron.*, vol. 9, no. 5, pp. 463–472, 1994
- [19] K.S. Kim, Y.G. Jung, and Y.C. Lim, "A New Hybrid Random PWM Scheme" *IEEE Trans. Power Electron.*, vol. 24, no. 1, pp.192-200, 2009
- [20] S. Kaboli, J. Mahdavi, and A. Agah "Application of Random PWM Technique for Reducing the Conducted Electromagnetic Emissions in Active Filters" *IEEE Trans. Ind. Electron.*, vol. 54, no. 4, pp.2333-2343, 2007
- [21] A. M. Hava, E Ün, "Performance Analysis of Reduced Common-Mode Voltage PWM Methods and Comparison With Standard PWM Methods for Three-Phase Voltage-Source Inverters" *IEEE Trans. Power Electron* ;vol. 24, no. 1, pp.241-252, 2009
- [22] Y.C. Lim, S.O. Wi, J.N. Kim, and Y.G. Jung "A Pseudorandom Carrier Modulation Scheme" *IEEE Trans. Pow. Electron* ;vol. 25, no. 4, pp.797-805, 2010
- [23] J.-Y. Chai, Y.-H. Ho, Y.-C. Chang, and C.-M. Liaw, "On acoustic noise reduction control using random switching technique for switch mode rectifiers in PMSM drive," *IEEE Trans. Ind. Electron.*, vol. 55, no. 3, pp. 1295–1309, 2008.
- [24] H. Khan, E. Miliani, and K. E. K. Drissi, "Discontinuous random space vector modulation for electric drives: A digital approach," *IEEE Trans. Power Electron.*, vol. 27, no. 12, pp. 4944–4951, 2012
- [25] R. Gamoudi, D. Chariag and L. Sbita, "A review of spread spectrum based PWM techniques—A novel fast digital implementation", *IEEE Trans. Power Electron.*, vol. 33, no. 12, pp. 10292-10307, Dec. 2018.
- [26] G. Wang, L. Yang, G. Zhang, X. Zhang and D. Xu, "Comparative investigation of pseudorandom high-frequency signal injection schemes for sensorless IPMSM drives", *IEEE Trans. Power Electron.*, vol. 32, no. 3, pp. 2123-2132, Mar. 2017.
- [27] Sreej P, Muthukumar P, Padmasuresh L (2018) Boost up of random pulse width modulation over sinusoidal pulse width modulation for three phase voltage source inverter. *Int J Pure Appl Math* 119:407–429
- [28] K. T. Chau and Z. Wang, *Chaos in Electric Drive Systems-Analysis, Control and Application*. Singapore: Wiley, 2011.
- [29] H. Li, Z. Li, B. Zhang, F. Wang, N. Tan, and W. A. Halang, "Design of analogue chaotic PWM for EMI suppression," *IEEE Trans. Electromagn.* vol. 52, no. 4, pp. 1001–1007, 2010.
- [30] Y. Xu , Q. Yuan , J. Zou and Y. Li "Analysis of triangular periodic carrier frequency modulation on reducing electromagnetic noise of permanent magnet synchronous motor" *IEEE Trans. Magn.*, vol. 48, no. 11, pp. 4424-4427, 2012
- [31] M.E.Asker, A.B. Ozer, H. Kurum, Reduction of EMI with chaotic space vector modulation in direct torque control. *Elektronika ir Elektrotechnika* 2016; 22 (1): 8-13.
- [32] B. K. Bose, *Power Electronics And Motor Drives: Advances and Trends*, USA, elsevier, 2006

## BIOGRAPHIES



**MEHMET EMIN ASKER** was born in Diyarbakır, Turkey, in 1976. He received the B.S. degree in electrical electronics engineering, from Firat University, Elazig, Turkey in 1993, the M.S. degree and the Ph.D. degree in electrical machines, power electronics from Firat University, Elazig, Turkey,

in 2009 and 2016, respectively. He is an Assistant Professor with Dicle University, Department of electrical power and energy. Where he teaches courses on power system, power electronics, circuit theory and electrical machines since 2007. His research interests include electrical machines, power electronics and power systems.



**HASAN KURUM** received the B.S., M.S., and Ph.D. degrees from Firat University (FU), Elazig, Turkey, in 1979, 1984, and 1990, respectively, all in electrical and electronics engineering. In 1997 and 2003, he became an Associate Professor and a Professor, respectively, at the Department of Electrical and

Electronics Engineering, FU. He was also a Chief of Data Processing Center in 1997–2000 and 2004–2006 and a Founder Member and the Chief of Informatics Department at F.U. in 1990–2000 and 2002–2006. He designed the Infrastructure of Computer Data Processing and Computer Network. Between 2006 and 2009, he was the Dean of the Faculty of Communication. He completed Firat TV's new digital communication infrastructure and established Radio Firat. He was assigned as a Founder Dean at the Department of Engineering Faculty, Tunceli University, which was established in 2009. He is currently the Head of the Department of Electrical and Electronics Engineering, FU

# Classification of Urease Activity in Full-Fat Soybean Production by Extrusion Using Machine Learning Algorithms

Ilyas Ozer

**Abstract**—Soybean is an important food source that is frequently preferred in animal feeds with its high protein value. However, soybeans contain many bioactive compounds that are antinutritional and/or poisonous. Urease is one of the most important of these. Processes such as extrusion is used to reduce these components' effect. Here, factors such as steam pressure and temperature affect the cooking level of the product. In the case of undercooked soybeans, components that harm animal health preserve their effect, while their nutritional value decreases in case of overcooking. The urease test has been used for many years to evaluate the cooking level of soybean. Here, according to the color change on the product as a result of the test, the cooking level is evaluated by an expert. This process is mostly done manually and is dependent on expert judgment. In this study, a machine learning-based approach has been proposed to evaluate the images of urease test results. Accordingly, samples were taken from the extruder during the processing of full-fat soybean. A data set consisting of overcooked, well-cooked and undercooked sample images was prepared by performing the urease test. A binary classification process as cooked and undercooked and a classification process with three classes was carried out with four different machine learning models on the data set. In this way, it is aimed to both automate the process and minimize the problems that may arise from expert errors. Classification achievements of 96.57% and 90.29% were achieved, respectively, for two and three class tests with the CNN-LSTM model in 10-fold cross-validation tests.


**Index Terms**—Convolutional neural network, Long short-term memory network, Soybean urease test.

## I. INTRODUCTION

SOYBEAN MEAL is a very important part of all protein sources used in animal feed worldwide [1] due to its high protein concentration [2][3][4]. In addition, soybean meal extracted from oil (SBM) and full-fat (FFSB) are the major global raw materials for broiler diets [5]. The high protein content of soy and the wide availability of oil-extracted soybean by-products have made soybean a widely used alternative to animal protein sources.

Still, soybeans contain an exceptionally high concentration of bioactive compounds that are antinutritional and/or poisonous that have a detrimental effect on animals' metabolism [6].

İLYAS ÖZER, is with Department of Computer Engineering University of Bandırma Onyedi Eylül University, Balıkesir, Turkey, (e-mail: iozer@bandirma.edu.tr).

 <https://orcid.org/0000-0003-2112-5497>

Urease is one of these factors. The harmful effects of feeding urease-containing meals to animals have been reported in the literature. When unprocessed soybeans are combined with urea, ammonia is released due to the activity of urease, which is an unwanted result in the feed [2].

Ammonia reaches the bloodstream rapidly in ruminants and can cause a variety of negative effects, including decreased feed intake, decreased animal health, ammonia poisoning, and death [7]. Heat treatment is the most common procedure for removing or reducing the effects of antinutritional and/or harmful factors, such as urease, in soybeans [8][9][10][11][12]. On the other hand, as a result of Maillard (browning) reactions caused by overcooking raw soybean grain (high cooking temperature, excessive steam pressure or prolonged), lysine combines with carbohydrates to form a complex and its usefulness is greatly reduced [2][6][13].

Various processes such as microwave heating, fluidized-bed drying, spouted bed drying, extrusion, superheated steam and boiling can be used to inactivate the undesirable components of soybeans [10][14]. The high temperature of the extrusion and the screw speed effectively releases cellulosic microcrystals in the cell wall structure and, consequently, in the fragmentation of the wall. In addition, it is effective in reducing soybean-based anti-nutritional factors such as trypsin inhibitors [11][12]. Extrusion is also environmentally friendly due to its short processing time, low cost, protection of heat sensitive components, industrial ability, and the absence of hazardous chemical waste [11][12] has several advantages. Figure 1 shows an example extruder machine.

In summary, if soybeans are not adequately processed, undesirable conditions such as urease activity occur. On the other hand, its usefulness decreases significantly if it is overcooked. Biological experiments are the most effective method of determining processing performance and final soybean meal content (Real-Guerra et al., n.d.). However, the expense, time required, and difficulty of these tests limit their usage. Because of its rapidity and low laboratory equipment requirements, urease testing has been used as an indirect method of determining the heat treatment capacity of soybeans since the 1940s. An analysis (Yalcin and Basman, 2015) discovered a strong association between the activities of trypsin inhibitors, urease, and lectins, demonstrating that these analytical parameters could greatly predict the performance of soybean production. Many protocols have been established over the years to promote the calculation of urease behavior. These protocols measure the ammonia emitted either directly or indirectly. The Caskey-Knapp



process, one of the first developed (Caskey and Knapp, 1944), involves incubating the meal with urea in a buffered solution before adding phenol red. Unprocessed meals cause a rise in the pH of the solution with a color change (from red-orange to pink) after incubation, while adequately processed meals cause little or no color change.



Fig.1. An example of an industrial extruder machine.

Urease test is also frequently preferred in the production of industrial-sized full-fat soybean by extrusion. Here, soybeans are classified as undercooked, well-cooked and over-cooked according to the color changes after testing by an expert. This process is entirely manual. It also depends heavily on the experience of the expert who made the assessment. In this study, an approach is presented on the classification of images obtained as a result of the urease test with machine learning techniques. In this way, it is aimed to both automate the process and eliminate the wrong evaluation results that may arise from human errors. Within the scope of his study, a data set consisting of 175 images, including at least 57 images from each class, was prepared. The prepared data set was classified with different machine learning methods and the results were reported. Many studies in the literature use soybean and machine learning approaches together, such as determination of legume type [15], yield estimation [16][17][18], evaluation of crop damage [19] and determination of seed and seedling quality [20]. According to the author's knowledge, this is the first study to analyze urease activity after extrusion on TYS with machine learning techniques.

## II. MATERIALS AND METHODS

### A. Data set

Periodic samples were taken from a soybean extruder to create the data set. The samples' contact with the appropriate solution was ensured, and the images of the outputs were labeled and recorded in accordance with the expert opinions. For this process, 25 ml of amber-colored urea-phenol red solution was added to the homogenized soybean meal and shaken gently. After this process, all samples were kept for 5 minutes and according to the red color formation on them, the class was decided by the experts. If there is no red color on the surface, there is no urease activity and the sample is over-cooked. If there are a few small scattered red particles, there is little urease activity and the product is considered well-cooked. If a large part of the sample surface is covered with red particles, the urease activity is high and the product is undercooked. In Figure 2, samples are belonging to all three classes.



Fig.2. Samples of urease test images (From left to right: well-cooked, undercooked and overcooked).

As a result of all these processes, a total of 175 pictures of 57 undercooked, 60 well-cooked and 58 over-cooked samples were prepared.

### B. Fully Connected Neural Network

Fully Connected Neural Networks (FCNN) are among the most basic elements of artificial neural networks and have been used in numerous applications to date. Being structure agnostic is one of the main features of these networks [21]. These networks do not make any special assumptions about input. This makes them applicable to many different kinds of problems. However, the performance of FCNNs tends to be lower than networks adapted to solve a particular problem [21].

FCNN is created by placing fully connected layers one after the other. The fully connected layer can be defined as a function from  $x \in \mathbb{R}^m$  to  $\mathbb{R}^n$ . Figure 3 shows a sample fully connected layer.

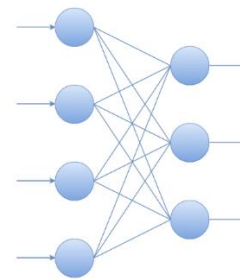


Fig.3. Representations of fully connected layer.

Where  $x \in \mathbb{R}^m$  is the input,  $w_i$  is the learnable parameters,  $f$  is the non-linear function for the fully connected layer and  $y_i \in \mathbb{R}^m$  is the  $i$ -th output of the fully connected layer, here  $y_i$  is calculated as follows:

$$y_i = \begin{pmatrix} f(w_{1,1}x_1 + \dots + w_{1,m}x_m) \\ \vdots \\ f(w_{n,1}x_1 + \dots + w_{n,m}x_m) \end{pmatrix} \quad (1)$$

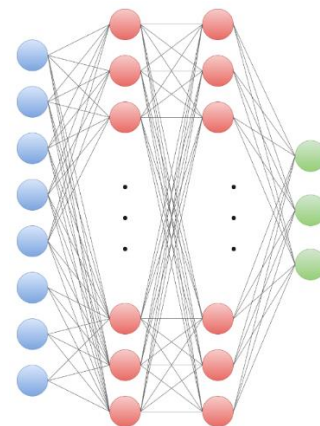


Fig.4. FCNN model architecture.

### C. Convolutional Neural Network

CNN is a typical multilayer neural network structure, often used to analyze image-related applications [22][23][24]. The working principle of CNN architectures can be summarized as extracting the features of the image taken from the input layer and classifying the extracted features. Here fully connected layers are commonly used for the classification process. CNN's greatly adorn feed-forward neural networks. CNN-based machine learning models differ from traditional machine learning methods through convolution layers that can automatically extract features [25], [26]. CNN models generally consist of convolution, pooling and fully connected layers [25].

Filter size and the number of generated maps are used to define the convolution layer. Here, filters are a basic unit used to extract different features related to lines, corners and edges on the images [27]. These filters are shifted across the image matrix. During the shifting process, the values of the image matrix are multiplied by the values in the filter. The net result is found by summing the values obtained afterward. This process is applied to the entire image to generate feature maps. As a result, a new matrix is created [28]. Here  $y_l$  is the output vector, the number of elements in the input signal  $x_n$ , the filter  $h_{l-n}$ , the feature map values can be calculated as follows [29]:

$$y_l = \sum_{n=0}^{N-1} x_n h_{l-n} \quad (2)$$

To add non-linearity to the convolution layer, a rectified linear unit (ReLU) is generally used as the activation function. In this function, negative input values are removed by setting them to zero. To represent the  $x$  is input, the ReLU function can be expressed as:

$$f(x) = \begin{cases} x, & x \geq 0 \\ 0, & \text{otherwise} \end{cases} \quad (3)$$

In CNN architectures, there is usually the pooling layer after the convolution layer. These small rectangular blocks are used to reduce the size of the output of the convolution layer [29]. Thus, both computational costs are reduced and the problem of overfitting is minimized. In this study, the max-pooling method that takes the largest value in each rectangular block is used.

$$p_j = \frac{e^{x_j}}{\sum_1^k e^{x_k}} \quad j = 1, \dots, k \quad (4)$$

### D. Long Short-Term Memory Network

LSTM is a special form of recurrent neural networks (RNN). It can learn long-term dependencies. First proposed in the mid-90s, this model is widely used today [30]. RNNs aims to store and transfer the state information of the artificial neural network while working on data in the sequences. However, status information is continuously processed and transmitted. For this reason, it is often not possible to transfer long-term dependencies without breaking them. That is, short-term dependencies can be transferred effectively. However, there is a problem in transferring long-term dependencies intact. LSTMs are models developed to deal with this problem.

All RNN-based network models consist of repetitive structures in the form of a chain. The main feature that distinguishes RNN models from each other is that their internal structures are different. In basic RNN models, these structures usually consist of a tanh layer or contain a similar function. The internal structures of LSTMs are different from the basic RNN models, as seen in Figure 5.

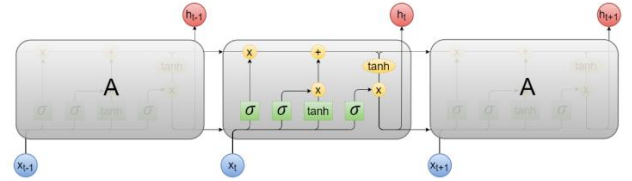


Fig.5. Internal structure of an LSTM module and its interaction with other modules

An LSTM module consists of three separate gates. These are the input, forgetting and output gates. The forgetting gate consists of a sigmoid function. The sigmoid function generates a value between 0 and 1. In case the generated value is 0, no information is transmitted. If it is 1, it means that all information must be transmitted. This process can be expressed mathematically as follows:

$$f_t = \sigma(W_f[h_{t-1}, x_t] + b_f) \quad (5)$$

It is then decided what information needs to be updated. For this operation, the sigmoid function is used again. In addition, these two processes are combined to create a list of candidate values.  $\tilde{C}_t$  is a list of candidate values, and these two operations can be mathematically expressed as:

$$i_t = \sigma(W_i[h_{t-1}, x_t] + b_i) \quad (6)$$

$$\tilde{C} = \tanh(W_c[h_{t-1}, x_t] + b_c) \quad (7)$$

After this step, the new state information of the memory cell is calculated. This process can be expressed as follows:

$$C_t = f_t C_{t-1} + i_t \tilde{C}_t \quad (8)$$

Finally, the output of the system  $h_t$  is calculated. This process can be expressed as follows:

$$h_t = o_t \tanh(C_t) \quad (9)$$

### E. CNN-LSTM Network

In CNN architectures, the process can be summarized in two basic stages. In the first step, feature extraction is performed on the input data. Afterward, these features are commonly classified using an FCNN. On the other hand, different network structures may be more capable of capturing different relationships. For example, while CNN is successful in spatial relationships, LSTM models are more successful in temporal relationships. Therefore, hybrid models can be used to combine the capabilities of different network structures. In the CNN-LSTM model used in this study, the features extracted with the CNN architecture are applied to the LSTM layer. Details on model parameters are shown in Table 1.

### F. Performance Evaluation Metrics

The metrics chosen for comparing machine learning models are very important. In this study, several different methods were used to compare the performance of different

machine learning algorithms. Classification accuracy (ACC), sensitivity (SENS), specificity (SPEC), precision (PREC), F-score, and k-fold cross-validation are the evaluation metrics used.

k-fold cross-validation is a widely used methodology for separating training and test data. In this method, the data is divided into k subgroups and each data in the data set is used for both testing and training. The classifier is trained with k-1 subsets and tested with the remaining subset to determine performance values. This process is repeated k times and the average of the performance values obtained for each subset gives the final performance of the model. 10-fold cross-validation was used in this study. In addition, the performance of the model was compared using the holdout test. For this process, the data set was set to be 80% training and 20% testing.

ACC is one of the most widely used methods to compare the performance of machine learning models. Here, N shows the test set,  $cn$  implies the class of the value of  $n$ ,  $Estimate(n)$  is classification result of  $n$ , k is the k-fold validation parameter, ACC can be expressed as follows:

$$Accuracy(N) = \frac{\sum_{i=1}^{|N|} estimate(n_i)}{|N|}, \quad n_i \in N \quad (10)$$

$$Estimate(n) = \begin{cases} 1, & \text{if } estimate(n) = cn \\ 0, & \text{otherwise} \end{cases} \quad (11)$$

$$Classification\ Accuracy(ML) = \frac{\sum_{i=1}^{|k|} Accuracy(N_i)}{|k|} \quad (12)$$

TABLE I  
PARAMETERS OF ALL MACHINE LEARNING MODELS USED IN THE STUDY

	LSTM	CNN	CNN-LSTM	FCNN
1. Layer	LSTM Layer Node Count: 150 Activation: tanh	Convolutional Layer Filter Count: 16 Filter Size: 3x3 Activation: ReLU	Convolutional Layer Filter Count: 16 Filter Size: 3x3 Activation: ReLU	Fully Connected Layer Node Count: 100 Activation: RELU
2. Layer	Dropout Layer Value: 0.2	Dropout Layer Value: 0.2	Dropout Layer Value: 0.2	Fully Connected Layer Node Count: 100 Activation: RELU
3. Layer	Fully Connected Layer Node Count: 2 or 3 Activation: Softmax	Max-pooling Size: 2x2	Max-pooling Size: 2x2	Dropout Layer Value: 0.2
4. Layer		Convolutional Layer Filter Count: 16 Filter Size: 3x3 Activation: ReLU	Convolutional Layer Filter Count: 16 Filter Size: 3x3 Activation: ReLU	Fully Connected Layer Node Count: 2 or 3 Activation: Softmax
5. Layer		Dropout Layer Value: 0.2	Dropout Layer Value: 0.2	
6. Layer		Max-pooling Layer Size: 2x2	Max-pooling Layer Size: 2x2	
7. Layer		Fully Connected Layer Node Count: 100 Activation: RELU	LSTM Layer Node Count: 150 Activation: tanh	
8. Layer		Dropout Layer Value: 0.2	Dropout Layer Value: 0.2	
9. Layer		Fully Connected Layer Node Count: 2 or 3 Activation: Softmax	Fully Connected Layer Node Count: 2 or 3 Activation: Softmax	

ACC alone may not be a sufficient parameter for performance comparison. Therefore, using the terms SPEC, SENS, PREC and F-score, which are statistical performance measures, is useful in many cases for accurate performance comparison. The term SPEC refers to the proportion of correctly predicted true negatives. On the other hand, the term SENS indicates the proportion of correctly predicted true positives. The ratio of correct positive predictions is expressed as PREC. The F score is the harmonic mean of SENS and PREC values. The formulas used to calculate SPEC, SENS, PREC and F-score are as follows:

$$SPEC = \frac{TN}{TN + FP} \quad (13)$$

$$SENS = \frac{TP}{TP + FN} \quad (14)$$

$$PREC = \frac{TP}{TP + FP} \quad (15)$$

$$F\text{-score} = \frac{2TP}{2TP + FP + FN} \quad (16)$$

Here, true positive (TP) refers to the number of correctly classified positive samples and true negative (TN) refers to the number of negative samples correctly classified. On the other hand, false-positive (FP) is the number of negative samples classified as positive, and false-negative (FN): the number of positive samples classified as negative.

#### G. Model Parameters

Four different machine learning models were used for classification processes. Table 1 shows the parameters of the machine learning models used. The weights of the trainable

layers in all models were started with Xavier [31]. In addition, cross-entropy is used as a loss function in all models. Also, Adam optimizer was used in all models [32]. Adam is an optimization algorithm widely used in deep learning studies in recent years.

The color values of the images were normalized from [0-255] to [0-1] before they were applied to the models. All images were resized to 80x160x3 dimensions before they were applied to the models to reduce computational costs. It has been applied to CNN and CNN-LSTM models with these dimensions. All images are flattened and applied to the FCNN network. In addition, it has been reshaped to 80x480 dimensions in the LSTM model. In addition to these, the

### III. RESULTS AND DISCUSSION

Soybean is an important food source for animals. However, problems such as urease activity are encountered if soybeans are not adequately processed. On the other hand, overcooking also reduces its benefits. The urease test is one of the commonly used methods to evaluate the cooking level of soybeans. According to the color change on the soybean, the cooking level of the product is evaluated by a expert. Automating the process will both minimize the risk of operator error and reduce time losses.

In this section, firstly, a binary classification process is performed on soybean images that have been tested for urease. In this context, the data were primarily evaluated as cooked and undercooked. The over-cooked and well-cooked class samples in the data set were evaluated in the same category. Classification performances were tested using four different machine learning models.

TABLE II  
10-FOLD CROSS-VALIDATION RESULTS FOR BINARY CLASSIFICATION

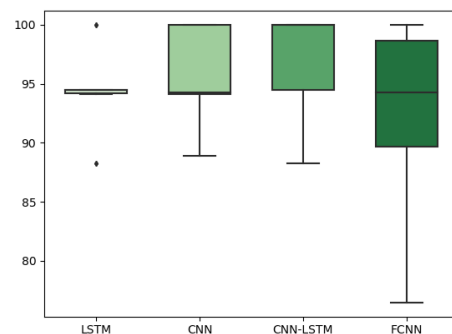
	ACC	SENS	SPEC	PREC	F-Score
<b>LSTM</b>	94.29	89.47	96.61	92.72	91.07
<b>CNN</b>	95.43	91.23	97.46	94.55	92.86
<b>CNN-LSTM</b>	<b>96.57</b>	<b>92.98</b>	<b>98.31</b>	<b>96.36</b>	<b>94.64</b>
<b>FCNN</b>	92.57	87.72	94.92	89.29	88.50

Table 2 shows the binary classification results obtained with 10-fold cross-validation. Here, undercooked samples were considered as positive classes and evaluation metrics were created accordingly. The best results in all evaluation metrics belong to the CNN-LSTM model. In this model, ACC, SENS, SPEC, PREC and F-Score values were obtained as 96.57%, 92.98%, 98.31%, 96.36% and 94.64%, respectively. The CNN model has an ACC value of 95.43% and an F-Score value of 92.86%. ACC and F-Score values of the LSTM model were 94.29% and 91.07%, respectively. On the other hand, the lowest performance in all evaluation metrics belongs to the FCNN model. In this model, ACC was achieved as 92.57%. As stated in the sections above, FCNNs can be applied to many problems due to their structure agnostic nature. However, their performance is generally inferior to networks adapted to solve a specific problem [21]. For this reason, its performance is considered to be lower compared to other models. On the other hand, CNN's are very successful in detecting spatial dependencies. Consequently, their performances in image-related applications are quite good. An important limitation of CNN architectures is their

image augmentation process was applied. Augmented images are used for validation purposes only. It was not used in the training process. The validation set was created by applying scaling on the images, turning the images vertically and horizontally, rotating and zooming randomly. Before each training process, images in the training data were randomly selected and augmented by the number of images in the test set. Finally, 140 images were used for training and 35 images were used for testing in the holdout test. In each part of the 10-fold cross-validation tests, 157 or 158 images were used for training and 18 or 17 images for testing. All models are trained for 200 epochs. Testing was carried out with the weights with the highest ACC value in the validation set.

weakness in learning sequential dependencies [33]. The combination of CNN and LSTM layout feature greatly improves classification [34]. Thus, the CNN-LSTM model's performance is considered to be higher than the other models. In addition, SPEC values are higher than SENS values in all models. It is considered that this is because machine learning models tend to the majority class.

In Graphic 1, box plot representation of ACC values obtained with 10-fold cross-validation in the binary classification process can be seen. It is seen that the lowest values of the FCNN model are different from other models. On the other hand, it is seen that CNN and CNN-LSTM models behave close to each other.



Graph 1. Box plot representation of 10-fold cross-validation results of the binary classification.

Table 3 shows the holdout test results for binary classification. SPEC and PREC values were obtained as 100% for all models. This means that no model mistakenly evaluates cooked grade samples as undercooked. On the other hand, models differ from each other depending on their SENS values. For other evaluation metrics, the results are very similar to the 10-fold cross-validation results. The best ACC value belongs to the CNN-LSTM model. In this model, ACC was realized at 94.29%. For the CNN-LSTM model, the F-Score value is 90.0%. The lowest ACC and F-Score values belong to the FCNN model as in the 10-fold cross-validation results. In the FCNN model, ACC and F-Score values are 82.86% and 62.50%, respectively.

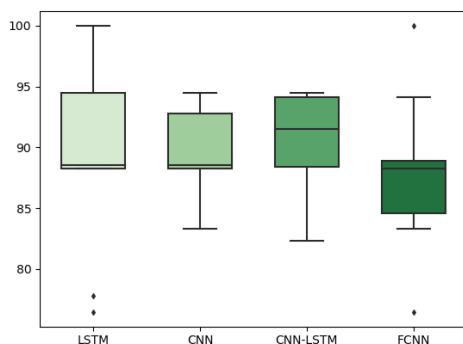
TABLE III  
HOLDOUT TEST RESULTS FOR BINARY CLASSIFICATION

	ACC	SENS	SPEC	PREC	F-score
<b>LSTM</b>	88.57	63.64	100.00	100.00	77.78
<b>CNN</b>	91.43	72.73	100.00	100.00	84.21
<b>CNN-LSTM</b>	94.29	81.82	100.00	100.00	90.00
<b>FCNN</b>	82.86	45.46	100.00	100.00	62.50

In addition to binary classification, a triple classification process was carried out as over-cooked, well-cooked and undercooked. Table 4 shows the 10-fold cross-validation results of the triple classification process. Here, very close scores were obtained in all comparison metrics in CNN and LSTM models. Both models have an ACC value of 89.14%. Like the binary classification problem, the lowest scores in all evaluation metrics belong to the FCNN model. ACC and F-Score values of this model are 88.0% and 87.85%, respectively. It is evaluated here that using a model in structure agnostic structure negatively affects its performance. On the other hand, the CNN-LSTM model has the best scores in all evaluation metrics. The performance value of this model was obtained as 90.29%. Here, it is evaluated that the sequential processing of the features extracted by CNN with LSTM increases the performance. In Graphic 2, box plot representation of ACC values of triple classification tests can be seen. Here, it is seen that CNN and CNN-LSTM models exhibit similar behaviors as in the binary classification tests.

TABLE IV  
10-FOLD CROSS VALIDATION RESULTS FOR THREE-CLASS CLASSIFICATION

	ACC	SENS	SPEC	PREC	F-score
<b>LSTM</b>	89.14	89.08	94.59	89.14	89.09
<b>CNN</b>	89.14	89.14	94.59	89.19	89.08
<b>CNN-LSTM</b>	<b>90.29</b>	<b>90.24</b>	<b>95.14</b>	<b>90.46</b>	<b>90.29</b>
<b>FCNN</b>	88.00	87.92	94.00	87.98	87.85



Graph 2. Box plot representation of 10-fold cross-validation results of the three-class classification.

Finally, in Table 5, the holdout test results of the triple classification process can be seen. The CNN-LSTM model performed better here compared to the other models as well. ACC and F-Score values of the CNN-LSTM model are 91.43% and 90.82%, respectively. The performance of the FCNN model is significantly lower than other models. FCNN model has an ACC value of 77.14% and an F-Score value of 77.09%.

TABLE V  
HOLDOUT TEST RESULTS FOR THREE-CLASS CLASSIFICATION

	ACC	SENS	SPEC	PREC	F-score
<b>LSTM</b>	82.86	84.18	89.38	85.93	84.73
<b>CNN</b>	85.71	87.21	92.15	84.87	85.79
<b>CNN-LSTM</b>	<b>91.43</b>	<b>92.09</b>	<b>95.50</b>	<b>90.05</b>	<b>90.82</b>
<b>FCNN</b>	77.14	80.30	88.80	76.80	77.09

#### IV. CONCLUSION

Soybean meal has a high protein concentration. For this reason, it constitutes a very important part of the protein sources used in animal feed throughout the world. On the other hand, soybeans contain many bioactive compounds that are antinutritional and/or poisonous, such as urease. For this reason, it is desired to reduce the effect of these components by cooking with machines such as extruders. However, many factors such as steam pressure, cooking time, temperature and screw speed affect the cooking level. Less cooking of soybeans negatively affects animal health, while overcooking negatively affects nutritional values.

The urease test has been used for many years to evaluate the cooking level of soybeans. Here, the cooking level of soybeans is evaluated by an expert according to the color change of the samples. In this study, a machine learning-based approach is proposed to evaluate urease test results to automate the process and minimize possible expert errors. In this context, a data set consisting of over-cooked, well-cooked and undercooked samples were prepared. The prepared samples were tested in both two classes and three classes. In the tests performed with four different machine learning models, it was observed that the highest performance values were obtained by the CNN-LSTM model, in which the features extracted by CNN are processed sequentially with the LSTM model. In 10-fold cross-validation tests, ACC was 96.57% for two classes and 90.29% for three classes.

According to the author's knowledge, it is the first study to evaluate images of urease tests in soybeans with machine learning models. The results obtained are very promising for future studies.

#### REFERENCES

- [1] G. L. Cromwell, "Soybean Meal-The 'Gold Standard,'" 1999. Accessed: Apr. 25, 2021. [Online]. Available: [https://www.nutritime.com.br/arquivos\\_internos/artigos/soybeanmeal-thegoldstandard.pdf](https://www.nutritime.com.br/arquivos_internos/artigos/soybeanmeal-thegoldstandard.pdf).
- [2] R. Real-Guerra, ... F. S.-A. C. S., and 2013, "Soybean urease: over a hundred years of knowledge," *books.google.com*, Accessed: Apr. 25, 2021. [Online]. Available: <https://books.google.com/books?hl=tr&lr=&id=87WiDwAAQBAJ&oi=fnd&pg=PA317&dq=Real-Guerra,+Rafael,+Fernanda+Stanisçuaski,+and+Célia+Regina+Carlini.+%22Soybean+urease:+over+a+hundred+years+of+knowledge.%22+A+Comprehensive+Survey+of+International+Soybean+Research>.
- [3] K. Zhang, Q. Wu, and Y. Chen, "Detecting soybean leaf disease from synthetic image using multi-feature fusion faster R-CNN," *Comput. Electron. Agric.*, vol. 183, p. 106064, Apr. 2021, doi: 10.1016/j.compag.2021.106064.
- [4] Y. Ni *et al.*, "Computational model and adjustment system of header height of soybean harvesters based on soil-machine system," *Elsevier*, Accessed: Apr. 25, 2021. [Online]. Available: <https://www.sciencedirect.com/science/article/pii/S0168169920331124>.
- [5] E. Clarke and J. Wiseman, "Effects of extrusion conditions on trypsin inhibitor activity of full fat soybeans and subsequent effects on their nutritional value for young broilers," *Br. Poult. Sci.*, vol. 48, no. 6, pp. 703–712, Dec. 2007, doi: 10.1080/00071660701684255.
- [6] I. E. Liener, "Implications Of Antinutritional Components In Soybean Foods," *Crit. Rev. Food Sci. Nutr.*, vol. 34, no. 1, pp. 31–67, Jan. 1994, doi: 10.1080/10408399409527649.
- [7] G. B. Huntington, D. L. Harmon, N. B. Kristensen, K. C. Hanson, and J. W. Spears, "Effects of a slow-release urea source on absorption of ammonia and endogenous production of urea by cattle," *Anim. Feed Sci. Technol.*, vol. 130, no. 3–4, pp. 225–241, Nov. 2006, doi: 10.1016/j.anifeedsci.2006.01.012.
- [8] G. Qin, E. R. Ter Elst, M. W. Bosch, and A. F. B. Van Der Poel, "Thermal processing of whole soya beans: Studies on the inactivation of antinutritional factors and effects on ileal digestibility in piglets," *Anim. Feed Sci. Technol.*, vol. 57, no. 4, pp. 313–324, Mar. 1996, doi:

- 10.1016/0377-8401(95)00863-2.
- [9] C. Luanga Ouédraogo, E. Combe, J.-P. Lallès, R. Toullec, S. Trèche, and J.-F. Grongnet, "Nutritional value of the proteins of soybeans roasted at a small-scale unit level in Africa as assessed using growing rats." Accessed: Apr. 25, 2021. [Online]. Available: [https://rmd.edpsciences.org/articles/rmd/pdf/1999/02/RND\\_0926-5287\\_1999\\_39\\_2\\_ART0005.pdf](https://rmd.edpsciences.org/articles/rmd/pdf/1999/02/RND_0926-5287_1999_39_2_ART0005.pdf).
- [10] S. Yalcin and A. Basman, "Effects of infrared treatment on urease, trypsin inhibitor and lipoxigenase activities of soybean samples," *Food Chem.*, vol. 169, pp. 203–210, Feb. 2015, doi: 10.1016/j.foodchem.2014.07.114.
- [11] F. S. Tabibloghmany, M. Mazaheri Tehrani, and A. Koocheki, "Optimization of the extrusion process through response surface methodology for improvement in functional and nutritional properties of soybean hull," *J. Food Sci. Technol.*, vol. 57, no. 11, pp. 4054–4064, Nov. 2020, doi: 10.1007/s13197-020-04439-w.
- [12] Y. Jing and Y. J. Chi, "Effects of twin-screw extrusion on soluble dietary fibre and physicochemical properties of soybean residue," *Food Chem.*, vol. 138, no. 2–3, pp. 884–889, Jun. 2013, doi: 10.1016/j.foodchem.2012.12.003.
- [13] N. Şenköylü, H. Akyürek, H. Ersin ŞAMLI, and A. Ağma, "Tam Yağlı Soyanın Metabolik Enerji Değerinin Broyler Performansından Tahmini," 2004. Accessed: Apr. 25, 2021. [Online]. Available: <https://dergipark.org.tr/en/pub/uluvfd/issue/13529/163661>.
- [14] K. Krishnamurthy, H. K. Khurana, J. Soojin, J. Irudayaraj, and A. Demirci, "Infrared heating in food processing: An overview," in *Comprehensive Reviews in Food Science and Food Safety*, Jan. 2008, vol. 7, no. 1, pp. 2–13, doi: 10.1111/j.1541-4337.2007.00024.x.
- [15] G. L. Grinblat, L. C. Uzal, M. G. Larese, and P. M. Granitto, "Deep learning for plant identification using vein morphological patterns," *Comput. Electron. Agric.*, vol. 127, pp. 418–424, Sep. 2016, doi: 10.1016/j.compag.2016.07.003.
- [16] R. A. Schwalbert, T. Amado, G. Corassa, L. P. Pott, P. V. V. Prasad, and I. A. Ciampitti, "Satellite-based soybean yield forecast: Integrating machine learning and weather data for improving crop yield prediction in southern Brazil," *Agric. For. Meteorol.*, vol. 284, p. 107886, Apr. 2020, doi: 10.1016/j.agrformet.2019.107886.
- [17] M. Yoosefzadeh-Najafabadi, H. J. Earl, D. Tulpan, J. Sulik, and M. Eskandari, "Application of Machine Learning Algorithms in Plant Breeding: Predicting Yield From Hyperspectral Reflectance in Soybean," *Front. Plant Sci.*, vol. 11, Jan. 2021, doi: 10.3389/fpls.2020.624273.
- [18] M. Herrero-Huerta, P. Rodriguez-Gonzalvez, and K. M. Rainey, "Yield prediction by machine learning from UAS-based multi-sensor data fusion in soybean," *Springer*, doi: 10.1186/s13007-020-00620-6.
- [19] J. Zhang, Y. Huang, K. N. Reddy, and B. Wang, "Assessing crop damage from dicamba on non-dicamba-tolerant soybean by hyperspectral imaging through machine learning," *Wiley Online Libr.*, vol. 75, no. 12, pp. 3260–3272, Dec. 2019, doi: 10.1002/ps.5448.
- [20] A. D. de Medeiros, N. P. Capobianco, J. M. da Silva, L. J. da Silva, C. B. da Silva, and D. C. F. dos Santos Dias, "Interactive machine learning for soybean seed and seedling quality classification," *Sci. Rep.*, vol. 10, no. 1, p. 11267, Dec. 2020, doi: 10.1038/s41598-020-68273-y.
- [21] J. Xia, S. Pan, M. Yan, G. Cai, J. Yan, and G. Ning, "Prognostic model of small sample critical diseases based on transfer learning," *Sheng Wu Yi Xue Gong Cheng Xue Za Zhi*, vol. 37, no. 1, pp. 1–9, Feb. 2020, doi: 10.7507/1001-5515.201905074.
- [22] Y. LeCun, L. Bottou, Y. Bengio, and P. Haffner, "Gradient-based learning applied to document recognition," *Proc. IEEE*, vol. 86, no. 11, pp. 2278–2323, 1998, doi: 10.1109/5.726791.
- [23] I. OZER, "Pseudo-colored rate map representation for speech emotion recognition," *Biomed. Signal Process. Control*, vol. 66, p. 102502, Apr. 2021, doi: 10.1016/j.bspc.2021.102502.
- [24] J. Ma, F. Wu, J. Zhu, D. Xu, and D. Kong, "A pre-trained convolutional neural network based method for thyroid nodule diagnosis," *Ultrasonics*, vol. 73, pp. 221–230, Jan. 2017, doi: 10.1016/j.ultras.2016.09.011.
- [25] Y. Lecun, Y. Bengio, and G. Hinton, "Deep learning," *Nature*, vol. 521, no. 7553, Nature Publishing Group, pp. 436–444, May 27, 2015, doi: 10.1038/nature14539.
- [26] Y. Bengio, A. Courville, and P. Vincent, "Representation learning: A review and new perspectives," *IEEE Trans. Pattern Anal. Mach. Intell.*, vol. 35, no. 8, pp. 1798–1828, 2013, doi: 10.1109/TPAMI.2013.50.
- [27] I. Ozer, Z. Ozer, and O. Findik, "Noise robust sound event classification with convolutional neural network," *Neurocomputing*, vol. 272, pp. 505–512, Jan. 2018, doi: 10.1016/j.neucom.2017.07.021.
- [28] L. Wen, X. Li, L. Gao, and Y. Zhang, "A New Convolutional Neural Network-Based Data-Driven Fault Diagnosis Method," *IEEE Trans. Ind. Electron.*, vol. 65, no. 7, pp. 5990–5998, Jul. 2018, doi: 10.1109/TIE.2017.2774777.
- [29] U. R. Acharya, S. L. Oh, Y. Hagiwara, J. H. Tan, and H. Adeli, "Deep convolutional neural network for the automated detection and diagnosis of seizure using EEG signals," *Comput. Biol. Med.*, vol. 100, pp. 270–278, Sep. 2018, doi: 10.1016/j.compbiomed.2017.09.017.
- [30] I. Ozer, S. Efe, and H. Ozbay, "A combined deep learning application for short term load forecasting," *Alexandria Eng. J.*, vol. 60.4, pp. 3807–3818, 2021, Accessed: Apr. 25, 2021. [Online]. Available: <https://www.sciencedirect.com/science/article/pii/S111001682100137X>.
- [31] X. Glorot and Y. Bengio, "Understanding the difficulty of training deep feedforward neural networks," *JMLR Workshop and Conference Proceedings*, Mar. 2010. Accessed: Apr. 25, 2021. [Online]. Available: <http://www.ijro.umontreal>.
- [32] J. B. Kingma, Diederik P., "Adam: A method for stochastic optimization," *International Conference on Learning Representations (ICLR)*, 2015. .
- [33] C. Feng, A. Mehmani, and J. Zhang, "Deep Learning-Based Real-Time Building Occupancy Detection Using AMI Data," *IEEE Trans. Smart Grid*, vol. 11, no. 5, pp. 4490–4501, Sep. 2020, doi: 10.1109/TSG.2020.2982351.
- [34] M. Z. Islam, M. M. Islam, and A. Asraf, "A combined deep CNN-LSTM network for the detection of novel coronavirus (COVID-19) using X-ray images," *Informatics Med. Unlocked*, vol. 20, p. 100412, Jan. 2020, doi: 10.1016/j.imu.2020.100412.

## BIOGRAPHIES



İLYAS ÖZER was born in Yozgat, Turkey, in 1984. He received a B.Eng. degree from the Department of Electric & Electronic Engineering at the University of Dumlupınar of Turkey, in 2006. He received a M.Sc. degree from the Department of Computer Engineering at the University of Sakarya of Turkey in 2011. Also, He received a Ph. D. degree from the Computer Engineering at the University of Karabük of Turkey in 2018. His current research interests include signal processing, sound event detection and advanced machine learning techniques.

# IoT based a Smart Home Automation System Design: Simulation Case

Erdal Ozdogan, Resul Das

**Abstract**—Today, solutions developed with the Internet of Things have started to find more and more application areas to make human life easier. Internet of Things solutions, which include many different types of new technologies, will be very useful to use simulation tools before prototyping for the most appropriate technology selection. In this study, IoT-based smart home design applications have been developed and analyzed. In this context, 3 different scenarios have been developed for smart home automation system design in the Cisco Packet Tracer simulation environment, and the use of tools has been demonstrated with examples according to different scenarios.

**Index Terms**—Smart home automation, IoT solutions, Packet tracer, Simulation, Internet of Things.


## I. INTRODUCTION


WITH THE spread of the Internet of Things (IoT), Smart Home Automation systems are increasingly being applied. By 2023, the smart home market is expected to reach \$ 141.2 billion, an increase of 17% compared to 2019 [1]. In addition to the existence of many commercial applications in smart home automation, application developers also develop home automation systems using various tools. On the other hand, the widespread use of Internet of Things technologies has caused home users to develop their own solutions with various hardware. The widespread use of microcontrollers (MCU) or single board computers (SBC) has been effective in the implementation of IoT systems in the home environment. Many different numbers and types of IoT systems are used for various purposes in home automation systems. However, this rich diversity requires understanding of many components in the development of IoT-powered home automation systems. Evaluating different products during the testing phase of the developed system causes additional labor and time loss. Prototyping on a large scale using a large number of hardware may not be practical at the design and evaluation stage due to economic and operational constraints, especially when the reliability and usefulness of the protocol in question has not yet been proven [2]. In addition, preparing the physical components for the connection and use of the connections prevents the focus from the solution. The use of simulation software will be beneficial in IoT ecosystem design due to

the advantages of using an unlimited number of devices, focusing on the solution to be developed, and also post-test before prototyping. Multiple technologies, device types, protocols and infrastructures are used in the development of IoT solutions. The IoT solution developed in such a complex situation requires many testing processes and methods to achieve the desired benefit. The use of simulation software in the development of IoT solutions will allow to focus directly on the intended test item and separate test items from other complex situations. In this study, it will be discussed how to use simulation tools effectively in the development of IoT supported home automation system, what advantages it will offer in creating prototypes, and a simulation-supported systematic approach is proposed to develop an IoT Home automation system. In the following parts of the study, IoT supported home automation systems, software and hardware used in this system will be explained. In addition, sample scenarios and solutions including different hardware types will be simulated for simulation-supported system development.

## II. RELATED WORK

Electronic equipment used in today's traditional home environments is generally hardware that works independently from each other. The purpose of home automation systems is to create smart environments by ensuring the interoperability and integration of these independent equipment. With IoT support, home automation becomes more capable and makes human life easier. IoT-supported home automation systems have become increasingly popular in recent years, and many academic studies have been done on this subject. Academic studies cover many different fields from security, technology, architectural design to energy efficiency due to the multidisciplinary nature of IoT. In particular, many different IoT solutions have been developed for elderly and disabled people in the field of health, and there are many applications in the literature [3], [4], [5] In a study aimed at integrating the functions of different home automation devices into a single application, a modular smart home solution was developed to connect more devices and manage them remotely [6]. In the study by T. Malche and P. Maheshwary [7], an IoT-supported smart home system was designed to remotely monitor and control home environments. In the mentioned study, applications such as smart lighting, gas detection and intrusion detection were carried out using Arduino hardware. H. Singh et al. developed a new solution that used a variety of sensors to control some home appliances such as light, fan, door, energy consumption and gas level [8]. In this solution, a system consisting of

 **ERDAL ÖZDOĞAN** is with the Ministry of National Education, General Directorate of Basic Education, Ankara - TURKEY e-mail: [erdalozd@gmail.com](mailto:erdalozd@gmail.com)

 **RESUL DAŞ** is with the Department of Software Engineering, Technology Faculty, Firat University, Elazığ, 23119 TURKEY e-mail: [rdas@firat.edu.tr](mailto:rdas@firat.edu.tr)

Manuscript received April 17, 2021; accepted July 26, 2021.

DOI: [10.17694/bajece.918826](https://doi.org/10.17694/bajece.918826)

system design, objectives and implementation details is also proposed. In another study on IoT powered home automation system design, a design methodology and an Arduino based application were developed by W.A. Jabbar et al. [9]. In the study of F. Yalçınkaya et al., the MQTT based smart home system was designed and evaluated in three different scenarios [10]. In the study of Ö.Sine and Y. Koçyiğit, an automation system that can be controlled over the internet was designed and its usage areas were specified in various application scenarios [11]. The study of Güneş et al, developed with the support of artificial intelligence, simulated a home environment consisting of thermostats, sockets and lamps in each of the three rooms. In the study, it was proposed to develop a simulation that includes different components [12]. In Eleyan and Fallon's study, an MQTT-based automation system was designed for individuals with special needs and people with physical disabilities [13]. In H. Nguyen-An et al's study, it was stated that there are a wide variety of IoT devices for different purposes in smart home environments and that the traffic generated from these devices has a strong effect on IoT. In the study, it was stated that the features of IoT traffics are not known enough and the importance of analysis is emphasized and that these traffics are produced synthetically [14]. In the study of M. Assim and A. Al-Omary, a design was made for the smart home environment using Packet Tracer simulation software and then a prototype was produced [15].

As can be seen in the related study, home automation systems have been developed using different sensor types, MCU and SBC hardware. However, these studies are limited because they examine smart home IoT devices in test environments or on a small scale. Since the majority of applications are geared towards a specific solution, they only show a part of home automation systems. Whereas, in simulation software, larger-scale applications can be developed thanks to the ability to add more devices and types.

### III. IOT BASED SMART HOME AUTOMATION

Home automation solutions are systems that consist of hardware that can communicate with each other and components that can be accessed remotely via web environment or mobile devices [15]. In other words, these systems are an example of an IoT ecosystem that requires the use of hardware, software and network infrastructure together. Because of the complexity that IoT brings, designing a home automation system becomes extremely important. The problems that IoT systems try to find solutions to are generally based on smart city applications and smart campus applications. IoT Home Automation systems can also be considered as small prototypes of these solutions. For this reason, IoT Home Automation Systems, which are correctly designed, tested and proven to be useful, will contribute to the formation of smart cities. Home automation systems, which are basically an IoT solution, consist of hardware, software / application and communication protocol components in accordance with the three-layer IoT architectural approach [16]. Each of these components are equally important components in designing an effective system. Different hardware components and communication protocols can be used for

various purposes. It may be necessary to evaluate multiple hardware, applications and protocols during design to reach the correct and optimum solution. Using simulation programs for IoT Home Automation Systems will provide an accurate assessment. Many advantages offered by IoT have contributed to the development of home automation systems [17]. The usefulness of home automation systems is directly related to the capabilities of IoT components. Below are some examples of IoT powered home automation systems:

- Intelligent lighting
- Air conditioning
- Garden management
- Motion sensitive home security systems
- Air / Water quality monitoring
- Intelligent lock systems
- Smart Energy Management

Apart from these examples, there are different application areas with the developing technology. However, it needs to be defined to help create a realistic model of which main components are involved in building a smart home automation.

#### A. IoT based Smart Home Automation System Components

Home automation systems are IoT supported applications that provide customization by controlling the living and working environment. These solutions usually consist of actuators and sensors. These are applications that provide the comfort and safety of people without user intervention [1]. In such applications, human-machine communication (H2M) can be provided by connecting to the devices in the house over the internet, as well as Machine-Machine (M2M) communication that triggers an alarm according to the value of the smoke detector. Sensors play an important role in both M2M and H2M communication [18]. Various sensor types that have been used in the industry for many years have taken their place in home automation systems with the widespread use of IoT the most common types of sensors are temperature sensor, light intensity sensor, water level sensor, and sensors that detect various gases in the air. Apart from these, various sensor types such as pressure, acceleration, humidity, infrared, vibration, flexibility, ultrasonic distance and sound sensor can be used in IoT Home Automation systems. These sensors used in applications are generally hardware with no computational capability or low computational capacity [2]. Also, many sensors do not have the ability to connect a network. Therefore, there is a need for components in the network, called IoT Gateways, that enable the transfer of digital or analog information received from sensors [19]. The IoT Gateway is a component that takes the properties of the physical world such as temperature, humidity, light intensity through sensors and is responsible for processing the received data and placing it in Internet Protocol (IP) packets. Another function of the IoT Gateway is the ability to send commands to actuators to perform various actions under conditions specified by programming. Although there are many different types and capabilities of IoT Gateway hardware in the industry, the most common characteristics of these devices are to provide wired or wireless connections and to establish an internet



connection. Microcontrollers (MCU) such as Arduino and single board computers (SBC) such as Raspberry-Pi are used for this purpose in small-scale applications and prototypes. Figure 1 shows a section of the basic components commonly used in smart home automation systems.



Fig. 1. A view from the smart house

Within the scope of this study, MCU and SBC equipment will be used in simulation environments regardless of manufacturer and brand. Thus, it will be possible to focus directly on system solution development without focusing on manufacturer and model-based differences.

**B. IoT Communication Protocols**

One of the most important issues to be considered in home automation system development is determining the communication protocol. Communication protocols are application layer protocols that allow data to be transported in IP packets over the network. Different communication techniques are used in the development of IoT solutions. In the classification of IoT communication protocols, it can be seen that there are protocols communicating via a central server (publish/subscribe method) and protocols that communicate directly without an intermediary server (request-response method) [20]. MQTT, which is the most used protocol in the development of IoT solutions, is a TCP-based IoT application protocol that works in the broadcast / subscriber architecture [21]. Internet-based MQTT resources can be used at the stage of designing a home automation system prototype [10]. Various licensed or free resources are available for this purpose. Also, local applications running on SBC hardware can be used. Another protocol used in IoT applications is the CoAP protocol that runs on the Request / Response architecture [22]. The advantage of the CoAP protocol is that on-demand queries can be made directly through the IoT Gateway without requiring an additional server. In this way, the bandwidth consumption is

reduced since there will be no need for periodic publishing. Another method that is becoming increasingly common in the development of IoT solutions is the use of REST API [23]. This method, like CoAP, is in a request-response architecture that provides low overhead over http messages. REST API is a programming interface that runs over http and works on the principles of the http protocol. The IoT Gateway can be directly communicated via REST-API and the value obtained from the sensor can be queried. Determining the most suitable protocol in IoT solutions is directly related to the purpose of the developed solution. In addition, evaluation criteria such as data transfer rate, security level, network topology, type of data transmitted and query frequency, distance should be taken into account. The ability to change these values easily in the simulation environment will contribute to the selection of the correct suitable protocol. Internet of Things protocols can be divided in three groups: infrastructure protocols, service discovery protocols and application protocols. The layout of these protocols in OSI layers is shown in the Fig. 2.

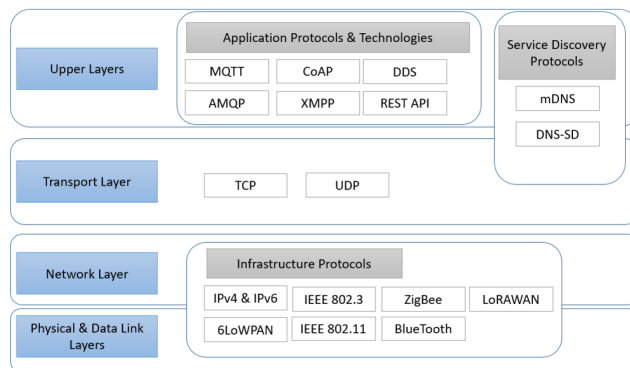


Fig. 2. IoT protocols

**C. Simulation Supported Home Automation System Design**

Within the scope of this study, a phased approach consisting of six steps shown in Figure 3 is proposed in the design of the simulation-supported home automation system.

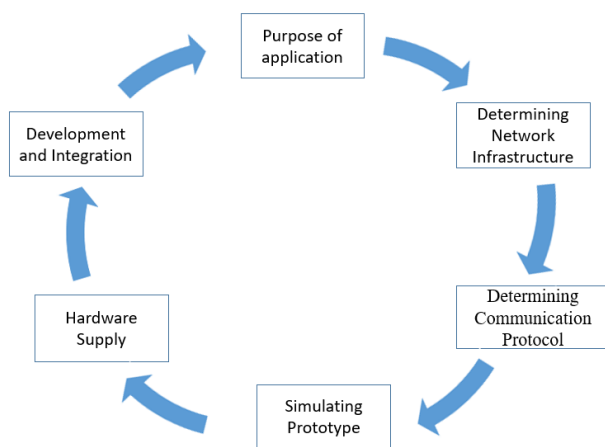


Fig. 3. Simulation-supported IoT solution design steps

At the stage of determining the purpose of the application, the purpose of the IoT solution to be developed is determined. Examples such as the motion-sensitive home security system and the air conditioning of the living area are determined at this stage. Determination of network infrastructure and technologies; The networks and technologies needed are determined according to the purpose of the problem. At this stage, it is determined which technologies such as NFC, Bluetooth or ZigBee to be used in wired or wireless infrastructure, sensor - IoT Gateway communication. At this stage, it is determined whether the communication will be kept locally or whether cloud services will be used. Local storage and communications can be used when there are concerns regarding the security of cloud Technologies [24]. Determining communication protocol; At this stage, the communication protocol to be used is determined according to the targeted purpose and network infrastructure. If there is a periodic query and a high bandwidth requirement, publish / subscribe protocols can be used, otherwise, REST-API or CoAP can be used. Simulating the prototype; According to the purpose and technology determined in the previous stage, the prototype to be developed in the simulation software is simulated. According to the problems encountered, changes can be made in the previous stages, or if the simulation result is successful, the next stage can be passed. At this stage, it is evaluated again whether the used bandwidth is calculated and the communication protocol works efficiently and in accordance with the purpose. Provision of necessary hardware: After the success of the previous stage, the hardware used in the simulation is provided. The solution developed during the development and integration phase of the system is implemented. At this stage, a new system or integration to an existing system can also be made.

#### D. Sample Simulation Scenarios

Within the scope of this study, sample IoT solutions will be developed using Packet Tracer simulation software over sample scenarios.

There are many types of sensors that can be used in IoT applications in simulation software. These tools are shown in Figure 4. In addition to these tools, various actuators are shown in Figure 5. In Packet Tracer simulation software, advanced IoT systems can be developed using Python, JavaScript or microcontroller and single-board computer hardware that can function as an IoT Gateway with block-based visual programming capability.

1) *Sample scenario - 1 (M2M Sample)*: In the home automation system, there is a need to take the temperature values in various locations and generate an alarm for the positions far above the average value and send an IP packet to a specific location. The topology of this scenario in which the wired infrastructure is used is shown in Figure 6. Data will be sent to the server with 192.0.2.10 IP address in the internet environment in the topology. In the example scenario, 4 temperature sensors located in different locations were connected to the MCU hardware and the temperature of the location where a sensor is located was consciously increased.

Pre-existing Python codes in the simulation were changed according to the scenario, and the value that deviated from the averaging from the MCU device was sent to the server using the UDP protocol. It is provided to receive the package sent by using Python codes on the server. Python codes in both hardware are shown in Figure 7.

2) *Sample scenario - 2*: There is a need to subscribe to the status of a sensor and send data to the MQTT broker using the MQTT protocol. The sample simulation topology for the scenario is shown in Figure 8.

In this scenario, the garage environment where the smoke sensor associated with the SBC is located will be checked periodically. SBC will work as the MQTT Publisher and report the smoke amount to the MQTT broker (192.168.1.100) with the "Home/Garage" topic at 60 second intervals. The tablet computer used by the home user is in the MQTT subscriber role and subscribed to the "Home/Garage" topic via the MQTT server. The subscription of the tablet computer to the relevant topic and the message sent from the publisher via the MQTT broker are shown in Figure 9. One of the advantages offered in the simulation program is the advantage of using ready-made MQTT python codes. In this way, MQTT based applications can be used without focusing on the coding feature.

3) *Sample scenario - 3*: A home with an IoT Gateway component from a specific manufacturer needs multiple contingent, customizable IoT solutions. Sample simulation topology for the scenario is shown in Figure 10. In this scenario, the energy needs of the lamp and coffee machine in the house are met by the battery by using the solar panel. Besides, the IoT Gateway device controls all components in the home automation system. When the smoke level rises above 10 units through the MCU, it will open the house door, garage door, window, and turn on the fan. The corresponding JavaScript codes in the MCU device are shown below.

```

1 var smkSensor = A0;
2 var grgDoor = 5;
3 var window = 4;
4 var door = 3;
5 var houseFan = 2;
6 function setup() {
7   pinMode(grgDoor, OUTPUT);
8   pinMode(door, OUTPUT);
9   pinMode(window, OUTPUT);
10  pinMode(houseFan, OUTPUT);
11 }
12 function loop() {
13   var newVal = analogRead(smkSensor);
14   newVal = newVal /10;
15   if (newVal > 10) {
16     customWrite(grgDoor, 1);
17     customWrite(door, 1);
18     customWrite(window, 1);
19     customWrite(houseFan, 2);
20   } else {
21     if (newVal < 2) {
22       customWrite(grgDoor, 0);
23       customWrite(door, 0);
24       customWrite(window, 0);
25       customWrite(houseFan, 0);
26     }
27   }
28   Serial.println("Smoke Level : " + newVal);
29 }

```

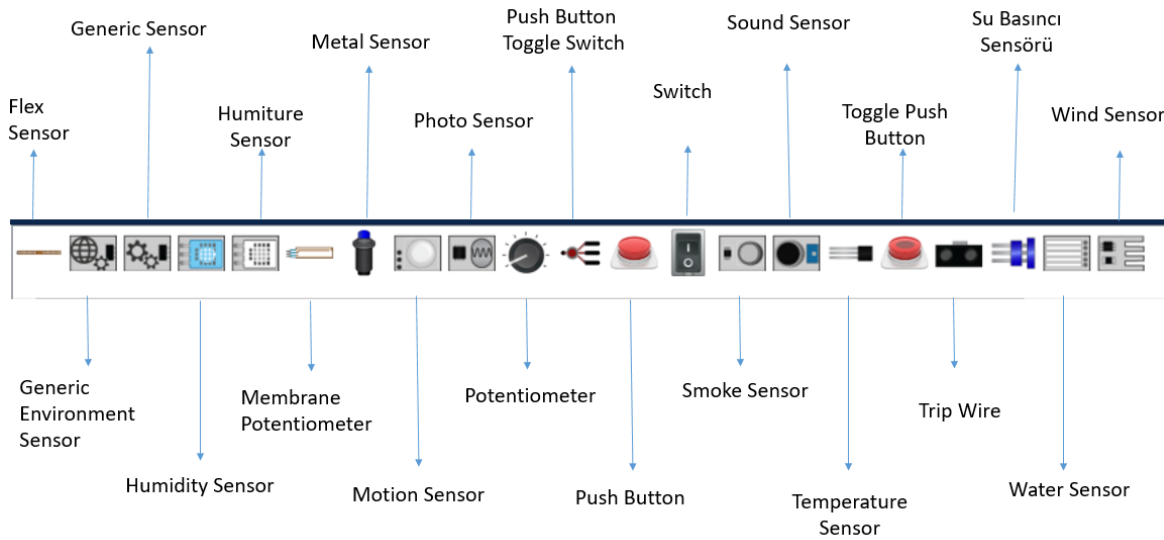


Fig. 4. Sensors in simulation software

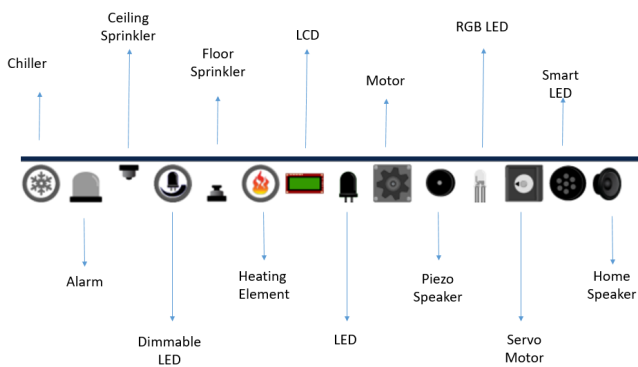


Fig. 5. Actuators in simulation software

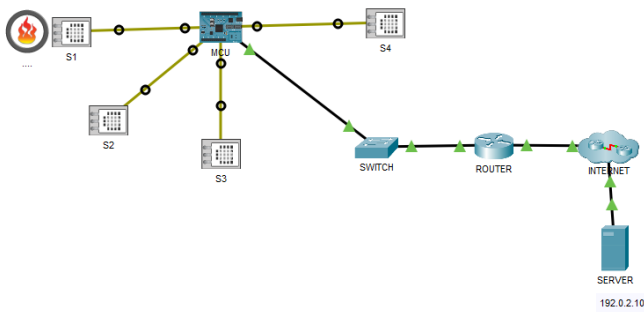


Fig. 6. Simulation topology for M2M communication scenario

In the scenario, the automobile was started to create smoke and it was evaluated whether the simulation worked correctly. In this simulation automation system, the reaction of the automation system can also be followed when the smoke level is above certain units. As shown Figure 11, the IoT Home Gateway hardware provides control from the web interface (192.168.25.1 in the example).

Accordingly, if the status of the solar panel is below 1Wh

or the battery is below 20%, the lamp will be half opened and the window will be opened.

#### IV. CONCLUSION

IoT solutions, which are developed for humans use contribute to building large networks of IoT devices, reducing complexity, enabling device efficiency, and driving innovation among industries seeking operational efficiency. IoT solutions cover everything IoT device designers, software developers, and product manufacturers need to develop and implement IoT ideas, including hardware IP and software platforms. End-to-end security, multiple workloads, secure network systems, and cyber-security measures developed using artificial intelligence methods are effectively used in IoT solutions. Since the physical realization of all these systems requires high cost, simulation tools are used effectively.

Simulations are tools that can be used in situations that may be difficult or dangerous to do in the real world and help understand how the real environment works. Simulations are used to develop the first proof of concept of the research life cycle. They are also very useful tools that allow you to analyze the behavior of a system by making changes in parameters, eliminating various additional tasks that are not directly related to the purpose in the real environment. While developing IoT solutions, working with simulation software before prototyping prevents unnecessary waste of time and helps to detect possible error situations in advance. In this study, various IoT solution examples were introduced using Cisco Packet Tracer 8.0 simulation software and IoT Supported Home Automation Systems were developed with sample scenarios. Software-ready Python, Java Script or block-based code keeps the attention focused directly on the IoT solution. In this study, analysis of network traffic and bandwidth consumption is not examined. Depending on the number of IoT devices, new scenarios can be developed using such criteria.

```

MCU:
66:         "value": "DATA: {data}",
67:         "size": 32
68:     }
69: }
70: }
71: }
72: }
73: socket = UDPSocket()
74:
75: # set callback with pdu info
76: socket.onReceiveWithPDUInfo(onUDPReceiveWithPDUInfo)
77: print(socket.begin(port))
78:
79: count = 0
80: while True:
81:     ortalama=sensorOku()
82:     print(ortalama)
83:     count += 1
84:     if (ortalama>0):
85:         data = "uyari " + str(ortalama)
86:
87:         pduInfo = PDUInfo(pduColor)
88:         pduInfo.setOutFormat(protocolName, pduType, {"typ
89:         pduInfo.addOutMessage("I am sending some data.")
90:
91:         socket.sendWithPDUInfo(dst, port, data, pduInfo)
92:
SERVER:
1: from udp import *
2: from time import *
3: from simulation import *
4:
5: dst = "1.1.1.1"
6: port = 1235
7: protocolName = "MyProtocol"
8: pduType = "MyPDU"
9: pduColor = 0xffff00
10:
11: def onUDPReceiveWithPDUInfo(ip, port, data, pduInfo):
12:     print("received from "
13:         + ip + ":" + str(port) + ":" + data)
14:
15:     # add a msg to pdu info and set it as accepted
16:     pduInfo.addInMessage("I got some data.")
17:     pduInfo.setAccepted()
18:
19: def main():
20:
21:     # add custom PDU with definition
22:     if not Simulation.hasCustomPDU(protocolName, pduType):
23:         Simulation.addCustomPDU(protocolName, pduType, {
24:             "title": "My PDU",
25:             "units": "Bits",
26:             "unit_marks": [
27:                 "\u00d72"
28:             ]

```

Fig. 7. Python codes used in UDP communication

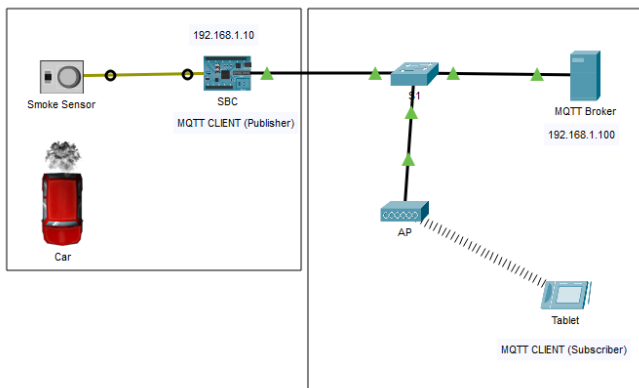


Fig. 8. Simulation topology for the MQTT sample

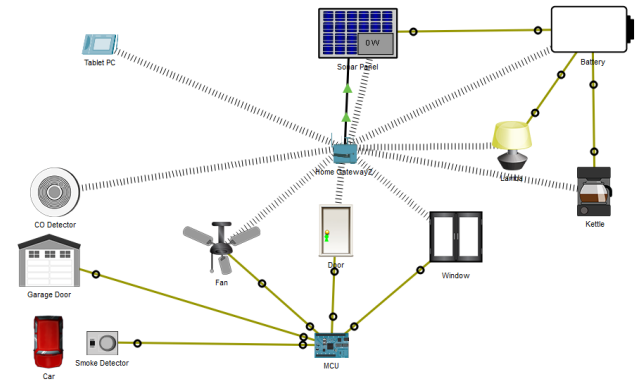


Fig. 10. IoT Gateway solution topology

```

Event Log

{"cmd": "ID", "ID": "397f87f87272f0L"}
{"cmd": "CONNECT", "client": "SBC (397f87f87272f0L)", "protocolId": "MQTT", "protocolVersion": "3.1.1", "clean": 1, "clientId": "397f87f87272f0L", "keepalive": 60, "username": "", "password": "", "will": {}}
{"cmd": "CONNACK", "client": "SBC (397f87f87272f0L)", "returnCode": 0, "sessionPresent": 0}
{"cmd": "SUBSCRIBE", "client": "SBC (397f87f87272f0L)", "packetId": 24941, "topic": "Home/Garage", "qos": 0}
{"cmd": "SUBACK", "client": "SBC (397f87f87272f0L)", "packetId": 24941, "topic": "Home/Garage", "qos": 0, "returnCode": 0}
{"cmd": "PUBLISH", "client": "SBC (397f87f87272f0L)", "qos": 0, "dup": 0, "topic": "Home/Garage", "payload": "2", "retain": 0}
{"cmd": "PUBLISH", "client": "SBC (397f87f87272f0L)", "qos": 0, "dup": 0, "topic": "Home/Garage", "payload": "2", "retain": 0}
{"cmd": "PUBLISH", "client": "SBC (397f87f87272f0L)", "qos": 0, "dup": 0, "topic": "Home/Garage", "payload": "2", "retain": 0}
{"cmd": "PUBLISH", "client": "SBC (397f87f87272f0L)", "qos": 0, "dup": 0, "topic": "Home/Garage", "payload": "2", "retain": 0}

```

Fig. 9. Client side view of messages received from MQTT broker

Fig. 11. IoT Gateway automation configuration from the web interface

## REFERENCES

- [1] M. Stoyanova, Y. Nikoloudakis, S. Panagiotakis, E. Pallis, and E. K. Markakis, "A Survey on the Internet of Things (IoT) Forensics: Challenges, Approaches, and Open Issues," *IEEE Communications Surveys and Tutorials*, vol. 22, no. 2, pp. 1191–1221, 2020.
- [2] M. Chernyshev, Z. Baig, O. Bello, and S. Zeadally, "Internet of things (IoT): Research, simulators, and testbeds," *IEEE Internet of Things Journal*, vol. 5, no. 3, pp. 1637–1647, jun 2018.
- [3] G. Tuna and R. Daş, "Wireless sensor network-based health monitoring system for the elderly and disabled," *International Journal of Computer Networks and Applications*, vol. 2, no. 6, pp. 247–253, 2015. [Online]. Available: <http://www.ijcna.org/issues.php?vol=2&issue=6http://files/107/Vol-2-issue-6-M-02.pdf>
- [4] R. Daş, G. Tuna, and A. Tuna, "Design and implementation of a smart home for the elderly and disabled," *International Journal of Computer Networks and Applications*, vol. 2, no. 6, pp. 242–246, 2015. [Online]. Available: <http://www.ijcna.org/issues.php?vol=2&issue=6http://files/109/Vol-2-issue-6-M-01.pdf>
- [5] R. Das, A. Tuna, S. Demirel, and M. K. Yurdakul, "A survey on the internet of things solutions for the elderly and disabled: Applications, prospects, and challenges," *International Journal of Computer Networks And Applications*, vol. 4, no. 3, pp. 84–92, jan 2017. [Online]. Available: <http://www.ijcna.org/Manuscripts/IJCNA-2017-O-08.pdfhttp://files/111/IJCNA-2017-O-08.pdf>
- [6] I. I. Pătru, M. Carabaş, M. Bărbulescu, and L. Gheorghe, "Smart home IoT system," *Networking in Education and Research: RoEduNet International Conference 15th Edition, RoEduNet 2016 - Proceedings*, 2016.
- [7] T. Malche and P. Maheshwary, "Internet of Things (IoT) for building smart home system," in *2017 International Conference on I-SMAC (IoT in Social, Mobile, Analytics and Cloud)*, 2017, pp. 65–70.
- [8] H. Singh, V. Pallagani, V. Khandelwal, and U. Venkanna, "IoT based smart home automation system using sensor node," *Proceedings of the 4th IEEE International Conference on Recent Advances in Information Technology, RAIT 2018*, pp. 1–5, 2018.
- [9] W. A. Jabbar, M. H. Alsibai, N. S. S. Amran, and S. K. Mahayadin, "Automation System for Smart Home," *2018 International Symposium on Networks, Computers and Communications (ISNCC)*, pp. 1–6, 2018.
- [10] F. Yalcinkaya, H. Aydılek, M. Y. Erteen, and I. Nihat, "IoT based Smart Home Testbed using MQTT Communication Protocol," *Uluslararası Mühendislik Araştırma ve Gelistirme Dergisi*, p. 317, 2020.
- [11] Y. Kocyigit and Ö. Sine, "İnternet Üzerinden Kontrol Edilen Tam Otomasyonlu Akıllı Ev Sistemleri İçin Örnek Bir Uygulama," *DÜMF Mühendislik Dergisi*, vol. 11, no. 2, pp. 521–532, 2020.
- [12] H. Gunes, S. Bicakci, E. Orta, and D. Akdas, "Akıllı evlerde kullanılan yapay zekâ teknikleri için simülasyon geliştirilmesi," *Gazi Üniversitesi Fen Bilimleri Dergisi Part C: Tasarım ve Teknoloji*, vol. 7, no. 3, pp. 554–563, 2019.
- [13] A. Eleyan and J. Fallon, "IoT-based home automation using android application," *2020 International Symposium on Networks, Computers and Communications, ISNCC 2020*, pp. 3–6, 2020.
- [14] M. Assim and A. Al-Omary, "Design and Implementation of Smart Home using WSN and IoT Technologies," *2020 International Conference on Innovation and Intelligence for Informatics, Computing and Technologies, 3ICT 2020*, 2020.
- [15] A. Ozturk and N. Sepanta, "Akıllı ESistemlerinde KullanılanYöntemlerin Farklari, Avantajlari Ve Dezavantajlari," *Istanbul Aydın Üniversitesi Dergisi*, vol. 9, no. 4, pp. 115–125, 2017.
- [16] P. Sethi and S. R. Sarangi, "Internet of Things: Architectures, Protocols, and Applications," *Journal of Electrical and Computer Engineering*, vol. 2017, p. 25, 2017.
- [17] P. Sivagami, D. Jamunarani, P. Abirami, M. Pushpavalli, V. Geetha, and R. Harikrishnan, "Smart Home Automation System Methodologies-A Review," in *2021 Third International Conference on Intelligent Communication Technologies and Virtual Mobile Networks (ICICV)*. IEEE, feb 2021, pp. 1386–1390. [Online]. Available: <https://ieeexplore.ieee.org/document/9388491/>
- [18] L. Dürkop, B. Czybik, and J. Jasperneite, "Performance evaluation of M2M protocols over cellular networks in a lab environment," *2015 18th International Conference on Intelligence in Next Generation Networks, ICIN 2015*, pp. 70–75, 2015.
- [19] E. Ozdogan and O. A. Erdem, "Nesnelerin İnterneti İçin Hibrit Uygulama Katmanı Protokol Tasarımı," *Mühendislik Bilimleri ve Tasarım Dergisi*, vol. 8, no. 1, pp. 285–304, mar 2020. [Online]. Available: <https://dergipark.org.tr/tr/doi/10.21923/jesd.530295>
- [20] A. Talaminos-Barroso, M. A. Estudillo-Valderrama, L. M. Roa, J. Reina-Tosina, and F. Ortega-Ruiz, "A Machine-to-Machine protocol benchmark for eHealth applications – Use case: Respiratory rehabilitation," *Computer Methods and Programs in Biomedicine*, vol. 129, pp. 1–11, 2016. [Online]. Available: <https://www.sciencedirect.com/science/article/pii/S0169260715302959>
- [21] Edited by Andrew Banks and Rahul Gupta, "MQTT Version 3.1.1," 2014. [Online]. Available: <http://docs.oasis-open.org/mqtt/mqtt/v3.1.1/mqtt-v3.1.1.html>
- [22] R. Herrero, "Analytical model of IoT CoAP traffic," *Digital Communications and Networks*, vol. 5, no. 2, pp. 63–68, 2019.
- [23] A. Keranen, M. Kovatsch, and K. Hartke, "RESTful Design for Internet of Things Systems," 2017. [Online]. Available: <https://tools.ietf.org/id/draft-keranen-t2trg-rest-iot-05.htm>
- [24] H. Luo, C. Wang, H. Luo, F. Zhang, F. Lin, and G. Xu, "G2F: A Secure User Authentication for Rapid Smart Home IoT Management," *IEEE Internet of Things Journal*, vol. XX, no. XX, pp. 1–12, 2021.



**Erdal Ozdogan** graduated B.Sc. degree from Ankara University Astronomy and Space Science in 2000, and a second B.Sc. degree, from Anadolu University Management Information Systems in 2019, Turkey. He graduated with his master's degree from Gazi University, Department of Computer Science in 2012, and his Ph.D. in 2020 at the Department of Information Systems. He serves instructor training to public institutions and organizations about computer networks, cybersecurity, and IoT at the Cisco Networking Academy.



**Resul Das** is a full professor in the Department of Software Engineering at the University of Firat, where he has been a faculty member since 2011. From 2000 to 2011 he served as both instructor and network administrator at the Department of Informatics at the Firat University. He has been the instructor and the coordinator of the Cisco Networking Academy Program since 2002 at this university. He graduated with B.Sc. and M.Sc. degrees from the Department of Computer Science at the Firat University in 1999 and 2002 respectively. Then he completed his Ph.D. degree at the Department of Electrical-Electronics Engineering at the same university in 2008. He also worked between September 2017 and June 2018 as a visiting professor at the Department of Computing Science at the University of Alberta, Edmonton, Canada. He has authored more than a hundred papers in international conference proceedings and also he has been serving as Associate Editor for the Journal of IEEE Access and the Turkish Journal of Electrical Engineering and Computer Science. His current research areas include computer networks and network security, cybersecurity, software design and architecture, IoT/M2M applications, knowledge discovery, and data fusion.

# Automatic Cell Nuclei Segmentation Using Superpixel and Clustering Methods in Histopathological Images

Gamze Mendi and Cafer Budak

**Abstract**— It is seen that there is an increase in cancer and cancer-related deaths day by day. Early diagnosis is vital for the early treatment of the cancerous area. Computer-aided programs allow for the early diagnosis of unhealthy cells that specialist pathologists diagnose due to efforts.

In this study, clustering and superpixel segmentation techniques were used to detect cell nuclei in high-resolution histopathology images automatically. As a result of the study, the successful performances of the segmentation algorithms were analyzed and evaluated. It is seen that better success is obtained in the Watershed and FCM algorithms in high-resolution histopathological images used. Quickshift and SLIC methods gave better results in terms of precision. It is seen that there are k-Means and FCM algorithms that provide the best performance in F measure (F-M), and the correct negative rate (TNR) is more successful in Quickshift, k-Means, and SLIC methods.

**Index Terms**— Segmentation, histopathological image analysis, superpixels, image processing

## I. INTRODUCTION

CANCER, HAS been among the serious health problems in recent years, is among the world's top causes of death. Humans with different age groups and other characteristics are getting cancer and lose their life. When this situation is analyzed with Turkey's health statistics, approximately 96 thousand men and 67 thousand women get cancer in a year.


While lung and prostate cancers are common in men, one in four women are diagnosed with breast cancer compared to other cancers [1]. Early diagnosis of the tumor plays a crucial role in early treatment. Evolving visualization devices allow high-resolution histopathological images to allow laboratory examination that causes early treatment for cancer [2]. The development of high-resolution devices enables specialist pathologists to analyze texture with lesser

effort. It is seen that digital image processing, compared to microscopy, is advantageous. The fact that a certain number of people can observe with the microscope at the same time, and the specialized pathologist who repeatedly has no opportunity to examine this tissue, can be considered a disadvantage. With digital imaging devices, hundreds of specialist pathologists can read the tissue simultaneously [2]. Expert pathologists perform microscopic examinations of patients' tissues or organs for diagnosis. Before reviewing the biopsy tissue, they undergo it to certain stages.


The tissue taken undergoes preliminary processes such as fixation, staining, cutting, and scanning. When these processes are performed successfully, fat tissue, cytoplasm, and cellular structures become distinguishable. Making these procedures unhealthy prevents the differentiation of systems in the tissue. It reduces the success of segmentation in the computer-aided analysis due to destructive processes [3]. There are many studies of researchers related to this subject. Kayaalti and Aksebzeci [4] studied a data set containing benign and malignant tumor images in breast cancer. They perform the Gray Level Co-Occurrence Matrices feature extraction matrix. They achieved 82.06% success with the Random Forests classifier. Albayrak and Bilgin [5] used a deep learning-based SegNet method to divide cellular structures in high-resolution histopathological images. They observed that SegNet was quite successful in segmentation cellular networks compared to other methods (k-Means, Otsu, Irshad) that are frequently used.

Çakır vd. [6] designed a system that automatically detects cancer precursor lesions in their study using the convolutional neural networks method of precursor lesions in cervical cancer. The system achieved 92% success in distinguishing lesions from images. They created a model with an 81.71 percent booming segment according to the Dice coefficient. Turan and Bilgin [7] used histopathological images obtained as a result of hematoxylin and eosin staining of deep learning and cancer diagnosed biopsy samples on breast pathology images, and comparatively evaluated the semantic segmentation process using SegNet [8] and U-Net [9] algorithms, and they found that the average F-measure of SegNet was 0.73, the training sensitivity was 85.64%, the average F-measure of U-Net was 0.73, the training sensitivity was 72.87%. They have achieved successful results in the KNN, as long as the number of neighbors is below 10. They achieved a success rate of 0.99 in terms of precision, sensitivity, and f1-score. Many studies related to segmentation in the literature [11-14] Human et

**GAMZE MENDI**, is with the Department of Electrical and Electronics Engineering University of Batman University, Batman, Turkey.(e-mail: gamzemendi2@gmail.com).

 <https://orcid.org/0000-0003-4295-0410>

**CAFER BUDAK** is with the Department of Biomedical Engineering, Dicle University, Diyarbakir Turkey, (e-mail: cafer.budak@dicle.edu.tr).

 <https://orcid.org/0000-0002-8470-4579>

Manuscript received January 19, 2021; accepted May 25, 2021.

DOI: [10.17694/bajece.864266](https://doi.org/10.17694/bajece.864266)

Copyright © BAJECE

ISSN: 2147-284X

<http://dergipark.gov.tr/bajece>

al. [15] suggest automatic identification of diseased leaf areas. The technique used the SLIC algorithm in zones called superpixels with a similar color to form a group. They used it to train neural networks to classify whether superpixels are healthy or unhealthy. They found the average F-score to be 0.67. Yuan et al. [16] developed a superpixel-based and boundary-sensitive convolutional neural network for superpixel-based liver disease zone automatic segmentation. They divided them into three classes as inner liver, liver border, and posterior liver. They obtained an SBBS-CNN with an average membrane similarity coefficient of  $97.31 \pm 0.36\%$  and an average symmetrical surface of  $1.77 \pm 0.49$  mm. Superpixel algorithms have been used in many areas in the literature [17-19].

In this study, various methods were used in the segmentation of high-resolution histopathological images, and their success rates are compared. This proposed study includes the method performed in part 2, the experimental results obtained within the study's scope in part 3, and the conclusion in part 4.

## II. METHODOLOGY

Segmentation methods used in our study are presented in this chapter. Superpixel approaches are used in various areas of image processing.

### A. K-Means Method

K-means method is used for segmentation to reduce the distance between the data and the cluster to a minimum and divide 'N' data into 'c' clusters [20]. Algorithm steps are as follows;

- A random k number of cluster centers are determined
- The distance between cluster centers and each pixel is calculated
- The average of each cluster is calculated.
- The pixel is assigned to the closest cluster center. The process ends when the stop criteria are met. If not, the process continues from step 2.

$$b_n = \sum_{j=1}^N \max(d_{k-1}^j - \|x_n - x_j\|^2, 0) \quad (1)$$

$$i = \arg b_n \quad (2)$$

In Equation 1  $d_{k-1}^j$  is the square distance between the closest cluster centers located between cluster centers. In other words, it is the cluster center of  $x_j$ .  $b_n$  aims to reduce the error by placing a new cluster center at the  $x_n$  location.  $x_j$ , are the cluster centers obtained so far [21]. In the K-means clustering algorithm, as the number of data and the number of clusters increases, the calculation time increases.

### B. Fuzzy C-Means Method

The Fuzzy C-Means method is an algorithm that ensures data can be assigned to more than one cluster. With the help

of its membership degree, it can have more than one cluster. The degree of membership taking values between 0 and 1 and that determines how much they join in which cluster. In the algorithm steps, first, the membership matrix ( $U^0$ ) is created with random values. The threshold value ( $\epsilon$ ) and the number of clusters (c) the stopping condition is determined. The value of m, which is the fuzzy parameter, is determined. [22]

In the Fuzzy C Means method, the cluster center is calculated as in Equation 3.  $u_{ij}$  is the membership value of the pixel in the cluster

$$c_j = \frac{\sum_{i=1}^n (u_{ij}^k)^m y_i}{\sum_{i=1}^n (u_{ij}^k)^m} \quad (3)$$

The membership matrix is calculated as in Equation 4 using  $U^{k+1}$ .

$$u_{ij}^{k+1} = \frac{1}{\sum_{k=1}^c \left(\frac{d_{ij}}{d_{kj}}\right)^{\frac{2}{m-1}}} \quad (4)$$

$$d_{ij} = \|y_i - c_i\|^2 \quad (5)$$

The process continues until  $\max_{ij} \|u_{ij}^k - u_{ij}^{k+1}\| < \epsilon$  condition is met. When the process is achieved, it returns to the central matrix.

### C. Simple Linear Iterative Clustering (SLIC) Method

Simple Linear Iterative Clustering (SLIC) is a superpixel segmentation algorithm proposed by Achanta et al. SLIC is a k-Means based algorithm that clusters neighboring pixels considering color and coordinate information [23]. When SLIC is used as a superpixel preprocessing step, it provides computational speed, memory savings [24]. The process performed by the segmentation method for each pixel is given in equation 6.

$$d_c = \sqrt{(I_j - I_i)^2 + (a_j - a_i)^2 + (b_j - b_i)^2} \quad (6)$$

In Equation 7, how the coordinate information of each pixel is calculated is specified. In the equation, j is the pixel accepted as the center and i value is the value that wants to be clustered.

$$d_s = \sqrt{(x_j - x_i)^2 + (y_j - y_i)^2} \quad (7)$$

What is calculated in Equation 8 is the realization of assigning the relevant pixel to a center.

$$D' = \sqrt{\left(\frac{d_c}{N_c}\right)^2 + \left(\frac{d_s}{N_s}\right)^2} \quad (8)$$

The maximum expected spatial distance ( $N_s$ ) within a given cluster should correspond to the sampling interval. SLIC superpixels correspond to clusters on the lab color image plane. Determining the maximum color distance ( $N_c$ ) will not be easy as the color distances will vary significantly from image to image and cluster to cluster. This situation can be avoided by fixing  $N_c$  to a fixed value of m.

$$D = \sqrt{d_c^2 + \left(\frac{d_s}{S}\right)^2 m^2} \quad (9)$$

The  $m$  value in Equation 9 also determines the relative importance between color similarity and spatial proximity.

#### D. Quick Shift Segmentation Method

Quickshift is one of the popular superpixel segmentation algorithms. The principle of that algorithm is that it identifies and repeats data in a series of data points. Quickshift can be used in any field. When all data points are connected, the threshold value is used to distinguish the modes from each other. Different sets of data are separated from each other [25].

This method aims to generate superpixels by automatically changing the fast transition parameters according to a definition. Neighbours are considered within a spatial distance with a Gaussian kernel [25].

Then, as shown in the equation, it creates a tree with a higher density value that connects each image pixel  $(x, y)$  to the nearest neighbour  $(x', y')$

$$P(X_i) = \frac{1}{N} \sum_{j=1}^N k(D(x_i, x_j)), x_i, x_j \in R^d \quad (10)$$

$N$  is data and  $k(x)$  value is the kernel function with a Gaussian window.  $D(x_i, x_j)$  is the distance between  $x_i$  and  $x_j$ . The distances are calculated with the equation in 11 using the Euclidean distance in the spatial and color field.

$$d_q(i, j) = d_{xy}(i, j) + w_q \cdot d_{lab}(i, j) \quad (11)$$

The  $w_q$  in Equation 11 is the weighting parameter, and the smaller the weighting parameter, the more critical the spatial field [26].

#### E. Felzenszwalb Segmentation Method

Felzenszwalb is an algorithm based on local variation graphics. Since the algorithm does not have a density limitation, it typically produces zones of irregular shapes and sizes [27]. The algorithm works almost linearly with time and is fast in practice. The critical segmentation method is ignoring the detail in high variable images while preserving low variable images [28].

Graph-based algorithm input is  $G = (V, E)$  with  $n$  corners and  $m$  sides. Its output is the division of  $V$  into  $S = (C_1, C_2, \dots, C_r)$  components [29].

$C \subseteq V$  is the component's, internal difference; the maximum weight covering the component minimum is expressed as  $MST(C, E)$ . So;

$$Int(C) = w(e) \quad (12)$$

The difference between  $C_1, C_2$  components and  $V$  are defined as the minimum weight edge connecting the two parts. So;

$$Dif(C_1, C_2) = w(v_i, v_j) \quad (13)$$

#### F. Watershed Segmentation Method

Watershed is well suited for superpixel production; It provides good adherence to the object's boundaries when the image gradient is calculated and allows control by selecting the resulting images number and spatial arrangement [30]. The grayscale gradient image where it states the boundaries in the algorithm is required. It sees the bright pixels in the image as the landscape where it consists of high peaks. Then it creates a distinct image segment from high hills and flood basins [31].

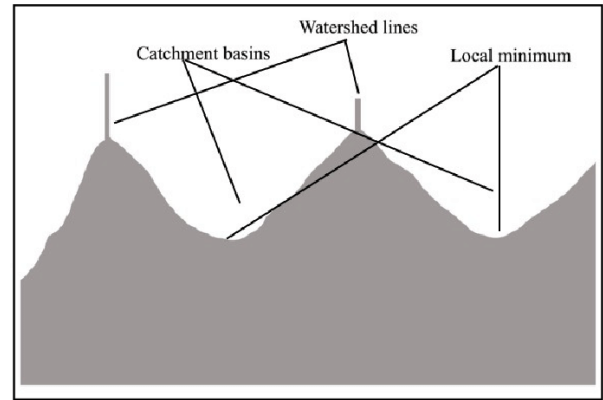


Fig.1. Modeling of the Watershed algorithm [32]

A grayscale image is defined as  $G = (D, E, f)$ . You assume that the image  $f$  is the continuous space  $C(D)$ , only critical points in a connected domain  $D$  form function on  $D$ . The distance between points is calculated as in the following equation [33]:

$$T_f(p, q) = \inf_{\lambda} \int_{\lambda} \|\nabla f(\lambda(s))\| ds \quad (14)$$

#### G. ERS Segmentation Method

ERS segmentation is a graph-based superpixel segmentation method proposed by Lui et al. Unlike well-known superpixels such as SLIC, and ERS attempts to find compact and homogeneous superpixels using a graph-based approach. ERS consists of two components as the entropy ratio and balancing term. Entropy ratio, tight formation, homogeneous clusters, and the balancing period that create compact appearance provide similar clusters [34]. In the ERS algorithm; Similarities between neighbouring vertices ( $w_{ij}$ ) are calculated, the number of clusters ( $k$ ) and the weight factor ( $\lambda$ ) are set. The original subset is set to  $A = \emptyset$ , and the edge is set to  $U = E$ . For each side  $a \in U$ , the function  $F(A \cup \{a\}) - F(A)$  is calculated. It has found a value that provides the greatest success. The function continues until  $A$  becomes  $U = \emptyset$  independent of  $U$ . The superpixel segmentation in the original subset ( $A$ ) is created [35]. The uncertainty of the random variable is measured by entropy ( $H$ ). With the probability mass function  $p(x)$ , the entropy of  $X$ , which is a discrete random variable, is calculated as in the equation [36];



$$H(X) = - \sum_{x \in X} p(x) \log p(x) \quad (15)$$

### G. Measurements Used to Evaluate Segmentation Performance

Some measurements were used to determine the operating performance in the experiments. These are: True Positive Ratio (TPR), True Negative Ratio (TNR), Precision (P), Overlap Ratio (OR), False Positive Ratio (FPR), False Negative Ratio (FNR) are the measures used to evaluate the segmentation performance of FM [37].

Metric	Equation	
Precision	$\frac{TP}{TP + FP}$	(16)
True Positive Ratio (TPR)	$\frac{TP}{TP + FN}$	(17)
F- Measure (F-M)	$\frac{2 \times \text{precision} \times TPR}{\text{precision} + TPR}$	(18)
True Positive Ratio (TNR)	$\frac{TN}{TN + FP}$	(19)
Overlap Ratio (OR)	$\frac{A(S) \cap A(G)}{A(S) \cup A(G)}$	(20)

In formula 16, A (S) represents the segmented image area, while A (G) describes the actual image's location. The parameters specified in the formulas are true positive (TP), true negative (TN), false positive (FP), false negative (FN), precision, and recall. True positive represents the number of pixels correctly affected as positive samples in the area of cellular structure. In contrast, true negative refers to the number of pixels outside the cellular systems and are negatively affected [35].

The data set used in our study was taken from the Beck Laboratory of Harvard University. The dataset is selected from TCGA (The Cancer Genome Atlas) data containing high-resolution histopathological images of kidney carcinoma. Histopathological images had cropped  $400 \times 400$  images. Expert pathologists marked cellular structures in the images, and 64 histopathological images were used.

### III. EXPERIMENTAL RESULTS

Automatic detection of diseased cellular structures on high-resolution histopathological images is of great importance for cancer detection. Different segmentation methods were used for 64 histopathological images. Some of the parameters were used to evaluate the results obtained. This study evaluated the performance of using methods for automatic cell detection in high-resolution histopathological images.

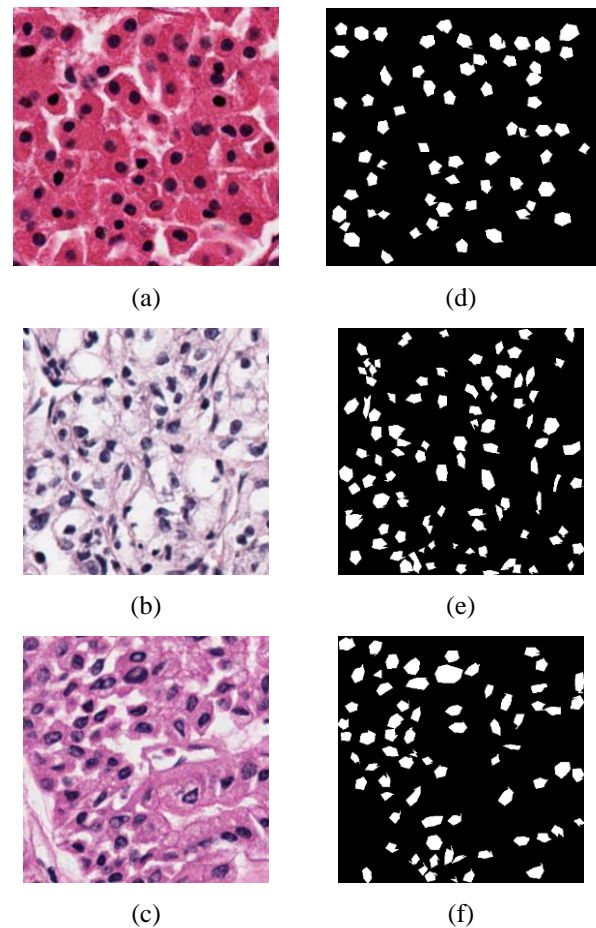


Fig.2. High-resolution images obtained in the dataset are (a), (b), and (c). The reference image of the image marked by expert pathologists are (d), (e), and (f).

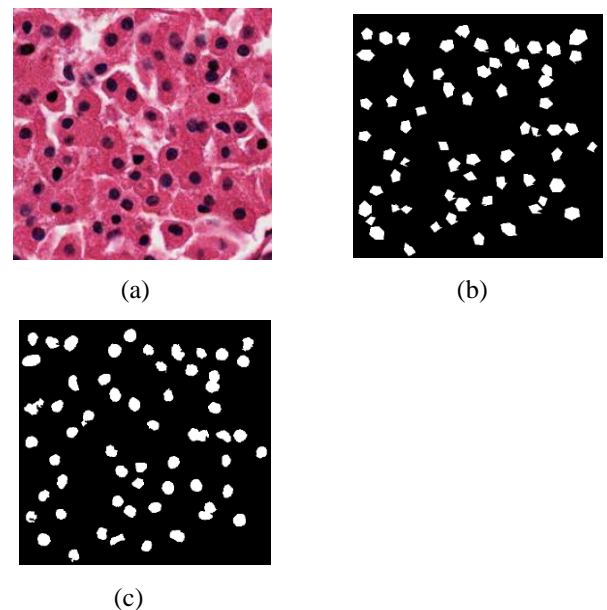


Fig.3. (a) High-resolution image obtained in the data set (b) image marked by expert pathologists (c) k-Means segmentation result

The results of k-means, fuzzy C-means, and superpixel segmentation algorithms (SLIC, Watershed, Quickshift, Felzenszwalb, ERS) were obtained on 64 high-resolution histopathological images.

In each method, different values were given for the parameters, and the results were evaluated.

TABLE I  
THE PERFORMANCE OF THE STUDIES ON THE SAME DATA SET

Method	True Positive	Precision	F-Measure	True Negative
KMeans	0,60%	0,69%	0,61%	<b>0,97%</b>
FCM	0,60%	0,68%	0,61%	<b>0,97%</b>
SLIC+KO	0,69%	0,67%	0,63%	0,96%
SLIC+BCO	0,66%	0,68%	0,64%	0,96%
SLIC-DBSCAN	0,74%	0,61%	0,64%	0,94%
ERS	0,65%	0,64%	0,61%	0,95%
TPRS	0,65%	0,63%	0,61%	0,96%
SegNet	0,70%	<b>0,71%</b>	<b>0,69%</b>	0,95%
Irshad vd.	<b>0,76%</b>	0,62%	0,65%	0,96%
Otsu	0,67%	0,64%	0,62%	0,95%

Table I shows the success rates of the studies belonging to the same data set. It was seen that the TPR value gave better results in FCM and K-Means methods. Quickshift, Watershed, and Felzenszwalb methods are used as different methods from the previously used dataset.

### Success Graphic

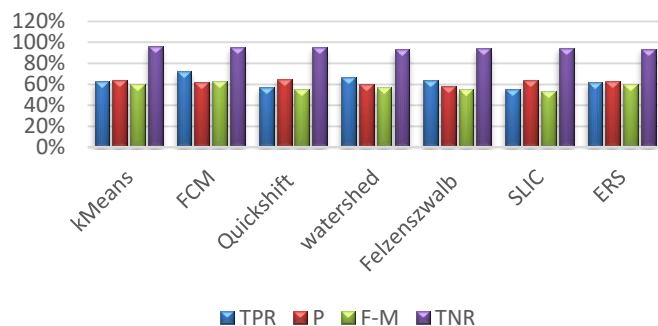


Fig.4. Performance chart of segmentation results

In Figure 4, the performance graph of segmentation algorithms used is shown.

## IV. CONCLUSION

TABLE II  
PERFORMANCE OF THE USED SEGMENTATION ALGORITHMS

Method	True Positive	Precision	F-Measure	True Negative
kMeans	63%	64%	60%	96%
FCM	73%	62%	63%	95%
Quickshift	57%	65%	55%	96%
Watershed	67%	60%	57%	93%
Felzenszwalb	64%	59%	55%	94%
SLIC	56%	64%	53%	95%
ERS	64%	63%	60%	94%

As seen in Table II, seven segmentation methods were used in the study. It is seen that better success is obtained in the Watershed and FCM algorithms in high-resolution histopathological images used. Quickshift and SLIC methods gave better results in terms of precision. It is seen that there are k-Means and FCM algorithms that provide the best performance in F measure (F-M), and the true negative ratio is more successful in Quickshift, k-Means, and SLIC methods. Because the borders of the cells marked by the pathologists are not precisely marked, their performance decreases.

## REFERENCES

- [1] Anonim,2017. Erken Teşhis Hayat Kurtarıcı [Online] <https://www.saglik.gov.tr/Eklenti/8635.kanser-istatistikleridocx.docx?0>
- [2] A. Albayrak and G. Bilgin, 2017. Superpixel approach in high resolution histopathological image segmentation. In 2017 25th Signal Processing and Communications Applications Conference (SIU) (pp. 1-4). IEEE.
- [3] J. Xu, L. Xiang, Q. Liu, H. Gilmore, J. Wu, J. Tang, and A. Madabhushi,2015. Stacked sparse autoencoder (SSAE) for nuclei detection on breast cancer histopathology images. IEEE transactions on medical imaging, 35(1), 119-130.
- [4] B. H. Aksebzeci, and Ö. Kayaalti, 2017. Computer-aided classification of breast cancer histopathological images. In 2017 Medical Technologies National Congress (TIPEKNO) (pp. 1-4). IEEE.
- [5] A. Albayrak, and G. Bilgin, (2018). Segmentation of cellular structures with encoder-decoder-based deep learning algorithm in histopathological images. In 2018 Medical Technologies National Congress (TIPEKNO) (pp. 1-4). IEEE.
- [6] A.Albayrak, A. Ünlü, N. Çalık, G. Bilgin İ. Türkmen A. Çakı, ... and L. D. Ata, (2017). Segmentation of precursor lesions in cervical cancer using convolutional neural networks. In 2017 25th Signal Processing and Communications Applications Conference (SIU) (pp. 1-4). IEEE.
- [7] S. Turan, and G. Bilgin, (2019). Semantic nuclei segmentation with deep learning on breast pathology images. In 2019 Scientific Meeting on Electrical-Electronics & Biomedical Engineering and Computer Science (EBBT) (pp. 1-4). IEEE.
- [8] B. Li, W. J. Niessen, S. Klein, M. de Groot, M.A. Ikram, M. W.Vernooij, and E. E. Bron,(2019). A hybrid deep learning framework for integrated segmentation and registration: Evaluation on longitudinal white matter tract changes. In International Conference on Medical Image Computing and Computer-Assisted Intervention (pp. 645-653). Springer, Cham.
- [9] O. Ronneberger, P. Fischer, and T. Brox (2015). U-net: Convolutional networks for biomedical image segmentation. In International Conference on Medical image computing and computer-assisted intervention (pp. 234-241). Springer, Cham.
- [10] M. E. Bagdigen, and G. Bilgin, (2019). Detection and Grading of Breast Cancer via Spatial Features in Histopathological Images. In 2019 Medical Technologies Congress (TIPEKNO) (pp. 1-4). IEEE.
- [11] A. Feng-Ping, and L. Zhi-Wen, (2019). Medical image segmentation algorithm based on feedback mechanism convolutional neural network. Biomedical Signal Processing and Control, 53, 101589.
- [12] K. Xia, H. Yin, P. Qian, Y. Jiang, and S. Wang, (2019). Liver semantic segmentation algorithm based on improved deep adversarial networks in a combination of weighted loss function on abdominal CT images. IEEE Access, 7, 96349-96358.
- [13] Y. Feng, H. Zhao, X. Li, X. Zhang, and H. Li, (2017). A multi-scale 3D Otsu thresholding algorithm for medical image segmentation. Digital Signal Processing, 60, 186-199.
- [14] T. H. Farag, W. A. Hassan, H. A. Ayad, A.S AlBahussain, U. A. Badawi, and M. K. Alsmadi, (2017). Extended absolute fuzzy connectedness segmentation algorithm utilizing region and boundary-

- based information. *Arabian Journal for Science and Engineering*, 42(8), 3573-3583.
- [15] I. F. Salazar-Reque, S. G. Huamán, G. Kemper, J. Telles, and D. Diaz, (2019). An algorithm for plant disease visual symptom detection in digital images based on superpixels. *Int. J. Adv. Sci. Eng. Inf. Technol*, 9(1), 194-203.
- [16] W. Qin, J. Wu, F. Han, Y. Yuan, W. Zhao, B. Ibragimov, ... and L. Xing, (2018). Superpixel-based and boundary-sensitive convolutional neural network for automated liver segmentation. *Physics in Medicine & Biology*, 63(9), 095017.
- [17] O. F. Kar, A. Güngör, S. Ilbey, and H. E. Güven, (2018, May). An efficient parallel algorithm for single-pixel and fpa imaging. In *Computational Imaging III* (Vol. 10669, p. 106690J). International Society for Optics and Photonics.
- [18] H. Yu, M. Jiang, H. Chen, J. Feng, Y. Wang, and Y. Lu, (2017). Super-pixel algorithm and group sparsity regularization method for compressed sensing MR image reconstruction. *Optik*, 140, 392-404.
- [19] S. Kaur, R. K. Bansal, M. Mittal, L. M Goyal, I. Kaur, and A. Verma, (2019). Mixed pixel decomposition based on extended fuzzy clustering for single spectral value remote sensing images. *Journal of the Indian Society of Remote Sensing*, 47(3), 427-437.
- [20] T. Kanungo, Mount, DM, Netanyahu, NS, Piatko, CD, Silverman, R., and Wu, AY (2002). An effective k-mean clustering algorithm: Analysis and application. *IEEE processes on model analysis and machine intelligence*, 24 (7), 881-892.
- [21] A. Likas, N. Vlassis, and J. J. Verbeek, (2003). The global k-means clustering algorithm. *Pattern recognition*, 36(2), 451-461.
- [22] B. K. Tripathy, A. Basu, and S. Govel, (2014). Image segmentation using spatial intuitionistic fuzzy C means clustering. In 2014 IEEE International Conference on Computational Intelligence and Computing Research (pp. 1-5). IEEE.
- [23] S. Zhang, Z. Ma, G. Zhang, T. Lei, R. Zhang, and Y. Cui (2020). Semantic Image Segmentation with Deep Convolutional Neural Networks and Quick Shift. *Symmetry*, 12(3), 427.
- [24] R. Achanta, A. Shaji, K. Smith, A. Lucchi, P. Fua, and S. Süsstrunk, (2012). SLIC superpixels compared to state-of-the-art superpixel methods. *IEEE transactions on pattern analysis and machine intelligence*, 34(11), 2274-2282.
- [25] S. Zhang, Z. Ma, G. Zhang, T. Lei, R. Zhang, and Y. Cui, (2020). Semantic Image Segmentation with Deep Convolutional Neural Networks and Quick Shift. *Symmetry*, 12(3), 427.
- [26] F. M. Osman, and M. H. Yap, (2020). Adjusted Quick Shift Phase Preserving Dynamic Range Compression method for breast lesions segmentation. *Informatics in Medicine Unlocked*, 100344.
- [27] A. Levinshtein, A. Stere, K. N. Kutulakos, D. J. Fleet, S. J. Dickinson, and K. Siddiqi, (2009). Turbopixels: Fast superpixels using geometric flows. *IEEE transactions on pattern analysis and machine intelligence*, 31(12), 2290-2297.
- [28] P. F. Felzenszwalb, and D.P. Huttenlocher, (2004). Efficient graph-based image segmentation. *International journal of computer vision*, 59(2), 167-181.
- [29] L. Yao, and S. Muhammad, (2019). A novel technique for analysing histogram equalized medical images using superpixels. *Computer Assisted Surgery*, 24(sup1), 53-61.
- [30] V. Machairas, E. Decencière, and T. Walter, (2014). Waterpixels: Superpixels based on the watershed transformation. In 2014 IEEE International Conference on Image Processing (ICIP) (pp. 4343-4347)
- [31] J. Schönberger, A. Siqueira, A. Mueller, E. Gouillart, G. Lee, M. Harfouche, J. Warner, J.N. Iglesias, L. Grüter, M. Corvellec, R. Fezzani, F. Boulogne, E. Panfilov, and S. Walt, (2014) <https://scikit-image.org/> [Online]
- [32] Benson, CC, V. Deepa, Lajish, VL, and K. Rajamani, (2016). Brain tumor segmentation from MR brain images using advanced fuzzy c-averaged clustering and watershed algorithm. In the 2016 International Conference on Informatics, Communication and Informatics Advances (ICACCI) (p.187-192).
- [33] J. B. Roerdink and A. Meijster, (2000). The watershed transform: Definitions, algorithms and parallelization strategies. *Fundamenta Informatica*, 41(1, 2), 187-228
- [34] A. Albayrak, and G. Bilgin, (2019). Automatic cell segmentation in histopathological images via two-staged superpixel-based algorithms. *Medical & biological engineering & computing*, 57(3), 653-665.
- [35] W. Wang, D. Xiang, Y. Ban, J. Zhang, and J. Wan, (2017). Superpixel segmentation of polarimetric SAR images based on integrated distance measure and entropy rate method. *IEEE Journal of Selected Topics in Applied Earth Observations and Remote Sensing*, 10(9), 4045-4058.
- [36] M. Y. Liu, O. Tuzel, S. Ramalingam, and R. Chellappa, (2011). Entropy rate superpixel segmentation. In *CVPR 2011* (pp. 2097-2104). IEEE.
- [37] A. S. Glas, J. G. Lijmer, M. H. Prins, G. J. Bonsel, and P. M. Bossuyt, (2003). The diagnostic odds ratio: a single indicator of test performance. *Journal of clinical epidemiology*, 56(11), 1129-1135.

## BIOGRAPHIES



**GAMZE MENDİ** received the B.S. degree in electrical and electronics engineering from Siirt University, Siirt, Turkey in 2017. She received the M.S in electrical and electronics engineering from Batman University Batman, Turkey in 2021. I am working as an engineer in DEDAS since 2018



**CAFER BUDAK** received his B.Sc. and M.Sc. degrees in the department of Electrical Electronics Engineering from Dicle University in 1998 and 2008, respectively. He is received his PhD degree in the department of Electrical Electronics Engineering from Fırat University in 2014. He is currently an Assistant Professor at the department of

Biomedical Engineering at the Dicle University in Turkey. His research interests include artificial intelligence, deep learning, machine learning, image processing, Graph Neural Network, and histopathological images

# Solar Energy Potential in Horn of Africa: A Comparative Study Using Matlab/Simulink

Erkan Dursun

**Abstract**— Geographically, the Horn of Africa is one of the regions that the Equator passes over, providing the opportunity for vigorous solar energy. However, despite the enormous solar energy resources, more than half of the region, 132 million populations have not yet access to electricity. This study presents an overview of the potential of solar energy in the region. Then review the current solar energy status and policies related to it. A Matlab/Simulink model is developed to show the comparative analyses of the solar radiation graphically on the photovoltaic modules and electricity outputs for the Horn of African countries' capitals. As a result of the simulation model, Ethiopia-Addis Ababa receives the highest annual solar radiation of 2915.03 kWh/m<sup>2</sup>-year while Eritrea-Asmara with the lowest annual solar radiation of 2198.47 kWh/m<sup>2</sup>-year. The annual electrical output of the photovoltaic modules in Ethiopia-Addis Ababa is the highest with 286.685 kWh/year and Eritrea-Asmara 216.214 kWh/year as the lowest in the region. The number of photovoltaic modules and the optimum tilt angles are calculated. For Ethiopia-Addis Ababa, the lowest photovoltaic module number is 10, and the optimum PV tilt angle is 11.163°. For Eritrea-Asmara, the highest photovoltaic module number is 14, with a tilt angle of 15.397°.


**Index Terms**— The Horn of Africa, solar energy, Matlab

## I. INTRODUCTION

THE HORN of Africa refers to the eastern-most edge of Africa's mainland, which lies on the Indian Ocean to the east, Red sea to the northwest, and the Gulf of Aden to the north [1]. It is just a few hundreds of miles into the Arabian sea and has a link with Arabian Peninsula geographically and culturally. In terms of the geopolitical situation of the world, the region's location and its closeness connections to east and west of the world's maritime transport and energy supplies are a crucial factor of the region's importance with vast natural resources and minerals (Figure 1). Geographically, the region covers four states, which are Somalia, Ethiopia, Djibouti, and Eritrea, known as the horn of African countries [2-3].

Ethiopia has the highest population ratio, followed by Somalia, Eritrea, and Djibouti (Table 1), respectively.

**ERKAN DURSUN** is with Department of Electrical and Electronics Engineering, Marmara University, Istanbul, Turkey (e-mail: [erkandursun@marmara.edu.tr](mailto:erkandursun@marmara.edu.tr)).

 <https://orcid.org/0000-0002-7914-8379>

Manuscript received May 12, 2021; accepted July 25, 2021.  
DOI: [10.17694/bajece.974404](https://doi.org/10.17694/bajece.974404)

According to Table 1, Eritrea has the highest annual population growth rate with 8.7%, and Djibouti has the lowest with 1.5%. Thus, a high-energy demand follows the high population growth rate.

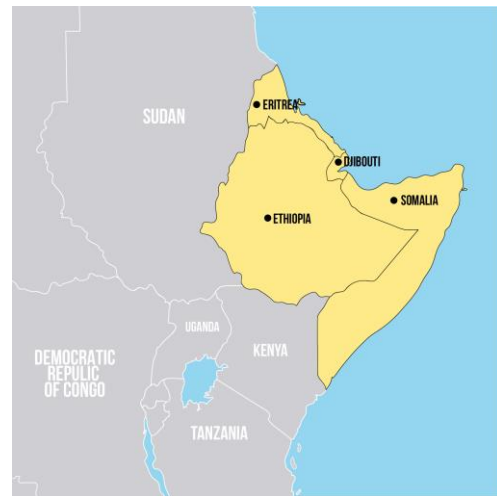


Fig. 1. The horn of Africa region map

TABLE I  
HORN OF AFRICAN COUNTRIES PROFILE [4]

Country	Area [km <sup>2</sup> ]	Population	Population growthrate [%]	Urban population
Ethiopia	1,000,000	114,963,583	2.57	21.695 %
Somalia	637,657	15,893,219	2.874	46.141 %
Eritrea	101,000	3,608,143	8.7	40.72 %
Djibouti	23,200	1,005,379	1.5	78.062 %

The continuous rise in oil prices and environmental concerns of fossil fuels is pushing the horn of African countries to find alternative energy resources. Therefore, the solar energy potential of the Horn of Africa Countries has been analyzed in Section I. The calculated solar radiation values are evaluated in Section II. The regional problems and alternative solutions are reviewed in Section III.

## II. SOLAR ENERGY POTENTIAL OF THE HORN OF AFRICA

Most of the population of the horn of Africa live in rural and remote areas, as shown in Table 1. Due to lack of poor grid infrastructure, communities have no access to electricity. To

overcome this issue, solar energy, with its vast availability throughout the year in the region, is the right option for off-grid applications. In the following section, the potential of solar energy for each country is reviewed separately.

### A. Somalia

Somalia has a high potential for solar energy. Somalia annually receives an average of 2,900 to 3,100 hours of sunshine duration, which is ideal for solar energy utilization [5]. The country has one of the highest daily total solar radiation averages on the earth. Somalia's annual solar radiation estimation is over 2450 kWh/m<sup>2</sup>/year, as shown in [Figure 2]. The daily average of solar radiation is 6.4 kWh/m<sup>2</sup>/day. Furthermore, the country's average annual temperature is 27 °C, which is ideal for the operational life of Photovoltaic (PV) systems [6].

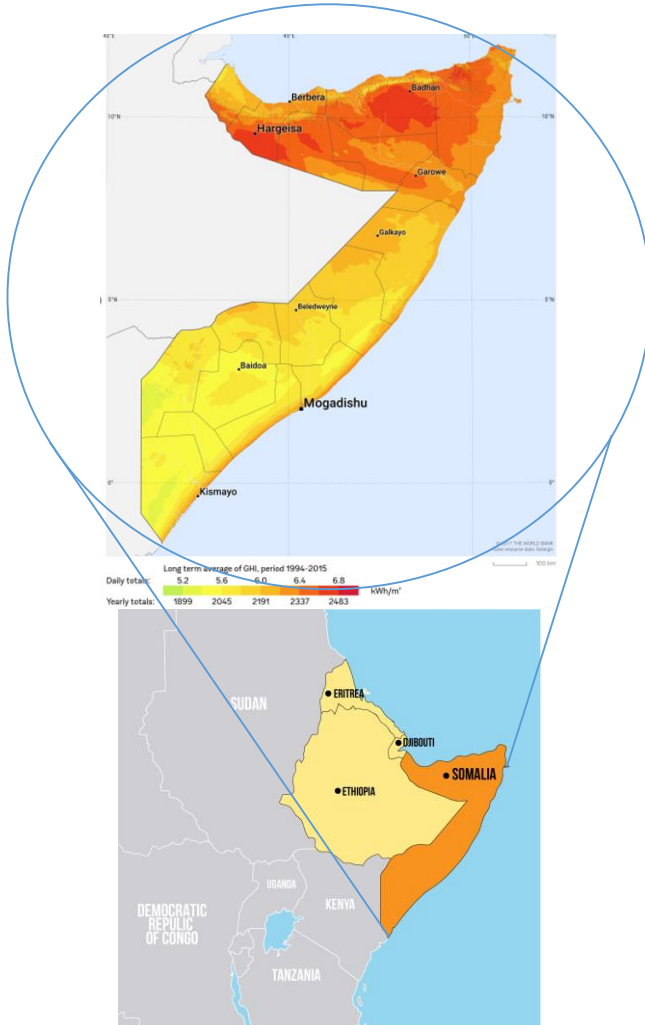


Fig. 2. Somalia solar energy potential map [7]

Over the past years, solar energy is progressively becoming a popular alternative among regional countries. However, the main barrier to develop this widely available energy resource is the traditional habits of the nations on using biomasses, charcoal, and firewood for energy consumption. Somalia depends on foreign oil for practically 82% of its energy needs [8].

TABLE II

MONTHLY AVERAGE SOLAR RADIATION IN SOMALIA [7]

Months	Air temperature [°C]	Daily solar radiation [kWh/m <sup>2</sup> /day]
January	26.4	7.05
February	26.7	7.15
March	27.8	7.14
April	28.9	6.76
May	28.3	6.49
June	26.4	5.72
July	25.6	5.85
August	25.6	6.59
September	26.1	7.13
October	27.2	7.15
November	27.2	6.84
December	27.0	6.63

Most of the electricity consumption is supplied through diesel generators that are running on imported fuel. According to the African Development Bank study on Somalia, the country can potentially generate over 2,000 kWh/m<sup>2</sup> of solar power. Due to higher tariffs of electricity compared to other countries such as Ethiopia and poor infrastructure, around 35% of the country's population has access to electricity according to the United Nation's Somalia energy report.

The Banaadir Electric Company (BECO) is the largest energy provider in the country, operates in Mogadishu and its surroundings as well as some other cities like Kismayo, Afgoye, and supplies 50 MW of electricity [9]. The company aims to increase its annual solar power generation capacity by 5.5 MW, gradually decreasing the share of power generation from fossil fuels, primarily diesel and coal to less than 40%. PV panel installations do not only ensure the access of off-grid power to Somalia, but they also provide electricity to the communication infrastructure [10].

Apart from big cities in the country, there are no bank branches or electricity in the country, particularly in remote areas, which makes it difficult for the rural communities to charge their phones and banking activities. To overcome this, digital money transfers via mobile is in use in the country. As in Figure 3, the PV chargers are used for cell phones in remote areas.



Fig. 3. Somalia's solar chargers for Mobiles and bills

Digital technologies are too expensive for the general public. Rural customers pay in small payments because they are not able to afford to pay the cost of PV panels. Occasionally, utilities have to take a combination of cash and swap with goats

to make a deal. The natural abundance of the sun in Somalia makes it an attractive prospect for investment in renewable energy, particularly solar energy. However, the still-active conflicts in the country cause significant barriers to the investments in this tremendous and vast available solar source [11].

The challenges that influence the activities to exploit solar energy resources of the region. These challenges can be stated in two aspects such as PV installations capacity and finance. For Somalia's case, the main challenge to harness solar energy is public security and national energy regulation policy. With the overthrow of the central government of Somalia an internal conflict started. The national energy company went out of business and its responsibilities for generation, transmission, and distribution vanished. Constituting new regulatory policies is a must for the development of the Somalia energy sector. Off-grid applications for mobile charging and lighting are on high demand, which is a huge opportunity for service providers. Diversification of solar technology systems such as lighting and mobile charging lanterns, water heaters, solar water pumps, and refrigerators is the untapped market, which is ready to invest by related companies. One of the alternative solutions to energy challenges in the horn of Africa is through education. Most of the population is not aware of the abundant solar resources in their region, thus educating the population could allow the rural community to adopt and harvest solar energy with the support of governments. Enforcement and development of energy regulations are also much needed to tackle the lack of electricity. Lowering solar product costs by evaluating the margins, such as entering product duty-free and freight charges. Introducing a different financial mechanism for solar energy consumers is an important aspect to get out of the lack of electricity in the horn of Africa [12-14].

### B. Djibouti

PV systems are gaining significant interest in recent years in both on-grid and off-grid applications, especially refrigeration, lighting, communications, water pumping in Djibouti [15]. Due to the lack of proper infrastructures in rural areas, access to electricity is limited. Electricity generation is expensive. Also, grid infrastructure is lacking investment and maintenance. However, Djibouti has two maximum solar radiation periods between March-April and September-October [16-17]. The solar radiation changes are very slim among the highest and lowest values. It experiences the least amount of solar radiation in June, July, and August, but even in the following months, the country gets enough solar radiation around 5-6 kWh/m<sup>2</sup>/day.

Djibouti has over 3000 hours/year of sunshine duration and solar radiation of 2300 kWh/m<sup>2</sup>/year [Figure 4]. In line with the government's objective to increase the rural area electrification between 2010 and 2025 from 1% to 100%, respectively [18].

Currently, the country imports 70% of its electricity from neighboring Ethiopian. Through the interconnected grid, and the remaining 30% comes from locally running diesel generation units [19]. Regarding the increasing population in the main cities, such as the capital Djibouti, the electricity

demand is getting high and higher. The government improves energy regulations and creates financial support to the energy sector [20].

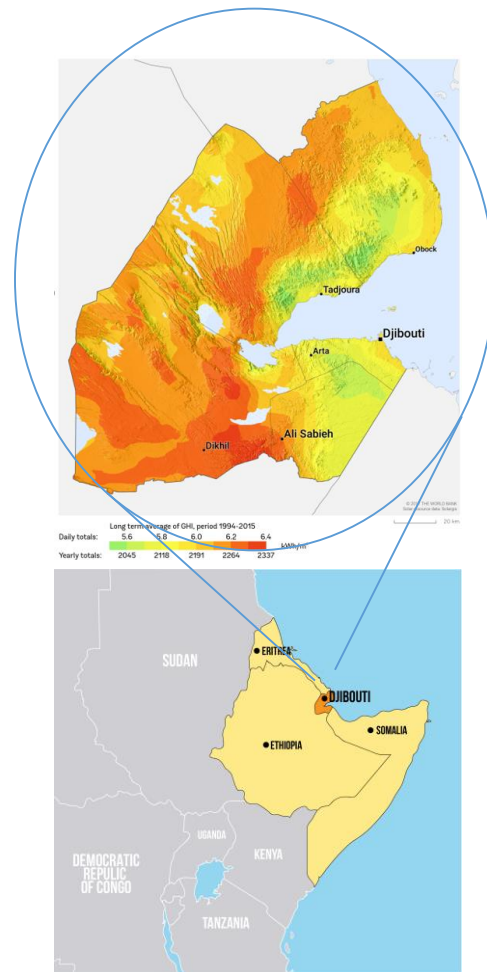


Fig. 4. Djibouti solar energy potential map [7]

TABLE III  
MONTHLY AVERAGE SOLAR RADIATION IN DJIBOUTI [7]

Months	Air temperature [°C]	Daily solar radiation [kWh/m <sup>2</sup> /day]
January	25.1	4.76
February	25.7	5.60
March	27.0	6.24
April	28.7	6.57
May	31.0	6.44
June	34.2	5.79
July	36.0	5.88
August	33.1	5.96
September	29.3	6.21
October	26.9	6.10
November	25.4	5.71
December	36.0	5.08

The rural population's access to electricity increased from 1% in 2010 to 30% in 2017. The first solar power plant of 62 kW in Ali-Addeh, provides electricity to 203 households through the mini-grid system. The second one, 100 kW capacity power plant financed by Korean owned KC Cottrell with a cost of \$2.5M. The third one power plant is in the Dikhil district. The

government of Djibouti is studying the energy needs of four main villages in the country. The Djiboutian Agency for Social Development (ADDS) will provide finance for the villages' energy projects. The ministry of energy is estimating the solar energy potential is as 70MWh/year. To diversify the power generating sources for the whole country through on-grid and off-grid solar energy solutions. Also, international investors have noticed this untapped solar potential in the country. The energy ministry announced several solar energy projects financed by foreign investors. A 300 MW solar power plant with a cost of €360M at the Grand Bara site and other smaller solar projects are notable projects which international investors will finance [21].

### C. Eritrea

Most of the Eritrean highland regions receive around 2200 kWh/m<sup>2</sup>/ of solar radiation each year. This situation shows that solar energy is the right option to meet the population's energy needs in both central cities and rural areas (Figure 5).

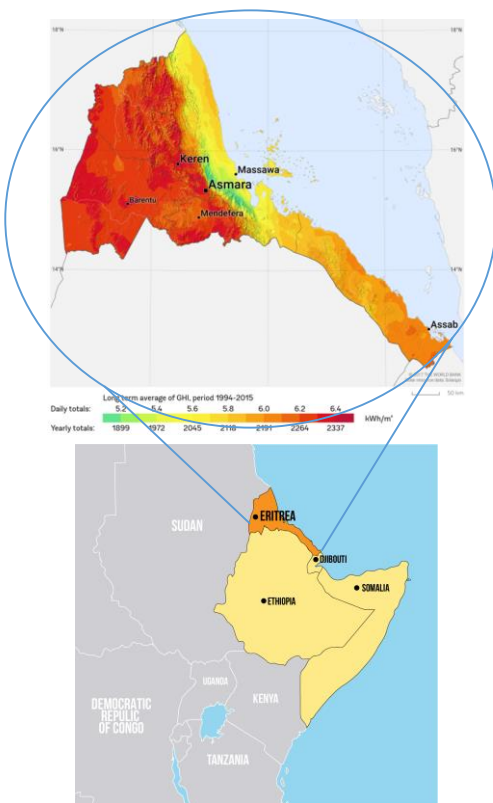


Fig. 5. Eritrea solar energy potential [7]

Till now, the installed solar energy systems in the country are generally for welfare purposes such as powering educational facilities, health stations, communications, village water pumping, and electricity generation. With more regulations and finance, it is possible to feed the main grid with PV systems as well as households in rural areas with solar energy. Average global solar radiation in Eritrea is varying between 5 to 6.55 kWh/m<sup>2</sup>/daily. Currently, traditional biomass is the leading alternative energy in Eritrea. The utilization of firewood and biomass makes up about %78.25 of the total energy output. PV panels are primarily used for electricity production in public

buildings like health stations and educational centers [22]. Biomass-based energy was about 94.5% in the household sector, suggesting only a 5.4% contribution is from electricity, which shows poor access to the country's population to modern energy solutions. In 2009, the PV panel's electricity production accounted for only 0.04%, which shows the low-level solar energy installation in the country [23]. 98% of the generated electricity in the country is from imported fossil fuels. These put a heavy financial weight on the government budget as it subsidizes this electricity. Moreover, due to outdated infrastructure in transmission lines and municipal grids, losses are rising to 23%. The solar photovoltaic systems, solar water heaters, solar desalination plants, tobacco curing, solar crop dryers, solar cooling are among the possible investment opportunities of solar energy in Eritrea. Finally, the generation of electricity from biomass and imported fossil fuels leads to the pollution that contributes to climate change [24].

TABLE IV  
MONTHLY AVERAGE SOLAR RADIATION IN ERITREA [7]

Months	Air temperature [°C]	Daily solar radiation [kWh/m <sup>2</sup> /day]
January	18.9	5.18
February	20.2	5.72
March	22.1	6.23
April	23.9	6.74
May	25.0	6.68
June	24.7	6.62
July	21.7	6.05
August	21.2	5.77
September	22.1	6.19
October	20.9	5.87
November	19.8	5.27
December	18.9	4.90

Areza and Maidma towns of Eritrea had micro-grids installed this year, bringing clean power to 40,000 people funded by the government. It's a hybrid system that uses PV panels, batteries, and diesel generators for back-up. The project aims to serve more than 40,000 residents: 40 different neighborhoods, more than 513 small businesses, 17 education centers, 7 hospitals, as well as and 80 organizations. This € 11.7 million project offers a replication model in other areas of Eritrea. The two plants have a generating capacity of 1.5 MW of PV, 600 kW of a generator, 1 MW PV, and 400 kW generators. These sites have been selected for being off-grid and densely populated areas [25].

Apart from Ethiopia, some of the ongoing solar energy projects in other countries in the region are summarized below.

TABLE V  
SOMALIA, DJIBOUTI, AND ERITREA SOLAR PROJECTS [26]

	Project Name	Size [MW]	Country	Developer	Operator
1	Grand Bara	300	Djibouti	Green, Enerys	EED
2	Jabad gelle hybrid	25	Somalia	BECO	BECO
3	Growe solar	5.9	Somalia	EPS	NECSOM
4	Areza, Maidma	2.25	Eritrea	EEC	EEC
5	Darusalam	2.5	Somalia	BECO	BECO

D. Ethiopia

The average annual solar radiation in the country is more or less uniform, and it's estimated around 5.2kWh/m<sup>2</sup>/day with seasonal variations [27].

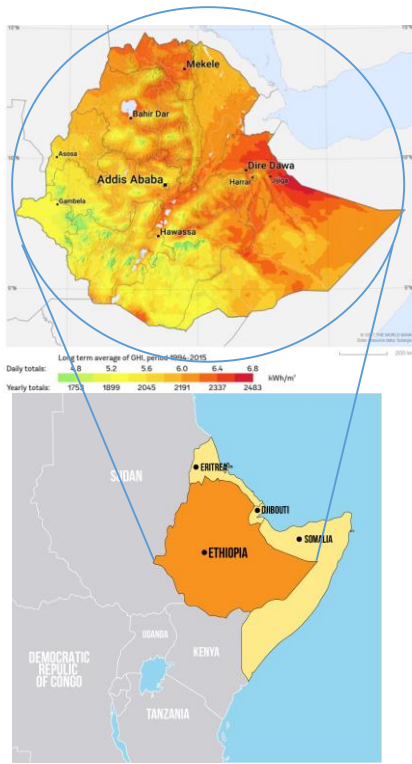


Fig. 6. Global horizontal irradiation map of Ethiopia [7]

Economically, Ethiopia is one of the world's fastest-growing nations, bringing an enormous increase in energy demand. Thus, it is expected the energy demand to growth 10-14% annually until 2037. Today just 27% of the citizens have electricity access [28]. To expand the 27% and connect more community to modern energy, the government is extending the main grid and increase the number of off-grid and mini-grid systems in the country. The majority of current PV electricity production is consumed in telecommunications. Also, other usages of existing solar power are health care centers, educational facility lighting, and village well pumps. The government is planning to connect over 150,000 households to electricity through PV systems. The first large PV plant installed in Ethiopia was a 10.5 kW village grid in 1985, and after four years in 1989, the PV plant is extended to 30 kW [29]. The Ethiopian government is planning to have over 500 MW of installed solar capacity by 2020 [30].

Solar PV capacity in Ethiopia has almost tripled in the past five years. However, 14 MW of solar PV systems has been installed up to now, counting for 0.3% of the Nation's total energy capacity. Ethiopia's solar capacity is expected to increase in the coming years with the number of ongoing solar PV projects [31]. Most of this installed 14 MW solar PV capacity is used for telecom systems, both mobile and landline network stations. In May 2016, the state-owned power

company Ethiopian Electric Power (EEP) initiated the Metehara project, which was Ethiopia's first solar plant tender for 100 MW.

TABLE VI  
MONTH AVERAGE SOLAR RADIATION IN ETHIOPIA [7]

Months	Air temperature [°C]	Daily solar radiation [kWh/m <sup>2</sup> /day]
January	15.9	5.48
February	16.4	5.47
March	17.9	5.64
April	17.6	5.27
May	17.8	5.17
June	17.0	4.47
July	16.6	3.77
August	15.0	3.73
September	15.6	4.50
October	15.8	5.47
November	15.2	5.65
December	15.6	5.27

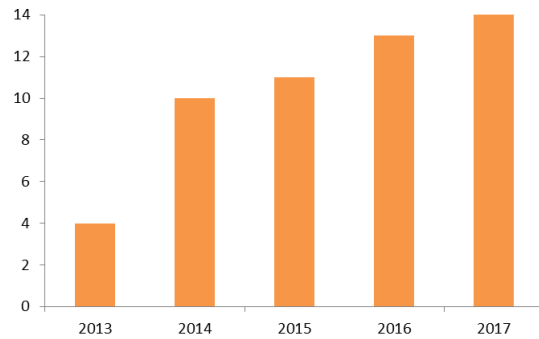


Fig. 7. PV size in Ethiopia (2013-2017)



Fig. 8. Location of Metehara Solar PV Project [32]

In October 2017, the construction of two 125 MW solar PV was launched in two regions Amhara and Dire Dawa of Ethiopia. The latest solar tender, which is 750 MW of solar capacity, is initiated in this year of 2019 [33]. The Ethiopian finance ministry's Public-Private Partnership (PPP) Directorate General on 3 April 2019 launched a request for proposals for two 125MW PV projects being developed through the World Bank Group's Scaling Solar programme [34]. Following the successful issuance of the RFP for Ethiopia Round 1, PPP-DG (Public-Private Partnerships Directorate General) and EEP announced that it would be procuring up to an additional 750MW under the Scaling Solar initiative and formally requested IFC support to implement Ethiopia Scaling Solar Round 2. The RFQ process is ongoing [35-36] The Ethiopian government expects to make sure more than 7 million rural



households to access electricity with stand-alone systems, by 2025 [37-38]. To prevent sub-standard or poor quality products from being flooded. The government approved regulations last year in December that enabled Ethiopian Energy Agency to specify minimum and maximum energy efficiency performance standards for appliances and equipment and provide efficiency certificates to wholesalers or retailers. The new regulation also gives priority to off-grid companies, which generate and supply power to off-grid areas. Some of the ongoing or announced solar projects are summarized below.

TABLE VII  
ETHIOPIA'S SOLAR PV PROJECTS [31]

	Project Name	Cost [\$million]	Capacity [MW]	State	Status
1	Metehara	120	100	Oromia	Scaling Solar
2	Humera	120	100	Tigray	Pending RFP
3	Mekele	120	100	Tigray	Pending RFP
4	Hurso	150	125	Dire Dawa	Awaiting approval
5	Gad	150	125	Somali	Scaling solar
6	Metema	150	125	Amhara	To approve
7	Dicheto	150	125	Afar	Scaling solar
8	Weranso	165	150	Afar	Pending RFP
9	Welenchiti	150	150	Oromia	Pending RFP

### III. A COMPARATIVE CALCULATION MODEL FOR SOLAR POTENTIALS

The solar radiation values that fall on the PV module are calculated for each day by taking the latitude, the longitude, and day numbers of the Horn of Africa countries. The calculated annual solar radiation values are shown graphically in Figure 11. The solar radiation falling on the PV module consists of three parts (Figure 9), such as diffuse radiation, beam radiation, and reflected radiation [39]. Calculations were made by modeling in Matlab Simulink environment (Figure 10).

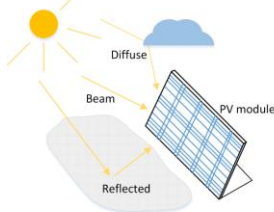


Fig. 9. Solar radiation types striking on the module [40]

$$\delta = 23.45 \sin \left[ \frac{360}{365} (n - 81) \right] \quad (1)$$

$$\beta_A = 90 - L + \delta \quad (2)$$

$$PV_{tilt} = 90 - \beta_A \quad (3)$$

$\delta$ = Solar declination angle

$\beta_A$ = Altitude angle, The altitude angle is the angle between the sun and the local horizon directly beneath the sun.

$PV_{tilt}$ =Optimum PV panel tilt angle

$L$ = the latitude of the site.

$n$ = day number

$$I_{total} = I_{beam} + I_{diffuse} + I_{reflected} \quad (4)$$

$$I_{beam} = I_{BH} R_B \quad (5)$$

$$I_{BH} = I_H - I_{DH} \quad (6)$$

$$R_B = \frac{\cos(L - PV_{tilt}) \cos \delta \sin H_{SRC} + H_{SRC} \sin(L - PV_{tilt}) \sin \delta}{\cos L \cos \delta \sin H_{SR} + H_{SR} \sin L \sin \delta} \quad (7)$$

$$H_{SR} = \cos^{-1}(-\tan L \tan \delta) \quad (8)$$

$$H_{SRC} = \min\{\cos^{-1}(-\tan L \tan \delta), \cos^{-1}[-\tan(L - PV_{tilt}) \tan \delta]\} \quad (9)$$

$$C = \frac{I_H}{I_0} \quad (10)$$

$$\frac{I_{DH}}{I_H} = 1.390 - 4.207C + 5.531C^2 - 3.108C^3 \quad (11)$$

$$I_{diffuse} = I_{DH} \left( \frac{1 + \cos(PV_{tilt})}{2} \right) \quad (12)$$

$$I_0 = \left( \frac{24}{\pi} \right) SC \left[ 1 + 0.034 \cos \left( \frac{360n}{365} \right) \right] (\cos L \cos \delta \sin H_{SR} + H_{SR} \sin L \sin \delta) \quad (13)$$

$$I_{reflected} = \rho I_H \left( \frac{1 - \cos(PV_{tilt})}{2} \right) \quad (14)$$

$I_{total}$ =Total daily solar radiation on the PV module

$I_{beam}$ = Beam solar radiation on the PV module

$I_{diffuse}$ =Diffuse solar radiation on the PV module

$I_{reflected}$ = Reflected solar radiation on the PV module

$I_H$ = Total average daily horizontal solar radiation

$I_{BH}$ = Beam radiation on the horizontal surface

$R_B$ = Beam tilt factor

$H_{SRC}$ =The sunrise hour angle for the collector (when the sun first strikes the collector face,  $\theta = 90^\circ$ )

$H_{SR}$ =The sunrise hour angle (in radians)

$C$ = Clearness index

$I_0$ = Extraterrestrial insolation on a horizontal surface the site

$I_H$ =Insolation on a horizontal surface

$\rho$ =Ground reflectivity

As in Figure 11 depicts, Ethiopia has the highest solar radiation, while Eritrea has the lowest solar radiation. In these calculations, the annual solar radiation values of each city are obtained with the proposed MATLAB model.

Mogadishu, Addis Ababa, Asmara, and Djibouti's annual solar radiation are used to calculate the number of PV modules and the optimum tilt angles concerning the typical load profile. The annual average electrical energy of the load group created for this study is 2,759.4 kWh (Table 8).

TABLE VIII  
TYPICAL DAILY LOAD PROFILE IN THE HORN OF AFRICA REGION

Appliances	#	Running hours/day	Power [W]	Energy [Wh]
Refrigerator	1	6	200	1200
Air conditioner	1	4	1500	6000
Lighting	4	5	18	360

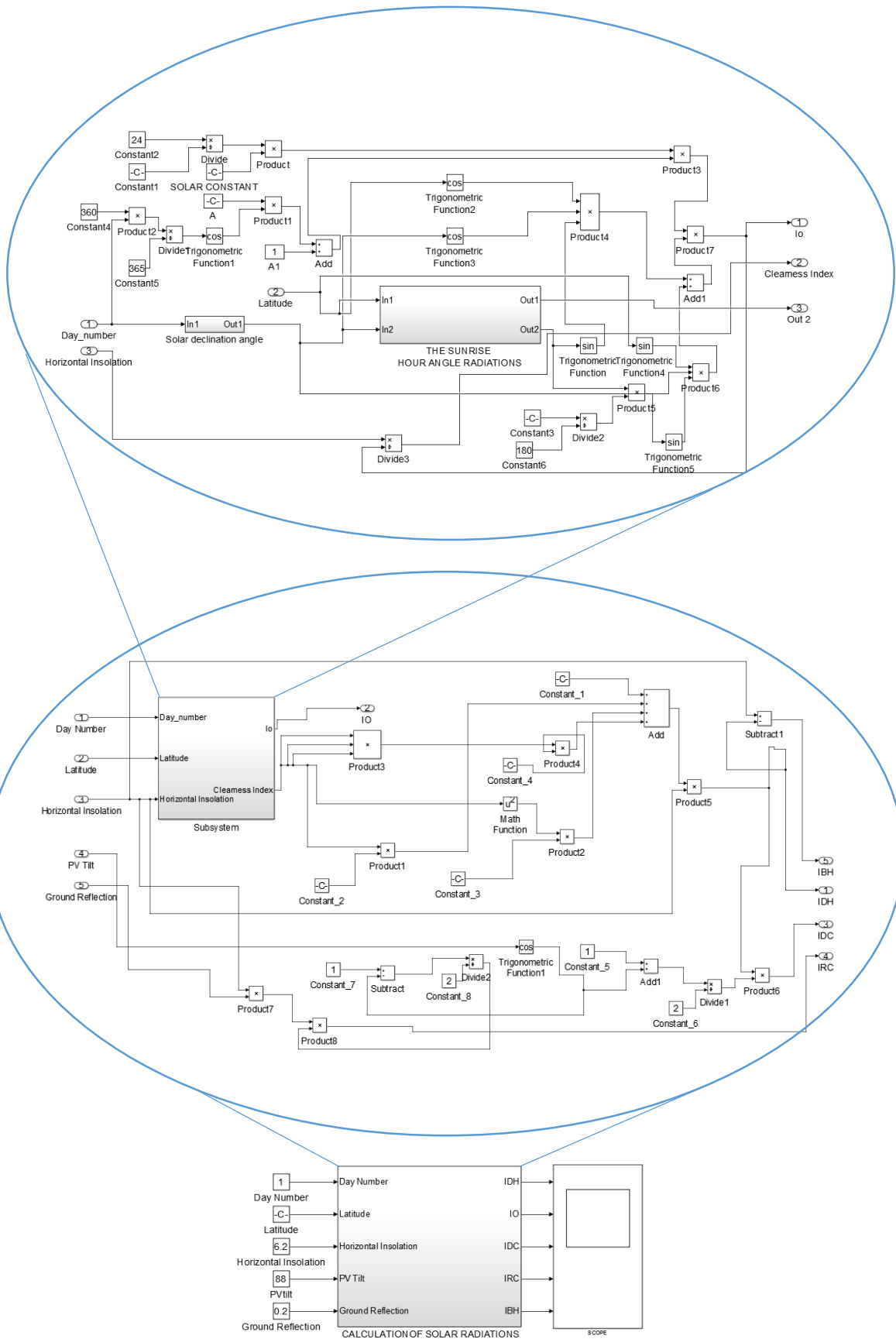


Fig.10. Created Matlab-Simulink model for solar calculations of The Horn of Africa



Fig.11. Annual solar radiation model outputs for the horn of African countries

When Table 9 is analyzed, it is seen that citizens of the Horn of Africa country have very low access to electricity. While forming the load group, the average energy consumption is taken into consideration rather than the electricity access rates. Although the average energy consumption per capita in the world is 2770 kWh per year, this rate is around 570 kWh per year in African countries [33].

TABLE IX  
ELECTRICITY ACCESS RATES OF THE HORN OF AFRICA COUNTRIES [41]

Country	Percentage of Population with access to electricity [%]
Ethiopia	26.6
Somalia	32.7
Eritrea	36.1
Djibouti	53.3

Average daily energy consumption of a typical house based on a sample load model in the region is 11.490 kWh/day, 344.7 kWh/month. The average house annual energy consumption in the horn of African countries is 4136.4 kWh. The technical details of the sample PV module are shown in Table 10.

TABLE X  
JKM380M-72H SOLAR MODULE CHARACTERISTICS [42]

Cell Type	Mono-crystalline
No.of Half-cells	144 (12×12)
Dimensions	1987×992×40mm
Weight	22.5kg
Maximum Power (Pmax)	STC (380Wp)
Maximum Power Voltage (Vmp)	40.5V
Maximum Power Current (Imp)	9.39A
Open-circuit Voltage (Voc)	48.9V
Short-circuit Current (Isc)	9.75A
Module Efficiency STC (%)	19.28%
Operating Temperature(°C)	-40°C~+85°C
Maximum system voltage	1000V DC (IEC)
Maximum series fuse rating	20A
Temperature coefficients of Pmax	-0.37%/°C
Temperature coefficients of Voc	-0.29%/°C
Temperature coefficients of Isc	0.048%/°C
Nominal operating cell temperature (NOCT)	45±2°C
Power tolerance	0~+3%

$$PF=0.86, A_{cell}=0.0225, A_{module}=0.93, n=54$$

$$\eta_{cell} = \% 16.4$$

$$\eta_{module} = \eta_{cell} \cdot PF \gg \% 16.4 \cdot 0.86 = 0.141 \quad (16)$$

$$A_{module} \text{ is } 0.93 \text{ m}^2 \text{ and } \eta_{module} \text{ is calculated as } 0.141$$

$$E_{total} = A \cdot \eta \cdot H \cdot PR \quad (17)$$

Where,

$E_{total}$  = Total produced energy from the PV module [kWh]

$A$  = Total solar panel area [m<sup>2</sup>]

$\eta$  = PV module efficiency [%]

$H$  = Annual average of solar radiation (shadings not included) on tilted PV modules.

$PR$  = Performance ratio, coefficient for losses (range 0.5 to 0.9, default value = 0.75).

$PR$  is a significant value for determining the quality of a photovoltaic installation [43]. It gives the installation performance regardless of inclination and the orientation of the module. It includes all losses. Ethiopia-Addis Ababa receives the highest annual solar radiation (2915.03 kWh/m<sup>2</sup>-year) followed by Somalia-Mogadishu (2215.47 kWh/m<sup>2</sup>-year) then Djibouti-Djibouti (2212.73 kWh/m<sup>2</sup>-year) of solar irradiation and Eritrea with the lowest annual solar irradiation 2198.47 kWh/m<sup>2</sup>-year. Where  $n$  is the season's number of days and  $PV_{tilt}$  is optimum PV module tilted angle.

TABLE XI  
THE CAPITALS ANNUAL SOLAR RADIATION, TOTAL ANNUAL OUTPUT ENERGY AND PV MODULE NUMBER

Country/City	Total annual solar radiation [kWh/m <sup>2</sup> -year]	Total output energy of the system [kWh/year]	Optimum PV module number	Optimum PV tilt angle
Ethiopia-Addis Ababa	2915.03	286.685	10	11.163°
Somalia-Mogadishu	2215.47	217.885	13	2.118°
Eritrea-Asmara	2198.47	204.017	14	15.397°
Djibouti-Djibouti	2212.73	217.616	13	11.900°

Ethiopia-Addis Ababa has the highest total annual solar radiation, which is 2915.03 kWh/m<sup>2</sup>-year, and Eritrea has the lowest 2198.47 kWh/m<sup>2</sup>-year. In terms of the total annual output energy of the PV system, Ethiopia has the lowest PV module number of 10 and an optimum PV tilt angle (fixed system) of 11.163°. In contrast, Eritrea-Asmara have the highest with 14 of PV module numbers with 15.397° of optimum PV tilt angle respectively.

#### IV. CONCLUSIONS

More than half of the population of the region lives in rural and remote areas. Due to lack of weak grid infrastructure, most of these areas, communities have not accessed to electricity, which makes it isolated. To overcome this issue, solar energy with its vast availability throughout the year in the region, is the right option through off-grid solutions.

In this study, annual average solar radiation values that will fall to the off-grid PV system to be established for a typical

house in Horn of Africa countries are calculated on Matlab-Simulink model. Calculations were made by taking into account the number of days, latitude-longitude angles of the region where the PV system will be installed and the PV inclination angles of the optimum. Comparative analyses of the capitals of the countries in the region were performed. As a result of the calculations, Ethiopia-Addis Ababa receives the highest annual solar radiation (2915.03 kWh/m<sup>2</sup>-year) while Eritrea with the lowest annual solar irradiation of (2198.47 kWh/m<sup>2</sup>-year). The total annual energy output of the PV system is also calculated as Ethiopia has the highest with 286.685 kWh/year and Eritrea 216.214 kWh/year as the lowest in the region. Calculations of PV module number and optimum tilt angle are conducted with Ethiopia has the lowest PV module number (10) with the optimum PV tilt angle of 11.163°, Somalia (13) with 2.118°, Eritrea (14) with 15.397° and Djibouti both (13) of PV modules with 11.9°.

#### REFERENCES

- [1] AEEP (Africa EU Energy Partnership), "Country Power Market Brief: Djibouti," Jan. 12, 2021. [www.ruralelec.org/fileadmin/DATA/Documents/06\\_Publications/Market\\_intelligence/AEEP\\_Djibouti\\_Country\\_market\\_brief\\_EN.pdf](http://www.ruralelec.org/fileadmin/DATA/Documents/06_Publications/Market_intelligence/AEEP_Djibouti_Country_market_brief_EN.pdf).
- [2] EIA (Energy Information Administration), Jan. 20, 2021. <https://www.eia.gov/beta/international/regionstoc.php?RegionTopicID=WOTC>
- [3] B. Pillot, M. Muselli, P. Poggi, P. Haurant, I. Hared, "The first disaggregated solar atlas of Djibouti: A decision-making tool for solar systems integration in the energy scheme," *Renewable Energy*, 2013, vol. 57, pp. 57-69.
- [4] AfDB (African Development Bank). "The Horn of Africa Opportunity," Jan. 20, 2021. [https://www.afdb.org/fileadmin/uploads/afdb/Documents/Generic-Documents/Investing\\_in\\_Transition\\_States-The\\_Horn\\_of\\_Africa\\_Opportunity\\_-\\_A\\_briefing\\_note\\_for\\_South\\_Korean\\_investors.pdf](https://www.afdb.org/fileadmin/uploads/afdb/Documents/Generic-Documents/Investing_in_Transition_States-The_Horn_of_Africa_Opportunity_-_A_briefing_note_for_South_Korean_investors.pdf)
- [5] J.M. Huacuz, L. Gunaratne, *Photovoltaics and Development, in: Handbook of Photovoltaic Science and Engineering*, Wiley, England, 2003, pp. 1043-1071.
- [6] U. Deichmann, C. Meisner, S. Murray, D. Wheeler, "The economics of renewable energy expansion in rural Sub-Saharan Africa," *Energy Policy*, 2011, vol. 39, pp. 215-227.
- [7] World Bank Group, Energy Sector Management Assistance Program, Solargis [Online] Available: <https://globalsolaratlas.info/map>
- [8] State Minister for Environment, Office of the Prime Minister and Line Ministries and Ministry of Planning Federal Government of Somalia, "Somalia's intended nationally determined contributions," Jan. 12, 2021. <https://www4.unfccc.int/sites/ndcstaging/PublishedDocuments/Somalia%20First/Somalia%27s%20INDCs.pdf>
- [9] International Labor Organization (ILO), "Scoping study for a renewable energy skills development Public Private Development Partnership (PPDP) in Somalia" Apr. 2021. [https://www.ilo.org/wcmsp5/groups/public/---africa/---ro-abidjan/---sro-addis\\_ababa/documents/publication/wcms\\_547596.pdf](https://www.ilo.org/wcmsp5/groups/public/---africa/---ro-abidjan/---sro-addis_ababa/documents/publication/wcms_547596.pdf)
- [10] BECO (The Banaadir Electric Company). <https://www.beco.so/>
- [11] P.A Trotter, R. Maconachie, M.C. McManus, "Solar energy's potential to mitigate political risks: The case of an optimised Africa-wide network," *Energy Policy*, 2018, vol. 117, pp. 108-126.
- [12] N. Plain, B. Hingray, S. Mathy, "Accounting for low solar resource days to size 100% solar microgrids power systems in Africa," *Renewable Energy*, 2019, vol. 131, pp. 448-458.
- [13] Federal Government of Somalia and African Development Bank, "Somalia: Energy Sector Need Assessment and Action/Investment Programme," Apr. 16, 2021. [https://www.afdb.org/fileadmin/uploads/afdb/Documents/Generic-Documents/Final\\_Somalia\\_Energy\\_Sector\\_Needs\\_Assessment\\_FGS\\_AfDB\\_November\\_2015.pdf](https://www.afdb.org/fileadmin/uploads/afdb/Documents/Generic-Documents/Final_Somalia_Energy_Sector_Needs_Assessment_FGS_AfDB_November_2015.pdf)
- [14] The United Nations Children's Fund (UNICEF), "Evaluation of the Performance of Solar Powered Water Systems in Somalia," Apr. 18, 2021. [https://www.unicef.org/evaldatabase/index\\_95035.html](https://www.unicef.org/evaldatabase/index_95035.html)
- [15] B. Pillot, M. Muselli, P. Poggi, J.B. Dias, "Satellite-based assessment and in situ validation of solar irradiation maps in the Republic of Djibouti," *Solar Energy*, 2015, vol. 120, pp. 603-619.
- [16] International Renewable Energy Agency (IRENA), "Renewable energy technologies cost analysis series-biomass," Apr. 22, 2021. <https://www.irena.org/publications/2012/Jun/Renewable-Energy-Cost-Analysis---Biomass-for-Power-Generation>
- [17] A.I. Omar, J. Virgone, E. Vergnault, D. David, A. I. Idriss, "Energy Saving Potential with a Double-Skin Roof Ventilated by Natural Convection in Djibouti," *Energy Procedia*, 2017, vol. 140, pp. 361-373.
- [18] M. Mussard, M. Amara, "Performance of solar photovoltaic modules under arid climatic conditions: A review," *Solar Energy*, 2018, vol. 174, pp. 409-421.
- [19] S. Baurzhan, G.P. Jenkins, "Off-grid solar PV: Is it an affordable or appropriate solution for rural electrification in Sub-Saharan African countries?" *Renewable and Sustainable Energy Reviews*, 2016, vol. 60, pp. 1405-1418.
- [20] International Renewable Energy Agency (IRENA), "Djibouti Renewables readiness assessment," Apr. 23, 2021. [https://www.irena.org/-/media/Files/IRENA/Agency/Publication/2015/IRENA\\_RRA\\_Djibouti\\_2015\\_EN.pdf](https://www.irena.org/-/media/Files/IRENA/Agency/Publication/2015/IRENA_RRA_Djibouti_2015_EN.pdf)
- [21] Djibouti Social Development Agency. <http://www.adds.dj/en/rural-electrification-ali-addeh-adds-strengthens-the-capacity-of-the-central/>
- [22] IEA (International Energy Agency). <https://www.iea.org/countries/Eritrea>
- [23] International Energy Agency (IAE) International Renewable Energy Agency (IRENA), United Nations Statistics Division, World Bank Group, "2019 The Energy Progress Report," Apr. 19, 2021. [https://sustainabledevelopment.un.org/content/documents/2019\\_Tracking\\_SDG7\\_Report.pdf](https://sustainabledevelopment.un.org/content/documents/2019_Tracking_SDG7_Report.pdf)
- [24] Climate Technology Centre & Network and United Nations Industrial Development Organization (UNIDO), Apr. 25, 2021. <https://www.ctc-n.org/content/eritrea-2012>
- [25] S. Cox, P. Gagnon, S. Stout, O. Zinaman, A. Watson, E. Hotchkiss, "Distributed generation to support development-focused climate action," United States Agency for International Development (USAID) and National Renewable Energy Laboratory (NREL), Apr. 25, 2021. <https://www.nrel.gov/docs/fy16osti/66597.pdf>
- [26] The main issues and opportunities were identified in the "EU TAF for the SE4All initiative – Eastern and Southern Africa, Mission to Eritrea in the energy sector" report, October 2014.
- [27] United States Agency for International Development (USAID), "Off-Grid Solar Market Assessment," Apr. 25, 2021. [https://www.usaid.gov/sites/default/files/documents/1860/PAOP-Ethiopia-MarketAssessment-Final\\_508.pdf](https://www.usaid.gov/sites/default/files/documents/1860/PAOP-Ethiopia-MarketAssessment-Final_508.pdf)
- [28] Solar Energy Development Association Ethiopia, Ethio Resource Group (ERG), "Solar energy vision for Ethiopia Opportunities for creating a photovoltaic industry in Ethiopia," Apr. 28, 2021. [https://www.sun-connect-news.org/fileadmin/DATEIEN/PV-Industry-ET-04-09-12\\_final.pdf](https://www.sun-connect-news.org/fileadmin/DATEIEN/PV-Industry-ET-04-09-12_final.pdf)
- [29] G. A. Tiruye et al, "Opportunities and Challenges of Renewable Energy Production in Ethiopia," *Sustainability*, 2021, vol. 13, 10381.
- [30] World Bank, "Project Appraisal Document on a Proposed Credit in the Amount of SDR 86.0 Million (US\$ 130 million Equivalent) to the Federal Democratic Republic of Ethiopia for a Second Electricity Access Rural Expansion Project," Apr. 30, 2021. <https://documents1.worldbank.org/curated/en/154751468038131697/pdf/38158.pdf>
- [31] Ministry of Finance and Economic Development, "Federal Democratic Republic of Ethiopia (2015) The Second Growth and Transformation Plan," Apr. 30, 2021. <http://extwprlegs1.fao.org/docs/pdf/eth144893.pdf>
- [32] Solar Energy Development Association Ethiopia, Ethio Resource Group (ERG), "Off-grid solar development in Ethiopia: Market intelligence study report". Addis Ababa: Ethiopia Resource Group. Study commissioned by the Climate and Development Knowledge Network (CDKN), May, 12, 2021. [https://cdkn.org/wp-content/uploads/2018/09/Ethiopia-Solar-Power-PB\\_for-web.pdf](https://cdkn.org/wp-content/uploads/2018/09/Ethiopia-Solar-Power-PB_for-web.pdf)
- [33] E. Baker, M. Fowlie, D. Lemoine, S.S. Reynolds, "The Economics of Solar Electricity," *Annual Review of Resource Economics*, 2013 vol. 5: Submitted. Doi: 10.1146/annurevresource-091912-151843

- [34] International Renewable Energy Agency (IRENA), 2012a. Renewable energy technologies: Cost analysis series; Volume 1: Power Sector Issue 2/6, Concentrating Solar Power.
- [35] Cross-border Information (CbI), <https://www.africa-energy.com/live-data/article/ethiopia-scaling-solar-rfp-launched>
- [36] Cross-border Information (CbI), <https://www.ifc.org/wps/wcm/connect/f4df6171-1018-4003-ad9d-938ce4866c15/scaling-infra-solar-08.pdf?MOD=AJPERES&CVID=Msczfcy>
- [37] World Bank Group, Apr. 10, 2021. <https://www.scalingsolar.org/active-engagements/ethiopia/>
- [38] World Bank, Apr. 12, 2021. <http://documents.worldbank.org/curated/en/724741556102180951/pdf/Environmental-and-Social-Impact-Assessment-for-Metehara-Solar-Power-PV-Plant.pdf>
- [39] R. Celikel, A. Gundogdu, "Comparison of PO and INC MPPT methods using FPGA in-the-loop under different radiation conditions", *Balkan Journal of Electrical&Computer Engineering*, vol.9, 2, pp. 114-122.
- [40] Gilbert M. Masters, *Renewable and Efficient, Electric Power Systems*, John Wiley & Sons, Inc., Hoboken, New Jersey
- [41] United Nations Environment Programme (UNEP), Apr. 11, 2021. <https://wedocs.unep.org/>
- [42] Jinko Solar, JKM380M-72H solar module. Apr. 13, 2021. <https://jinkosolar.eu/files/jinko/module/datasheets%2007.2019/SWAN%20DG%20JKM380-400M-72H-BDVP-F40-A2-EN.pdf>
- [43] O. Cicek, M.A.M. Millad, F. Erken, "Energy prediction based on modelling and simulation analysis of an actual grid-connected photovoltaic power plant in Turkey", *European Journal of Technique (EJT)*, vol. 9, 2, pp. 2019.

## BIOGRAPHIES



**Erkan Dursun** (Member, IEEE) received the B.Sc., M.Sc., and Ph.D. degrees in Electric Education from the Faculty of Technical Education, Marmara University, Istanbul, Turkey, in 2001, 2006, and 2013, respectively. From 2010 to 2012, he was a Visiting Fellow with the United Nations Industrial Development

Organization-International Centre for Hydrogen Energy Technologies (UNIDO-ICHET). From 2012 to 2013, he was a Researcher with the Joint Research Center, European Commission, Italy. His research interests include distributed generation, hybrid power systems, and smart grid. His papers have received more than 600 citations in SCI database of Thomson Reuters

# Publication Ethics

The journal publishes original papers in the extensive field of Electrical-electronics and Computer engineering. To that end, it is essential that all who participate in producing the journal conduct themselves as authors, reviewers, editors, and publishers in accord with the highest level of professional ethics and standards. Plagiarism or self-plagiarism constitutes unethical scientific behavior and is never acceptable.

By submitting a manuscript to this journal, each author explicitly confirms that the manuscript meets the highest ethical standards for authors and coauthors

**The undersigned hereby assign(s) to *Balkan Journal of Electrical & Computer Engineering* (BAJECE) copyright ownership in the above Paper, effective if and when the Paper is accepted for publication by BAJECE and to the extent transferable under applicable national law. This assignment gives BAJECE the right to register copyright to the Paper in its name as claimant and to publish the Paper in any print or electronic medium.**

Authors, or their employers in the case of works made for hire, retain the following rights:

1. All proprietary rights other than copyright, including patent rights.
2. The right to make and distribute copies of the Paper for internal purposes.
3. The right to use the material for lecture or classroom purposes.
4. The right to prepare derivative publications based on the Paper, including books or book chapters, journal papers, and magazine articles, provided that publication of a derivative work occurs subsequent to the official date of publication by BAJECE.
5. The right to post an author-prepared version or an official version ( preferred version) of the published paper on an internal or external server controlled exclusively by the author/employer, provided that (a) such posting is noncommercial in nature and the paper is made available to users without charge; (b) a copyright notice and full citation appear with the paper, and (c) a link to BAJECE's official online version of the abstract is provided using the DOI (Document Object Identifier) link.



ISSN: 2147- 284X  
Year: July 2021  
Volume: 9  
Issue: 3

### CONTENTS

- M. E. Başoğlu;** Comparisons of Different Maximum Power Point Tracking Strategies with Zeta Converter,..... 221-228
- A. Bas, H. E. Kocer;** Real-Time Hand Motion Recognition: A Robust Low-Cost Approach,.....229-234
- B. Buz, B. Gülççek, Ş. Bahtiyar;** A Hybrid Machine Learning Model to Detect Reflected XSS Attack,.....235-241
- Murat Aslan;** An Approach Based on Tunicate Swarm Algorithm to Solve Partitional Clustering Problem,.....242-248
- H. Ali, E. Erçelebi;** Development of an Embedded System for Building System Management Based on PV-Powered,.....249-254
- H. Savci, H. Sajjad, S. Khan, F. Kaburcuk;** A Compact Multi-Band Antenna on Textile for Wearable Body Area Network Devices,.....255-260
- S. Doğusan;** Design and Optimization of Directive Circular Patch Antenna with Asymmetric Pixels Using Genetic Algorithm,.....261-267
- S. I. Omurca, E. Ekinci, E. Yakupoğlu, E. Arslan, B. Çapar;** Automatic Detection of the Topics in Customer Complaints with Artificial Intelligence,.....268-277
- G. Ertaş;** Signal Attenuation Model Free Classification of Diffusion MR Signals of the Breast Tissue using Long Short-Term Memory Networks,.....278-283
- M.E.Asker, H. Kürüm;**A Novel Chaotic Switched Modulation for EMI Suppression in Electrical Drive System,284-289
- İ. Özer;** Classification of Urease Activity in Full-Fat Soybean Production by Extrusion Using Machine Learning Algorithms,.....290-296
- E. Ozdogan, R. Das;** IoT based a Smart Home Automation System Design: Simulation Case,.....297-303
- G. Mendi, C. Budak;** Automatic Cell Nucleus Segmentation Using Superpixels and Clustering Methods in Histopathological Images,.....304-309
- E. Dursun;** Solar Energy Potential in Horn of Africa: A Comparative Study Using Matlab/Simulink ,.....310-319

## BALKAN JOURNAL OF ELECTRICAL & COMPUTER ENGINEERING

(An International Peer Reviewed, Indexed and Open Access Journal)

#### Contact

Batman University  
Department of Electrical-Electronics Engineering  
Bati Raman Campus Batman-Turkey

Web: <http://dergipark.gov.tr/bajece>  
<http://www.bajece.com>  
e-mail: [bajece@hotmail.com](mailto:bajece@hotmail.com)

